VERSLAGEN EN VERHANDELINGEN

REPORTS AND TRANSACTIONS

NATIONAAL LUCHTVAARTLABORATORIUM

NATIONAL AERONAUTICAL RESEARCH INSTITUTE

AMSTERDAM

XV — 1949

ERRATA VOL. XV, 1949.

Report V. 1543:	page number	V 60	should	read	V 2
	„ „	V 61	„	„	V 3
	„ „	V 62	„	„	V 4

Report V. 1547: page V 6: In eq. (3.9) H_n should read K_n.

Preface

This volume of "Verslagen en Verhandelingen" contains, as usual, a collection of reports on the research work carried out at the National Aeronautical Research Institute during the latter years.

For a brief review of the research organization and the publication policy reference may be made to the preface of Vol. XIII (1947). For various reasons, the contents of this volume consist mainly of reports of the Flutter and Structures Sections, the main reason being the intensive engagement of other sections with ad-hoc research and with the development of modern experimental equipment. Thus, no true representation is given of the total work of the institute, an impression of which may be gained from the Annual Reports (in Dutch), which are available upon request.

All of the reports contained in this volume were distributed upon completion to research institutes and workers actively engaged in the relevant field of aeronautical science. Reprints are available upon request as long as the stock lasts.

Publications of the members of the scientific staff of the institute which were issued in typescript form or published in scientific journals during the period from November 1947 to the end of 1949 are listed on the following pages.

C. KONING
Scientific Director

Amsterdam, January 1950.

Contents

List of Publications Issued in Typescript or Published in Scientific Journals between 1st November 1947 and 1st January 1950

N.B. These reports are in English, unless indicated otherwise.

A. 1035	Slotboom, J. G.	Lift distribution for tapered wings with prismatic centre section. (Interpolation curves) (in Dutch)	1946
A. 1096	Slotboom, J. G.	The efficiency of diffusors. (in Dutch)	1948
A. 1104	Dobbinga, E.	A new type of balance for windtunnels (coefficient balance) (in Dutch)	1948
A. 1122	Zwaaneveld, J.	Important data of some high speed windtunnels	1949
A. 1125	Slotboom, J. G.	Investigation of some model-diffusors for the low-turbulence tunnel. (in Dutch)	1949
A. 1136	De Lathouder, A.	The development of the windtunnel complex of the Nationaal Luchtvaartlaboratorium. (in Dutch)	1948
A. 1159	Thomas, C.	Application of Young's experiment to measurements on systems of lenses. (in Dutch)	1948
A. 1161	Slotboom, J. G.	Preliminary investigations on the behaviour of a suction-slot for the diffusor of the low-turbulence windtunnel. (in Dutch)	1949
A. 1165	Benthem, J. P.	Investigation of the influence of gauzes on a uniform and a non-uniform flow. (in Dutch)	1949
A. 1180	Slotboom, J. G.	Investigations on the behaviour of a suction-slot for the diffusor of the low-turbulence windtunnel (in Dutch)	1949
A. 1184	De Bruijn, J. A. M.	The required air exchange for cooling the pilot tunnel (1:5 scale model of the H. S. tunnel) (in Dutch)	1949
A. 1194	—	Three-component measurements on a circular-arc plate profile. (in Dutch)	1949
A. 1195	Hendal, W. P.	Some results of tests on strain gauges glued with "Araldit". (in Dutch)	1949
F. 9	Greidanus, J. H.	Electro-dynamic generation of mechanical vibrations. (in Dutch)	1947
F. 10	Greidanus, J. H.	Introductory consideration of some important problems in the aerodynamic theory of aerofoil profiles. (in Dutch)	1947
F. 11	Timman, R.	Mathematical principles of a method to obtain aerofoils with a prescribed distribution of pressure. (in Dutch)	1947
F. 12	Timman, R.	Computation of aerofoil profiles for a given pressure distribution. Part I: Symmetrical profiles. (in Dutch)	1947
F. 13	Timman, R.	Computation of aerofoil profiles for a given pressure distribution. Part II: Cambered profiles. (in Dutch)	1948
F. 14	Cohen, J.	Investigation into the application of the methods of Theodorsen and Garrick for the calculation of an aerofoil	1947
F. 21	Erdmann, S. F.	Note on the problem of initial values in the design of supersonic nozzles in connection with a measured velocity distribution	1947
F. 22	Greidanus, J. H.	Two theorems on the calculation of natural vibrations of linear elastic systems. (in Dutch)	1947
F. 23	Timman, R.	Investigation of the properties of convergence of coefficients in several formulae for numerical integration and interpolation. (in Dutch)	1948
F. 25	Greidanus, J. H.	Notes on the mathematical problem of the design of windtunnel contractions with axial symmetry	1948
F. 29	V. d. Vooren, A. I.	Remarks on formulae and numerical methods used in the gust load calculations of Report F. 28	1948
F. 30	Greidanus, J. H.	Symmetrical gust loads (lecture). De Ingenieur 10 September, p. 0—77. (in Dutch)	1948

F. 31	Timman, R.	The calculation of the aerodynamic forces on oscillating wings in compressible flow (lecture). De Ingenieur 8 October, p. 0—87. (in Dutch)	1948
F. 32	Timman, R.	The numerical evaluation of the Poisson integral	1948
F. 38	Van Heemert, A.	A generalisation of the formula of Parseval	1948
F. 39	Erdmann, S. F.	A small supersonic windtunnel of the Nationaal Luchtvaartlaboratorium. (published in TNO-Nieuws, Febr.) (in Dutch)	1949
F. 40	Van Heemert, A. Huiskamp, R. G. N.	Determination of the field of flow in a certain windtunnel-contraction cone by a relaxation method. (in Dutch)	1948
F. 43	Greidanus, J. H. V. d. Vooren, A. I.	Mathematical principles of flutter analysis	1949
F. 46	Timman, R.	Asymptotic formulae for special solutions of the hodograph equations in compressible flow	1949
F. 49	Greidanus, J. H.	Aerodynamics of supersonic rockets. (Dutch with English summary). Also published in: Symposium over raketten. Voordrachten Kon. Inst. van Ingenieurs, no. 6	1949
F. 50	V. d. Vooren, A. I.	Calculation of eigenvalues and eigenvectors of matrices. (in Dutch)	1949
F. 51	Van Heemert, A.	The calculation of downwash fields for a lifting plane in steady flow	1949
F. 53	Timman, R.	Some remarks on the theory of near-sonic, near-parallel flow and its application to channel flow	1949
F. 54	Timman, R. V. d. Vooren, A. I.	Theory of the oscillating wing with aerodynamically balanced control-surface in a two-dimensional subsonic compressible flow...	1949
M. 1275	Hartman, A.	Mechanical properties of glued metal-to-metal joints, I. (in Dutch)	1948
M. 1291	Hartman, A.	Testing of some cold-setting Dutch and foreign synthetic resin glues for wood. (in Dutch)	1948
M. 1296	Hartman, A.	Some experiments on the influence of the dimensions on the shear strength of glued beech test pieces. (in Dutch)	1948
M. 1475	—	Mechanical properties of glued metal-to-metal joints, II. (in Dutch)	1949
S. 323	—	Form factors of wooden box beams	1947
S. 325	Plantema, F. J.	Apparatus for strength testing aeroplanes (lecture). De Ingenieur 9 Januari 1948, p. L. 1. (in Dutch)	1948
S. 328	Floor, W. K. G.	Experimental investigation of the post-buckling behaviour of stiffened, flat, rectangular plates under combined shear and compression. Part II	1947
S. 329	—	Numerical example of the application of the manual for wing analysis. (Report S. 250). (in Dutch)	1947
S. 330	Plantema, F. J. Rondeel, J. H.	Compression tests on tubes with and without annealed ends	1948
S. 332	Plantema, F. J.	Calculation of the buckling load of sandwich plates by the energy method I. (in Dutch with English summary)	1948
S. 333	Plantema, F. J.	Calculation of the buckling load of sandwich plates by the energy method II. (in Dutch with English summary)	1948
S. 334	Plantema, F. J.	Literature search on sandwich constructions I. Theoretical papers concerning the stability of flat plates. (in Dutch with English summary)	1948
S. 339	Floor, W. K. G.	English methods and apparatus for static measurements with electrical resistance strain gauges. (in Dutch)	1948
S. 340	Floor, W. K. G.	Reliability of the drop weight reduction method for simulating wing lift effect in landing gear drop tests	1948
S. 342	—	Literature search on sandwich constructions III. Collection of material properties of core and face materials. (in Dutch with English summary)	1948
S. 343	—	Literature search on sandwich constructions II. Comparison of theory and experiments for flat plates. (in Dutch with English summary)	1948
S. 350	—	Shear and tensile tests on sandwich core materials	1949

S. 357	Van Meer, H. P. Plantema, F. J.	Fatigue of structures and structural components. (in Dutch with English summary)	1949
S. 361	De Kock, A. C. Plantema, F. J.	The analysis of observations. (in Dutch with English summary)...	1949
V. 1369	—	Strength requirements for glider take off when using a winch. (in Dutch)	1948
V. 1375	—	Comments on the English, American and International airworthiness requirements. (in Dutch)	1946
V. 1421	Marx, A. J. Buhrman, J.	Assisted Control II (the effect of spring tabs on the static longitudinal stability. (in Dutch with abstract in English)	1947
V. 1423	Marx, A. J.	Proposal for climb requirements on a rational basis	1947
V. 1430a	Lucassen, L. R.	Flight tests with the Sikorsky S. 51 helicopter PH-HAA. (in Dutch)	1949
V. 1431	Marx, A. J. Buhrman, J.	Assisted Control III. Power Operated Flight Controls. (in Dutch with abstract in English)	1948
V. 1438	—	Tail loads during a pull-up from horizontal flight IV. A method for computing aircraft tail loads during a pull-up from horizontal flight for any given elevator motion	1948
V. 1461	—	Determination of the frequency distribution of gust loads on the line Amsterdam—Bandung from strain measurements. (in Dutch)	1948
V. 1463	Lucassen, L. R. Meijer Drees, J. Senger, E. C.	Emergency landing after power failure with a Sikorsky S-51 helicopter	1948
V. 1464	Lucassen, L. R. Meijer Drees, J.	Flight tests with the Sikorsky S. 51 helicopter PH-HAA. (in Dutch)	1949
V. 1466	Meijer Drees, J.	Correction method for helicopters, in particular the Sikorsky S-51. Powered flight. (in Dutch)	1948
V. 1489	Van Munster, G. V. d. Linden, J. C. Pool, A.	Modification, testing and application of an electrical attitude gyro (made by Sperry, type no. F-1) for use as a measuring apparatus during flight tests. (in Dutch)	1949
V. 1494	Meijer Drees, J.	Airports for helicopters. (in Dutch)	1949
V. 1495	Meijer Drees, J. Lucassen, L. R.	Theoretical investigation of the performance of helicopters in curved flight. (in Dutch)	1949
V. 1500	—	Definitions. 3rd Edition. (in Dutch)	1949
V. 1532	Meijer Drees, J.	Experiences with the Sikorsky S-51 helicopter. (in Dutch)	1949
RB. 294	De Lathouder, A. Van Oosterom, T.	Report of the visit to the A. B. Aerotransport and the Flygtekniska Försöksanstalten, Stockholm, on 13th to 15th November 1945. (in Dutch)	1945
RB. 302	Palm, J. H. Plantema, F. J.	Report of a visit to Sweden in April 1947. (in Dutch)	1947
RB. 306	Plantema, F. J. Palm, J. H.	Report of a visit to Paris in November 1947. (in Dutch)	1947
RB. 312	Plantema, F. J.	Report of two visits to England in May and November 1947. (in Dutch)	1947
RB. 314	Timman, R.	Report on a stay in England during the first quarter of 1949. (in Dutch)	1949
—	Posthumus, S.	The proposed extensions of the NLL. De Ingenieur, 6 Febr. 1948 p. A. 45. (in Dutch)	1948
—	Timman, R.	A method of computing aerofoils for a specified pressure distribution (lecture). De Ingenieur, 9 April 1948, p. L. 15. (in Dutch)	1948
—	Palm, J. H.	The significance of the reversed-bending number for judging sheet metal. Metalen II, 10 June 1948, p. 210. (in Dutch)	1948
—	Marx, A. J.	Aeroplane flight research, methods of observation and apparatus (lecture). De Ingenieur, 11 June 1948, p. O. 53. (in Dutch) ...	1948
—	Palm, J. H.	Dissolved carbon and nitrogen causes of discontinuous yielding and strain ageing of mild ferritic steel. De Ingenieur, 2 July 1948, p. Mk. 81	1948

—	Marx, A. J.	Proposal for climb requirements on a rational basis. (Lecture; abbreviated version of report V. 1423). De Ingenieur, 27 Aug. 1948, p. L. 39	1948
—	Palm, J. H.	Stress-strain relations for uniaxial loading. Appl. Sci. Research, Vol. A. 1, p. 198	1948
—	De Lathouder, A. Wiselius, S. I.	The development of the windtunnel complex of the Nationaal Luchtvaartlaboratorium (lecture). De Ingenieur, 8/10/1948, p. L. 50 and 3/12/1948, p. L. 59. (in Dutch)	1948
—	V. d. Neut, A.	Experimental investigation of the post-buckling behaviour of flat plates loaded in shear and compression. Proc. VII Int. Congr. for Appl. Mech., Vol. I, pp. 174—186	1948
—	Plantema, F. J.	Some investigations on the Euler instability of flat sandwich plates with simply-supported edges. Proc. VII Int. Congr. for Appl. Mech., Vol. I, pp. 200—213	1948
—	Timman, R.	Linearisation of the equations of two-dimensional subsonic compressible flow by means of complex characteristics. Proc. VII Int. Congr. for Appl. Mech., Vol. IV, pp. 28—42	1948
—	Palm, J. H.	Evaluation of the cold brittleness of thin-sheet steel with the reversed bending test. (Dutch with English summary), Metalen, III, No. 7, 7 March 1949	1949
—	—	New calibrating equipment for testing machines at the NLL. (in Dutch). TNO-Nieuws, 4, no. 35, March 1949, p. 94	1949
—	Hartman, A.	Strength of glued metal-to-metal joints. (in Dutch). De Ingenieur, Vol. 61, nr. 11, 18-III-1949	1949
—	V. Munster, G.	Deviation of altimeter and airspeed indicator of an aeroplane during approach and landing. (in Dutch). Polyt. Tijdschrift, Vol. 4, no. 17—18, 3 May 1949, p. 320	1949
—	Palm, J. H.	Stress-strain relations and necking criteria for triaxial loading, two principal stresses being equal. Appl. Sci. Res. A 1. no. 5/6, pp. 353—377	1949
—	Palm, J. H.	Stress-strain relations for uniform monotonic deformation under triaxial loading. Appl. Sci. Res. A 2, no. 1, pp. 54—92	1949
—	Meijer Drees, J.	A theory of airflow through rotors and its application to some helicopter problems. J. Hel. Assoc. G. B., Vol. 3, no. 2, July-Aug.-Sep. 1949, pp. 79—104	1949
—	Hartman, A.	Stress corrosion of light metals. (in Dutch). Metalen Vol. 4, no. 2, 3 and 4, Oct., Nov. and Dec. 1949, pp. 21—27, 39—47 and 59—65	1949
—	Palm, J. H.	The relation between indentation hardness and strain for metals. J. of Metals, Vol. 1, no. 11, Nov. 1949, p. 904	1949
—	V. Oosterom, T.	Speed record measurements with Meteor IV at Ameland. (in Dutch) Avia, Vol. 8, no. 21, 15 Nov. 1949, pp. 504—507	1949
—	Kulberg, S. H. Van Vegten, N.	Measurements by the NLL during the establishment of a Netherlands speed record. (in Dutch). T.N.O.-Nieuws, 4, no. 43, Nov. 1949, pp. 363—367	1949

CCL Class. E 501

REPORT F. 28.

Gust Load Coefficients for Wing and Tail Surfaces of an Aeroplane

by

Dr. J. H. GREIDANUS and Ir. A. I. VAN DE VOOREN.

Summary.

Accurate calculations are made for the gust load coefficients, taking into account rotations of the aeroplane about the lateral axis and the instationary establishment of aerodynamic forces. The influence of the most important parameters on the gust loads is investigated. The results, which are shown in diagrams at the end of the report, are explained. Derivations of formulae and computational details are omitted, but the basic assumptions on which the method of calculation is founded, are mentioned.

Contents.

1 Introduction.

In view of the increasing importance to obtain detailed information about the effect of gusts upon the structural parts of an aeroplane, in particular upon the wing and the horizontal tail surfaces, extensive calculations of gust loads have been performed at the National Aeronautical Research Institute (Nationaal Luchtvaartlaboratorium), by order of the Netherlands Civil Air Service (Rijksluchtvaartdienst). This work was started during the war by one of the authors. Results (after a long delay published recently; ref.1) pointed to a marked influence of the static stability $\frac{\partial c_m}{\partial \alpha}$ of the aeroplane, especially on the tail loads. It was considered desirable to investigate this dependence more completely, and to adapt the underlying calculations to modern post-war civil aeroplanes. Though no major change was brought in the methods applied, the introduction of a suitable method for numerical integration of the equations of motion (carried out previously by operator methods) made it possible to retain more details in these equations and to raise, thereby, the level of accuracy. In this way, a rather great number of cases, covering a wide variation of the most important parameters, has been investigated.

Results are, as far as necessary, in good agreement with the older work, but the attained advantages, particularly with respect to the tail loads, are manifest.

In this report a complete survey of all basic assumptions is given. Further, ample consideration is given to the results. All computational details and derivations of formulae are, however, omitted. They will be collected in a separate report (ref. 2), available on request.

It may be mentioned that all results communicated in this report apply to a perfectly rigid aeroplane. It is known that the corresponding loads may be too low in consequence of oscillations, generated by the gust, of elastic parts (e. g. the flexible wing) of the aeroplane.

2 Basic assumptions.

2.1 *Gust velocity.*

The distribution of the gust velocity along the flight path of the aeroplane is assumed to be

$$\begin{aligned} w_r &= 0 && \text{if } s \leq 0, \\ w_r &= {}^1/_2\, w_0 \left(1 - \cos \pi \frac{s}{s_g}\right) && \text{if } 0 \leq s \leq s_g, \quad (2.1) \\ w_r &= w_0 && \text{if } s_g \leq s, \end{aligned}$$

s giving the distance along the flight path in terms of the mean aerodynamic semichord l_0 of the wing [1]). The gradient distance, s_g, is likewise expressed in this unit of length and thus depends numerically on the dimensions of the aeroplane. By its introduction as unit of length, l_0 is eliminated from the argument of the lag functions in the aerodynamic forces (compare section 2.3). If $s_g = 0$ the gust is called a sharp-edged gust. The gust intensity w_0 is positive if it is directed upward.

The gust velocity is constant in planes perpendicular to the flight path, which leads to symmetrical loads. The right angle between the original path of flight and the direction of the gust leads to loads of almost optimal severity (ref. 1) (other conditions being given).

2.2 *Equations of motion.*

The equations of motion are formed with regard to a system of rectangular axes, fixed to the aeroplane and with its origin in the centre of gravity. Before the entrance of the aeroplane into the gust, the X-axis points in the horizontal direction of motion and the Z-axis is directed vertically upwards.

The disturbance of the aeroplane due to the gust is assumed to remain small, i. e. to introduce velocities, small compared with the original speed and rotations over small angles only. The equations of motion will be developed to the usual first order of approximation ($\sin\varphi \approx \varphi$, $\cos\varphi = 1$).

The forward speed V (in X-direction) is assumed to be unaffected by the gust, which is a usual approximation, having no important influence on the results (ref. 1). This is due to the short time in which the optimal loads are built up.

The remaining motion is described by two simultaneous equations, one representing the equilibrium of inertia and aerodynamic forces in the Z-direction and the other expressing the equilibrium of the corresponding moments about the lateral (Y-) axis. Both equations are integro-differential equations, the integral operators arising from the aerodynamic lag functions.

The initial steady state can, of course, be eliminated immediately. In the following, the term "aerodynamic forces" will always refer to the according changes, directly or indirectly caused by the gust.

In the equations of motion, the time t will consistently be replaced by the variable s by means of the obvious relation

$$s = \frac{Vt}{l_0}. \tag{2.3}$$

Hence, the motion of the aeroplane will ultimately be determined by the functions $w(s)$ and $\omega(s)$

[1]) Defined by the formula

$$2\,l_0 = \frac{\int\limits_{-b}^{b} (2\,l)^2\,dy}{\int\limits_{-b}^{b} 2\,l\,dy} = \frac{\int\limits_{-b}^{b} (2\,l)^2\,dy}{S_w} . \tag{2.2}$$

See section 4 for notations.

denoting respectively the speed in the Z-direction and the angular speed about the Y-axis.

It is necessary to add a convention as to the point of the aeroplane to which the coordinate s refers. This will not be identified with the centre of gravity, but with the fuselage nose. Hence, at the moment $s = s_1$, the nose of the fuselage reaches the point s_1 of the flight path. The disturbance of the aeroplane's motion by the gust thus starts at the moment $s = 0$.

2.3 *Aerodynamic forces on the wing.*

The total aerodynamic force on the wing consists of the superposition of forces resulting from:

(i) the change in circulation due to the disturbed motion of the wing
(ii) the change in circulation due to the partial motion of the air
(iii) the dynamic profile curvature
(iv) the inertia effects of the surrounding air.

At first the respective forces are considered for a wing strip of width Δy assuming two-dimensional flow and neglecting all compressibility effects.

(i) If at the moment σ an instantaneous change occurs in the angle of incidence at the three-quarter chord point, then the force at the moment s is given by

$$\Delta L(s) = \pi\,\rho\,V^2.\,k_1(s-\sigma).\,\Delta\alpha(\sigma).\,l\Delta y. \tag{2.4}$$

For the lag function k_1 Jones' approximation (ref. 3)

$$\begin{aligned} k_1(s) &= 0 && s \leq 0 \\ k_1(s) &= 2 - 0.33\,e^{-0.0455\,s} - 0.67\,e^{-0.300\,s} && s \geq 0 \end{aligned} \tag{2.5}$$

has been adopted in this report.

The disturbed motion of the aeroplane causes a continuous change in the angle of incidence. Thus the total change in this part of the aerodynamic force has been obtained by integration of (2.4) with respect to σ.

(ii) If, at the moment σ, the midpoint of the strip reaches a gust field of intensity Δw_r, the resulting force will be, at the moment s:

$$\Delta L(s) = \pi\,\rho\,V^2.\,k_2(s-\sigma).\,\frac{\Delta w_r(\sigma)}{V}\,.\,l\Delta y. \tag{2.6}$$

For k_2 the rigorous two-dimensional result has been used (refs 4, 5). $k_2(s)$ is equal to zero if $s \leq -1$.

For a gust field with gradient distance, the total increment in lift follows by integration of (2.6) to σ.

(iii) The variation of the angle of incidence along the profile, when it is rotating about the Y-axis, gives rise to an instantaneous force

$$\Delta L = \pi\,\rho\,V\omega l^2 \Delta y. \tag{2.7}$$

(iv) Due to the accelerated motion of the strip, there exists an instantaneous force (ref. 6)

$$\Delta L = -\,\pi\,\rho\,a\,l^2 \Delta y, \tag{2.8}$$

where a denotes the acceleration at the midpoint of the strip, and an instantaneous moment

$$\Delta M = -\,{}^{1}/_{8}\,\pi\,\rho\,\frac{d\omega}{dt}\,l^{4}\Delta y. \qquad (2.9)$$

The circulational forces (i) and (ii) act at the quarter chord point, the force (iii) at the three-quarter chord point and the force (iv) at the midpoint of the strip.

The forces on the total wing are deduced by integration to y with the following modifications:

The effect of finite span has been approximated by replacing the factor 2π by the actual lift slope for steady flow:

$$\left(\frac{\partial c_L}{\partial \alpha}\right)_w = p_w \frac{\partial c_L}{\partial \alpha} \qquad (2.10)$$

of the wing [1]).

The tapered wing has been replaced by a rectangular wing of the same mean aerodynamic chord and the same area. The major consequence of the neglected taper will presumably be that the assumed lift force builds up somewhat too slowly near the tips and somewhat too quickly near the wing root. Another consequence is that all wing chords enter at the same moment into the gust field.

It must be noted that the force (ii) begins to build up at the moment that the wing nose (and not the nose of the fuselage, which is e_v semichords ahead) touches the boundary of the gust field. This can be represented by an appropriate change of the variable in the k_2-function.

2.4 *Aerodynamic forces on the horizontal tail plane.*

The aerodynamic force on the tail plane can be divided into a force resulting from conditions of free flow and a force due to the downwash of the wing.

The first part can clearly be obtained in a similar way as for the wing [2]). With

$$\left(\frac{\partial c_L}{\partial \alpha}\right)_s = p_s \frac{\partial c_L}{\partial \alpha} \qquad (2.11)$$

denoting the lift coefficient for the tail placed in a free steady flow (and again referred to the wing area S_w), the finite span effect for the tailplane has been taken into account by replacing 2π by $\left(\frac{\partial c_L}{\partial \alpha}\right)_s \frac{S_w}{S_t}$. Further, the argument $s-\sigma$ of the lag functions must be replaced by $\frac{s-\sigma}{\xi}$, if the mean aerodynamic semichord of the tail is equal to $\xi\, l_0$. Finally, the aerodynamic force directly due to the gust will not act before the moment $e_v + \beta + \frac{1}{2}(1-\xi)$, this being the distance of the leading edge of the tailplane behind the fuselage nose, expressed in wing semichords.

The force due to the downwash has been calculated as follows. The wing is replaced by a lifting line (bound vortex) through the quarter chord point of the mean aerodynamic chord of the wing. The length of this vortex has been put equal to $2\,b' = 2\,\lambda'\,l_0$ (b' somewhat smaller than b, λ' proportionally smaller than the wing aspect ratio λ), while its strength Γ is independent of y, which implies that trailing vortices are concentrated in the points $y = \pm\, b'$. Changes in the circulation about the wing, i. e. changes in the strength of the lifting line vortex, will be accompanied by the formation of equally strong but oppositely directed vortices of the same length $2\,b'$, carried off by the flow and forming the wake. The strength of the trailing vortices varies accordingly. Hence, the complete vortex system can, at any moment, be decomposed in a system of rectangular vortices of constant strength. In calculating the change of the downwash, the initial horseshoe vortex must be left out of consideration. For points of the tailplane the change in downwash has been put equal to the velocity induced by the system of vortices described above, in that point of the intersection of the plane of symmetry and the vortex plane, which has the same x-coordinate as the quarter chord point of the mean aerodynamic tail-chord. The slight underestimation of the effective downwash, caused by the fact that the theoretical induced velocity along a line parallel to the lateral axis is minimal in this point, has been compensated by a small numerical reduction of the value of λ' resulting from other considerations (e. g. induced drag).

In calculating the forces due to the changed downwash, no aerodynamic lag has been included in the part generated by the slow variation in wing circulation, which results from the disturbance of the aeroplane's motion. To the part generated by the swiftly varying wing circulation resulting from the direct influence of the gust on the wing, the k_2-function has been applied, though this implies an insignificant approximation, because the downwash is not constant when shifting over the tailplane.

It is, of course, also possible to obtain the derivative of the lift coefficient of the steady state downwash force from the vortex model considered above (reducing to a single horseshoe vortex).

If the result is written in the form

$$\left(\frac{\partial c_L}{\partial \alpha}\right)_n = p_n \frac{\partial c_L}{\partial \alpha}, \qquad (2.12)$$

it can be shown that p_n takes the value

$$p_n = -\frac{p_w p_s \frac{\partial c_L}{\partial \alpha} S_w}{8\,\pi\,(\lambda'\,l_0)^2}\left\{1 + \sqrt{1 + \left(\frac{\lambda'}{\beta}\right)^2}\right\}. \qquad (2.13)$$

The slope of lift curve for the tail, placed in a steady flow and in the wake of the wing, will be denoted by

$$\left(\frac{\partial c_L}{\partial \alpha}\right)_t = p_t \frac{\partial c_L}{\partial \alpha}, \qquad (2.14)$$

where

$$p_t = p_s + p_n. \qquad (2.15)$$

---

[1]) All aerodynamic coefficients refer to the wing area S_w: Thus $L = c_L \,.\, \frac{1}{2}\,\rho\, V^2 \,.\, S_w$.

[2]) No elevator motion is assumed to occur.

2.5 *Aerodynamic forces on fuselage and nacelles.*

From investigations in a windtunnel for a single wing and for the combination of the same wing with a fuselage and nacelles, it appears that an appreciable lift and moment are introduced by the fuselage and the nacelles. Introducing a fuselage lift coefficient $(c_L)_f$, it is found that in the equation

$$\left(\frac{\partial c_L}{\partial \alpha}\right)_f = p_f \frac{\partial c_L}{\partial \alpha} \qquad (2.16)$$

p_f may attain a value of about 0.07. This relatively large value suggests that the circulatory flow about the fuselage is not completely due to interference with the wing, but that fuselage or nacelles itself also produce circulation. From the measurements of the moment it follows that the resulting force acts at a distance el_0 ahead of the quarter chord point of the mean aerodynamic wing chord, where e is only slightly smaller than e_v.

It will be assumed that, also under circumstances of unsteady flow, the lifting force on fuselage and nacelles is not subject to aerodynamic lag. This supposition is supported by the following argument.

If the circulation about the fuselage is supposed to be generated by some suitable system of bound lateral vortices, the adjoined free lateral vortices forming the wake are, in view of the small width of the fuselage, so short that they induce velocities at the place of the bound vortices, which are small compared with the case of a wing in two-dimensional flow. This, however, implies that the steady final values will be attained much quicker and the remaining lag might well be negligible.

Thus, for the fuselage, the k_1-function is supposed to be equal to 2 if $s > 0$. However, the k_2-function does not suddenly take the value 2, since the fuselage penetrates gradually into the gust. As long as the fuselage has not entered over its full length into the gust, it is reasonable to expect a reduced lift e. g. a lift proportional to the part within the gust. In fact the following assumption has been made for the k_2-function:

$$\begin{aligned} k_2 &= 0 && \text{if} \quad s \leq 0, \\ k_2 &= \frac{2s}{e_v + e_a} && \text{,,} \quad 0 \leq s \leq e_v + e_a, \\ k_2 &= 2 && \text{,,} \quad e_v + e_a \leq s. \end{aligned} \qquad (2.17)$$

It is supposed that the lift on the fuselage acts, under all circumstances, at the point indicated by the steady state measurements. Further, the angle of incidence at the point which has the same x-coordinate as the quarter chord point of the mean aerodynamic chord has been assumed to be the effective angle of incidence for the fuselage lift.

Inertia and dynamic curvature contributions to this lifting force have been omitted.

2.6 *Two important parameters.*

For representation of results it will appear convenient to introduce two new parameters, viz.

$$C = \frac{{}^1/_2\, \rho \dfrac{\partial c_L}{\partial \alpha} S_w l_0}{m}, \qquad (2.18)$$

$$\begin{aligned} \frac{\partial c_m}{\partial c_L} &= \varepsilon p_w - (\beta - \varepsilon) p_t + (e + {}^1/_2 + \varepsilon) p_f = \\ &= \varepsilon - \beta p_t + (e + {}^1/_2) p_f \,.\,^{1)} \end{aligned} \qquad (2.19)$$

The parameter C, of which the factor ${}^1/_2\, \rho \dfrac{\partial c_L}{\partial \alpha} S_w$ is proportional to the aerodynamic forces, while $\dfrac{m}{l_0}$ is proportional to the inertia forces (with s instead of t as variable), governs the trend of the aeroplane to adapt its vertical motion to the gust [2]. It must be remarked that c_m denotes the moment coefficient, taken about the centre of gravity ($M = c_m \,.\, {}^1/_2\, \rho V^2 \,.\, S_w \,.\, l_0$).

The derivatives $\dfrac{\partial c_m}{\partial c_L}$ and $\dfrac{\partial c_L}{\partial \alpha}$ can easily be obtained from measurements applying to the complete aeroplane. They both refer to steady flow conditions.

It will, further, be seen that

$$p_w + p_t + p_f = 1. \qquad (2.20)$$

2.7 *Representation of results.*

If w and ω are solved from the equations controlling the aeroplane's reaction to the gust, the resulting motion is completely known and all loads on wing and tail can easily be determined. They consist of a positive aerodynamical load and a negative inertia load. Both parts do not, for a part of the aeroplane, balance each other (in general), though the resultants for the complete aeroplane do (first equation of motion). Both components of the load have been determined for the wing and the tailplane and will be stated separately.

(1) *Aerodynamic wing load.*

The aerodynamic force on the whole wing due to the gust can be written in the form

$$\Lambda_{l,w} \,.\, {}^1/_2\, \rho \frac{\partial c_L}{\partial \alpha} V S_w w_0 p_w. \qquad (2.21)$$

$\Lambda_{l,w}$ denotes the function of s representing the course of the aerodynamic force if the aeroplane proceeds into the gust. It has the significance of a load coefficient, whose maximum value is always smaller than 1, this value representing the imaginary case of an aeroplane prevented to adopt any disturbed motion (i. e. forced to proceed with $w = \omega = 0$), or, what turns out to be the same, of an aeroplane which is at once completely submitted to the constant gust intensity w_0 and for which aerodynamic lag does not exist. With regard to this case the maximum load coefficient has the character of a reduction factor.

(2) *Inertia wing load.*

It is assumed that the centre of gravity of the wing coincides with the projection of the quarter

---

[1]) Making use of (2.20).

[2]) Thus C determines in first approximation the quantity $\dfrac{dw}{ds} + l_0 \omega$

chord point of the mean aerodynamic wing chord on the plane of symmetry. The inertia force on the whole wing then becomes equal to

$$-\Lambda_{m,w} \cdot {}^1/_2\, \rho\, \frac{\partial c_L}{\partial \alpha} V S_w w_0 \frac{m_w}{m}. \qquad (2.22)$$

The maximum value of the load coefficient $\Lambda_{m,w}$ can also be considered as a reduction factor, the case $\Lambda_{m,w} = 1$ applying to an aeroplane, submitted at once to the full gust, affected by it without aerodynamic lag and prevented to pitch.

If the aeroplane may perform a pitching motion, $\Lambda_{m,w}$ can be obtained as follows.

From the increase in the moment

$$\frac{\partial c_m}{\partial c_L} \cdot {}^1/_2\, \rho\, \frac{\partial c_L}{\partial \alpha} V S_w w_0 l_0,$$

an angular acceleration

$$\frac{1}{m j^2 l_0} \cdot \frac{\partial c_m}{\partial c_L} \cdot {}^1/_2\, \rho\, \frac{\partial c_L}{\partial \alpha} V S_w w_0$$

results.

Hence, the total acceleration at the wing centre of gravity becomes equal to

$$\left\{ 1 + \frac{\varepsilon \dfrac{\partial c_m}{\partial c_L}}{j^2} \right\} {}^1/_2\, \rho\, \frac{\partial c_L}{\partial \alpha} V S_w w_0.$$

Thus, for an aeroplane submitted at once to the full gust and affected by it without aerodynamic lag

$$\Lambda_{m,w} = 1 + \frac{\varepsilon \dfrac{\partial c_m}{\partial c_L}}{j^2}.$$

(3) *Aerodynamic tail load.*

The increase in aerodynamic force on the horizontal tail plane is equal to

$$\Lambda_{l,t}\, {}^1/_2\, \rho \frac{\partial c_L}{\partial \alpha} V S_w w_0 p_t. \qquad (2.23)$$

The load coefficient $\Lambda_{l,t}$ has the maximum value 1 if the motion of the tail would be undisturbed until the tail itself enters the gust and aerodynamic lag is neglected (implying that the downwash assumes immediately its steady state value).

(4) *Inertia tail load.*

It is assumed that the centre of gravity of the tail coincides with the projection of the quarter chord point of the mean aerodynamic tail chord. The inertia force on the whole tail then becomes

$$-\Lambda_{m,t} \cdot {}^1/_2\, \rho\, \frac{\partial c_L}{\partial \alpha} V S_w w_0 \frac{m_t}{m}. \qquad (2.24)$$

$\Lambda_{m,t}$ reaches the value 1 under the same circumstances as $\Lambda_{m,w}$.

If a pitching motion is allowed, $\Lambda_{m,t}$ is given by

$$\Lambda_{m,t} = 1 - \frac{(\beta - \varepsilon) \dfrac{\partial c_m}{\partial c_L}}{j^2}.$$

Remark.

The aerodynamic inertia forces have been incorporated in $\Lambda_{l,w}$ and $\Lambda_{l,t}$. It is possible to shift them to the inertia loads by applying the corresponding corrections to m_w and m_t (without change of $\Lambda_{m,w}$ resp. $\Lambda_{m,t}$). In this case $\Lambda_{l,w}$ must be increased with a small amount ranging from 0.006 for small values of C ($C \approx 0.01$) to 0.012 for high values ($C \approx 0.05$) while corrections of the same order of magnitude must be applied to $\Lambda_{l,t}$.

The resulting force on the wing is given by

$$\left(p_w \Lambda_{l,w} - \frac{m_w}{m} \Lambda_{m,w} \right) {}^1/_2\, \rho\, \frac{\partial c_L}{\partial \alpha} V S_w w_0 \quad (2.25)$$

and the resulting force on the tail by

$$\left(p_t \Lambda_{l,t} - \frac{m_t}{m} \Lambda_{m,t} \right) {}^1/_2\, \rho\, \frac{\partial c_L}{\partial \alpha} V S_w w_0. \quad (2.26)$$

The resulting tail force is mainly determined by the aerodynamic load, since $\frac{m_t}{m} \Lambda_{m,t}$ is at most about 30 % of $p_t \Lambda_{l,t}$. For the wing, the two terms may compensate each other for the greater part.

The forces on any part of wing or tail can easily be calculated if functions for the distribution of lift and mass along the span are known.

2.8 *Range of parameters investigated.*

For the values assigned to parameters in each case investigated, the reader is referred to table 1. These values are chosen in such a way that

(i) they agree roughly with the mean values of some large, modern civil aeroplanes

(ii) the applied variation gives a fairly complete insight into how the gust loads are influenced by numerical changes of parameters. Attention has especially been paid to changes in the neighbourhood of values leading to high load coefficients.

3 Discussion of results.

The load coefficients $\Lambda_{l,w}$, $\Lambda_{m,w}$, $\Lambda_{l,t}$ and $\Lambda_{m,t}$ are functions of the parameters

$$C,\ s_g,\ \varepsilon,\ \frac{p_s}{p_w}\ \frac{p_n}{p_w}\ \frac{p_f}{p_w},\ j \text{ and } \beta. \qquad (3.1)$$

The quantities ρ, $\frac{\partial c_L}{\partial \alpha}$, S_w, l_0, m, m_w, m_t, V and w_0 are only of importance — for the load coefficients — as far as they influence one of the values (3.1).

In fig. 1 the load coefficients are plotted as functions of s for case 2. It appears from this figure that aerodynamic and inertia loads reach their maximum values nearly at the same time; these values are reached a little sooner for the wing than for the tail. Thus, the maximum value of the resulting force can be deduced from the maximum values of aerodynamic and inertia loads. This conclusion holds for all cases.

The parameters C, s_g and ε are varied in the cases 1 to 12. The parameter ε will often be replaced by $\frac{\partial c_m}{\partial c_L}$ which differs by a constant amount from ε, according to equation (2.19). The maxi-

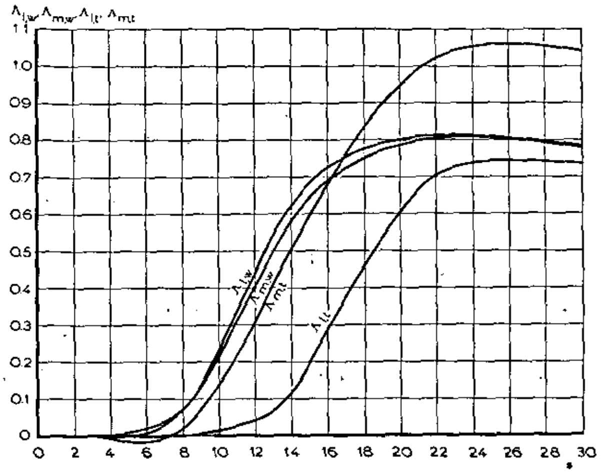

Fig. 1. Wing and tail load coefficients as functions of s for case 2.

mum values of the load coefficients are shown in figs. 2/5 as functions of $\frac{\partial c_m}{\partial c_L}$. Any combination of C and s_g yields its own curve.

Investigation of the cases 13 to 23 shows that, within rather good approximation (errors less than $1^1/_2$ %), the maximum values of the wing load coefficients are only dependent on

$$C,\ s_g \text{ and } \frac{\partial c_m}{\partial c_L}.$$

Indeed, it appears from figs. 2 and 3, that the

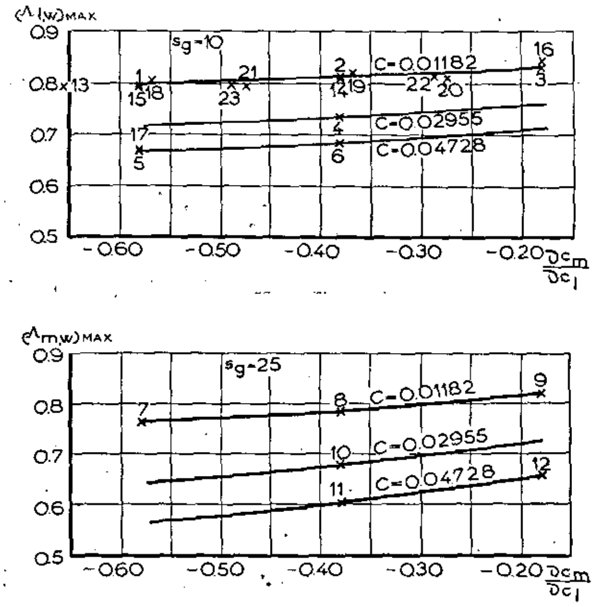

Fig. 2. Maximal aerodynamic wing load coefficients.

maximum coefficients for the cases 13 to 23, which all have nearly the same value of C as the cases 1 to 3, are in the immediate vicinity of the curve connecting the coefficients of these last cases.

A similar reasoning does not hold for the tail load coefficients with the exception of case 13

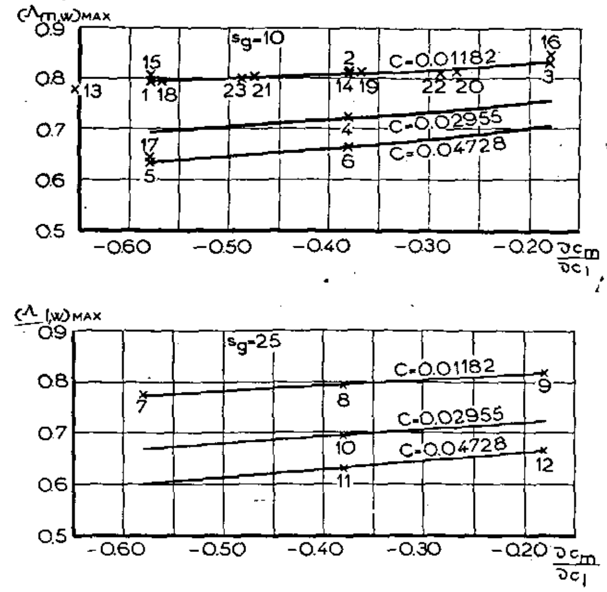

Fig. 3. Maximal inertia wing load coefficients.

(fig. 4 and 5), signifying that these coefficients depend on the parameters

$$C,\ s_g,\ \varepsilon,\ \frac{p_s}{p_w},\ \frac{p_n}{p_w},\ j \text{ and } \beta.$$

It is shown in figs. 2/5 that an increase in C diminishes all loads, which is in accordance with its definition (section 2.6), denoting that an aero-

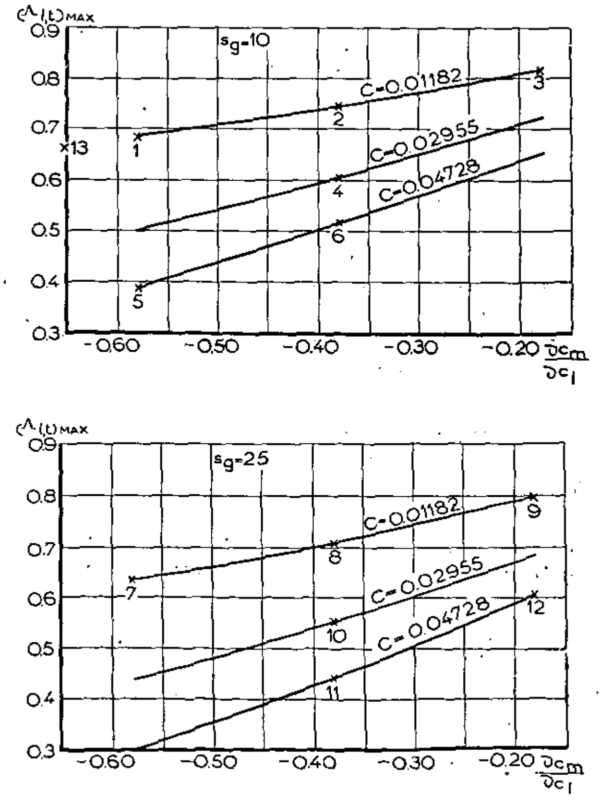

Fig. 4. The influence of C and $\frac{\partial c_m}{\partial c_L}$ on maximal aerodynamic tail and load coefficients.

plane with high C-value can easily adopt a vertical motion.

It is shown as well in figs. 2/5 that an increase

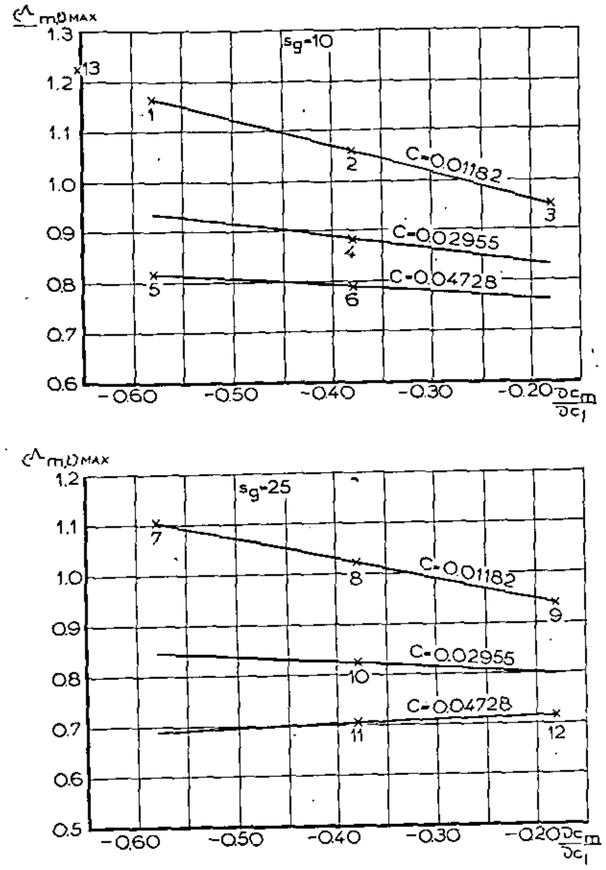

Fig. 5. The influence of C and $\frac{\partial c_m}{\partial c_L}$ on maximal inertia tail load coefficients.

in s_g diminishes all loads. This too is evident, since the aerodynamic forces are built up slower if s_g is greater.

The position of the centre of gravity has a relatively slight influence on the wing loads (though a backward displacement of the centre of gravity definitely increases them), but is more important for the tail. If the centre of gravity lies forward (negative ε), the tail acquires already an evading motion by the aerodynamic force of the wing, thus diminishing the aerodynamic tail load, but increasing the inertia tail load.

Since neither tail nor wing loads are affected appreciably by the aerodynamic forces of the fuselage it is permitted to neglect them in computations, provided C and $\frac{\partial c_m}{\partial c_L}$ retain their original values. All calculations in this report, however, are performed with fuselage forces (except case 13).

It follows from fig. 6 that an increase in radius of gyration leads to smaller values of $(\Lambda_{l,t})_{max}$ if $\frac{\partial c_m}{\partial c_L}$ takes small negative values (i. e. $\varepsilon \sim 0.2$), but to greater values of $(\Lambda_{l,t})_{max}$ if $\frac{\partial c_m}{\partial c_L}$ is strongly negative ($\varepsilon \sim -0.2$). Hence, the curves connecting

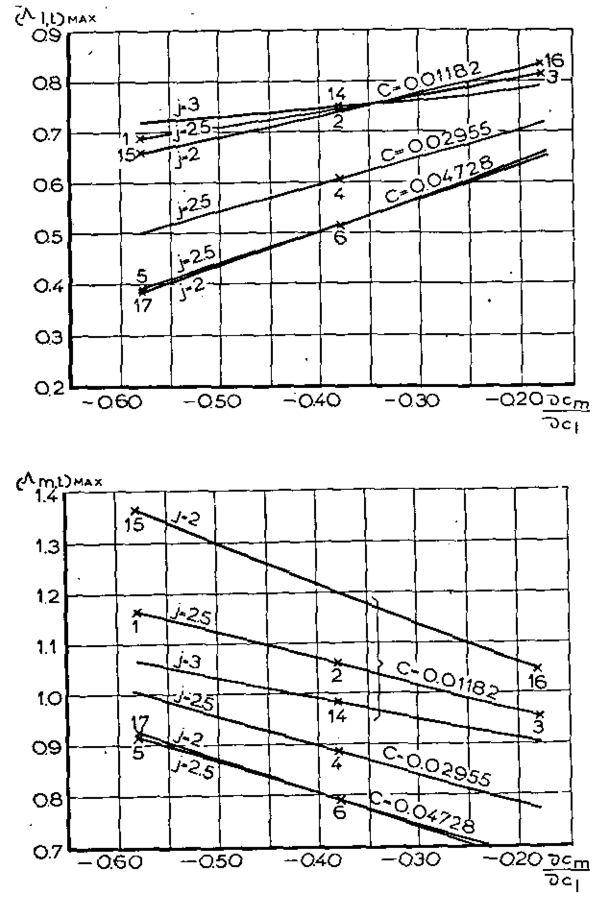

Fig. 6. Influence of j on maximal tail load coefficients.

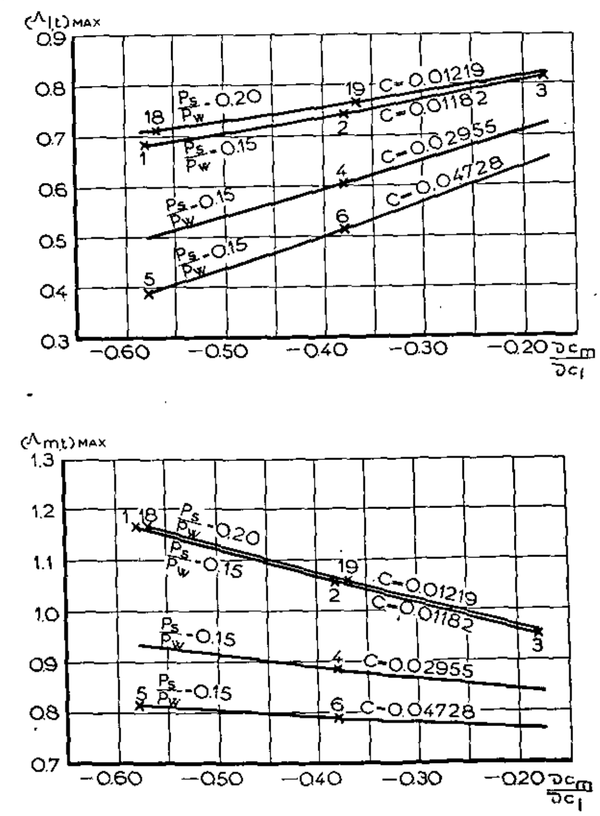

Fig. 7. Influence of $\frac{p_s}{p_w}$ on maximal tail load coefficients.

points of equal C in these diagrams are turned by a change in j. The curves of fig. 6 for large values of C have partly been estimated.

Finally it follows from figs 7, 8 and 9 that the maximum values of aerodynamic tail load coeffi-

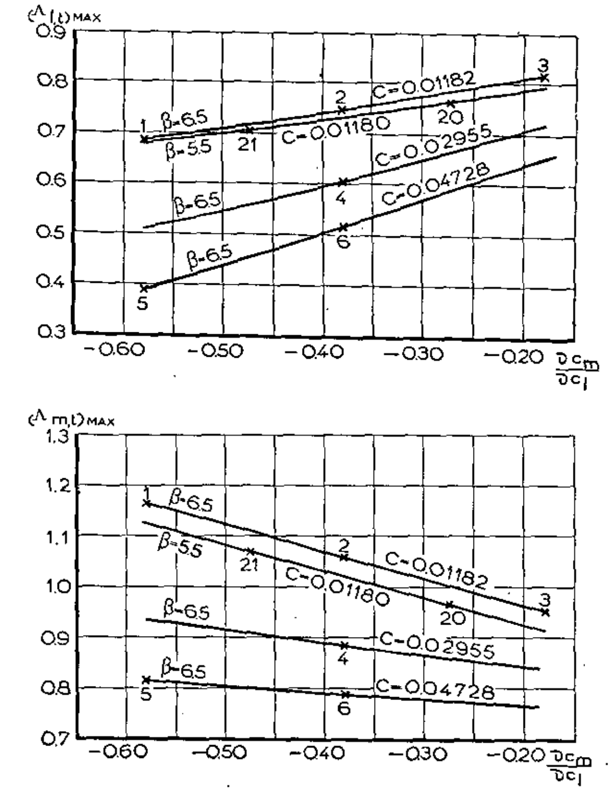

Fig. 8. Influence of β on maximal tail load coefficients.

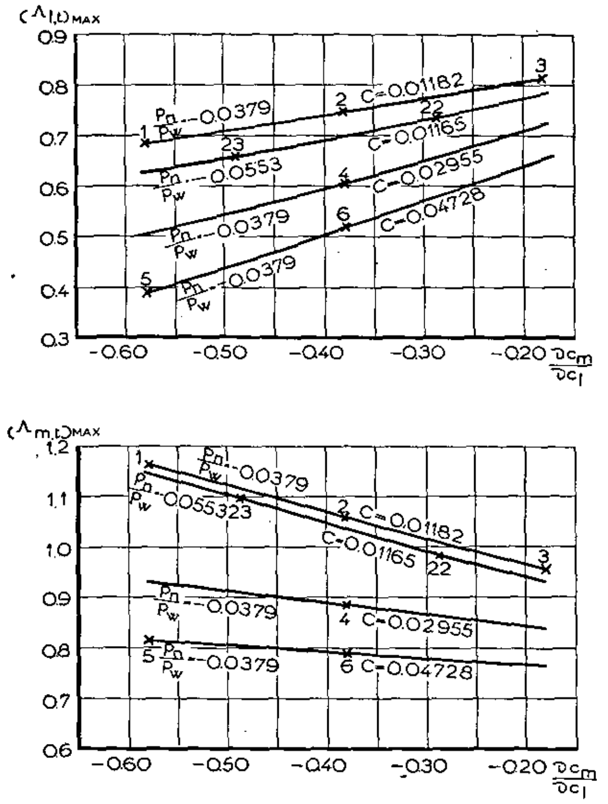

Fig. 9. Influence of $\frac{p_n}{p_w}$ on maximal tail load coefficients.

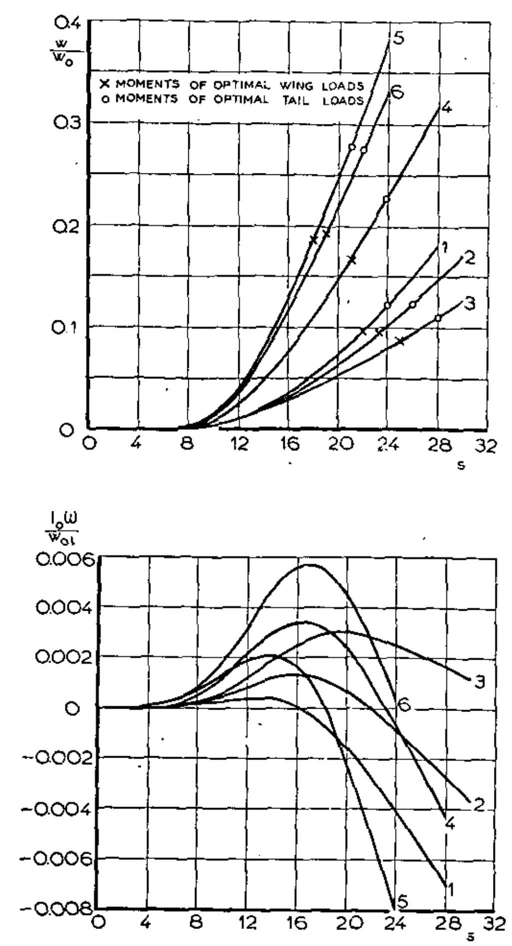

Fig. 10. Motion of the aeroplane (cases 1—6).

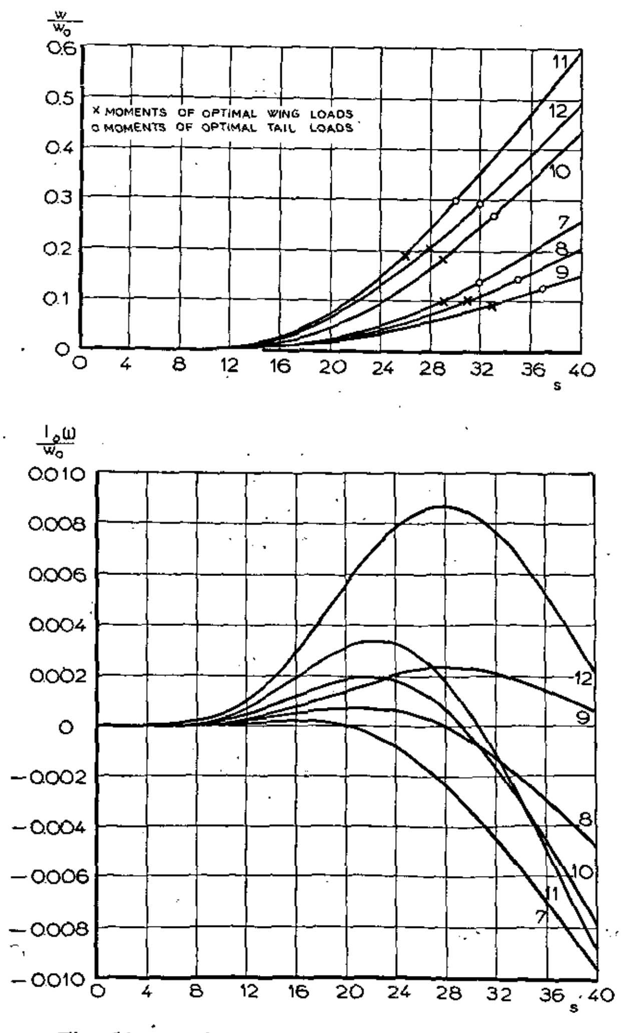

Fig. 11. Motion of the aeroplane (cases 7—12).

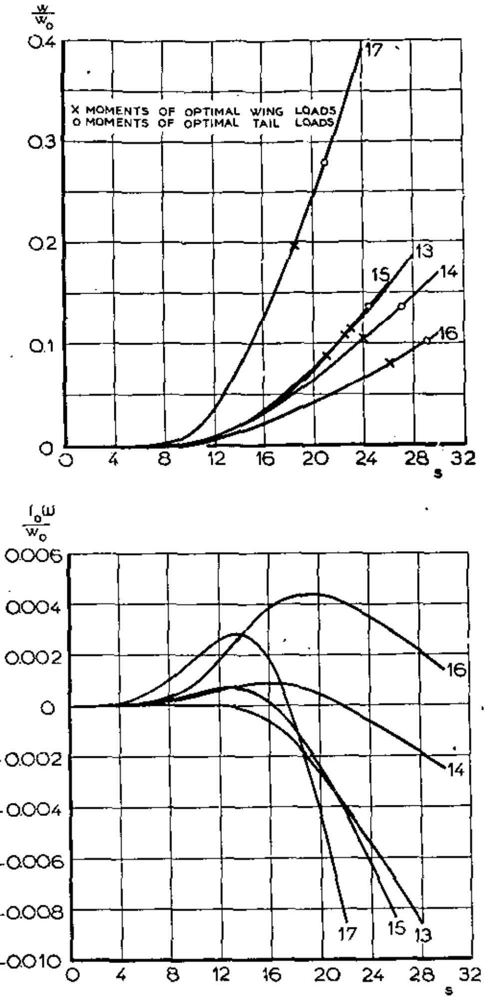

Fig. 12. Motion of the aeroplane (cases 13—17).

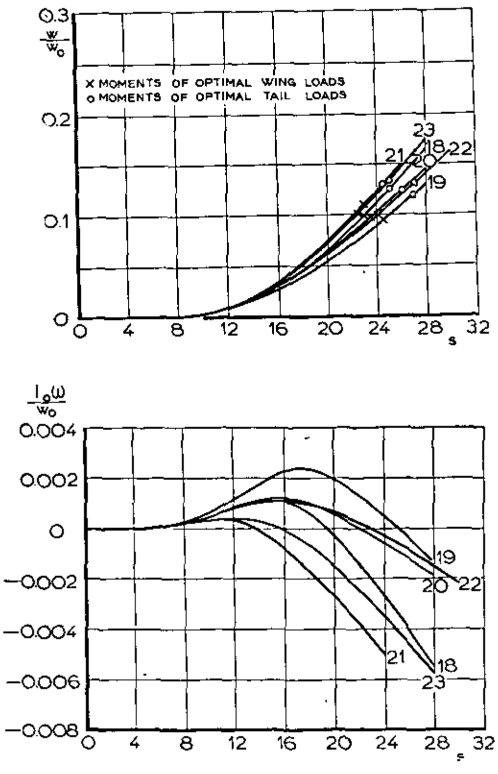

Fig. 13. Motion of the aeroplane (cases 18—23).

cients are raised by an increase of horizontal tail area, by an increase of the tail area or by assuming smaller values for the downwash, always comparing cases with equal C and $\frac{\partial c_m}{\partial c_L}$. The influence of the tail arm, however, is rather unimportant.

For readers who want to obtain a more thorough insight in the disturbed motion of the aeroplane, enabling them to analyse and understand better the changes in maximum load coefficients due to variation of parameters, figs 10—13 contain curves of w and $l_0\omega$ as functions of s. The accelerations can easily be determined from these graphs (e. g. the acceleration of the centre of gravity is $\frac{V}{l_0}\left(\frac{dw}{ds} + l_0\omega\right)$). The values of s for which the maximum wing and tail loads arise are indicated. The maximum wing loads always precede the maximum tail loads.

4 List of symbols.

X, Y, Z	coordinate axes, fixed to the aeroplane
V	forward speed (in X-direction)
w	velocity of the aeroplane in Z-direction, positive upward
ω	angular velocity of the aeroplane about Y-axis, positive backward
w_r	gust velocity
w_0	constant gust velocity behind gradient distance
l_0	mean aerodynamic semi-chord of wing
ξl_0	„ „ „ „ horizontal tail plane
l	wing semi-chord at an arbitrary section
$s_g l_0$	gust gradient distance
s	coordinate along the flight path
t	time
$b = \lambda l_0$	semispan of wing
λ	aspect ratio
$b' = \lambda' l_0$	y-coordinate of tip vortex
S_w	wing area
S_t	area of horizontal tailplane
βl_0	x-component of distance between quarter-chord point of mean aerodynamic wing chord and quarter-chord of mean aerodynamic tail chord
$j l_0$	radius of gyration about Y-axis
εl_0	x-component of distance between centre of gravity of the whole aeroplane and quarter-chord point of mean aerodynamic wing chord, positive if centre of gravity lies aft
$e_v l_0$	x-component of distance between foremost point of fuselage and leading edge of mean aerodynamic wing chord
$e l_0$	x-component of distance between the point at which the fuselage aerodynamic forces act and the leading edge of mean aerodynamic wing chord, positive if leading edge is aft
$e_a l_0$	x-component of distance between aftermost point of fuselage and leading edge of mean aerodynamic wing chord
ρ	air density

c_L — stationary lift coefficient of the whole aeroplane, referred to wing area

$(c_L)_w$ — stationairy lift coefficient of the wing, referred to wing area

$(c_L)_s$ — stationary lift coefficient of the tail in a free flow, referred to wing area

$(c_L)_n$ — negative stationary lift coefficient of the tail due to downwash referred to wing area

$(c_L)_t$ — $= (c_L)_s + (c_L)_n$, stationary lift coefficient of tail, including downwash (referred to wing area)

$(c_L)_f$ — stationary lift coefficient of fuselage and nacelles referred to wing area

c_m — stationary moment coefficient of the whole aeroplane (positive if tailheavy), referred to wing area S_w, to mean aerodynamic semi-chord of the wing l_0 and *taken about the centre of gravity*

α — angle of incidence

$$p_w = \left(\frac{\partial c_L}{\partial \alpha}\right)_w \bigg/ \frac{\partial c_L}{\partial \alpha}$$

$$p_s = \left(\frac{\partial c_L}{\partial \alpha}\right)_s \bigg/ \frac{\partial c_L}{\partial \alpha}$$

$$p_n = \left(\frac{\partial c_L}{\partial \alpha}\right)_n \bigg/ \frac{\partial c_L}{\partial \alpha}$$

$$p_t = \left(\frac{\partial c_L}{\partial \alpha}\right)_t \bigg/ \frac{\partial c_L}{\partial \alpha}$$

$$p_f = \left(\frac{\partial c_L}{\partial \alpha}\right)_f \bigg/ \frac{\partial c_L}{\partial \alpha}$$

k_1 — lag function of instationary aerodynamic forces when the aerofoil is subject to a change in angle of incidence

k_2 — lag function of instationary aerodynamic forces, due to partial motion of the air

$$C = \frac{{}^1/_2\, \rho \dfrac{\partial c_L}{\partial \alpha} S_w\, l_0}{m}$$

m — mass of the whole aeroplane

m_w — wing mass

m_t — mass of horizontal tail plane

$\Lambda_{l,w}$ — aerodynamic wing load coefficient, see eq. (2.21)

$\Lambda_{m,w}$ — inertia wing load coefficient, see eq. (2.22)

$\Lambda_{l,t}$ — aerodynamic tail load coefficient, see eq. (2.23)

$\Lambda_{m,t}$ — inertia wing load coefficient, see eq. (2.24)

5 References.

1. GREIDANUS, J. H.: The loading of aeroplane structures by symmetrical gusts (in Dutch, with English abstract). Reports and Transactions of the National Aeronautical Research Institute, Vol. XIV, 1948 (Amsterdam).
2. VAN DE VOOREN, A. I.: Remarks on formulae and numerical methods used in report F. 28 (gust load coefficients). Report F. 29 (1948).
3. JONES, R. T.: The unsteady lift of a finite wing. N.A.C.A.-Technical Note 682 (1939).
4. KÜSSNER, H. G.: Das zweidimensionale Problem der beliebig bewegten Tragfläche. Luftfahrtf. Bd. 17 (1940), p. 355—361.
5. PRICHARD JONES, W.: Aerodynamic forces on wings in non-uniform motion. R and M 2117 (1945).
6. GLAUERT, H.: The accelerated motion of a cylindrical body through a fluid. R and M 1215 (1929).

Completed: April 1948.

TABLE 1.

Values of parameters.

Case	s_g	ε	$p_w C$	C	p_w	$\frac{p_s}{p_w}$	$\frac{p_n}{p_w}$	$\frac{p_f}{p_w}$	j	β	$\frac{\partial c_m}{\partial c_L}$
1	10	— 0.2	0.01	0.01182	0.8460	0.15	— 0.0379	0.07	2.5	6.5	— 0.5796
2	,,	0	,,	,,	,,	,,	,,	,,	,,	,,	— 0.3796
3	,,	+ 0.2	,,	,,	,,	,,	,,	,,	,,	,,	— 0.1796
4	,,	0	0.02^{5}	0.02955	,,	,,	,,	,,	,,	,,	— 0.3796
5	,,	— 0.2	0.04	0.04728	,,	,,	,,	,,	,,	,,	— 0.5796
6	,,	0	,,	,,	,,	,,	,,	,,	,,	,,	— 0.3796
7	25	— 0.2	0.01	0.01182	,,	,,	,,	,,	,,	,,	— 0.5796
8	,,	0	,,	,,	,,	,,	,,	,,	,,	,,	— 0.3796
9	,,	+ 0.2	,,	,,	,,	,,	,,	,,	,,	,,	— 0.1796
10	,,	0	0.02^{5}	0.02955	,,	,,	,,	,,	,,	,,	— 0.3796
11	,,	0	0.04	0.04728	,,	,,	,,	,,	,,	,,	— 0.3796
12	,,	+ 0.2	,,	,,	,,	,,	,,	,,	,,	,,	— 0.1796
13	10	0	0.01	0.01112	0.8992	,,	,,	0	,,	,,	— 0.6552
14	,,	0	,,	0.01182	0.8460	,,	,,	0.07	3	,,	— 0.3796
15	,,	— 0.2	,,	,,	,,	,,	,,	,,	2	,,	— 0.5796
16	,,	+ 0.2	,,	,,	,,	,,	,,	,,	,,	,,	— 0.1796
17	,,	— 0.2	0.04	0.04728	,,	,,	,,	,,	,,	,,	— 0.5796
18	,,	0	0.01	0.01219	0.8200	0.20	— 0.0505	,,	2.5	,,	— 0.5672
19	,,	+ 0.2	,,	,,	,,	,,	,,	,,	,,	,,	— 0.3672
20	,,	0	,,	0.01180	0.8477	0.15	— 0.0404	,,	,,	5.5	— 0.2736
21	,,	— 0.2	,,	,,	,,	,,	,,	,,	,,	,,	— 0.4736
22	,,	0	,,	0.01165	0.8586	,,	— 0.0553	,,	,,	6.5	— 0.2881
23	,,	— 0.2	,,	,,	,,	,,	,,	,,	,,	,,	— 0.4881

$\frac{p_n}{p_w}$ has been calculated in accordance with (2.13), assuming $\lambda' = 7.5$ for the cases 1 till 21 and $\lambda' = 6$ for the cases 22 and 23,

while $\frac{p_w S_w}{l_0^2} \frac{\partial c_L}{\partial \alpha} = 141.37$ for all cases.

Other parameters, which have for all cases the same value, are

$$\xi = {}^2/_3, \quad e_v = 5, \quad e = 3^1/_2 \quad \text{and} \quad e_a = 9.$$

TABLE 2.

Maximum values of load coefficients.

Case	$(\Lambda_{l,w})_{max}$	$(\Lambda_{m,w})_{max}$	$(\Lambda_{l,t})_{max}$	$(\Lambda_{m,t})_{max}$
1	0.797	0.798	0.687	1.167
2	0.812	0.810	0.746	1.060
3	0.832	0.830	0.816	0.951
4	0.737	0.721	0.605	0.884
5	0.666	0.634	0.390	0.817
6	0.686	0.663	0.517	0.790
7	0.775	0.766	0.635	1.104
8	0.796	0.789	0.710	1.023
9	0.819	0.816	0.798	0.940
10	0.693	0.679	0.551	0.822
11	0.626	0.607	0.442	0.702
12	0.663	0.657	0.605	0.715
13	0.794	0.780	0.660	1.227
14	0.810	0.808	0.749	0.983
15	0.793	0.802	0.658	1.363
16	0.846	0.843	0.834	1.045
17	0.668	0.644	0.386	0.924
18	0.806	0.798	0.712	1.167
19	0.822	0.812	0.766	1.059
20	0.811	0.811	0.762	0.964
21	0.795	0.802	0.707	1.070
22	0.813	0.810	0.734	0.986
23	0.797	0.799	0.660	1.097

CCL Class. E 501

REPORT F. 33

Loads on Wing and Tail Surfaces of an Aeroplane due to a Sinusoidal Gust Wave

by

Ir. A. I. VAN DE VOOREN.

Summary.

Gust load coefficients are calculated for the case of a single sinusoidal gust wave. The rotation of the aeroplane about its lateral axis and the dynamic features of unsteady flow (aerodynamic lag) have both been taken into account. Besides the length of the gust wave, two other parameters with predominant influence on the resulting loads have also been varied. The results are compared with those pertaining to persisting gusts (where, beyond a small gradient zone, the gust velocity retains a constant value), which have been communicated in a former report (ref. 1).

Contents.

1 Introduction.

In report F. 28 (ref. 1), results have been communicated of extensive calculations of gust loads on wing and horizontal tail surfaces of a perfectly rigid aeroplane. These calculations pertain to persisting gusts, where, beyond a small gradient zone of sinusoidal velocity distribution, the velocity remains constant (fig. 1*a*).

The present report contains gust load calculations for a single sinusoïdal gust wave, whose

Fig. 1*a*. Persisting gust.

velocity distribution is shown by fig. 1*b* (see also formula (2.1)).

The case of the gust wave may seem less interesting, since loads should, at first sight, be smaller than for a persisting gust of equal maximum velocity w_0. This conclusion, however, is premature, as can be explained in the following way.

Paying attention to the aeroplane's vertical motion only, the gust of fig. 1*a* gives rise to a

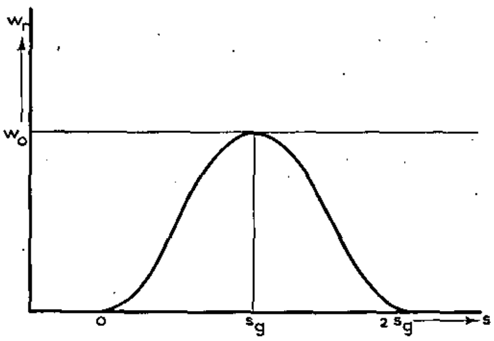

Fig. 1*b*. Gust wave.

vertical acceleration of the centre of gravity of the aeroplane, increasing from zero to a peak value and subsequently decreasing monotonically in an approximatively exponential way. The ultimate vertical velocity attained is obviously equal to w_0. In the case of a gust wave, however, the vertical velocity must ultimately vanish again, which implies that the period of acceleration is followed by a period of deceleration. So, the loads first reach a positive extreme and later on a negative extreme. Now, it can easily be shown that, if rotations of the aeroplane about the lateral axis would really be absent, the second extreme would be less severe than the first. (The argument is that the upward velocity of the aeroplane at the moment of maximum gust velocity has not yet attained the value w_0, which means that it enters the "subsequent downward gust" of the resulting gust wave with an unloading downward initial velocity). Actually, the occurring rotations do not affect the loading on the wing to such an extent (in the cases considered), that this provisional conclusion is invalidated, but the influence on the tail loads is appreciable, making it impossible in certain cases to attain a definite conclusion with respect to the ratio of the accelerative and decelerative extremes of the tailload without detailed analysis.

For this reason the case of the gust wave attains some independent significance.

Moreover, the gust wave can well be considered as a typical element of irregular gusts. So, results applying to this case may facilitate the tracing of those features of actual gusts which decisively affect the optimum loads.

Finally, the extension of these calculations to the case of the gust wave may also facilitate the comparison with other calculations pertaining to non-persisting (for instance triangular) gusts.

All calculations have been performed in exactly the same way as explained in report F. 28 (ref. 1), changing only the velocity distribution in the gust. Referring to this report, and to report F. 29 (ref. 2), containing details of the mathematics involved, the most important principles may be summarized, for sake of convenience, as follows:

(i) two degrees of freedom are admitted for the disturbed motion of the aeroplane, viz: vertical translation and rotation about the lateral axis,

(ii) aerodynamic lag is properly included in the formulae representing the unsteady aerodynamic forces,

(iii) direct numerical methods are used for the integration of the equations of motion.

2 Gust velocity.

The distribution of the gust velocity along the flight path of the aeroplane is assumed to be

$$
\begin{aligned}
w_r &= 0 && \text{if } s \leq 0 \text{ or } s \geq 2\, s_g, \\
w_r &= {}^1/_2\, w_0 \left(1 - \cos \pi \frac{s}{s_g}\right) && \text{if } 0 \leq s \leq 2\, s_g,
\end{aligned}
\tag{2.1}
$$

s giving the distance along the flight path in terms of the mean aerodynamic semichord l_0 of the wing. The length of the gust wave, $2\, s_g$, is likewise expressed in this unit and thus depends numerically on the dimensions of the aeroplane. The maximal gust intensity w_0 is positive for an upward gust. The gust velocity is constant in planes perpendicular to the flight path, which leads to symmetrical loads.

3 Results.

3.1 The load coefficients $\Lambda_{l,w}$, $\Lambda_{m,w}$, $\Lambda_{l,t}$ and $\Lambda_{m,t}$, determining the total loads by aid of formulae (2.21), (2.22), (2.23) and (2.24) of ref. 1, have been calculated as functions of s for the same cases 1 to 12 which also were investigated in ref. 1 and for one additional case, number 24. Figure 2 gives a representative result (case 11). According to this figure, aerodynamic and inertia loads reach their optimum values nearly at the same time. Thus, the maximum value of the resulting force can be deduced from the maximum values of aerodynamic and inertia loads. This conclusion holds for all cases.

The extreme values of the positive as well as of the negative load (compare the introduction) are given in table 1 and are plotted in figs. 3/6 (being reduced to absolute values in the latter figures) as functions of the parameters $\dfrac{\partial c_m}{\partial c_L}$ and C. In principle, the load coefficients depend on the same parameters as in ref. 1, but from

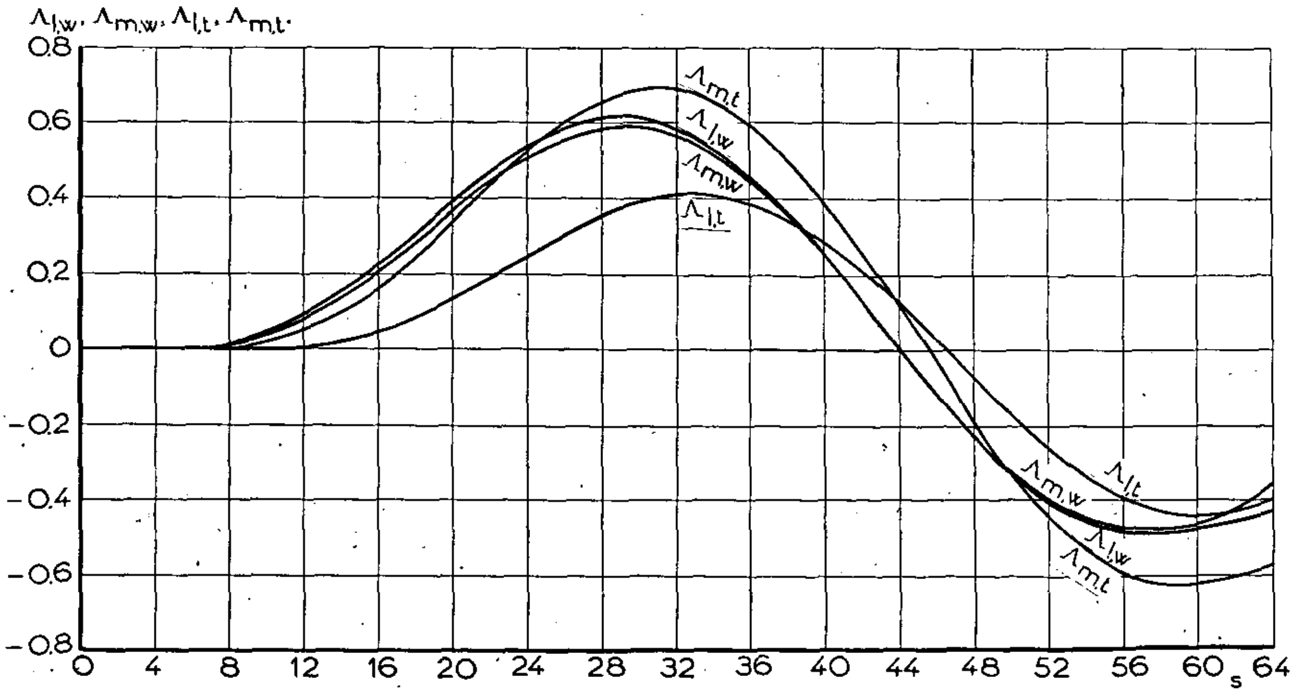

Fig. 2. Wing and tail load coefficients as functions of s for case 11.

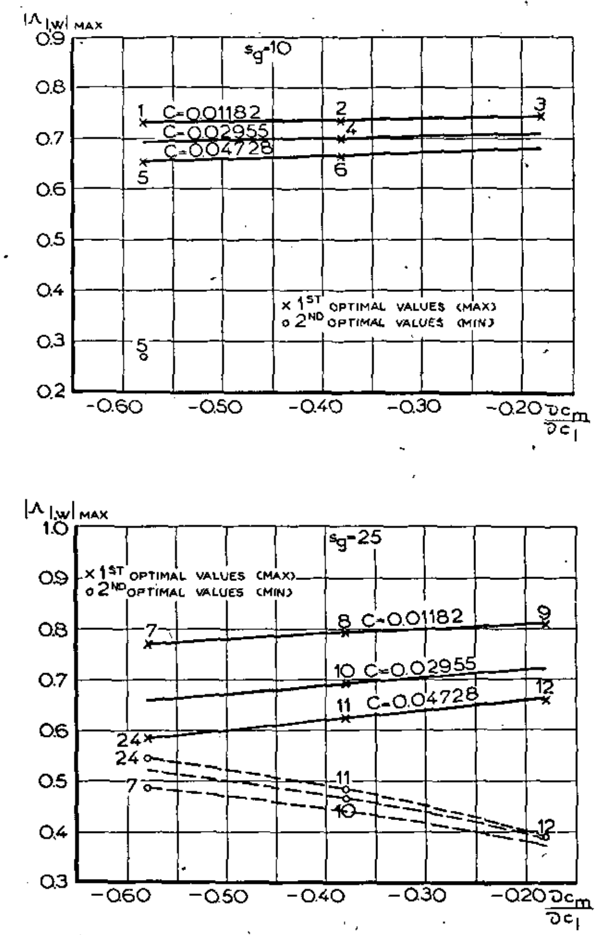

Fig. 3. Extremes of aerodynamic wing load coefficients.

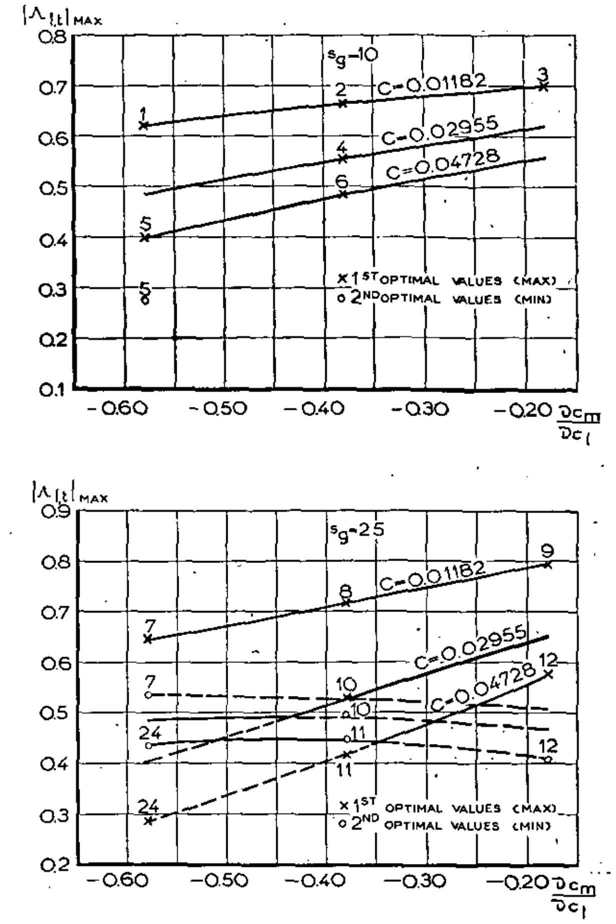

Fig. 5. Extremes of aerodynamic tail load coefficients.

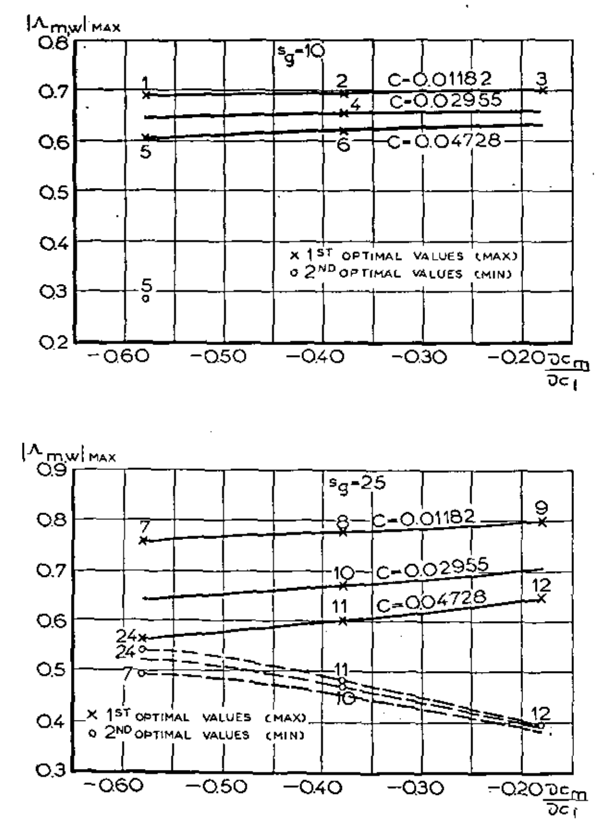

Fig. 4. Extremes of inertia wing load coefficients.

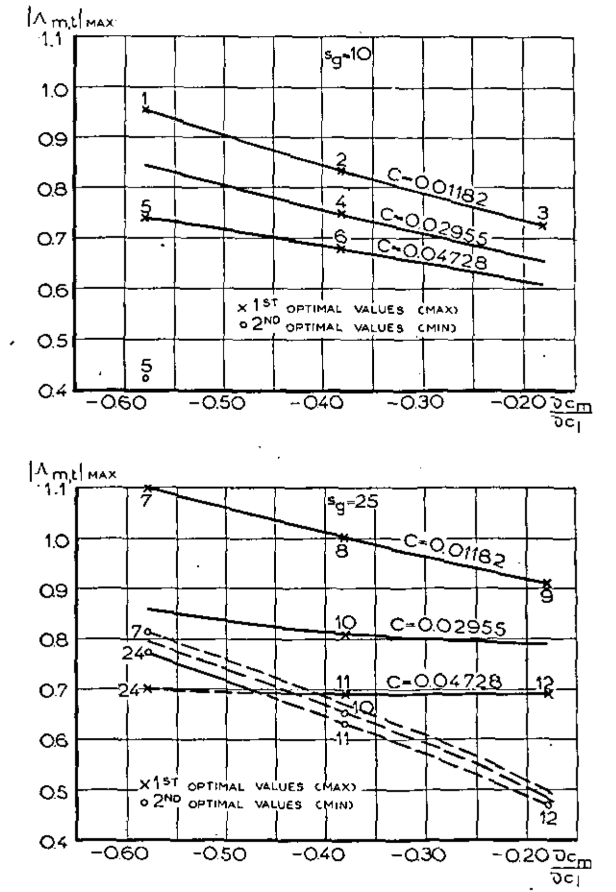

Fig. 6. Extremes of inertia tail load coefficients.

these parameters only $\frac{\partial c_m}{\partial c_L}$, C and s_g, being of decisive importance, are varied in this investigation.

3.2 *Wing loads.* It appears from figs. 3 and 4 that for the wing structure the first extreme is critical, as expected. Comparing results with those of ref. 1, it is seen that the replacement of the persisting gust by a gust wave does not affect the load coefficients very much, particularly if C is great, unless s_g is remarkably small. Indeed, the maxima for $s_g = 25$ scarcely have changed at all. This can be explained by considering the moment at which these maximum loads are reached (this moment has been marked in figs. 7 and 8). The later this moment occurs for a given value of s_g, the greater the difference between the loads for the persisting gust and the gust wave will be. If C is small — which means that the aeroplane adopts only slowly a vertical motion — the moment of maximum load will be later than for large values of C. For long gust waves, the maximum wing loads are reached at a moment, that the gust velocity has not yet decreased very much.

3.3 *Tail loads.* For the tail structure, the second extreme appears to be more important than the first (figs. 5 and 6) if C and s_g are great and $\frac{\partial c_m}{\partial c_L}$ has a great negative value (corresponding to a forward position of the centre of gravity). All these factors promote a relatively great pitching rotation of the aeroplane, causing a great upward velocity of the tailplane which must evidently amplify the second extreme. In these circumstances the gust wave leads to greater tail loads than the persisting gust.

It will be clear that, for tail loads too, the results for the persisting gust and the gust wave

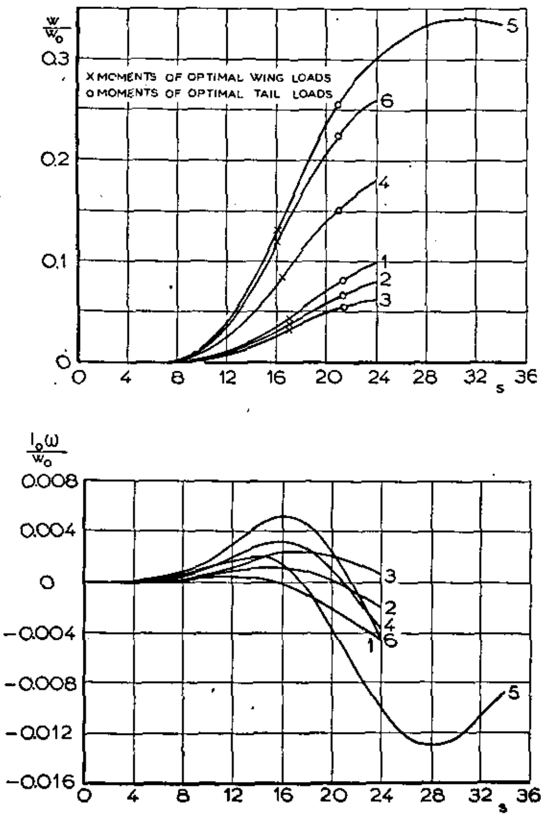

Fig. 7. Motion of the aeroplane ($s_g = 10$).

will differ more if the moment of maximum loads occurs later. Since a backward centre of gravity (small negative value of $\frac{\partial c_m}{\partial c_L}$) opposes the up-

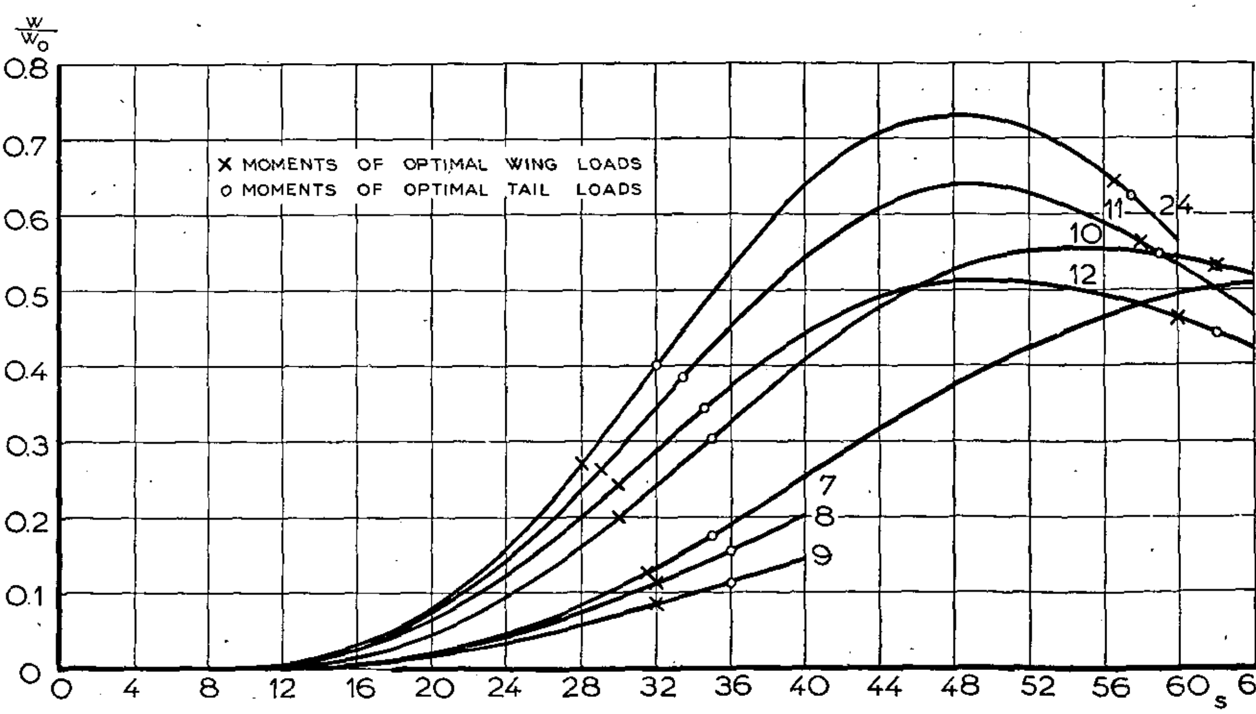

Fig. 8. Motion of the aeroplane ($s_g = 25$).

ward tail velocity, it delays the moment of maximum load. Hence, for the tail loads, differences in results for persisting gust and gust wave will be more pronounced if C and s_g are small and $\frac{\partial c_m}{\partial c_L}$ is negative and small.

Figs. 7/9 refer to the motion of the aeroplane. The velocity w is the velocity of the centre of gravity in the direction of the normal axis of the aeroplane. Acceleration velocity and angle of incidence, both for wing and tail surfaces, can be deduced from these graphs. The moments of maximum wing and tail loads are indicated in the figures.

4 References.

1 GREIDANUS, J. H. and VAN DE VOOREN, A. I.: Gust load coefficients for wing and tail surfaces of an aeroplane. Report F. 28.

2 VAN DE VOOREN, A. I.: Remarks on formulae and numerical methods used in the gust load calculations of report F. 28. Report F. 29.

Completed: October 1948.

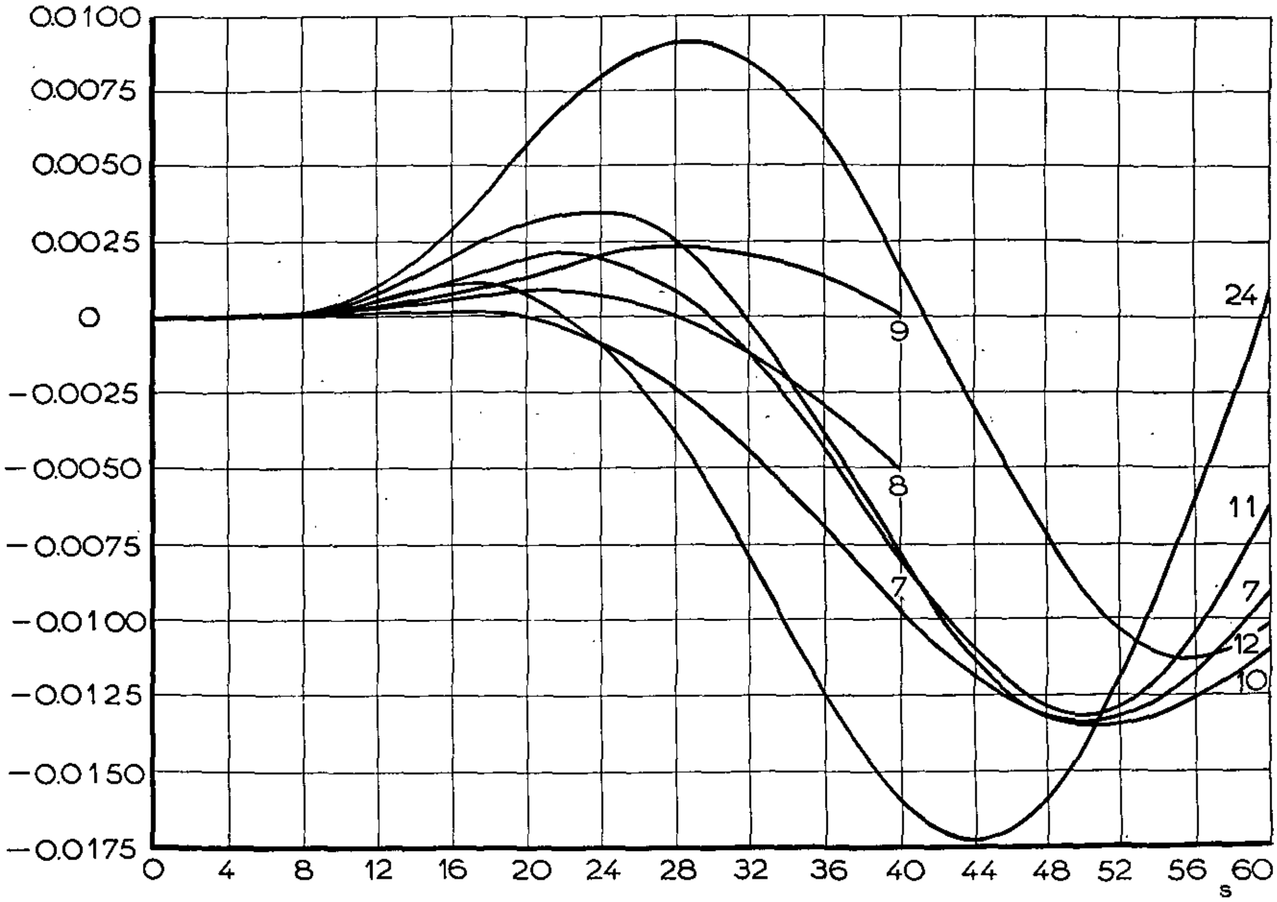

Fig. 9. Motion of the aeroplane ($s_g = 25$).

TABLE 1.

Maximum values of load coefficients. If two numbers are given, the first refers to the first extreme (maximum) and the second to the second extreme (minimum)

Case	$(\Lambda_{l,w})_{\max}$	$(\Lambda_{m,w})_{\max}$	$(\Lambda_{l,t})_{\max}$	$(\Lambda_{m,t})_{\max}$	$\frac{\partial c_m}{\partial c_L}$
1	0.733	0.689	0.624	0.952	— 0.5796
2	0.737	0.696	0.665	0.835	— 0.3796
3	0.742	0.703	0.700	0.727	— 0.1796
4	0.699	0.654	0.556	0.750	— 0.3796
5	0.654	0.606	0.397	0.741	— 0.5796
	— 0.271	— 0.282	— 0.274	— 0.428	
6	0.666	0.619	0.486	0.681	— 0.3796
7	0.767	0.762	0.642	1.101	— 0.5796
	— 0.487	— 0.497	— 0.531	— 0.815	
8	0.789	0.777	0.714	1.003	— 0.3796
9	0.810	0.800	0.794	0.910	— 0.1796
10	0.691	0.671	0.526	0.813	— 0.3796
	— 0.466	— 0.472	— 0.495	— 0.657	
11	0.621	0.599	0.419	0.692	— 0.3796
	— 0.483	— 0.484	— 0.446	— 0.636	
12	0.661	0.648	0.575	0.693	— 0.1796
	— 0.396	— 0.398	— 0.410	— 0.469	
24	0.584	0.560	0.285	0.701	— 0.5796
	— 0.546	— 0.543	— 0.433	— 0.770	

REPORT F. 45.

Proposal for an Airworthiness Requirement Referring to Symmetrical Gust Loads

by

Dr. J. H. GREIDANUS and Ir. A. I. VAN DE VOOREN.

Summary.

Four conditions of aerodynamic loading of a conventional aeroplane are indicated, each determined by a steady angle of attack, augmented with respect to the condition of undisturbed steady horizontal flight by an amount arc tan $F_j \frac{U}{V}$ (U: gust velocity; V: speed of flight; F_j, $j=1, 2, 3$ or 4: "alleviating factors"), apt to represent by suitable intercombination and completion with appropriate inertia forces symmetrical gust loads on wing, fuselage and tailplane.

Simple formulae have been established for the alleviating factors, leading to close agreement of resulting loads with the maxima of symmetrical gust loads as calculated with great care in earlier work. A corresponding modification of existing ICAO standards is proposed.

Transient overstresses are not considered and should be determined by separate calculation.

Contents.

1 Introduction.

At the National Aeronautical Research Institute much attention has been paid during the last seven years to the calculation of gust loads. Extensive results, published in ref. 1, have given rise to still more careful calculations published recently in ref. 2 and ref. 3. This work has been done on request of the Netherlands Civil Air Service (Rijksluchtvaartdienst); one of the aims was to obtain reliable data for the establishment of rational gust-load requirements in the Airworthiness Standards.

An analysis of the results has, indeed, led to a proposal, intended to improve the present recommendation in the PICAO Doc. 3031, Proposed 1947 Edition of Airworthiness (AIR) Standards and Recommended Practices.

In this report it is presented, discussed and compared with the existing recommendation.

2 Proposal for a new airworthiness requirement.

It is suggested that the articles 3.3.1.4; 3.3.1.4.1; 3.3.1.4.2 and 3.3.1.4.3 in Doc. 3031 of the PICAO (Proposed 1947 Edition of Airworthiness (AIR) Standards and Recommended Practices) be maintained in their present form and that the articles 3.3.1.4.4 and 3.3.1.4.5 be changed as follows.

3.3.1.4.4 Equivalent gust loads.

Recommendation. Apart from transient overstresses, an acceptable approximation for gust loads is to derive them from 4 conditions of aerodynamic loading, each determined by a steady angle of attack of the whole aeroplane, augmented with respect to the condition of undisturbed steady horizontal flight by an amount arc tan $F \frac{U}{V}$, taking

$F = F_w$ in the first case,
$F = {}^2/_3 F_t$ in the second case,
$F = F_t$ in the third case,
$F = {}^1/_2 F_t$ in the fourth case,

while:

U is the maximum prescribed gust velocity;
V is the flight speed (EAS).

The alleviating factor F_w is given by the following formula (see also Fig. 3.3)

$$F_w = 1 - a_w E^{0.4},$$

where $a_w = 0.5 + 0.0005 \left(\frac{d}{c}\right)^2 - 0.6 \frac{\partial c_m}{\partial c_L}$

and $E = \dfrac{\gamma \frac{\partial c_L}{\partial \alpha} c}{W/S}$.

The alleviating factor F_t shall be taken equal to the greater of the two values

$$(F_t)_1 = 1 - a_t \sqrt{E},$$

$$(F_t)_2 = 0.68 - 0.6\,E - 1.5\,\frac{c}{d},$$

with $a_t = 0.40 + 0.001\left(\frac{d}{c}\right)^2 - 3.2\,\frac{\partial c_m}{\partial c_L}$.

Moreover

$\frac{\partial c_L}{\partial \alpha}$ slope of lift curve of the whole aeroplane (steady aerodynamic lift being equal to $L = c_L \,.\, {}^1/_2\, \rho\, V^2 \,.\, S$, where ρ denotes the air density)

c_m coefficient of moments in steady flow (aerodynamic moment of the whole aeroplane being equal to $M = c_m \,.\, {}^1/_2\, \rho\, V^2 \,.\, S \,.\, c$), referring to the centre of gravity and positive if tailheavy

c mean aerodynamic wing chord

d assumed gradient distance of the gust

γ specific weight of the air (weight per unit of volume)

W appropriate aeroplane design weight

S design wing area.

Then

(i) The approximated gust load on the wing is obtained by combining the aerodynamic loads on wing and fuselage from case 1 with the aerodynamic load on the horizontal tailplane of case 2 and assuming inertia forces resulting from these combined external loads.

(ii) The approximated gust load on the horizontal tailplane is equal to the resulting load on this plane when the whole aeroplane is subject to the aerodynamic loads of case 3 and appropriate balancing inertia forces are assumed.

(iii) The approximated gust load on the fuselage is obtained by combining the aerodynamic load of the wing from case 1 with the aerodynamic loads on fuselage and horizontal tailplane from case 4, assuming inertia forces, resulting from these combined external loads.

3 Equivalent gust loads.

3.1 *Wing.*

It has been shown in ref. 2, eq. (2.21), that the aerodynamic force on the whole wing can be written as

$$p_w\, \Lambda_{l,w}(s) \,.\, {}^1/_2\, \rho\, \frac{\partial c_L}{\partial \alpha}\, V\, S\, U; \qquad (3.1)$$

where

$$p_w = \left(\frac{\partial c_L}{\partial \alpha}\right)_{wing} \bigg/ \frac{\partial c_L}{\partial \alpha}, \qquad (3.2)$$

while s is a coordinate along the flight path of the aeroplane in the gust, measuring the distance between the nose of the aeroplane and the boundary of the gradient zone of the gust in terms of mean aerodynamic wing chords.

Clearly this aerodynamic loading is identical with the loading due to a steady angle of attack increased by an amount arc tan $\Lambda_{l,w}(s)\frac{U}{V}$ with respect to the steady horizontal flight condition.

The function $\Lambda_{l,w}(s)$ depends on the parameters of the aeroplane and on the characteristics of the gust field.

The alleviating factor F_w has been determined in such a way that it approximates the maximum of the function $\Lambda_{l,w}(s)$, obtained in ref. 2 for a sinusoidal velocity increase in the gradient zone of the gust. For a gust field with linear velocity distribution in the gradient zone the maxima are practically the same.

An increase of the angle of attack of the whole aeroplane leads to a linear acceleration in the centre of gravity equal to

$$\frac{1}{m}\, \Lambda_{l,w}(s) \,.\, {}^1/_2\, \rho\, \frac{\partial c_L}{\partial \alpha}\, V\, S\, U.$$

However, the inertia load on the wing is actually given by (compare eq. (2.22) of ref. 2):

$$-\frac{m_w}{m}\, \Lambda_{m,w}(s) \,.\, {}^1/_2\, \rho\, \frac{\partial c_L}{\partial \alpha}\, V\, S\, U. \qquad (3.3)$$

$\Lambda_{l,w}(s)$ and ${}_{m,w}(s)$ are not identical for the two following reasons:

(i) The aerodynamic loads on the tailplane show a lag with respect to those of the wing, due to the smaller penetration of the tail into the gust.

(ii) The centre of gravity of the wing does not coincide with the centre of gravity of the whole aeroplane.

The first reason being more important, $\Lambda_{m,w}$ is always smaller than $\Lambda_{l,w}$ until its maximum is reached (see fig. 1 of ref. 2). This has two consequences:

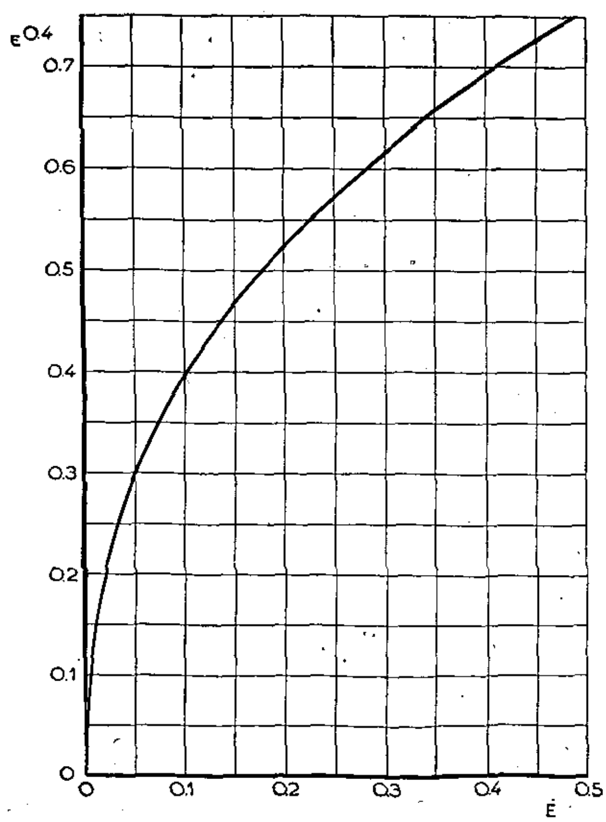

Fig. 1. Diagram for determining $E^{0.4}$.

(i) The unloading inertia forces are overestimated if the change in angle of attack $\Lambda_{l,w}\frac{U}{V}$ is also accepted for the tailplane.

(ii) The resulting load, being equal to the sum of (3.1) and (3.3), has a maximum which is shifted towards the values of s, where the greatest difference between $\Lambda_{l,w}$ and $\Lambda_{m,w}$ occurs, especially if $p_w \Lambda_{l,w}$ and $\frac{m_w}{m}\Lambda_{m,w}$ are almost equal. This makes the overestimation still more serious.

These difficulties are solved by assuming an aerodynamic loading at the tailplane corresponding to an increase of the angle of attack of the whole aeroplane of arc tan $^2/_3\, F_t \frac{U}{V}$. The alleviating factor F_t has been determined as an approximation to the maximum of the function $\Lambda_{l,t}(s)$.

With symbols explained under table 6, the inertia load at the wing turns out to be

$$-\frac{m_w}{m}\left[\left\{ p_w\left(1+\frac{\varepsilon^2}{j^2}\right)+ + p_f\left(1+\frac{\varepsilon\,(e+{}^1/_2+\varepsilon)}{j^2}\right)\right\}F_w + + p_t\left\{1-\frac{\varepsilon\,(\beta-\varepsilon)}{j^2}\right\}{}^2/_3\,F_t\right]{}^1/_2\,\rho\,\frac{\partial c_L}{\partial\alpha}\,V\,S\,U. \tag{3.4}$$

Omitting the constant factor $^1/_2\,\rho\frac{\partial c_L}{\partial \alpha} V\,S\,U$, the resulting load is given by

$$p_wF_w-\frac{m_w}{m}\left[\left\{p_w\left(1+\frac{\varepsilon^2}{j^2}\right)+ + p_f\left(1+\frac{\varepsilon\,(e+{}^1/_2+\varepsilon)}{j^2}\right)\right\}F_w + + p_t\left\{1-\frac{\varepsilon\,(\beta-\varepsilon)}{j^2}\right\}{}^2/_3\,F_t\right], \tag{3.5}$$

which must be compared with the maximum of the exact load:

$$p_w\,\Lambda_{l,w}-\frac{m_w}{m}\Lambda_{m,w}\,. \tag{3.6}$$

Table 6 gives the values of the parameters. The result of the comparison between (3.5) and (3.6) for some of the cases investigated is shown in table 1.

The gust load for a part of the wing can be obtained by replacing in (3.1), but not in (3.4), p_w by the ratio of $\frac{\partial c_L}{\partial \alpha}$ for the part considered to $\frac{\partial c_L}{\partial \alpha}$ for the whole aeroplane. Similarly, in (3.3) m_w should be replaced by the mass of the part considered.

Since it is shown in table 1 that the approximation for the gust load tends to become more conservative for decreasing ratio of inertia to aerodynamic load and this ratio decreases towards the wing tip, it will be clear that the approximation for the bending moment will be more conservative than that for the total force (the latter being given in table 1).

3.2 *Horizontal tailplane.*

From ref. 2 it follows that the aerodynamic force on the tailplane is equal to

$$p_t\Lambda_{l,t}(s)\;{}^1/_2\,\rho\frac{\partial c_L}{\partial\alpha}\,V\,S\,U, \tag{3.8}$$

where

$$p_t=\left(\frac{\partial c_L}{\partial\alpha}\right)_{tail}\Big/\frac{\partial c_L}{\partial\alpha}$$

and that the inertia force is equal to

$$-\frac{m_t}{m}\Lambda_{m,t}(s)\,.\,{}^1/_2\,\rho\,\frac{\partial c_L}{\partial\alpha}\,V\,S\,U. \tag{3.9}$$

The alleviating factor F_t has been determined as an approximation to the maximum of the factor $\Lambda_{l,t}(s)$. It has been shown in 3 that in the case of a gust wave, where the gust velocity after having attained its maximum, decreases again to zero, a second load maximum of opposite sign occurs, which for the tail may exceed the first. The second maximum is approximated by $(F_t)_2$, while $(F_t)_1$ gives the first, practically agreeing with that for a persisting gust.

The aerodynamic and inertia loads of the horizontal tailplane are well approximated by assuming a steady angle of attack, increased by the amount $F_t\,\frac{U}{V}$, of the whole aeroplane with regard

TABLE 1.

Case	p_w	$\frac{m_w}{m}$	(3.5)	(3.6)	Max. load reached at $s =$
2	0.846	0.8	0.060	0.069	7
,,	,,	0.7	0.140	0.135	8
,,	,,	0.5	0.297	0.284	11
3	,,	0.8	0.059	0.064	7
,,	,,	0.7	0.140	0.137	9
,,	,,	0.5	0.299	0.289	11
6	,,	0.8	0.055	0.073	8
,,	,,	0.7	0.120	0.134	8
,,	,,	0.5	0.250	0.259	9

See table 6 for case numbers.

to the steady flight condition. The inertia load at the tailplane then becomes equal to

$$-\frac{m_t}{m}\left[p_w \left\{ 1 - \frac{\varepsilon(\beta-\varepsilon)}{j^2} \right\} + \right.$$

$$+ p_f \left\{ 1 - \frac{(\beta-\varepsilon)(e+{}^1/_2+\varepsilon)}{j^2} \right\} +$$

$$\left. + p_t \left\{ 1 + \frac{(\beta-\varepsilon)^2}{j^2} \right\} \right] F_t \,.\, {}^1/_2\, \rho \frac{\partial c_L}{\partial \alpha} V S U,$$

which by making use of eq. (2.19) and (2.20) of ref. 2 may be simplified to

$$-\frac{m_t}{m}\left\{ 1 - \frac{\beta-\varepsilon}{j^2}\frac{\partial c_m}{\partial c_L} \right\} F_t \,.\, {}^1/_2\, \rho \frac{\partial c_L}{\partial \alpha} V S U. \tag{3.10}$$

Again omitting a constant factor, the approximated resulting load at the tailplane becomes

$$p_t F_t - \frac{m_t}{m}\left\{ 1 - \frac{\beta-\varepsilon}{j^2}\frac{\partial c_m}{\partial c_L} \right\} . F_t, \tag{3.11}$$

which is compared in table 2 with the maximum of the exact load

$$p_t \Lambda_{l,t} - \frac{m_t}{m}\Lambda_{m,t}. \tag{3.12}$$

It is seen in table 2 that the approximation is satisfactory and generally conservative.

TABLE 2.

Case	p_t	$\frac{m_t}{m}$	(3.11)	(3.12)	Max. load reached at $s =$
2	0.095	0.02	0.053	0.050	13
,,	,,	0.01	0.063	0.060	13
3	,,	0.02	0.061	0.058	14
,,	,,	0.01	0.070	0.067	14
6	,,	0.02	0.037	0.030	12
,,	,,	0.01	0.045	0.038	12
See table 6 for case numbers					

In the same way as for the wing the gust load for a part of the tailplane is obtained by replacing in (3.11) p_t by the ratio of $\frac{\partial c_L}{\partial \alpha}$ for the part considered to $\frac{\partial c_L}{\partial \alpha}$ for the whole aeroplane and m_t by the mass of the part considered.

3.3 *Fuselage.*

The loading of the fuselage is almost entirely due to the inertia forces. The acceleration at a point of the fuselage at a distance $x\,c$ behind the quarter-chord point of the mean aerodynamic wing chord is proportional to

$$\frac{(\beta-x)\,\Lambda_{m,w} + x\,\Lambda_{m,t}}{\beta}$$

$\Lambda_{m,w}$ and $\Lambda_{m,t}$ being proportional to the accelerations at wing and tail respectively.

Hence, the bending moment of the part of the fuselage behind the wing, due to these inertia forces and taken with respect to the quarter-chord point of the wing, is equal to

$$\int_0^\beta \frac{m_r}{m}\,\frac{(\beta-x)\,\Lambda_{m,w} + x\,\Lambda_{m,t}}{\beta}\,x\,dx \,.\, {}^1/_2\, \rho \frac{\partial c_L}{\partial \alpha} V S U c^2,$$

if m_r denotes the mass of the fuselage per unit length. This moment will be written as

$$\left\{ \frac{m_R s_R}{m}\Lambda_{m,w} + \frac{m_R j_R^2}{m\beta}(\Lambda_{m,t} - \Lambda_{m,w}) \right\} {}^1/_2\, \rho \frac{\partial c_L}{\partial \alpha} V S U c,$$

where m_R denotes the mass, $s_R\,c$ the distance aft of the wing quarter-chord point of the center of gravity and $j_R c$ the radius of gyration, all refering to the part of the fuselage behind the wing and including the tail. Further, there is an unloading contribution to this moment, arising from the aerodynamic force of the tailplane, amounting to

$$-\beta\, p_t \Lambda_{l,t} \,.\, {}^1/_2\, \rho \frac{\partial c_L}{\partial \alpha} V S U c.$$

Hence, the total moment is proportional to

$$\frac{m_R s_R}{m}\Lambda_{m,w} + \frac{m_R j_R^2}{m\beta}(\Lambda_{m,t} - \Lambda_{m,w}) - $$

$$-\beta\, p_t \Lambda_{l,t}. \tag{3.13}$$

With the approximative calculation of the proposed gust load recommendation, the following substitution must be made

$$\Lambda_{l,t} = {}^1/_2 F_t,$$

$$\Lambda_{m,w} = p_w\left(1 + \frac{\varepsilon^2}{j^2}\right)F_w +$$

$$+\left[p_f \left\{ 1 + \frac{\varepsilon(e+{}^1/_2+\varepsilon)}{j^2} \right\} + \right.$$

$$\left. + p_t \left\{ 1 - \frac{\varepsilon(\beta-\varepsilon)}{j^2} \right\} \right] {}^1/_2 F_t,$$

$$\Lambda_{m,t} - \Lambda_{m,w} = -\frac{\beta}{j^2}\,[\varepsilon\, p_w F_w +$$

$$+ \{ (e+{}^1/_2+\varepsilon)p_f - (\beta-\varepsilon)p_t \}\, {}^1/_2 F_t]. \tag{3.14}$$

Comparisons are made in table 3 between the maximum values of (3.13) calculated by aid of the results of ref. 2 and those calculated with the substitutions of formulae (3.14).

Along the same lines, the bending moment in any other fuselage section may be obtained. For sections more aft than that considered above, the ratio between the contributions of aerodynamic and inertia loads increases. This tends to make, as is shown in table 3, the approximation less conservative. It is, thought, however, that in the critical fuselage section the approximation will remain satisfactory.

4 The formulae for F_w and F_t.

It was shown in ref. 2 and ref. 3, that the maximum aerodynamic wing load depends chiefly on the static stability of the aeroplane $\left(\frac{\partial c_m}{\partial c_L}\right)$, on the gradient distance of the gust and on a parameter E ($= 4\,C$, C being the parameter used in ref. 2 and ref. 3). Other parameters have only a minor influence. An approximation formula was *established, containing only these three quantities.* It will be clear from table 6 that in the considered ranges of the parameters it gives an approximation to $(\Lambda_{l,w})_{\max}$, which is accurate within 4 %, being generally conservative.

For very great values of E (i. e. $E = 0.36$), the proposed formula gives the following results

$\frac{d}{c}$	$\frac{\partial c_m}{\partial c_L}$	F_w
5	— 0.19	0.584
12.5	— 0.19	0.540

while calculations published in ref. 1 lead to maximum values of $\Lambda_{l,w}$ amounting to 0.57 and 0.47 respectively.

The quadratic relation between F_w and $\frac{d}{c}$ holds up to a certain value of $\frac{d}{c}$ only. This value lies usually well above 50 showing that this restriction is unimportant for gust calculations.

The maximum aerodynamic load at the horizontal tailplane also depends chiefly on $\frac{\partial c_m}{\partial c_L}$, $\frac{d}{c}$ and E, but other parameters have more influence than in the case of the wing. The formula for $(F_t)_1$ is kept more conservative in order to account for unfavourable changes in those additional parameters.

TABLE 3.

Case	$\beta\, p_t$	$\frac{m_R s_R}{m}$	$\frac{m_R j_R^2}{m\beta}$	(3.13) exact	(3.13) with (3.14)	Max. load reached at $s =$
2	0.308	1.0	0.2	0.631	0.662	11
,,	,,	,,	0.5	0.705	0.708	12
,,	,,	0.6	0.2	0.323	0.362	9
,,	,,	0.3	,,	0.126	0.137	7
,,	,,	,,	0.1	0.133	0.121	7
3	,,	1.0	0.2	0.608	0.641	11
,,	,,	0.6	,,	0.298	0.333	8
,,	,,	0.3	,,	0.106	0.102	7
,,	,,	,,	0.1	0.128	0.102	7
6	,,	1.0	0.2	0.545	0.553	9
,,	,,	0.6	,,	0.298	0.307	8
,,	,,	0.3	,,	0.118	0.123	7
,,	,,	,,	0.1	0.127	0.111	7

See table 6 for case numbers

In table 4, the alleviating factor of the present ICAO recommendation has been compared with the alleviating factors F_w and F_t proposed in this report. It is seen that for flight conditions with backward position of the center of gravity, the new values for the wing are higher. The values for the tail are for these conditions also higher if the wing loading is large.

It is not quite clear in the present ICAO-recommendation if aerodynamic loads at the tailplane must be assumed, when considering wing gust loads. Consequently, an uncertainty in the balancing inertia forces exists. If no aerodynamic load at the tailplane is assumed, the proposal of this report means, in spite of its higher alleviating factor, a generally less severe requirement than the ICAO recommendation since the unloading inertia forces are larger in the proposal. If at the tailplane the same change in angle of attack

TABLE 4.

W/S (kg/m²)	$c(m)$	$\frac{\partial c_m}{\partial c_L}$	F (ICAO)	F_w	F_t	E [1])
100	2	—0.10	0.630	0.684	0.631	0.15
,,	,,	—0.30	,,	0.627	0.492	,,
,,	3	—0.10	,,	0.664	0.589	0.225
,,	,,	—0.30	,,	0.597	0.397	,,
,,	4	—0.10	,,	0.637	0.574	0.30
,,	,,	—0.30	,,	0.563	0.303	,,
200	2	—0.10	0.700	0.759	0.739	0.075
,,	,,	—0.30	,,	0.716	0.564	,,
,,	4	—0.10	,,	0.724	0 699	0.15
,,	,,	—0.30	,,	0.668	0.451	,,
300	2	—0.10	0.725	0.796	0.787	0.05
,,	,,	—0.30	,,	0.760	0.644	,,
,,	4	—0.10	,,	0.766	0.754	0.10
,,	,,	—0.30	,,	0.719	0.552	,,

[1]) Assuming $\gamma = 1.25$ kg/m³, $\frac{\partial c_L}{\partial \alpha} = 6$ and $d = 30.5$ m (100 ft)

TABLE 5.

	W/S (kg/m²)	$c(m)$	E [1])
Airspeed Ambassador	183	3.2	0.131
Avro Tudor	275	3.6	0.098
Bristol Freighter	127	4.1	0.242
de Havill. Dove	124	1.8	0.109
Vickers Viking	188	3.0	0.120
Aérocentre Martinet (Siebel)	122	2.1	0.130
S. E. Languedoc	205	3.7	0.135
S. A. A. B. Scandia	159	3.1	0.146
Consolidated Convair	210	3.0	0.107
Douglas DC 6	280	3.8	0.102
Lockheed Constellation	236	4.1	0.130

[1]) Assuming $\gamma = 1.25$ kg/m³, $\frac{\partial c_L}{\partial \alpha} = 6$.

is assumed as at the wing, the proposal is more stringent.

In table 5 the values of wing loading, chord and parameter E are tabulated for some modern transport planes (ref. 4).

For the fuselage, the proposal seems to be less severe *than the present ICAO recommendation*, since in the proposal aerodynamic tail load increasements due to the gust are taken into account *for 50 %*.

5 References.

1 GREIDANUS, J. H.: The loading of aeroplane structures by symmetrical gusts (in Dutch with English abstract). Reports and Transactions of the National Aeronautical Research Institute, Vol. XIV (1947).

2 GREIDANUS, J. H. and VAN DE VOOREN, A. I.: Gust load coefficients for wing and tail surfaces of an aeroplane. Report F. 28 (1948).

3 VAN DE VOOREN, A. I.: Loads on wing and tail surfaces of an aeroplane due to a sinusoidal gust wave. Report F. 33 (1948).

4 Jane's all the worlds aircraft, 1947.

Completed: Febr. 1949.

TABLE

Comparison of F_w and F_t with the maxima

Case	$\frac{d}{c}$	E	$\frac{\partial c_m}{\partial c_L}$	ε	p_w	$\frac{p_s}{p_w}$	$\frac{p_n}{p_w}$	$\frac{p_f}{p_w}$	j
1	5	0.04728	—0.290	—0.1	0.8460	0.15	—0.0379	0.07	1.25
2	,,	,,	—0.190	0	,,	,,	,,	,,	,,
3	,,	,,	—0.090	0.1	,,	,,	,,	,,	,,
4	,,	0.11820	—0.190	0	,,	,,	,,	,,	,,
5	,,	0.18912	—0.290	—0.1	,,	,,	,,	,,	,,
6	,,	,,	—0.190	0	,,	,,	,,	,,	,,
7	12.5	0.04728	—0.290	—0.1	,,	,,	,,	,,	,,
8	,,	,,	—0.190	0	,,	,,	,,	,,	,,
9	,,	,,	—0.090	0.1	,,	,,	,,	,,	,,
10	,,	0.11820	—0.190	0	,,	,,	,,	,,	,,
24	,,	0.18912	—0.290	—0.1	,,	,,	,,	,,	,,
11	,,	,,	—0.190	0	,,	,,	,,	,,	,,
12	,,	,,	—0.090	0.1	,,	,,	,,	,,	,,
13	5	0.04448	—0.328	0	0.8992	,,	,,	0	,,
14	,,	0.04728	—0.190	0	0 8460	,,	,,	0.07	1.5
15	,,	,,	—0.290	—0.1	,,	,,	,,	,,	1
16	,,	,,	—0.090	0.1	,,	,,	,,	,,	,,
17	,,	0.18912	—0.290	—0.1	,,	,,	,,	,,	,,
18	,,	0.04876	—0.284	0	0.8200	0.20	—0.0505	,,	1.25
19	,,	,,	—0.184	0.1	,,	,,	,,	,,	,,
20	,,	0.04720	—0.137	0	0.8477	0.15	—0.0404	,,	,,
21	,,	,,	—0.237	—0.1	,,	,,	,,	,,	,,
22	,,	0.04660	—0.144	0	0.8586	,,	—0.0553	,,	,,
23	,,	,,	—0.244	—0.1	,,	,,	,,	,,	,,

$p_w = \left(\frac{\partial c_L}{\partial \alpha}\right)_w \Big/ \frac{\partial c_L}{\partial \alpha}$, if $(c_L)_w$ denotes the lift coefficient of the wing in steady flow (referred to wing area)

$p_s = \left(\frac{\partial c_L}{\partial \alpha}\right)_s \Big/ \frac{\partial c_L}{\partial \alpha}$, if $(c_L)_s$,, ,, ,, ,, ,, ,, tail in a free, steady flow (referred to wing area)

$p_n = \left(\frac{\partial c_L}{\partial \alpha}\right)_n \Big/ \frac{\partial c_L}{\partial \alpha}$, if $(c_L)_n$,, ,, (negative) lift coefficient of the tail due to steady downwash of the wing (referred to wing area)

$p_f = \left(\frac{\partial c_L}{\partial \alpha}\right)_f \Big/ \frac{\partial c_L}{\partial \alpha}$, if $(c_L)_f$,, ,, lift coefficient of the fuselage in a steady flow (referred to wing area)

$p_t = p_s + p_n$

εc = backward position of the centre of gravity with respect to the wing quarter-chord point

βc = distance between quarter-chord points of wing and tail

jc = radius of gyration of the aeroplane about its lateral axis

ec = foreward position of the point, at which the fuselage aerodynamic forces act, with respect to wing leading edge of mean aerodynamic chord

In all calculations e was taken equal to 1.75 and the tail chord was taken equal to $^2/_3$ c.

6.

of $\Lambda_{l,w}$ and $\Lambda_{l,t}$, as obtained in refs. 1 and 2.

β	$(\Lambda_{l,w})_{max}$	F_w	Δ in %	$(\Lambda_{l,t})_{max.1}$	$(F_t)_1$	Δ in %	$(\Lambda_{l,t})_{max.2}$	$(F_t)_2$	Case
3.25	0.797	0.798	0.1	0.687	0.706	2.8			1
,,	0.812	0.815	0.4	0.746	0.775	3.9			2
,,	0.832	0.833	0.1	0.816	0.845	3.6			3
,,	0.737	0.734	—0.4	0.605	0.645	6.6			4
,,	0.666	0.648	—2.7	0.390	0.412	5.6	0.274	0.267	5
,,	0.686	0.679	—1.0	0.517	0.550	6.4			6
,,	0.775	0.778	0.4	0.635	0.677	6.6	0.531	0.532	7
,,	0.796	0.796	0	0.710	0.747	5.2			8
,,	0.819	0.814	—0.6	0.798	0.817	2.4			9
,,	0.693	0.705	1.7	0.551	0.600	8.9	0.495	0.489	10
,,	0.590	0.614	4.1	0.301	0.355	17.9	0.433	0.447	24
,,	0.626	0.645	3.0	0.442	0.494	11.8	0.446	0.447	11
,,	0.663	0.676	2.0	0.605	0.633	4.6	0.410	0.447	12
,,	0.794	0.796	0.3	0.660	0.691	4.7			13
,,	0.810	0.815	0.6	0.749	0.775	3.5			14
,,	0.793	0.798	0.6	0.658	0.706	7.3			15
,,	0.846	0.833	—1.5	0.834	0.845	1.3			16
,,	0.668	0.648	—3.0	0.386	0.412	6.7			17
,,	0.806	0.796	—1.2	0.712	0.705	—1.0			18
,,	0.822	0.814	—1.0	0.766	0.776	1.3			19
2.75	0.811	0.825	1.7	0.762	0.813	6.7			20
,,	0.795	0.807	1.5	0.707	0.743	5.1			21
3.25	0.813	0.825	1.5	0.734	0.809	10.0			22
,,	0.797	0.807	1.3	0.660	0.740	12.1			23

REPORT F. 35.

A One Parameter Method for the Calculation of Laminar Boundary Layers

by

Dr. R. TIMMAN.

Summary.

Based on Von Karman's momentum equation for boundary layer flow a new assumption for the velocity profile is made, taking account of as many boundary conditions at the wall as is possible and of the asymptotic behaviour at the outer edge of the boundary layer.
The results are checked with known exact calculations and show a definite improvement over those obtained from the well-known Pohlhausen method, particularly in the region of retarded flow.

Contents.

1 Description of the method.

1.1 *Introduction.*

For calculations of the flow in a laminar boundary layer it is useful to have the disposition of a method by which a solution of the boundary layer equations, warranting a reasonable accuracy, can quickly be obtained.

The classical Pohlhausen method (ref. 7) yields the desired results in a very convenient way; however, they are not sufficiently accurate for many important purposes, especially in regions of retarded flow. For the calculation of the stability of laminar boundary layer flow, in which the second derivative of the velocity profile in the boundary layer is needed, the Pohlhausen method cannot be used.

For this purpose Schlichting and Ullrich derived another method, which, however, fails completely in the neighbourhood of a stagnation point.

In this paper, using the same principle as Pohlhausen and Schlichting, i.e. the equation of momentum transport, first given by Von Karman (ref. 5), a new method will be developed.

The accuracy will be tested by comparing the results with known cases of carefully computed boundary layers.

1.2 *Classical approximation methods, based on the momentum equation.*

The equations for boundary layer motion are:

$$\begin{cases} u\,u_x + v\,u_y = UU' + \nu\,u_{yy}, & (2.1)\\ u_x + v_y = 0. & (2.2)\end{cases}$$

Here, u and v are the velocity components of the flow in the boundary layer, U is the velocity of the free flow and U' is the derivative $\frac{dU}{dx}$ of this velocity, x and y are coordinates along and normal to the surface, ν is the kinematical viscosity and the suffixes denote partial differentiation.

A solution of this equation, describing a physical flow, has to satisfy the following boundary conditions

$$y = 0 : u = 0,\ v = 0, \qquad (2.3)$$

$$\nu\,u_y = \tau_0/\rho, \qquad (2.4)$$

where τ_0 is the skin friction per unit length.

Now, from eq. (2.1) and (2.2) von Karman has derived the momentum equation (ref. 5) in the form:

$$\frac{\tau_0}{\rho U^2} = \frac{U'}{U}(\delta_1 + 2\,\delta_2) + \frac{d\delta_2}{dx}. \qquad (2.5)$$

Here, δ_1 is the displacement thickness, defined by

$$\delta_1 = \int_0^\infty \left(1 - \frac{u}{U}\right) dy \qquad (2.6)$$

and δ_2 is the momentum thickness

$$\delta_2 = \int_0^\infty \frac{u}{U}\left(1 - \frac{u}{U}\right) dy. \qquad (2.7)$$

The fundamental idea of the approximation methods based on this equation is to assume, that the dependence on y of the solution $u(x, y)$ of the original equations, can be expressed by some known expression of y, in which appear coefficients to be considered as provisionally unknown functions of x.

For large values of y the velocity u approaches indefinitely the value U of the free stream velocity outside the boundary layer, while its derivatives tend to vanish.

So, putting for a certain value of x

$$\frac{u}{U} = f(y), \qquad (2.8)$$

the conditions

$$y \to \infty: \quad f(y) \to 1, \qquad (2.9)$$

$$f^{(n)}(y) \to 0 \quad \text{for all } n, \qquad (2.10)$$

hold.

Boundary conditions for $y = 0$ are given by (2.3) and (2.4), but it should be remarked that τ_0 is not an a priori given function of x, but a function resulting from the calculations. Additional boundary conditions can be obtained from eq. (2.1) and its successive derivatives to y by putting $y = 0$.

$$UU' = -\nu\, u_{yy}, \qquad (2.11)$$

$$0 = u_{yyy}, \qquad (2.12)$$

$$+ u_y\, u_{xy} = \nu\, u'_{yyyy}. \qquad (2.13)$$

Generally, as many boundary conditions for $y \to \infty$ and $y = 0$ are taken into account as is necessary to express all unknown coefficients in the expression $f(y)$ for the velocity profile in one parameter λ, which is to be considered as a function of x. All quantities occurring in eq. (2.5) can then be expressed in λ, reducing this equation to an ordinary differential equation in x, from which $\lambda(x)$ can be determined. W a l t z has given this equation a very simple form by reducing the distance to the wall y to a non-dimensional quantity with the help of the momentum thickness

$$y = \eta_2 \,.\, \delta_2\,.$$

Then:

$$\delta_1 = \Delta_{12}\delta_2\,.$$

The non-dimensional parameter is given by:

$$\lambda_2 = \frac{\delta_2^{\,2}}{\nu}\, U' = -\,\delta_2^{\,2}\left(\frac{\delta^2 f}{\delta y^2}\right)_{y=0} = -\left(\frac{\delta^2 f}{\delta \eta_2^{\,2}}\right)_{\eta_2=0}. \qquad (2.14)$$

The non-dimensoinal quantity representing the skin friction is

$$T_2 = \frac{\tau_0}{\rho\, U^2}\;\frac{U\,\delta_2}{\nu} = \delta_2\left(\frac{\delta f}{\delta y}\right)_{y=0} = \left(\frac{\delta f}{\delta \eta_2}\right)_{\eta_2=0}. \qquad (2.15)$$

After multiplication with $\dfrac{U\,\delta_2}{\nu}$ the momentum equation can be transformed into

$$U\,\frac{d}{dx}\left(\frac{\lambda_2}{U'}\right) = 2\,[T_2 - \lambda_2\,(2 + \Delta_{12})\,] = H(\lambda_2), \qquad (2.16)$$

or

$$\frac{d}{dx}\left(\frac{U\,\lambda_2}{U'}\right) = +\,\lambda_2 + H(\lambda_2). \qquad (2.17)$$

The advantage of this form of the momentum equation with respect to other forms (P o h l h a u s e n — ref. 7, H o w a r t h — ref. 3) is implied in the fact that it is not necessary to make use of the values of U'', which, generally, have to be calculated by numerical differentiation and which are, hence, unreliable. P o h l h a u s e n (ref. 7) identifies the function $f(y)$ with a polynomial of the 4th degree, satisfying the boundary conditions (2.3), (2.4), (2.11), and for a value $y = \delta$, the "boundary layer thickness", the additional conditions

$$f(\delta) = 1, \qquad (2.18)$$
$$f'(\delta) = 0,$$
$$f''(\delta) = 0.$$

hold.

This leads, if

$$\frac{y}{\delta} = \eta, \qquad (2.19)$$

to the expression

$$f(\eta) = 2\,\eta - 2\,\eta^3 + \eta^4 + {}^1/_6\,\lambda(1-\eta)^3\,\eta, \qquad (2.20)$$

from which it is found that

$$\Delta_1 = \frac{\delta_1}{\delta} = \frac{1}{120}\,(36 - \lambda),$$

$$\Delta_2 = \frac{\delta_2}{\delta} = \frac{1}{315}\,(37 - \frac{1}{3}\,\lambda - \frac{5}{144}\,\lambda^2),$$

$$\lambda_2 = +\,\lambda\,\Delta_2^{\,2},$$

$$T_2 = (2 + \frac{1}{6}\,\lambda)\,\Delta_2\,,$$

$$H(\lambda) = 2\,\Delta_2\left[\,2 + \frac{1}{6}\,\lambda - \lambda\,(2\,\Delta_2 + \Delta_1)\,\right] = + \frac{1}{1\,190\,700}\left(37 - \frac{1}{3}\,\lambda - \frac{5}{144}\,\lambda^2\right)[15\,120 - 2\,784\,\lambda + 79\,\lambda^2 + {}^5/_3\,\lambda^3].$$

In a stagnation point $U = 0$. From (2.16) it is seen that, in such a point, $H(\lambda)$ must vanish also.

So, if the boundary layer calculation starts at the forward stagnation point, λ should here be equal to one of the roots of the equation $H(\lambda) = 0$. P o h l h a u s e n takes the root $\lambda = 7.052$, which is the only one having physical significance.

This method gives acceptable results in conditions of accelerated flow outside the boundary layer.

In cases with an adverse pressure gradient (retarded flow) the method fails to indicate the point of separation, i. e. the point where the skin friction becomes zero.

Moreover, the method does not yield sufficiently accurate information about the shape of the velocity profile, required to calculate the location of the transition point, which frequently will be situated in the region of retarded flow. For this reason Schlichting and Ullrich (ref. 9) attempted to obtain improved results by using a polynomial of the 6th degree, satisfying one more condition for $y=\delta$ and the condition (2.12).

In this case, however, no suitable representation of conditions at the stagnation point could be obtained, the roots of the equation $H=0$ being complex.

For a one parameter method, using polynomial approximations, no improvement can be expected by using higher polynomials, as higher boundary conditions at $y=0$ involve the derivatives with respect to x.

Therefore, attention is payed to the conditions at the outer edge of the boundary layer.

The polynomial methods are all based upon a transition to the free stream velocity with smooth derivatives up to a certain order.

From an investigation of the asymptotic character of the solutions of the boundary layer equations it is possible to introduce assumptions for the velocity profile having the right asymptotic character, the free constants are then only used to satisfy the boundary conditions at the wall.

1.3 *The asymptotic behaviour of the solutions of the boundary layer equations.*

Von Karman and Millikan (ref. 6) indicated a transformation of the boundary layer equations, which admits a determination of the asymptotic behaviour of the solutions for large values of y. In consequence of (2.2) the components of the velocity in the boundary layer can be derived from a stream function $\psi\,(x, y)$

$$u=-\frac{\partial\psi}{\partial y}\,, \tag{3.1}$$

$$v=\frac{\partial\psi}{\partial x}\,. \tag{3.2}$$

Introducing further a new parameter

$$\varphi=\int_0^s U(s)ds,$$

i. e. the line integral of the free stream velocity outside the boundary layer, the functions ψ and φ are considered as new independent variables.

Transformation of (2.1) then leads to the equation

$$\frac{\partial}{\partial\varphi}\left(\frac{U^2-u^2}{2}\right)=\nu\,\frac{u}{U}\,\frac{\partial^2}{\partial\psi^2}\left(\frac{U^2-u^2}{2}\right). \tag{3.3}$$

Denoting the expression

$$\frac{U^2-u^2}{2}$$

the energy defect, by z, (3.3) yields

$$\frac{\partial z}{\partial\varphi}=\nu\,\frac{u}{U}\,\frac{\partial^2 z}{\partial\psi^2}\,. \tag{3.4}$$

Now, considering the outer edge of the boundary layer, where $u\rightarrow U$, this equation is seen to reduce to the typical equation of heat conduction.

Its solution, pertaining to the boundary conditions

$$\begin{aligned} z&=0 &&:\ \psi=\infty\,,\\ z&=z_0=\frac{U^2(\varphi)}{2} &&:\ \psi=0\,, \end{aligned} \tag{3.5}$$

is known to be

$$z=\frac{U^2-u^2}{2}=\frac{\psi}{2\sqrt{\pi}}\int_0^\varphi\frac{e^{-\frac{\psi^2}{\varphi-\xi}}}{(\varphi-\xi)^{3/2}}\,U^2(\xi)d\xi. \tag{3.6}$$

From this equation the asymptotic behaviour of the solutions of the boundary layer equations for large values of y can at once be inferred.

Introducing a new variable of integration

$$\beta^2=\frac{\psi^2}{\varphi-\xi}\,,$$

(3.6) becomes:

$$z=\frac{1}{\sqrt{\pi}}\int_{\frac{\psi}{\sqrt{\varphi}}}^\infty e^{-\beta^2}\,U^2\left(\varphi-\frac{\psi^2}{\beta}\right)d\beta. \tag{3.7}$$

Since for large values of y $u\rightarrow U$, the quotient

$$\frac{\psi}{y\sqrt{\varphi}}=\frac{-\int_0^y u\,dy}{y\sqrt{\varphi}} \tag{3.8}$$

will tend to the value $\frac{U}{\sqrt{\varphi}}$, which is only a function of x.

The expression for $z=\left(\frac{U+u}{2}\right)(U-u)$ tending to

$$z=U\,(U-u), \tag{3.9}$$

the asymptotic expression for u will be:

$$\frac{u}{U}=1-\frac{z}{U^2}=1-\frac{1}{\sqrt{\pi}}\int_{\frac{\psi}{\sqrt{\varphi}}}^\infty e^{-\beta^2}\frac{U^2\left(\varphi-\frac{\psi^2}{\beta}\right)}{U^2(\varphi)}\,d\beta. \tag{3.10}$$

The assumption to be introduced for the velocity profile is:

$$\frac{u}{U}=1-\sum_{k=0}^{n}\int_y^\infty e^{-\alpha^2\eta^2}\,c_k(x)\,\eta^k d\eta. \tag{3.11}$$

With a suitable choice of the functions $c_k(x)$ this function will be seen to have the desired asymptotic character.

Moreover, an approximate expression for α will be

$$\alpha(x) = \frac{U}{\sqrt{\varphi}}. \tag{3.12}$$

For a calculation, yielding satisfactory results for the whole boundary layer, the functions $c_k(x)$ have to be determined by the boundary conditions for $y = 0$.

1.4 *The new calculation method.*

Formula (3.11) leads to a new approach to the velocity profiles, apt to replace the polynomials used by Pohlhausen and others.

A suitable choice for the velocity profile, having the desired asymptotic behaviour, is, as is shown in (1.3)

$$\frac{u}{U} = f(\eta) = 1 - \\ - \int_{\eta}^{\infty} e^{-\eta^2} (a_1 + b_1\eta + c_1\eta^2 + d_1\eta^3 \ldots) d\eta, \tag{4.2}$$

where α, a, b, c, d ... are functions of x, to be determined by the boundary conditions for $y = 0$.

Now

$$\int_{\eta}^{\infty} e^{-\eta^2} \eta^{2k+1} d\eta = \frac{1}{2} \int_{\eta}^{\infty} e^{-\eta^2} \eta^{2k} d\eta^2 = \\ = \frac{1}{2} \eta^{2k} e^{-\eta^2} + k \int_{\eta}^{\infty} e^{-\eta^2} \eta^{2k-1} d\eta \tag{4.3}$$

are, obviously, elementary integrals, yielding functions of the type $e^{-\eta^2} \eta^{2k}$, $k \geq 0$.

Therefore the assumption

$$\frac{u}{U} = f(\eta) = 1 - \\ - \int_{\eta}^{\infty} e^{-\eta^2} (a + c\eta^2 \ldots) d\eta - e^{-\eta^2} (b + d\eta^2 + \ldots) \tag{4.4}$$

is a more simple alternative for (4.2).

In order to satisfy the boundary conditions for $\eta = 0$ an expansion into powers of η is useful:

$$f'(\eta) = e^{-\eta^2} (a + c\eta^2 \ldots) + 2\eta\, e^{-\eta^2} \\ (b + d\eta^2 + \ldots) - e^{-\eta^2}(2d\eta + \ldots) = \\ = a + 2(b - d)\eta + (c - a)\eta^2 + \\ 2(2d - b)\eta^3 + (\tfrac{1}{2} a - c)\eta^4 + \ldots \tag{4.5}$$

The boundary values of the function itself and of its successive derivatives are seen to be

$$f(0) = 1 - \int_0^{\infty} e^{-\eta^2} (a + c\eta^2 + \ldots) d\eta - b, \tag{4.6}$$

$$f'(0) = a, \tag{4.7}$$

$$f''(0) = 2(b - d), \tag{4.8}$$

$$f'''(0) = 2(c - a), \tag{4.9}$$

$$f''''(0) = 12(2d - b). \tag{4.10}$$

Now

$$\int_0^{\infty} e^{-\eta^2} \eta^{2n} d\eta = \frac{1}{2} \int_0^{\infty} e^{-t} t^{n - 1/2} dt = \frac{1}{2} \Gamma (n + \tfrac{1}{2}) =$$

$$= \begin{cases} \sqrt{\pi}.\ \dfrac{1.3.5 \ldots (2n-1)}{2^{n+1}} & n > 0, \\ \tfrac{1}{2} \sqrt{\pi}, & n = 0. \end{cases} \tag{4.11}$$

So (4.6) becomes

$$f(0) = 1 - b - \tfrac{1}{2}\sqrt{\pi} \{ a + \tfrac{1}{2} c + \ldots \}. \tag{4.12}$$

The boundary conditions to be satisfied are

$$u = Uf(0) = 0, \tag{4.13}$$

$$u_y = U\alpha f'(o) = \frac{\tau_0}{\nu\rho}, \tag{4.14}$$

$$u_{yy} = U\alpha^2 f''(o) = -\frac{UU'}{\nu}, \tag{4.15}$$

$$u_{yyy} = U\alpha^3 f'''(o) = 0, \tag{4.16}$$

$$\nu u_{yyyy} = \nu U\alpha^4 f''''(o) = + u_y u_{xy} = Uf'(o). \\ . \{ (f'(o)\,)_x (\alpha_x U + \alpha U') + f'_x(o)\alpha U \}. \tag{4.17}$$

Hence,

$$1 - b = \tfrac{1}{2}\sqrt{\pi} \{ a + \tfrac{1}{2} c + \ldots\ldots \}, \tag{4.18}$$

$$a = \frac{\tau_0}{\nu\rho U\alpha}, \tag{4.19}$$

$$2 (b - d) = -\frac{U'}{\nu\alpha^2}, \tag{4.20}$$

$$2 (c - a) = 0, \tag{4.21}$$

$$\nu\alpha^3\, 12\, (2\, d - b) = \\ = + a \{ a (\alpha_x U + \alpha U') + a_x \alpha U \}. \tag{4.22}$$

Now, usually only the first four boundary conditions are used, since the occurrence of the derivatives to x in the higher ones leads to difficulties in a one parameter system. The same restriction will initially be adopted below.

The parameter λ, introduced in (2.20), is

$$\lambda = -f''(o) = -2\,(b - d). \tag{4.23}$$

From (4.18) it is found that

$$a = c = \frac{1 - b}{\tfrac{3}{4}\sqrt{\pi}}.$$

The expression for the velocity profile is:

$$f(\eta) = 1 - (1 - b)\, \frac{\int_{\eta}^{\infty} e^{-\eta^2}(1 + \eta^2) d\eta}{\tfrac{3}{4}\sqrt{\pi}} - \\ - be^{-\eta^2} - de^{-\eta^2}\eta^2 = \\ = (1 - b)\, \frac{\int_0^{\eta} e^{-\eta^2}(1 + y^2) d\eta}{\tfrac{3}{4}\sqrt{\pi}} + \\ + b(1 - e^{-\eta^2}) - d\eta^2 e^{-\eta^2}.$$

For this velocity profile the displacement thickness and the momentum thickness must be evaluated. After tedious calculations they are found to be equal to

$$\alpha\delta_1 = \Delta_1 = \int_0^\infty (1-f)dy = \frac{1-b}{\frac{3}{4}\sqrt{\pi}} + \\ + \tfrac{1}{2}\, b\sqrt{\pi} + \tfrac{1}{4}\, d\sqrt{\pi}.$$

$$\Delta_1 = 0.752\,253 + 0.133\,974\, b + 0.443\,114\, d.$$

$$\alpha\delta_2 = \Delta_2 = \int_0^\infty f(1-f)dy =$$

$$= (1-b)^2 \frac{47-24\sqrt{2}}{18\,\pi}\sqrt{\frac{\pi}{2}} + \frac{(1-b)b}{\sqrt{\pi}} + \\ + b^2\,\frac{(\sqrt{2}-1)}{2}\sqrt{\frac{\pi}{2}} + \\ + d\left\{\frac{1-b}{3\sqrt{\pi}} + \frac{b\sqrt{2}-1}{4}\sqrt{\frac{\pi}{2}}\right\} - \\ - d^2\,\frac{3}{32}\sqrt{\frac{\pi}{2}},$$

$$\Delta_2 = 0.289\,430 - 0.014\,670\, b - 0.015\,190\, b^2 + \\ + d(0.188\,063 - 0.058\,279\, b) - 0.117\,498\, d^2.$$

If now only four boundary conditions are taken into consideration, all terms in (4.4) must be dropped with the exception of three, viz. the terms with coefficients a, b and c. Putting, accordingly, $d=0$, it is found that in this case:

$$\lambda = -2\, b,$$

$$\lambda_2 = \lambda : \Delta_2^{\,2} = -2\, b \,.\, \Delta_2^{\,2},$$

$$T_2 = \Delta_2 \,.\, f'(o) = \frac{1-b}{\frac{3}{4}\sqrt{\pi}} \,.\, \Delta_2\,,$$

$$H = 2\left[\,T_2 - \lambda_2\left(2 + \frac{\Delta_1}{\Delta_2}\right)\right] = \\ = 2\,\Delta_2\left[\frac{1-b}{\frac{3}{4}\sqrt{\pi}} + 2\,b\,(2\,\Delta_2 + \Delta_1)\right].$$

The value of b in the stagnation point is given by the equation $H=0$,

$$-0.060\,760\,\lambda^3 + 0.209\,268\,\lambda^2 + 1.909\,973\,\lambda + \\ + 0.752\,253 = 0.$$

The relevant root of this equation is:

$$b = -\tfrac{1}{2}\,\lambda = 0.415\,02$$

giving

$$\Delta_2 = +\,0.292\,90 \qquad \lambda_2 = 0.071\,24.$$

This approximation gives reasonable results in the region of accelerated flow, as well as for the Blasius case of zero pressure gradient (comp. par. 2).

In the case of retarded flow, however, the approximation fails, as is demonstrated by calculating the separation point for a flow with a linear outer velocity (par. 5). This is due to the fact that already the fifth boundary condition is strongly violated in the separation point.

In fact, the separation point is characterized by

$$T_2 = 0, \text{ i.e. } b = 1.$$

In this case the fifth boundary condition requires

$$\nu\alpha^2\, 12\,(2\,d - b) = 0$$

for $b=1$, which obviously is not the case.

Now, in order to satisfy this boundary condition in the range of adverse pressure gradient, take for d the value

$$d = \tfrac{1}{2}\, b.$$

Then, for the separation point, the fifth condition is exactly fulfilled.

Thus,

$$\lambda = -2\,(b-d) = -\,b$$

and the functions Δ_1 and Δ_2 are:

$$\Delta_1 = 0.752\,253 + 0.355\,531\, b,$$

$$\Delta_2 = 0.289\,430 + 0.079\,361\,5\, b - 0.073\,704\, b^2.$$

The equation for the stagnation point value of b is, now,

$$-0.147\,406\, b^3 + 0.514\,253\, b^2 + 0.578\,86\, b + \\ + 0.752\,253 = 0.$$

Unfortunately this equation has no real root in the required region. This proves that the modification is not appropriate for the region of accelerated flow.

For retarded flow, however, the result of a calculation of the separation point for a flow with a constant pressure gradient gave a very good coincidence with the exact value.

Therefore, it was decided to use the first assumption ($d=0$) for accelerated flow ($\lambda < 0$) and the second one ($d = \frac{1}{2}\, b$) in the region of retarded flow ($\lambda > 0$), for $\lambda = 0$ the two velocity profiles being identical. The curves for H and T_2 to be used in the solution of the equation (2.17) show a slight discontinuity in the tangent in the point $\lambda = 0$; this, however, does not effect the results to any appreciable degree. The values of the functions λ_2, Δ_1, Δ_2, T_2, H are given in table 1 (fig. 1), together with an approximation formula. The velocity profiles, together with their first and second derivatives, are given in table 2 (fig. 2).

By numerical integration of equation (2.17) λ_2 can be obtained as a function of x.

With the help of table 1 and the corresponding graphs λ, Δ_1, Δ_2 and T_2 are, subsequently, evaluated.

The value of α can, further, be derived from eqs. (4.15), (4.23),

$$\alpha = \sqrt{\frac{U'}{\nu\lambda}}\,;$$

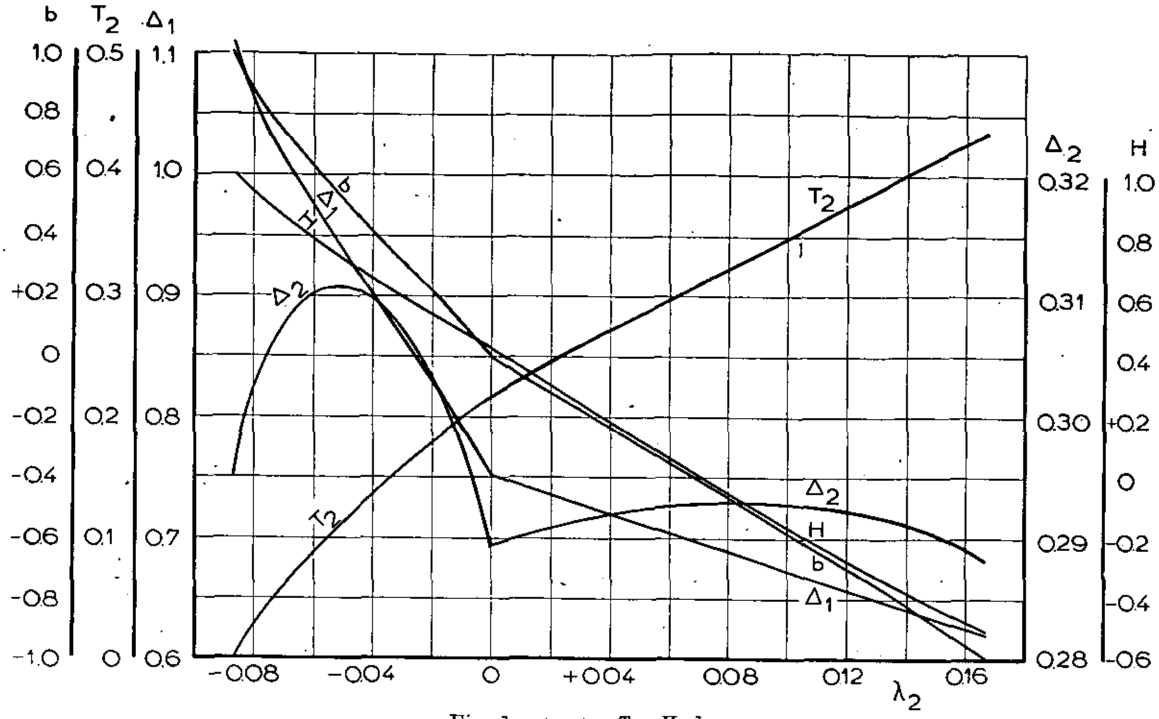

Fig. 1. Δ_1, Δ_2, T_2, H, b.

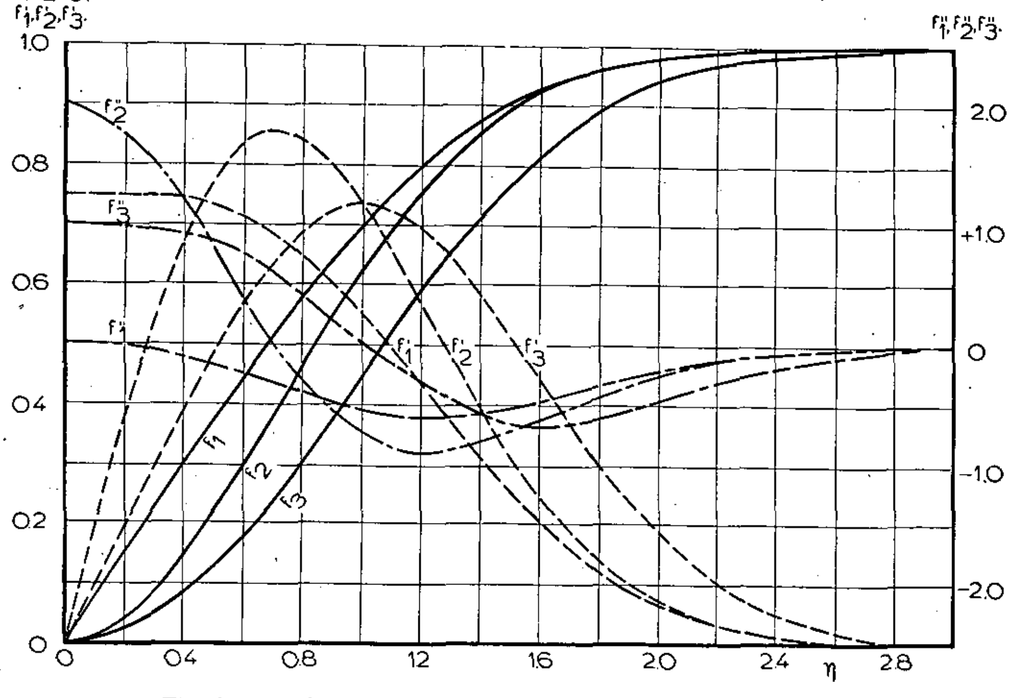

Fig. 2. Velocity profile functions f_1, f_2, f_3 and their derivatives.

Thereupon the values of δ_1, δ_2 and τ_0 can be calculated in accordance with the relations

$$\delta_1 = \frac{\Delta_1}{\alpha},$$

$$\delta_2 = \frac{\Delta_2}{\alpha},$$

$$\tau_0 = \nu\rho\, U\, \alpha f'(0) = \nu\rho\, U\, \alpha \frac{T_2}{\Delta_2} = \nu\rho\, U\, \frac{T_2}{\delta_2}.$$

2 Applications, checks and comparisons.

2.1 *Flow with constant velocity.*

As a check on the accuracy of the method several special cases have been investigated in which an accurate solution of the boundary layer equations is known. The simplest of these cases is the Blasius flow (ref. 3) with a constant velocity at the outer edge of the boundary layer.

Here, $U' = 0$ along the boundary layer and, consequently, the form (2.5) of the momentum equation is advantageous.

The boundary conditions yield

$$\lambda = 0,$$

so

$$\Delta_1 = 0.752\,253,$$
$$\Delta_2 = 0.289\,430$$

and, from (4.14),

$$U\alpha \frac{1}{\frac{3}{4}\sqrt{\pi}} = \frac{\tau_0}{\nu\rho}.$$

Substitution in the momentum equation

$$\frac{d\delta_2}{dx} = \frac{\tau_0}{\rho U^2}$$

gives:

$$\Delta_2 \frac{d\,{}^1/\alpha}{dx} = \frac{\alpha}{\frac{3}{4}\sqrt{\pi}} \frac{\nu}{U}.$$

Hence,

$$\frac{1}{\alpha} = 2.279\,952 \left(\frac{\nu x}{U}\right)^{1/2}.$$

and

$$\delta_1 = \frac{\Delta_1}{\alpha} = 1.715 \left(\frac{\nu x}{U}\right)^{1/2}$$
$$\delta_2 = \frac{\Delta_2}{\alpha} = 0.660 \left(\frac{\nu x}{U}\right)^{1/2}$$
$$\tau_0 = 0.330\,\rho U \left(\frac{\nu U}{x}\right)^{1/2}.$$

The exact values of these quantities have been calculated by Blasius (ref. 2, p. 136, 157). They are

$$\delta_1 = 1.721 \left(\frac{\nu x}{U}\right)^{1/2}.$$
$$\delta_2 = 0.664 \left(\frac{\nu x}{U}\right)^{1/2}.$$
$$\tau_0 = 0.332\,\rho U \left(\frac{\nu U}{x}\right)^{1/2}.$$

The errors in δ_1, δ_2 and τ_0 are $-0.35\,\%$, $-0.6\,\%$ and $-0.6\,\%$.

2.2 *Flow with a constant velocity gradient.*

The second example is the flow with a constant velocity gradient. The exact solution for this type of boundary layer has been calculated by Howarth (ref. 2).

Assuming

$$U = U_0 \left(1 - \frac{x}{L}\right), \tag{2.1}$$

the equation (2.16) becomes

$$-\left(1 - \frac{x}{L}\right) L \frac{d\lambda_2}{dx} = H(\lambda_2). \tag{2.2}$$

Putting

$$\xi = \frac{x}{L}, \tag{2.3}$$

this equation takes the form

$$(1-\xi)\frac{d\lambda_2}{d\xi} = -H(\lambda_2). \tag{2.4}$$

In the starting point $\xi = 0$ the boundary layer has zero displacement and momentum thickness, corresponding to $\alpha = \infty$. The initial value of λ_2 is, by (4.15), in view of $U' \neq 0$

$$\lambda = \lambda_2 = 0.$$

For positive values of L equation (2.4) has, with this initial value, been integrated by a modified Adam process (ref. 4); λ_2 being a known function of x, α is obtained from

$$\alpha = \sqrt{-\frac{dU}{dx}\frac{1}{\nu\lambda}} = \sqrt{\frac{U_0}{L\nu}\frac{1}{\lambda}}.$$

Subsequently, δ_1, δ_2 and τ_0 can be calculated.

The values of these quantities as functions of ξ are given in table 3, and compared with the values calculated by Howarth with the aid of power series (fig. 3). For a few values of x the velocity profiles have been determined and compared with the exact values (ref. 2) (fig. 4) (table 4).

2.3 *Boundary layer flow along an elliptic cylinder.*

A third example is given by the calculation of the laminar boundary layer for the elliptic cylinder ($b/a = 2.96$), for which the results of Schubauer (ref. 8) are available.

For the pressure distribution in the free stream the values of Schubauer are taken.

Near the stagnation point the equation

$$\frac{d}{dx}\left(\frac{U}{U'}\lambda_2\right) = \lambda_2 + H(\lambda_2)$$

is integrated by a development of u/u' and λ_2 in a power series of x.

For u/u' the series:

$$u/u' = x + 40.5\,x^3 - 86.2\,x^5$$

fits the measured values up to $x = 0.3$.

Substituting for λ_2 a series of even powers of x

$$\lambda_2 = 0.071\,2 + ax^2 + bx^4 + cx^6 + dx^8$$

and for $H(\lambda_2)$ the approximation formula

$$H(\lambda_2) = -(6.116 - 4.51\,\lambda_2)(\lambda_2 - 0.071\,2)$$

the following series for λ_2 is found:

$$\lambda_2 = 0.071\,2 - 1.109\,8\,x^2 + 26.638\,x^4 -$$
$$- 720\,x^6 + 21\,271\,x^8.$$

From $x = 0.08$ on, Adam's method is used.

The step length is indicated by

$$h < 0.03\,|u/u'|,$$

yielding

$0.08 < x < 0.160$	$h = 0.005$
$0.160 < x < 0.24$	$h = 0.01$
$0.24 < x < 0.30$	$h = 0.02$
$0.30 < x < 0.50$	$h = 0.04$
$0.50 < x < 2.0$	$h = 0.1$

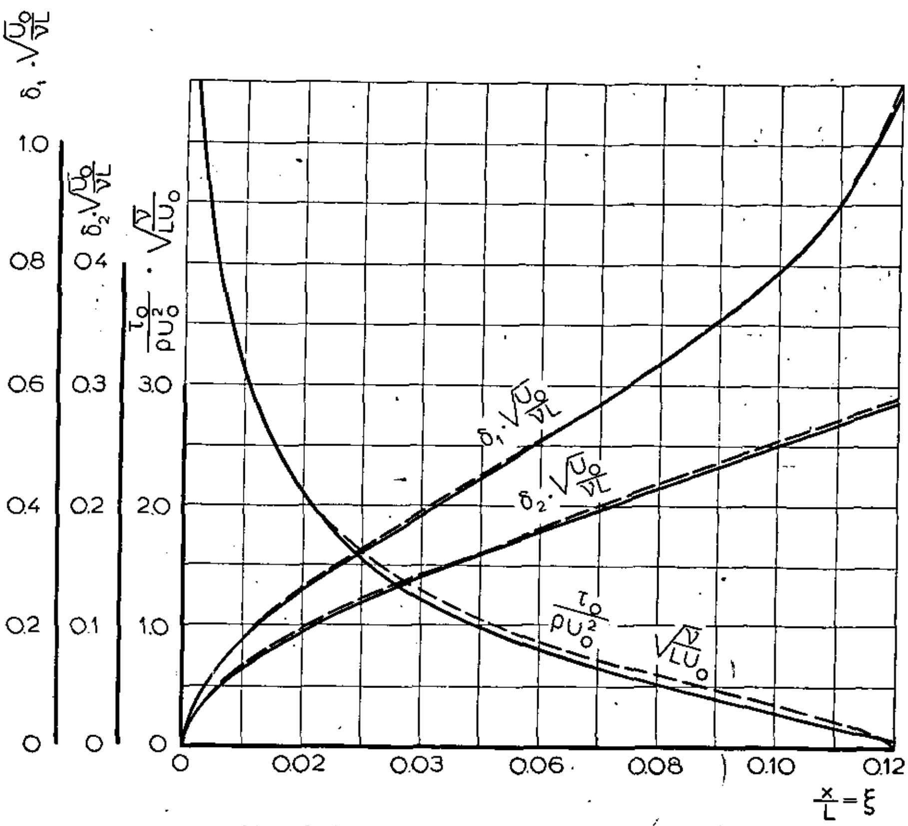

———— this calculation - - - - - - - - calculation by Howarth

Fig. 3. Displacement and momentum thickness and shear stress for flow with linear velocity gradient $U = U_0\,(1 - x/L)$.

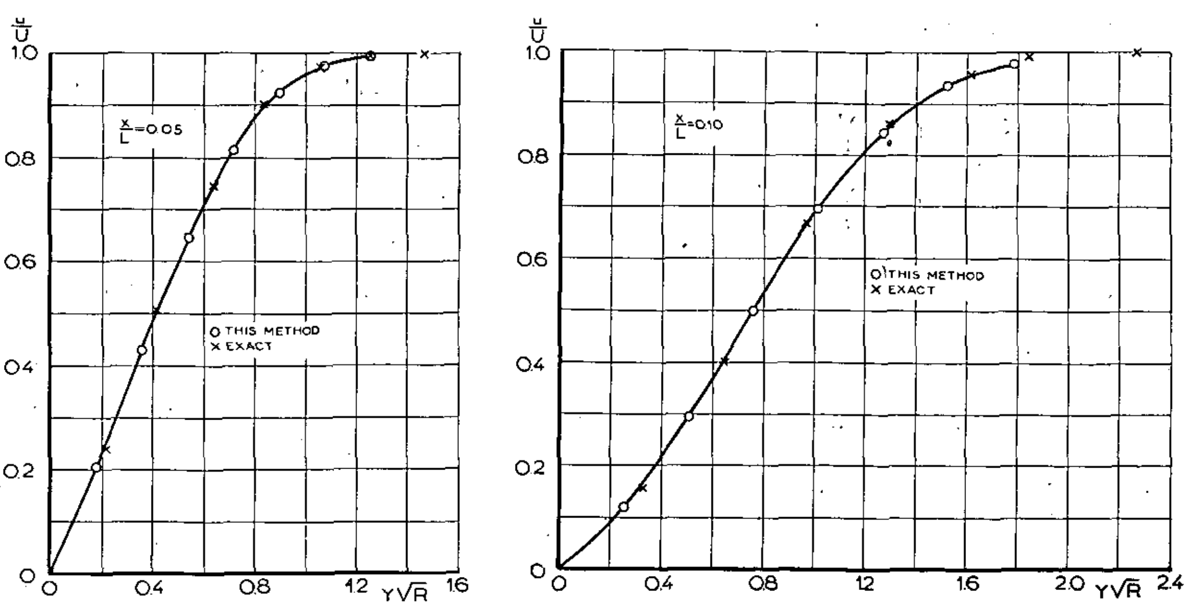

Fig. 4. Velocity profile for flow with linear velocity gradient $U = U_0\,(1 - x/L)$.

The results of the calculation are given in table 5, expressed in dimensionless quantities with the Reynolds number

$$R = \frac{U_0 L}{\nu}.$$

U_0 being the velocity at great distances from the cylinder and L the minor axis of the ellips.

In order to compare the calculated velocity profiles with the measured values these have been calculated too. Results are plotted, together with Schubauer's profiles in figs. 5 and 6.

The attained approximation is seen to be better than that of Pohlhausen in the range of retarded flow.

Pohlhausen's method did not give separation at all, while Schubauer observed separation at $x = 1.99$. The present method also fails to give separation; it yields, however, a very small

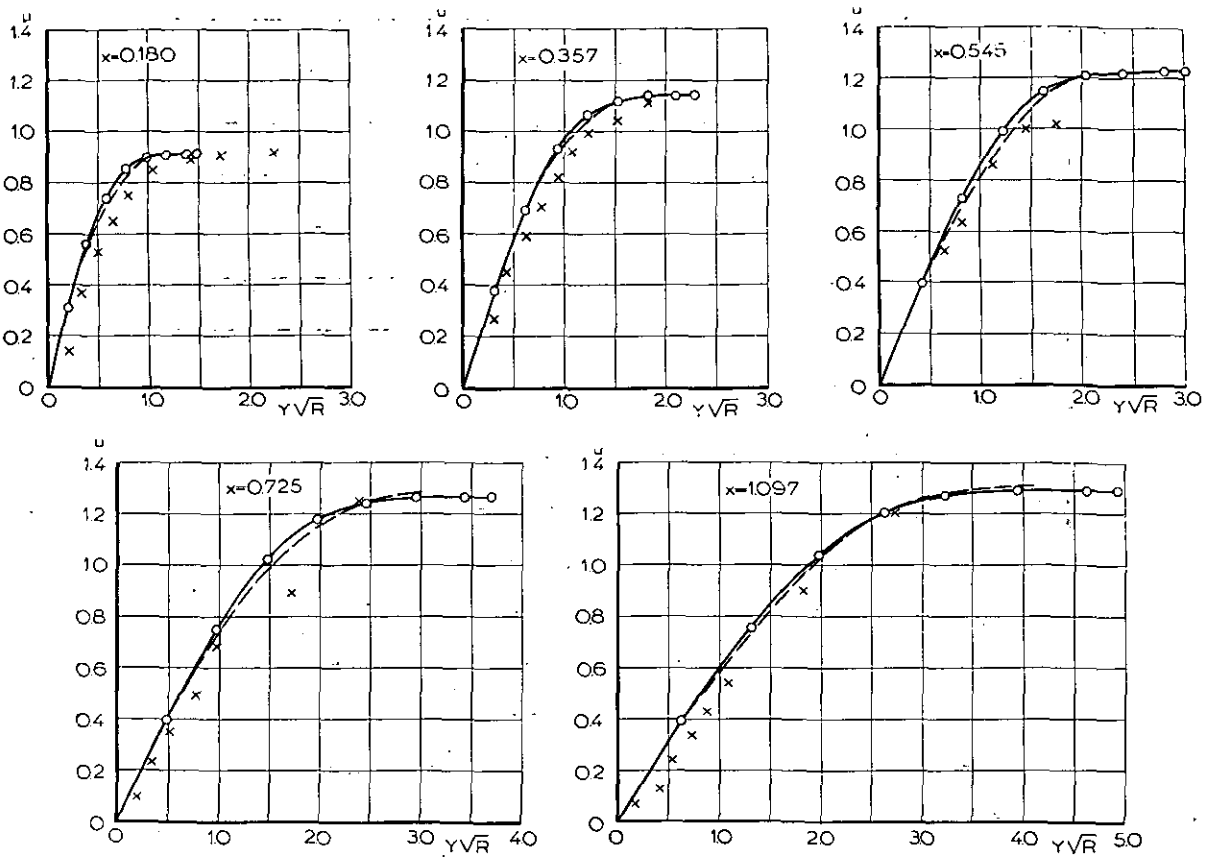

Fig. 5. Velocity profiles for Schubauer's elliptic cylinder.

xxx	experimental values	from NACA report 527.
ooo	„ „	„ „ „ „
- - - -	Pohlhausen calculations	„ „ „ „
——	this calculation.	

value of τ at the observed point of separation, *much smaller than* Pohlhausen's method.

Unfortunately, an exact calculation of the boundary layer with the given velocity, that would have been a more reliable check of the calculation performed here, was not available.

2.4 *Boundary layer flow along a circular cylinder.*

Finally, the calculation of the boundary layer flow along a circular cylinder has been performed, taking the values measured by Hiemenz for the velocity outside the boundary layer, pertaining to a circular cylinder, radius 4.87 cm, in a fluid with kinematical viscosity $\nu = 0.01$ and a velocity at infinity of 19.2 cm/sec.

$$U = 7.151 - 0.044\,97\, x^3 - 0.000\,330\,0\, x^5,$$

where x is the distance in cm to the forward stagnation point (ref. 2).

The integration of the equation

$$\frac{d}{dx}\left(\frac{U}{U'}\lambda_2\right) = \lambda_2 + H(\lambda_2)$$

is again performed by Adam's method (using an interpolation procedure instead of extrapolation). The step length is drawn from a well-known rule of the theory of numerical integration (see e. g. ref. 1).

If the equation

$$\frac{dy}{dx} = f(x, y)$$

is to be integrated, the step length h is determined by

$$\left| h \frac{\partial f}{\partial y} \right| < 0.15,$$

in the present case

$$y = \frac{U}{U'}\lambda_2,$$

so

$$\frac{\partial f}{\partial y} = \frac{U'}{U} \frac{\partial}{\partial \lambda_2}\{\lambda_2 + H(\lambda_2)\}.$$

Now it is easily seen that

$$\frac{dH}{d\lambda_2} \approx -6,$$

so

$$\left| h \frac{U'}{U} 5 \right| < 0.15$$

or

$$\left| h \frac{U'}{U} \right| < 0.03.$$

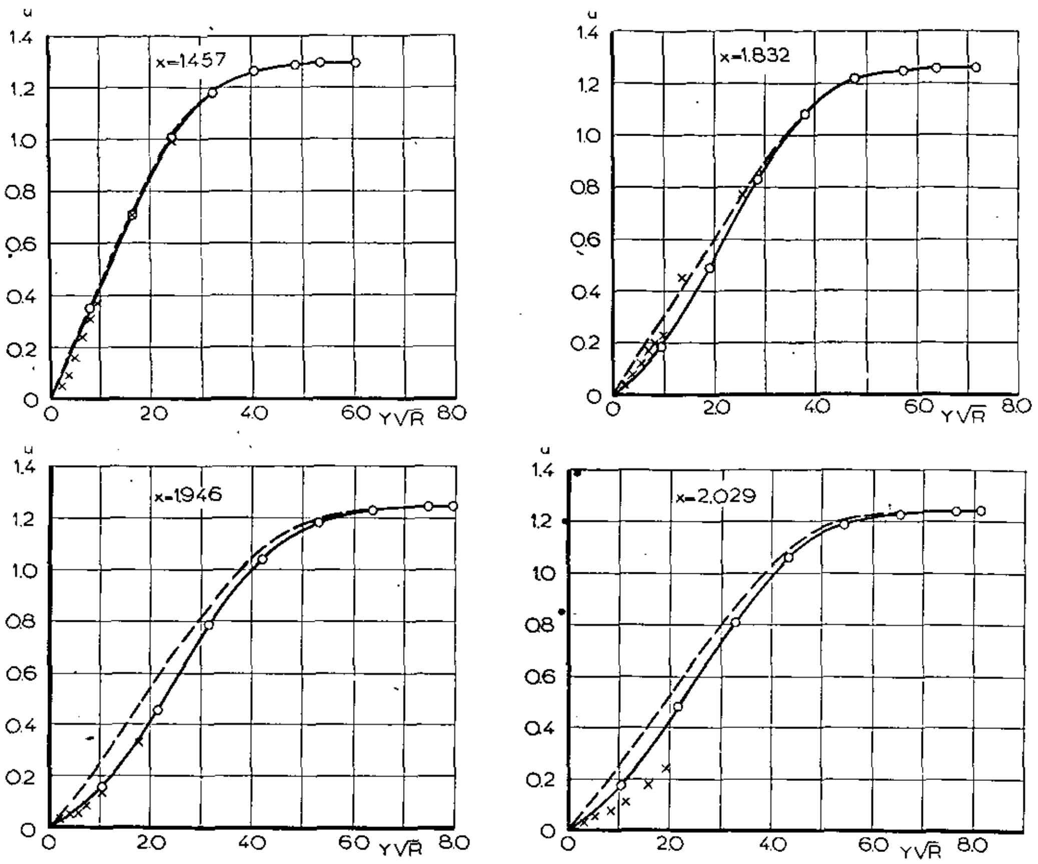

Fig. 6. Velocity profiles for Schubauer's elliptic cylinder.

XXX experimental values.
OOO " "
- - - - Pohlhausen calculation.
—— this calculation.

In the neigbourhood of the stagnation point $u/u' \approx 0$, so here the integration method fails. It is advisable to use in this range a power series approximation valid for small x.

Now

$$\frac{U}{U'} = \frac{7.151\,x - 0.044\,97\,x^3 - 0.000\,330\,0\,x^5}{7.151 - 0.134\,91\,x^2 - 0.001\,650\,0\,x^4} =$$
$$= x\,(1 + 0.012\,57\,x^2 + 0.000\,421\,7\,x^4 + $$
$$+ 0.000\,010\,51\,x^6 + 0.000\,000\,295\,x^8 + \ldots\ldots)$$

and the equation for λ_2 is:

$$\frac{d}{dx}\,[x\,(1 + 0.012\,57\,x^2 + 0.000\,421\,7\,x^4 +$$
$$+ 0.000\,010\,51\,x^6 + 0.000\,000\,295\,x^8)\,\lambda_2] =$$
$$= \lambda_2\,(6.116 - 4.51\,\lambda_2)\,(\lambda_2 - 0.071\,2).$$

Putting

$$\lambda_2 = 0.071\,2 + ax^2 + bx^4 + cx^6 + dx^8$$

and equating coefficients, a rather lengthy calculation gives

$$\lambda_2 = 0.071\,2 - 0.000\,344\,5\,x^2 - 0.000\,013\,069\,x^4 -$$
$$- 0.000\,000\,256\,93\,x^6 - 0.000\,000\,005\,522\,4\,x^8,$$

an expansion which is valid for small x.

This approximation is used up to $x = 3.6$. From 3.6 upward the step by step method is used with a step length 0.2.

The calculation gives a good agreement with the calculation by power series methods.

3 Recapitulation.

In order to be able to determine the properties of the laminar boundary layer with an accuracy definitely surpassing the accuracy attained by the methods using polynomial assumptions for the velocity profile (Pohlhausen, Schlichting-Ullrich), without, however, extending the involved scheme of computation, a new method has been devised which makes use of velocity profiles having the required asymptotic behaviour. They are made to satisfy the maximum number of boundary conditions at the wall that can be considered in one parameter methods.

The fundamental equation is von Karman's momentum equation

$$\frac{\tau_0}{\rho U^2} = \frac{U'}{U}\,(\delta_1 + 2\,\delta_2) + \frac{d\delta_2}{dx}\,.$$

U = free stream velocity,

δ_1 = displacement thickness,

δ_2 = momentum thickness,

τ_0 = skin friction per unit length.

The introduced velocity profile in the boundary layer is represented by a suitable function

$$\frac{u}{U} = f(y),$$

satisfying the conditions

$$y = 0: \qquad u = 0,$$

$$\nu u_y = \frac{1}{\rho}\,\tau_0,$$

$$\nu u_{yy} = -\frac{1}{\nu}\,UU',$$

$$u_{yyy} = 0.$$

It further contains one shape parameter λ, depending on x. Introducing the parameter

$$\lambda_2 = \frac{\delta_2^{\,2}}{\nu}\,U',$$

the momentum equation can be reduced to

$$\frac{d}{dx}\left(\frac{U\lambda_2}{U'}\right) = \lambda_2 + H(\lambda_2).$$

Instead of Pohlhausen's fourth degree polynomial, expressions for the velocity profile are used which have the asymptotic character for large values of y, that can be derived from the boundary layer equations with the aid of the von Karman and Millikan transformation.

For $\lambda_2 < 0$ (retarded flow) and $\lambda_2 > 0$ (accelerated flow), different representations of the velocity profile are used, the one applying to the region of retarded flow satisfying one more boundary condition in the point of separation and in this point only. This important property markedly raises the accuracy in the region of retarded flow, but threatens to spoil it in the region of accelerated flow. It is possible to drop it there without introducing noticeable discontinuities at the common point $\lambda_2 = 0$.

In order to check the method, a number of applications to wellknown cases has been made, viz. to

1) the Blasius flow along a flat plate
2) the flow with constant velocity gradient outside the boundary layer
3) the flow around an elliptic cylinder, as investigated experimentally by Schubauer
4) the flow around a circular cylinder (Hiemenz).

In each case a good agreement with known more or less exact solutions is obtained. In the case of the elliptic cylinder, the method, strictly, fails to reproduce the observed separation, but the calculated skin friction falls steeply to a very small minimum in the vicinity of the pertaining point, indicating that separation almost occurs. The error may, therefore, be only small. Unfortunately, no exact calculations applying to this case are available, which are apt to sharpen the check.

The calculated velocity distributions are in each case compared with the exact velocity profiles, wherever available.

The agreement is always good.

4 References.

1 COLLATZ, L.: Natürliche Schrittwerte bei numerischer Integration von Differentialgleichungssysteme. ZAMM. 22, 1942, p. 216.

2 GOLDSTEIN, S.: Modern Developments in Fluid Dynamics. Vol. I, Oxford, Clarendon Press, 1938.

3 HOWARTH, L.: Steady Flow in the Boundary Layer near the Surface of a Cylinder in a Stream. A. R. C. Rep. and Mem. 1632, 1934.

4 KAMKE, E.: Differentialgleichungen. I. Akademische Verlagsgesellschaft, Leipzig, 1942, p. 146.

5 VON KARMAN, TH.: Ueber laminare und turbulente Reibung. ZAMM 1, 1921, p. 235.

6 VON KARMAN, TH. and MILLIKAN, C. B.: On the theory of laminar layers involving separation. NACA Report 504, 1934.

7 POHLHAUSEN, K.: Zur näherungsweisen Integration der Differentialgleichung der laminaren Grenzschicht. ZAMM 1, 1921, p. 252.

8 SCHUBAUER, G. B.: Air flow in a separating laminar boundary layer. NACA Report 527, 1935.

9 SCHLICHTING, H. and ULLRICH, A.: Zur Berechnung des Umschlages laminar/turbulent. Jahrbuch 1942 der deutschen Luftfahrtforschung. S. 18.

Completed: August 1948.

TABLE 1.

The functions λ_2, Δ_1, Δ_2, T_2, H.

b	Δ_1	Δ_2	λ_2	T_2	H
— 1.0	0.618 279	0.288 190	0.166 938	0.434 667	— 0.512 926
— 0.9	0.631 676	0.290 329	0.151 724	0.414 962	— 0.437 189
— 0.8	0.645 074	0.291 444	0.135 903	0.394 631	— 0.355 960
— 0.7	0.658 471	0.292 256	0.119 579	0.373 746	— 0.269 662
— 0.6	0.671 869	0.292 764	0.102 853	0.352 372	— 0.178 745
— 0.5	0.685 266	0.292 967	0.085 830	0.330 578	— 0.083 683
— 0.4	0.698 663	0.292 868	0.068 617	0.308 435	+ 0.015 015
— 0.3	0.712 061	0.292 464	0.051 321	0.286 009	0.116 831
— 0.2	0.725 458	0.291 756	0.034 049	0.263 369	0.221 219
— 0.1	0.738 856	0.290 745	0.016 907	0.240 585	0.327 617
0	0.752 253	0.289 430	0	0.217 725	0.435 449
0.1	0.787 806	0.296 629	— 0.008 799	0.200 826	0.483 585
0.2	0.823 359	0.302 354	— 0.018 284	0.181 957	0.536 621
0.3	0.858 912	0.306 605	— 0.028 202	0.161 451	0.593 719
0.4	0.894 465	0.309 382	— 0.038 287	0.139 640	0.653 813
0.5	0.930 018	0.310 685	— 0.048 263	0.116 857	0.715 707
0.6	0.965 572	0.310 514	— 0.057 851	0.093 434	0.778 062
0.7	1.001 125	0.308 869	— 0.066 780	0.069 704	0.839 382
0.8	1.036 678	0.305 749	— 0.074 786	0.046 000	0.898 286
0.9	1.072 231	0.301 156	— 0.081 625	0.022 654	0.953 047
1.0	1.107 784	0.295 088	— 0.087 077	0	1.002 095

Approximation formulae :

$$\lambda_2 \geqq 0 \quad H(\lambda_2) = -(6.116 - 4.51\,\lambda_2)\,(\lambda_2 - 0.071\,2)$$

$$\lambda_2 \leqq 0 \quad H(\lambda_2) = 0.435\,4 - 5.653\,7\,\lambda_2 - 6.884\,2\,\lambda_2^2 - 191.65\,\lambda_2^3$$

TABLE 2.

The velocity profiles.

η	$f_1(\eta)$	$f_1'(\eta)$	$f_1''(\eta)$	$f_2(\eta)$	$f_2'(\eta)$	$f_2''(\eta)$	$f_3(\eta)$	$f_3'(\eta)$	$f_3''(\eta)$
0	0	0.752 3	0	0	0	2.000 0	0	0	1
0.2	0.150 4	0.751 6	—0.011 6	0.039 2	0.384 3	1.767 8	0.020 0	0.199 8	0.996 2
0.4	0.300 2	0.743 6	—0.082 0	0.147 9	0.681 7	1.158 8	0.079 7	0.395 4	0.944 8
0.6	0.445 5	0.713 7	—0.226 7	0.302 4	0.837 2	0.390 6	0.176 8	0.569 3	0.768 0
0.8	0.583 4	0.650 5	—0.406 2	0.472 7	0.843 7	—0.295 3	0.304 0	0.691 8	0.432 8
1.0	0.704 3	0.553 5	—0.553 5	0.632 1	0.735 7	—0.735 7	0.448 1	0.735 7	0
1.2	0.803 4	0.434 8	—0.615 9	0.763 1	0.568 6	—0.890 7	0.592 5	0.693 7	—0.357 2
1.4	0.878 1	0.313 6	—0.581 4	0.859 2	0.394 2	—0.822 4	0.721 2	0.583 4	—0.608 7
1.6	0.929 8	0.207 0	—0.476 2	0.922 7	0.247 4	—0.636 8	0.823 8	0.440 4	—0.691 6
1.8	0.962 6	0.124 9	—0.343 7	0.960 8	0.140 9	—0.429 3	0.897 3	0.298 7	—0.623 8
2.0	0.981 5	0.069 0	—0.220 8	0.981 7	0.073 4	—0.256 8	0.945 1	0.183 5	—0.475 8
2.2	0.991 6	0.034 7	—0.126 4	0.992 1	0.034 8	—0.137 0	0.974 4	0.101 6	—0.314 5
2.4	0.996 4	0.016 2	—0.066 4	0.996 8	0.015 4	—0.067 2	0.987 6	0.052 1	—0.186 2
2.6	0.998 6	0.006 7	—0.030 5	0.998 8	0.006 0	—0.028 9	0.994 7	0.023 3	—0.098 4
2.8	0.999 6	0.002 4	—0.011 7	0.999 6	0.002 0	—0.010 5	0.998 0	0.008 8	—0.044 9
3.0	0.999 9	0.000 7	—0.003 6	0.999 9	0.000 6	—0.003 0	0.999 4	0.003 0	—0.015 0

$$b \leqq 0 \quad f(\eta) = (1 - b)\, f_1(\eta) + b\, f_2(\eta) = u/U$$

$$b \geqq 0 \quad f(\eta) = (1 - b)\, f_1(\eta) + b\, f_3(\eta) = u/U$$

$$f_1(\eta) = \frac{\int_0^\eta e^{-\eta^2}(1+\eta^2)\,d\eta}{\frac{3}{4}\sqrt{\pi}}$$

$$f_2(\eta) = 1 - e^{-\eta^2}$$

$$f_3(\eta) = 1 - e^{-\eta^2}\left(1 + \tfrac{1}{2}\eta^2\right)$$

TABLE 3.

Flow with a constant velocity gradient.

$U = U_0\,(1 - x/L)$.

ξ $\dfrac{x}{L}$	$\delta_1 \sqrt{\dfrac{U_0}{\nu L}}$	$\delta_2 \sqrt{\dfrac{U_0}{\nu L}}$	$\dfrac{\tau_0}{\rho U_0^2} \sqrt{\dfrac{\nu}{L U_0}}$
0	0	0	∞
0.01	0.174	0.067	3.09
0.02	0.256	0.096	2.09
0.03	0.324	0.120	1.53
0.04	0.382	0.141	1.21
0.05	0.448	0.160	0.98
0.06	0.508	0.179	0.80
0.07	0.567	0.197	0.65
0.08	0.638	0.215	0.513
0.09	0.682	0.233	0.418
0.10	0.793	0.251	0.283
0.11	0.898	0.269	0.172
0.12	1.078	0.287	0.049

TABLE 4.

Boundary layer velocity profiles for flow with constant outer velocity gradient.

$U = U_0\,(1 - x/L)$.

$x/L = 0.05$ $\lambda = 0.273$

This calculation

$y \sqrt{\dfrac{U_0}{L\nu}}$	0.209	0.418	0.638	0.837	1.055	1.256	1.465
$\dfrac{u}{U}$	0.240	0.507	0.746	0.901	0.972	0.994	0.999

Calculated by Howarth (Goldstein, I. p. 175)

$y \sqrt{\dfrac{U_0}{L\nu}}$	0.179	0.358	0.537	0.713	0.893	1.073	1.253
$\dfrac{u}{U}$	0.205	0.430	0.645	0.815	0.923	0.975	0.994

$x/L = 0.10$ $\lambda = 0.656$

This calculation

$y \sqrt{\dfrac{U_0}{L\nu}}$	0.324	0.647	0.971	1.296	1.618	1.943	2.267
$\dfrac{u}{U}$	0.156	0.400	0.665	0.860	0.958	0.991	0.999

Calculated by Howarth

$y \sqrt{\dfrac{U_0}{L\nu}}$	0.253	0.507	0.758	1.013	1.266	1.518	1.781
$\dfrac{u}{U}$	0.120	0.294	0.498	0.692	0.844	0.936	0.978

TABLE 5.

Results for Schubauers elliptic cylinder.

x	U	U'	λ_2	Δ_1	Δ_2	T_2	λ	$\frac{L\alpha}{R}$	$\frac{\delta_1 R}{L}$	$\frac{\delta_2 R}{L}$	$\frac{\tau_0}{\rho U}\frac{R}{U_0^2 L}$
0.180	0.914	2.42	0.050 5	0.713	0.292	0.285	0.592	2.02	0.355	0.145	1.97
0.357	1.142	0.688	0.035 8	0.724	0.292	0.266	0.402	1.310	0.553	0.223	1.19
0.545	1.230	0.292	0.025 3	0.732	0.291	0.252	0.304	0.978	0.752	0.295	0.85
0.725	1.266	0.140	0.018 3	0.737	0.291	0.243	0.212	0.813	0.907	0.357	0.68
1.097	1.293	0.024 5	0.005 6	0.748	0.290	0.225	0.066	0.610	1.227	0.477	0.47
1.457	1.292	— 0.033 2	— 0.011 5	0.798	0.298	0.195	— 0.136	0.493	1.62	0.604	0.32
1.832	1.261	— 0.121	— 0.065 6	0.995	0.309	0.074	— 0.684	0.422	2.37	0.732	0.10
1.946	1.247	— 0.111	— 0.071 2	1.016	0.307	0.056	— 0.779	0.377	2.69	0.813	0.069
2.029	1.240	— 0.095	— 0.067 4	1.003	0.309	0.064	— 0.707	0.367	2.73	0.841	0.076

$$\frac{L\alpha}{R}=\sqrt{\frac{U'}{\lambda}}, \quad \delta_1=\frac{\Delta_1}{\alpha}, \quad \delta_2=\frac{\Delta_2}{\alpha}, \quad \frac{\tau_0}{\nu\rho U}=\frac{T_2}{\delta_2}.$$

TABLE 6.

Velocity profiles for various sections of the boundary layer about Schubauer's elliptic cylinder.

$x = 0.180$									$R = 24{,}400$
η	0	0.4	0.8	1.2	1.6	2.0	2.4	2.8	3.0
$y\sqrt{R} = \eta/\alpha$	0	0.197	0.394	0.593	0.788	0.986	1.183	1.382	1.475
u	0	0.315	0.563	0.745	0.851	0.897	0.910	0.914	0.914

$x = 0.357$									$R = 23{,}500$
η	0	0.4	0.8	1.2	1.6	2.0	2.4	2.8	3.0
$y\sqrt{R} = \eta/\alpha$	0	0.305	0.608	0.913	1.220	1.523	1.828	2.130	2.294
u	0	0.378	0.692	0.927	1.063	1.120	1.137	1.142	1.142

$x = 0.545$									$R = 24{,}000$
η	0	0.4	0.8	1.2	1.6	2.0	2.4	2.8	3.0
$y\sqrt{R} = \eta/\alpha$	0	0.408	0.816	1.222	1.630	2.040	2.44	2.85	3.06
u	0	0.397	0.738	0.996	1.145	1.207	1.225	1.230	1.230

$x = 0.725$									$R = 23{,}600$
η	0	0.4	0.8	1.2	1.6	2.0	2.4	2.8	3.0
$y\sqrt{R} = \eta/\alpha$	0	0.492	0.985	1.477	1.970	2.462	2.954	3.447	3.693
u	0	0.400	0.753	1.023	1.179	1.242	1.261	1.265	1.266

$x = 1.097$									$R = 22{,}700$
η	0	0.4	0.8	1.2	2.0	2.4	2.8	3.0	
$y\sqrt{R} = \eta/\alpha$	0	0.66	1.31	1.97	2.63	3.28	3.94	4.60	4.93
u	0	0.393	0.758	1.04	1.20	1.27	1.29	1.293	1.293

$x = 1.457$									$R = 22{,}700$
η	0	0.4	0.8	1.2	1.6	2.0	2.4	2.8	3.0
$y\sqrt{R} = \eta/\alpha$	0	0.081	1.62	2.43	3.23	4.05	4.86	5.67	6.07
u	0	0.349	0.704	1.001	1.182	1.262	1.286	1.291	1.292

$x = 1.832$									$R = 24{,}300$
η	0	0.4	0.8	1.2	1.6	2.0	2.4	2.8	3.0
$y\sqrt{R} = \eta/\alpha$	0	0.95	1.90	2.85	3.80	4.75	5.70	6.65	7.13
u	0	0.188	0.494	0.831	1.081	1.207	1.248	1.260	1.261

$x = 1.946$									$R = 23{,}900$
η	0	0.4	0.8	1.2	1.6	2.0	2.4	2.8	3.0
$y\sqrt{R} = \eta/\alpha$	0	1.06	2.12	3.18	4.24	5.30	6.36	7.42	7.95
u	0	0.160	0.456	0.797	1.056	1.188	1.235	1.244	1.247

$x = 2.029$									$R = 23{,}600$
η	0	0.4	0.8	1.2	1.6	2.0	2.4	2.8	3.0
$y\sqrt{R} = \eta/\alpha$	0	1.09	2.18	3.27	4.36	5.46	6.55	7.64	8.18
u	0	0.179	0.479	0.811	1.060	1.185	1.228	1.238	1.240

TABLE 7.

Calculation for Hiemenz circular cylinder.

x cm	U/U' cm	λ_2	Δ_1	Δ_2	T_2	λ	U' sec^{-1}	α cm^{-1}	δ_1 cm	δ_2 cm	$\frac{\tau_0}{\nu\rho U}$
3	3.474	0.066 8	0.700	0.292 8	0.306	0.772	5.803	27.5	0.025	0.010 6	28.9
3.5	4.366	0.064 4	0.702	0.292 8	0 303	0.748	5 251	26.5	0.026	0.011 1	27.3
4.0	5.555	0.060 9	0 705	0.292 7	0.299	0.708	4.57	25.5	0.028	0.011 5	26.0
4.5	7.341	0.055 8	0.708	0.292 6	0.292	0.652	3.74	24.0	0.030	0.012 2	24.9
5.0	10.594	0.046 5	0.716	0.292 3	0.286	0.543	2.75	22.5	0.032	0.013 0	22.0
5.5	19.350	0.031 4	0.727	0.291 6	0.260	0.368	1.56	20.6	0.035	0.014 2	18.3
6.0	196	0.003 9	0.749	0.289 8	0.223	0.046	0.156	18.4	0.041	0.015 7	14.2
6.5	— 20.3	— 0.05 14	0.942	0.310 8	0.109	— 0.532	— 1.487	16.7	0.056	0.018 6	5.9
6.7	— 14.9	— 0.087	1.108	0.295	0	— 1	— 2.25	15.0	0.074	0.019 6	0
	velocity profile for $x = 6.7$										
				$U = 31.6$	$U' = 0.156$	$\lambda = 0.046$		$\alpha = 18.4$			
η	0	0.4	0.8	1.2	1.6	2.0	2.4	2.8	3.0		
y/d	0	$2.23\ 10^{3}$	4.46	6.69	8.92	11.15	13.38	15.63	16.73		
u/U	0	0.304	0.585	0.805	0.929	0.981	0.995	0.998	1.000		

$d = 2 \times 4.87$ cm $\qquad \nu = 0.01$ cm/sec^2

$$\alpha = \sqrt{\frac{U'}{\nu\lambda}} \qquad \frac{\tau_0}{\nu\rho U} = \frac{T_2}{\delta_2}$$

REPRINTED FROM METALEN, VOL. 3, No. 5, JANUARY 1949

REPORT M. 1230 CCL G 101 : G 103

Reflections on Yielding and Aging of Mild Steel

by Ir J. H. Palm

Summary. The phenomena of discontinuous yielding and strain-aging, as they find expression in the conventional stress-strain - curve, are broadly discussed. It is shown that these phenomena cannot be attributed to precipitates in or around the ferrite crystals, but must both be due to C and N which is in solution in the lattice. New hypotheses are given. It is suggested that discontinuous yielding is related with a diffusion mechanism of C and N in the lattice during elastic straining, causing unlocking of the glide planes, i.e. a decrease of the initial critical shear stress. After plastic deformation the glide planes remain unlocked, due to internal stresses. Consequently the glide planes are locked again when the internal stresses diminish or vanish during aging. Strain aging, as far as the continuous part of the stress-strain curve is concerned, is suggested to be caused by migration of C and N to the zones with imperfect lattice (slipzones) in which solubility is increased. Overaging will then be due to restoration of the perfect lattice, i.e. to recrystallization.

I. The yield phenomenon.

The cause of the phenomenon of discontinuous yielding.

Many investigators have studied the characteristic yield phenomenon. The cause of the phenomenon itself and especially the way in which it is affected by the several factors, has been the subject of a great number of publications *).

Since it is possible to establish microscopically that the brittle cementite in mild steel is often present as a kind of network around the ferrite crystals, Nadaï 1) 2) and Ludwik 3) 4) suggested this to be the cause of the phenomenon. They assumed that the resistance to plastic deformation is much higher when the network is present than when it is missing, the nature and the structure of the ferrite being the same. When a tensile testpiece is strained, the network starts to break down locally at a certain load. The load is then transferred to the basic ferrite structure, which can deform plastically under a much lower stress. Consequently, the load stops increasing or at first decreases, dependent on the conditions among which the test is performed. Only after the network has failed in all parts of the test piece can the stress increase again continuously, due to strain hardening. Most of the subsequent investigators accepted this idea or have suggested similar ideas based on the stiffening of the ferrite grain boundaries or some planes in the ferrite crystals by precipitates. Even in the more recent publications of Kuroda 5), Edwards, Jones and Walters 6), Edwards, Phillips and Jones 7), Dies 8) Zener and Hollomon 9), we meet these assumptions with slight and hardly essential variations. In another paper Edwards, Phillips and Liu 10) suggest that yielding might commence on those slip planes in which the precipitation has caused a rather high resistance to shear and subsequently might continue on other slip planes with a lower resistance to shear. It is, however, hard to understand for what reason yielding just might prefer to start on planes with higher resistance to shear. A few other suggestions have also been made, but the argu-

*) Extentive lists of publications on discontinuous yielding, aging and related subjects are given in the references 45, 64 and 11, mentioned at the end of this paper.

ments, brought forward to support them, are still more weak or vague. A summary is given by Low and Gensamer 11) *). Superficially considered the yield phenomenon can be explained with the network theory. A closer consideration of the available data must lead to the conclusion that this idea is untenable.

Even if we leave out of consideration whether a network of a brittle substance, surrounding a plastic basic structure, may ever create discontinuous yielding, several objections can be raised against this theory. Similar networks are present in many multi-phase alloys, however, the yield phenomenon can appear only in some alloys, whereas in mild steel it shows some characteristic features, differing from those in other alloys. Even if the steel is deformed very strongly at room temperature and after that is stored during some time at this or slightly elevated temperatures, pronounced yielding re-appears. It is unimaginable that the highly destroyed network should be restored during the rest period. At room temperature, as will be shown below, a noticeable diffusion of carbon does take place, but this cannot lead to the restoration of the network. In contrast the distortion of the network can, when diffusion takes place, only stimulate the creation of the thermodynamically more favourable shape, to wit the globular cementite. When a steel with a few hundredths per cent carbon is annealed at a temperature of 700° C, quenched and after that heated a long time at 150° C, minute particles of cementite are precipitated uniformly in the ferrite. Already long before the precipitation is microscopically visible, the yield phenomenon has returned. Likewise, the network theory does not explain the fact that the upper yield point and the fundamentally related lower yield point are much more sensitive to the strain velocity than the continuous part of the stress-strain curve itself. Fettweiss 12), Winlock and Leiter 13), and Manjoine 14) observed that the percentage increase of the yield points at increasing strain velocity is about three times as high as that of the tensile strength. On the other hand, the fracture strength of brittle constituents like cementite depends very little on the strain velocity, so that a network of cementite or other brittle

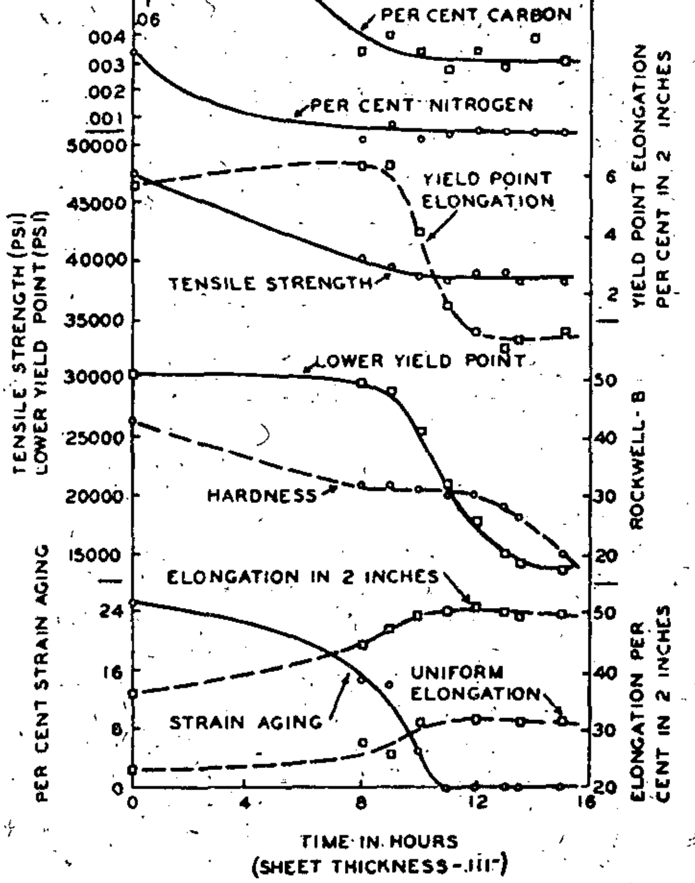

Fig. 1.
Effect of time of wet hydrogen treatment on carbon and nitrogen content, tensile properties and strain-aging in heavy-gauge, sheet steel (0,111-inch thick rimmedsteel). [Low and Gensamer 11)].

precipitates cannot be the origin of this sensitivity.

It is still more difficult to attribute the yield phenomenon to fine non-coherent particles, precipitated at the grain boundaries or in the ferrite crystals themselves. Such a precipitation will cause a higher resistance to shear in all stages of plastic deformation and not in the primary stage only.

Several phenomena now indicate that the carbon and nitrogen dissolved in the ferrite, must be the cause of the yield phenomenon, and that the quantity and shape of the separated cementite play, at most, a secondary part.

Snoek 15, 16) observed that steel wire, which is decarburized and denitrided as completely as possible with the aid of hydrogen, does not show discontinuous kinking, a direct consequence of the yield phenomenon, when it is bent. Addition of the slightest traces of carbon or nitrogen, however, causes a return of this effect.

Low and Gensamer 11) found that after annealing soft steel in moist hydrogen at 725° C, the yield phenomenon at room temperature was only slightly affected, as long as the car-

*) After this report had been finished, a paper by A. H. Cottrell **) was published in which the phenomena of discontinuous yielding and strain ageing are both attributed to locking of dislocations in the lattice by C and N atoms. This hypothesis is also suitable to explain these phenomena in several respects. However, it cannot explain for instance the great sensitivity of the yield points to the strain velocity and the striking difference in the ageing velocity of the yield points on the one hand and the continuous part of the stress-strain curve on the other hand. Moreover a similar kind of locking might then be expected in austenitic manganese steel, austenitic nickel steel and many other alloys.

**) Phys. Soc. London (1948) 30.

bon percentage did not decrease below approx: 0,004 % (fig. 1). After prolonged annealing discontinuous yielding became less pronounced and finally disappeared completely. A further fall of the carbon percentage could not be observed by the method of analysis employed, but the investigators rightly assumed it to occur. The size of the ferrite crystals did not change during annealing. From this we immediately can conclude that the cementite network, or rather the thin layers of cementite, situated at random between the ferrite crystals, as well as other precipitates of cementite, the dimensions of, which must start to decrease immediately in consequence of annealing in hydrogen, hardly influence the yield phenomenon.

The following interpretation of Low and Gensamer's observations readily presents itself. As long as there is more carbon in the steel than corresponds to the saturation concentration at room temperature, the yield phenomenon mainly remains unchanged. Not before the concentration decreases below saturation at room temperature, discontinuous yielding strongly diminishes and finally disappears at complete decarburization. Therefore, one of the causes of the yield phenomenon must be the carbon, dissolved in the ferrite.

As has already been mentioned, besides the carbon also the nitrogen is removed by the annealing treatment with hydrogen. Like Snoek, Low and Gensamer observed that the addition of minute quantities of nitrogen causes the yield phenomenon to return. Dissolved nitrogen must therefore also be considered as a cause of the yield phenomenon. These conclusions are confirmed quite well by the observations of Edwards, Phillips and Jones 7), Comstock 17, 18), and Dies 8), who established that the magnitude of the yield phenomenon decreases and finally disappears by adding elements like Ti, Va, Nb, Mo, Cr in increasing quantities. These elements strongly combine with carbon and nitrogen in steel, forming carbide and nitride and thus considerably reduce the saturation concentration of carbon and nitrogen in ferrite. The fact that the addition of larger quantities of aluminium also decreases the effect of the yield phenomenon, confirms that nitrogen too is responsible for discontinuous yielding. A complete elimination can however not be attained, because aluminium does not combine with carbon. Low and Gensamer's observation that the percentage of nitrogen in steel, deoxidised with aluminium, could hardly be diminished by annealing in moist hydrogen, confirms that indeed aluminium combines very strongly with nitrogen in steel.

The same authors also observed that, by annealing in moist hydrogen, the total percentage of oxygen did not decrease, although the yield phenomenon disappeared at last. This indicates that oxygen probably does not play any significant part in the yield phenomenon. Statistically considered, the yield phenomenon is as pronounced in rimmed steel as in silicon — killed steel. The restricted influence of aluminium, notwithstanding its strong affinity to oxygen, also indicates that this effect is due to the interaction with nitrogen only. According to Low and Gensamer sulphur and phosphorus are not removed by the treatment with moist hydrogen. From the foregoing we may therefore conclude that only the carbon and nitrogen, dissolved in the ferrite, are the causes of the yield phenomenon.

The mechanism that introduces the yield phenomenon.

Assuming that the dissolved carbon and nitrogen-atoms are the cause of the yield phenomenon, apparently minute quantities of these atoms are already able to block the glide planes of the ferrite lattice completely, as long as a definite stress (the upper yield point) is not attained. Then, however, a sudden unlocking or at least a considerable reduction of the locking effect occurs. As is wel known, the carbon and nitrogen atoms do not occupy positions of the iron atoms by substitution, as do dissolved foreign metal atoms, but they are assimilated by interposition between the iron atoms. The slight solubility of carbon and nitrogen in the ferrite indicates that these atoms might deform the lattice to a rather great extent. It is not unlikely now that the yield phenomenon must be attributed to a displacement of the carbon and nitrogen atoms, relative to their original position, which already takes place during the elastic deformation. In this connection the theory of Snoek 15) of the elastic after effect in mild steel, offers some ground for an explanation of the phenomenon of discontinuous yielding 15) 16). In

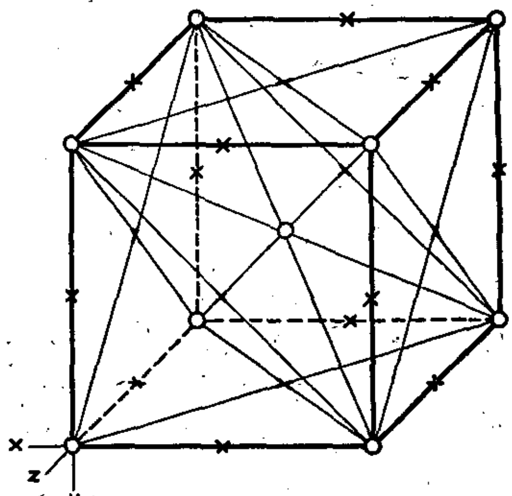

Fig. 2.
Equilibrium positions of the carbon and nitrogen atoms in the ferrite lattice. [Snoek 15) 16)].

short, this theory can be summarized as follows: The carbon and nitrogen atoms are distributed statistically equivalent along the three principal directions in the ferrite lattice, as long as the lattice is not deformed by external stresses. For reasons of symmetry Snoek considers the x-positions (½.0.0.) and (0.½.½), the y-positions (0.½.0.) and (½.0.½.) and the z-positions (0.0.½) and (½.½.0), which are mutually equivalent, as the positions where these atoms are in equilibrium (fig. 2) *). For reasons of simplicity only the x-positions are indicated in fig. 2. When the lattice is strained elastically in the x-direction, the y- and z-positions remain mutually equivalent, but become different from the x-positions. The equilibrium in the lattice is now disturbed and consequently a stronger diffusion of the atoms from the y- and x-positions to the x-positions than in the opposite direction, takes place, until a new state of equilibrium is reached. Although the distance, over which the atoms have to be displaced, is smaller than the lattice parameter, this displacement is a pure diffusion process. The velocity of displacement therefore strongly depends on the temperature and the degree of deformation. If the carbon and nitrogen atoms are distributed uniformly over the x-, y- and z-positions, they cause on the average an equal deformation of the lattice in all directions. When the atoms are more concentrated on x-positions, the deformation increases in the x-direction and decreases in the y- and z-directions. When the lattice is now loaded in the x-direction, at first a spontaneous strain in this direction takes place (fig. 3). There-after the strain still increases a finite amount, during the time in which the modified diffusion equilibrium is established. On unloading, at first a spontaneous contraction occurs followed by a further contraction during the time that the initial state of equilibrium is restored.

From a quantitative consideration of the

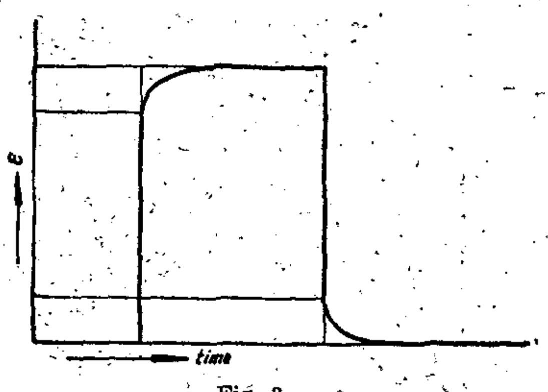

Fig. 3.
Elastic after-effect in steel at loading and unloading. [Snoek 15, 16].

*) Whether other equilibrium positions are more plausible will be left out of consideration here. In this connection it does not make any essential difference.

diffusion proces Snoek concludes that even at room temperature the carbon can diffuse with perceptible velocity. This may also be concludeded from the quench-aging behaviour of mild steel, discussed in more detail later on.

Naturally, every arbitrary state of stress which causes an unequal deformation of the lattice, causes the original states of equilibrium to become unequal and the dissolved atoms to concentrate at preferred positions. A conglomerate of ferrite crystals, orientated at random, will therefore behave essentially in the same way. For a qualitative explanation of the phenomenon the use of the simple picture is thus permitted.

It is obvious that the properties of the glide planes will also be changed during the diffusion process. Snoek's theory may therefore be extended as follows *). When the lattice is stressed in the x-direction slip along the [1.1.0] planes in the [1.1.0] direction, as well as the preferred [1.1.1.] direction, is at first impeded by the C- and N-atoms (0.½.0.) and (½.0.½), whilst slip on the [1.0.1] planes is at first impeded by the C- and N-atoms (0.0.½.) and (½.½.0.). It seems therefore very acceptable that slip will not occur before these atoms are migrated fully or to a certain degree to the remaining equilibrium positions (½.0.0.) and (0.½.½.). Consequently yielding will start at a higher shear stress and thereafter at first continue on a lower stress. Since after a certain plastic deformation, even when the external load is taken off, high internal stresses in the crystal fragments initially remain, it is also plausible that these stresses initially prevent the return of the yield phenomenon. As will be elucidated in more detail in following sections the essential aspects of the yield phenomenon can be explained on the basis of this hypothesis of unlocking of glide planes. Especially the great sensitivity of the yield points to the strain rate fully agrees with the supposition that the yield phenomenon is related with a diffusion process which already occurs during the elastic deformation of the lattice.

The fundamental character of the yield phenomenon.

The way in which the yield phenomenon finds expression in the stress-strain curve in tension not only depends on the steel itself, but also on the strain velocity, the type and construction of the testing machine and the shape and dimensions of the test bar. When a test bar is loaded, potential energy is accumulated in the combination of testing machine and test bar, dependent on the magnitude of the load. When yielding occurs under maintained or decreasing load; this energy is partially released in the form of kinetic energy of the parts of

*) See also „De Ingenieur" (1948) No. 27, Mk 7.

the machine and of the test bar. The part of the potential energy, accumulated by the testing machine, is determined on one side by the elastic deformation of the machine, on the other side by the type of testing machine; it is a measure of the regidity of the testing machine. Perfect rigidity, which means that the energy is zero, is of course unattainable. The potential energy of the test bar is only determined by the elastic deformation of the bar and as such related with the shape and dimensions of the test bar. In addition, these dimensions affect the stress distribution of the test bar. For a judgement of the fundamental properties of the steel with regard to the yield phenomenon, it is therefore necessary to eliminate the factors, which do not refer to the properties of the steel itself and exercise an uncontrolable by-influence. We therefore consider a straight cylindrical tension bar, to which the load is applied statistically uniformly, and which is tested in a perfect rigid testing machine. A completely uniform stress distribution on the end planes of the bar is impossible and even undesirable. In consequence of the anisotropy of the crystals, which are orientated at random, a complicated stress distribution occurs in the bar. These stresses are, however, statistically uniformly distributed, on condition that the crystals are small with respect to the thickness of the bar. Fig. 4 shows qualitatively the distribution of the longitudinal tensile stresses over the cross section. Now we imagine that the stress is carried over to the end planes in such a way that here the same state of stress exists as in the bar itself. We further leave the dimensions of the bar out of consideration, in so far that it is only assumed that the length of the bar is great in comparison with the width of the flowlines, which will be developed during discontinuous yielding. Now, the bar is strained with such a small velocity that the homogeneous equilibrium of the carbon and nitrogen in the lattice is fully

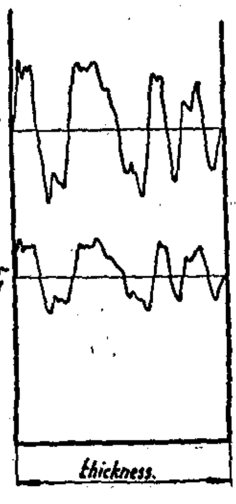

Fig. 4.
Simplified representation of the longitudinal stresses in elastically deformed test bar.

established during the purely elastic deformation of the lattice. At C (fig. 5), somewhere in the bar the critical stress (in reality a complicated state of stress), is reached, by which unlocking on the glide planes in question occurs, followed by yielding under decreasing load. It is evident that the corresponding nominal stress, at which yielding starts, is determined only by the properties of the steel itself.

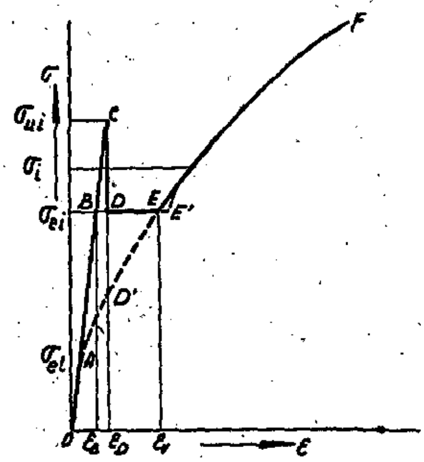

Fig. 5.
Fundamental shape of the stress-strain curve of mild steel in tension.

This stress has therefore to be considered as a characteristic material constant, which we might call the ideal upper yield point σ_{ui}. On reaching σ_{ui} the unlocked centre cannot stand the local high stress any longer, so that the stress decreases simultaneously with the occurrence of the plastic deformation. Consequently, a high stress concentration arises at the boundary of the primary yield centre and the still purely elastically deformed surroundings, so that the critical stress is reached here too. Unlocking continues quickly from the primary yield centre across the whole bar cross section, under development of one or more flow lines and simultaneous decrease of the nominal stress. This process continues under further deformation in the flow lines and, possibly, development of new ones at the boundary of the primary flow lines, till the nominal stress has decreased to such an amount that at D the critical stress remains exactly maintained in the boundary of the flow lines. A further decrease is therefore not possible without the yield process coming to a stop. On continued straining a front of flow lines passes through the bar, at constant nominal stress till at E, at a strain ε_y, unlocking has taken place throughout the whole bar. The corresponding nominal stress, which we might call the ideal lower yield point σ_{li}, is also a characteristic material constant. On the primary moment of unlocking, strain hardening starts simultaneously with the plastic deformation. The strain hardening increases, independent of the discontinuous shape of the stress-strain curve, continuously with the local plastic deformation, in the same way as in other plastic metals. This is already evident from the well-known fact that a uniform plastic deformation, which is smaller than the yield point elongation ε_y, is sufficient to make the stress-strain curve completely continuous. Such a deformation, which can be attained for instance by rolling, just eliminates the locking effect completely, while the strain hardening is still very small *).

Moser 19) and later Winlock and Leiter 13) have shown that the hardness increases continuously with the local strain in the flow lines, in spite of the discontinuous slope of the stress-strain curve. From this fact they concluded quite rightly that the stress-strain curve of steel should be continuous according to OAEF, if the cause of the yield phenomenon would be just eliminated without a further change of the properties. We might call the stress at A the elastic limit of the unlocked steel, σ_{ei}.

During discontinuous yielding the local strain, attained in the flow lines is equal to ε_y, apart from slight deviations caused by triaxial stresses. The strain hardening in the flow lines is therefore given by the increase of stress from σ_{ei} to σ_{li}. In E, after discontinious yielding has extended across the whole bar, the strain is uniform again. On further straining the unlocked state remains maintained and the bar now behaves in completely the same way as the bar which would be unlocked already at the outset. This means that the bar strains uniformly and the nominal stress therefore increases continuously.

Between C and D the bar is in a labile state and in this range the development of the flow lines and the decrease of the nominal stress thus occurs with a comparatively great velocity. At a very small rate of strain of the bar as a whole, the fall from C to D is therefore practically vertical. The strain in the flow lines is compensated by the elastic contraction of the entire bar. The strain in the section, which is only deformed elastically, decreases to ε_D.

Dependent on the ratio of the length to the thickness of the bar, (the thickness determines the width of the flow lines), slight deviations can occur in the stress-strain curve. When the length of the bar is greater, the width of the zone, over which the deformation must extend between C and D, increases. It now depends on the velocity of unlocking in the boundaries of the primary flow lines, the local strain velocity in these flow lines and other factors, whether or not the deformation already locally stops at a higher stress than σ_{li}. In the first case the local strain will be somewhat greater than corresponds to ε_y and in consequence the unlocking of the entire bar is not ended before E′, beyond E, is reached. At continued straining the bar does not become fully uniform before the stress is raised again to the highest stress σ_l, at which yielding in the primary flow lines has come to a standstill. This problem, however, is extremely difficult to discuss and is certainly of no importance for bars of usual length.

It is also hard to conclude whether or not the nominal stress might temporarily decrease till below σ_{li}, when the length of the bar is so small that, this stress being reached, only a very slight plastic deformation has taken place in the primary flow line. A drop to D′ is fundamentally impossible. The width of the flow line must always be smaller than the length of the bar, because the total length of the bar is practically unchanged. The local strain is therefore always greater than the total strain ε_D and consequently the normal stress must always remain greater thans σ_D. Moreover, in the flow line a complicated state of stress exists, due to the necking effect, which has the same effect as strain hardening and which helps to keep the stress at a still higher level. Anyhow, a drop in the stress below D could not be realized with certainty under conditions which were approximately the same as those mentioned above.

A macroscopically uniform stress distribution, the ideal condition from which we started, naturally cannot be attained in reality. As is wellknown a macroscopical stress concentration always exists in the transition of the

*) On the other hand roller levelling of narrow strips has only a small influence on the magnitude of the lower yield point. The fact, that the steel after this working does however show rather strong strain aging, proves that plastic deformation has taken place. The gliding in the crystals during this treatment is however alternating, and that will be the cause that the elastic deformation of the crystal fragments is too small to eliminate discontinous yielding.

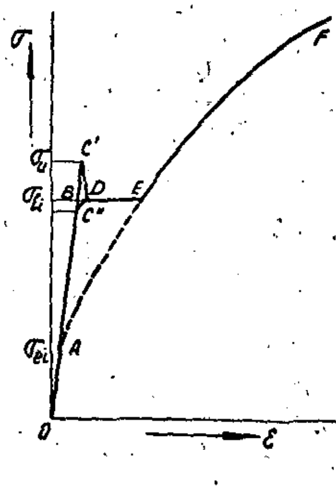

Fig. 6.
Influence of stress concentration on the stress-strain curve of mild steel in tension.

straight part of a test bar to the fillets. Therefore, the critical unlocking stress is already reached in C′ at a nominal stress σ_u smaller than σ_{ui} (fig. 6). As has been shown for instance, by Körber 20) Kuntze and Sachs 21) and Mac Gregor 22) the nominal stress at which the yield phenomenon starts is less as the stress concentration is greater.

Stress concentrations may also be caused by eccentric loading and by internal factors as residual stresses, slag inclusions etc.

When the stress concentration is greater than in the flow lines, local plastic deformation already starts in C″, at a nominal stress which is even lower than σ_{li} (fig. 6). Then an upper yield point is no longer possible. As has been emphasized by Körber the upper yield point observed on a real test bar does not therefore have the significance of a material constant.

For the lower yield point the case is quite different. Once a front of flow lines has developed in the cylindrical section of the bar, the state of stress in the boundaries of the flow lines is again defined by the characteristic properties of the steel itself. In good agreement, Körber also observed that the shape of the cross section of the bar hardly had any influence on the lower yield point. If, therefore, the tensile test is performed on a real test bar, with the required small strain velocity, the observed lower yield point is equal to the ideal lower yield point, provided the testing machine is sufficiently rigid with regard to the yield point elongation. The ideal lower yield point is therefore a material constant, which might be actually determined.

Effect of the strain velocity at room temperature.

As has already mentioned, unlocking of the glide planes takes place over the whole range CDE, and this phenomenon thus plays a role as well at the upper yield point as at the lower yield point. Since unlocking must be preceded by diffusion and this diffusion requires time, it is clear that both yield points must increase with the strain velocity to a greater extent than the slope of the continuous part of the stress-strain curve. This is in accordance with numerous observations. So Fettweis 12), Winlock and Leiter 13), and Manjoine 14) observed that the percentage increase of the lower yield point with increasing strain rate is about three times as large as that of the tensile strength. Edwards, Philips and Liu 10) observed that in vanadium-treated steel and steels decarburized by hydrogen, which showed no discontinuous yielding at a normal rate of strain, the yield phenomenon was clearly present at a high strain rate.

How far the upper yield point and the lower yield point are differently influenced by the strain rate can hardly or not at all be judged beforehand. Though, at the lower yield point the same internal stress is necessary to continue yielding as at the upper yield point to start yielding, as has also been pointed out by Davis 23), the further circumstances are different in many respects. Exactly up to the upper yield point the bar strains equally everywhere and only elastically. At the lower yield point the bar strains elastically as well as plastically in the proceeding flow lines. The strain rate at the moment that the upper yield point is reached is therefore much smaller than the local strain rate at the lower yield point, the strain rate of the bar as a whole being the same. The ratio of the local strain rate to the strain rate of the bar as a whole is constant for a definite length of the bar, however, it increases proportionally with the length of the bar. Therefore, the lower yield point is not only dependent on the strain rate of the bar as a whole, but also on the length of the bar. The state of stress in the bar at the lower and upper yield point is also not affected in the same way by the strain rate. Independent of the strain rate, the shape of the bar in the region where the unlocking starts, remains practically unchanged. This, however, is not the case in the flow lines, where at increasing strain rate the nominal stress, and therefore also the local plastic deformation, rather strongly increases. From the results of the investigations by Kühnel 24), Körber and Pomp 25), Elam 26), Morrison 27), Quinney 28), Docherty and Thorne 29), Miklowitz 35) a definite conclusion can hardly be drawn, because the conditions under which the effect of the strain rate was investigated are not comparable in every respect. Their data give, however, the impression that the difference between the upper yield point and the lower yield point at first increases with the strain rate. At very high strain rates, the difference between the upper yield point and the lower yield point in most cases seems to be

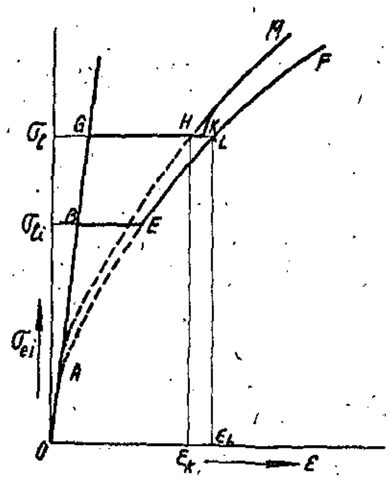

Fig. 7.
Influence of strain-rate on the stress-strain curve of mild steel in tension, no upper yield point being present.

very small, so that at higher strain rate the lower yield point apparently increases to a greater extent than the upper yield point.

When an upper yield point is absent, the stress-strain curve at greater strain velocity must follow O G K M, as is schematically represented in fig. 7. Naturally, at higher strain rates not a single point of the stress-strain curve corresponds to a state of equilibrium. As the front of flow lines, developed from G to K has passed a part of the bar earlier, the local strain more and more approximates the strain

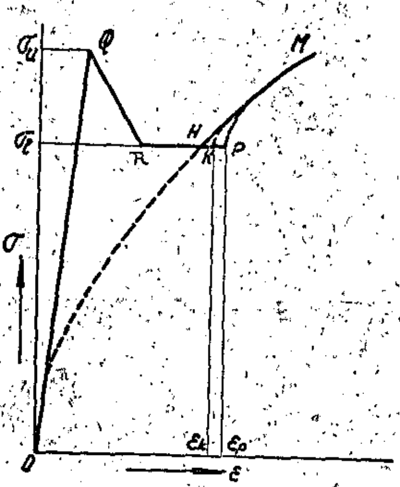

Fig. 8.
Influence of strain-rate on the stress-strain curve of mild steel in tension, an upper yield point being present.

ε_L, which is in equilibrium with the corresponding stress. If O H M represents the stress-strain curve of the steel unlocked beforehand at the strain rate concerned, then heterogeneous yielding will not be finished in H, but between H and L, e.g. in K, whilst the bar has not been strained uniformly. Consequently the continuous part of the stress-strain curve in K must be comparatively steep. This is in accordance with most observations.

The behaviour becomes more complicated, if an upper yield point is also present. At the same strain rate, a greater local strain results during the drop of the stress, than in the case that the upper yield point is absent. This causes heterogeneous yielding to be continued even beyond K, up to P (fig. 8). Dependent on the magnitude of σ_u and the local strain rate during the drop of the stress from Q to R, ε_p may be smaller as well as greater than ε_L (fig. 7).

At a higher strain rate it is also possible that no stationary state, which is shown by a horizontal part of the stress-strain curve, is attained at all, especially when the steel has a comparatively high upper yield point and a comparatively small local strain rate during the fall of the stress. This case is represented schematically in fig. 9.

Bach 30) and Quinney 28) observed that in exceptional cases the upper yield point can exceed the tensile strength at a normal strain rate. Manjoine 14), who made his experiments with annealed steel, observed no overstepping of the corresponding tensile strength by the upper yield point, even at very high strain rates, though the difference was small. At very high strain rates, the upper yield point as well as the lower yield point, however, exceed the static tensile strength. As will be shown below,

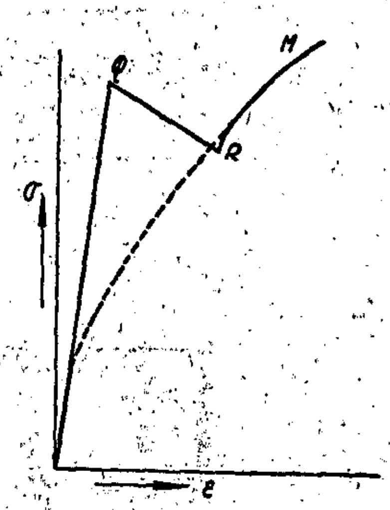

Fig. 9.
Influence of strain-rate on the stress strain curve of mild steel in tension; an upper yield point being present.

overstepping of the tensile strength by the upper yield point is easily possible at very low temperature, or when the steel is strongly plastically deformed and aged.

As has already been mentioned in the preceding pages, potential energy is accumulated in every tensile testing machine at loading. This energy is partly released again during

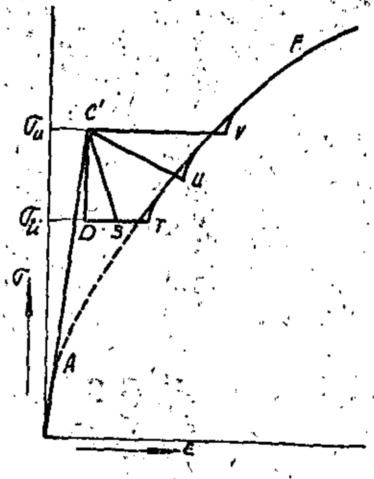

Fig. 10.
Influence of the rigidity of the testing machine on the stress-strain curve of mild steel in tension.

heterogeneous yielding at decreasing load or even at constant load, when the machine is of the direct laoding type. Hence, the strain rate is accelerated beyond control. The effect of the rigidity of the testing machine has been studied particularly by Siebel and Schwaigerer 31), Krisch 32), Esser 33), Welter 34) and quite recently by Miklowitz 35). The way in which the shape of the stress-strain curve is influenced by the rigidity of the testing machine, other conditions being the same and the strain rate during loading being very small, is represented schematically in fig. 10. If the rigidity is relatively large, the shape of the curve is according to OC'STF and the ideal lower yield point is still reached. In the case that the rigidity is relatively small the shape is according to OC'UF and ε_{11} is reached no more. If the machine is of the direct loading type a drop of the nominal stress is not possible at all. The shape of the curve is then according to OC'VF, in which the horizontal stretch CV' is passed with great velocity.

The influence of the temperature on the yield phenomenon.

Is is obvious from the investigations of Bach 30), Körber and Pomp 36) Kenyon and Burns 37) and Manjoine 14) that the yield points, the drop of the upper yield point to the lower yield point, and the yield point elongation all diminish at increasing temperature (fig. 11). At normal strain rate the yield phenomenon has disappeared completely at approx. 300° C and at a greater strain rate only a rather sharp knee appears. The effect of unlocking apparently decreases faster than the effect of strain hardening, which even at nominal strain rate increases again beyond approx. 80° C., in consequence of simultaneous aging during plastic deformation. Possibly, this might be connected with

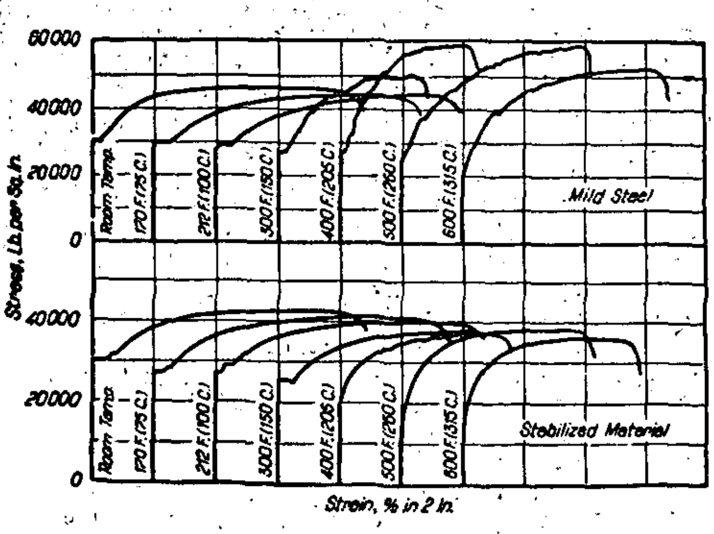

Fig. 11.
Stress-strain curves of mild steel and stabilized steel tested at various temperatures. [Kenyon and Burns 37)].

an alteration of the diffusion equilibrium at each stress with the temperature. Due to the higher diffusion velocity, the percentage of *carbon and nitrogen atoms*, which are really situated at every instant in the equilibrium positions, decreases with increasing temperature. A satisfactory explanation, however, can still not be given. It is also evident, from the investigation of Manjoine that the increase of the yield points with increasing strain rate is smaller as the temperature is higher, which is in accordance with the increasing diffusion velocity (fig. 12a and b).

Exact data concerning the behaviour of the yield phenomenon below room temperature are rather scarce. From the investigations of Maurer and Mailänder 38), Greaves and Jones 39), Bennek 40) and Mac Adam 41) it may be concluded that the yield points increase to a greater extent at decreasing temperature than does the tensile strength, especially below —70° C. In table I some data, from Maurer and Mailänder, are summarized.

Temp. °C	Yield point σ_b kg/mm² σ_o	Tensile strength kg/mm²	Elongation %	Reduction of area in %	True breaking strenght kg/mm²
−180	83−72	72	25	61	114
− 70	35−32	45	37	70	105
+ 20	32−30	42	31	73	95
+100	30−26	39	33	70	95

At —180° C, and possibly even at somewhat higher temperatures, the *upper yield point thus exceeds the tensile strength* when the steel is in a condition of normal heat treatment.

As long as the lower yield point does not exceed the tensile strength, the stress-strain curve, *apart from the presence of an uppr* yield point, will have the shape according to OD'E'F' (fig. 13), which is not essentially different from the curve at room temperature. If, however, the lower yield point exceeds the tensile strength, before the fracture strength, corresponding to the pure elastic state, is reached, the bar will continue to neck in the region of primary yielding, under continuous decrease of the nominal stress till fracture occurs. The other sections of the bar will in this case show no plastic deformation at all. The stress-strain curve will then be according to OD″W.

At a still lower temperature the fracture strength might be reached before yielding occurs, particularly if the upper yield point is comparatively high. In that case the bar will fracture practically brittle.

No data are available with regard to the effect of the strain rate on the yield phenomenon below room temperature. It is, however, not

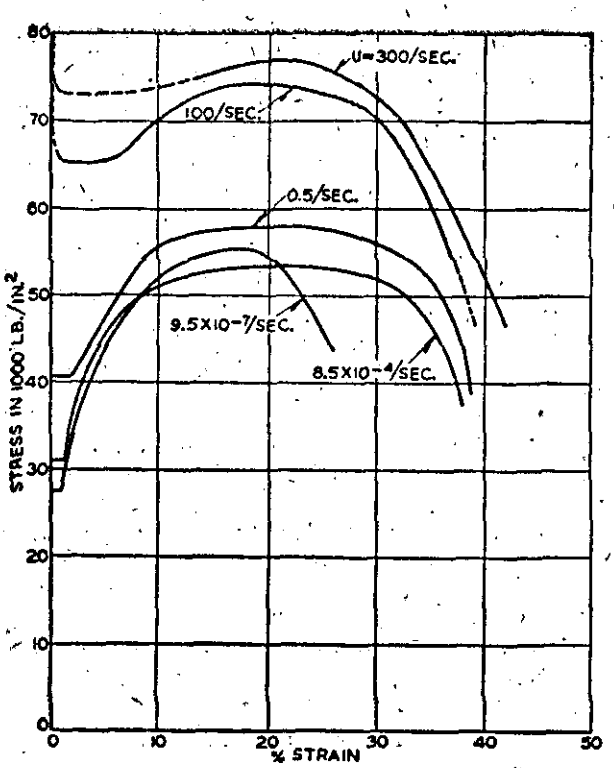

Fig. 12a.
Stress-strain curves of mild steel at room temperature for various rates of strain. [Manjoine 14)].

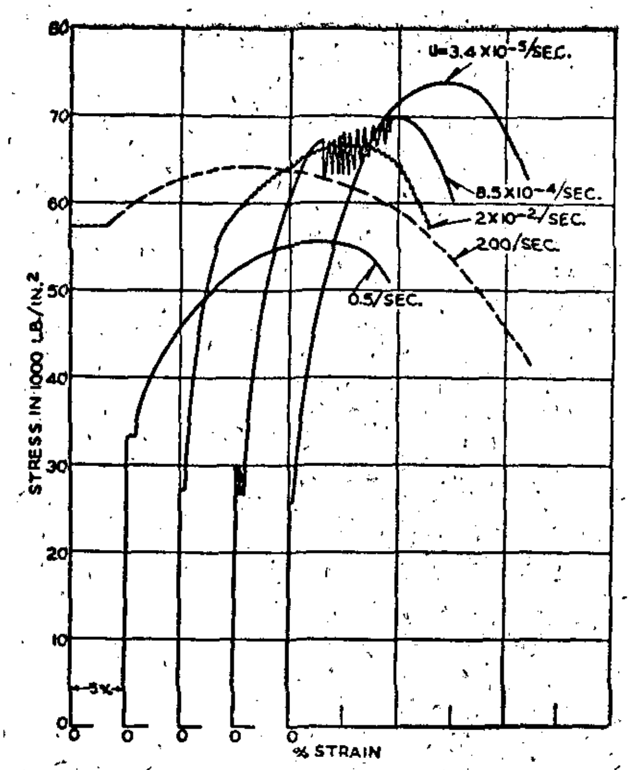

Fig. 12b.
Stress-strain curves of mild steel at 200° C for various rates of strain. [Manjoine, 14)].

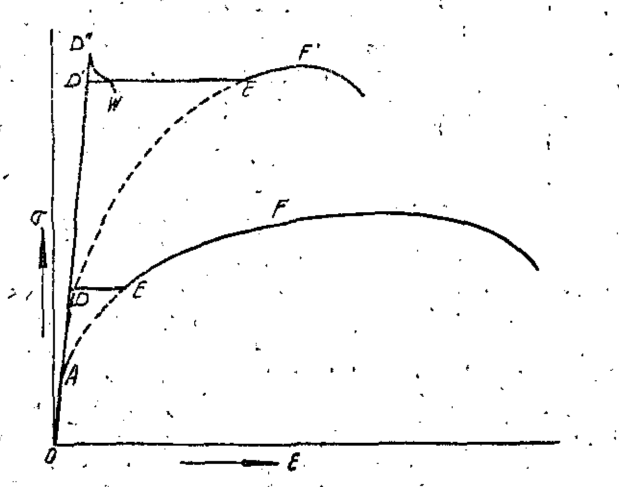

Fig. 13.
Influence of temperature below room temperature on the stress-strain curve of mild steel in tension.

doubtful that the yield points will react more strongly as the temperature is lower. Since the tensile strength and probably the fracture strength in particular, are much less sensitive to the strain rate, the temperature below which brittle fracture or continued necking in the primary yield region occur will strongly increase with increasing strain rate. Though the transition zone in the deformation energy-temperature curve, observed when testing notched bars of ferritic steels, probably does not find its origin in the mechanism of discontinuous yielding itself, certainly the shape of the curve in the transition zone and the corresponding temperature are influenced by this mechanism. This problem will be dealt with in more detail in a subsequent paper.

II. The strain-aging of steel.

Comparison of strain-aging and quench-aging and their causes.

When plastically deformed steel is stored some time at room temperature or a higher temperature, the yield phenomenon returns at a higher level. The tensile strength and the fracture strength increase as well, however, to a smaller extent, while the elongation and reduction of area decrease (fig. 14). The explanation of this behaviour, as given for instance by Pfeil 42), Köster 43), Krüger 44), Davenport and Bain 45) and now generally accepted with slight non-essential modifications, is based on the assumption that steel in practically all conditions of heat treatment, even after very slow cooling, is to some extent supersaturated with carbon, nitrogen and oxygen. It is now supposed that these elements or at least one of them, in combination with iron atoms, might rather easily be precipitated in submicroscopic dispersion, even at room temperature, if the steel is plastically deformed, and thus cause an increased resistance to plastic deformation. This explanation is based upon the analogous explanation of the quench-age phenomenon of steel and other multi-phase

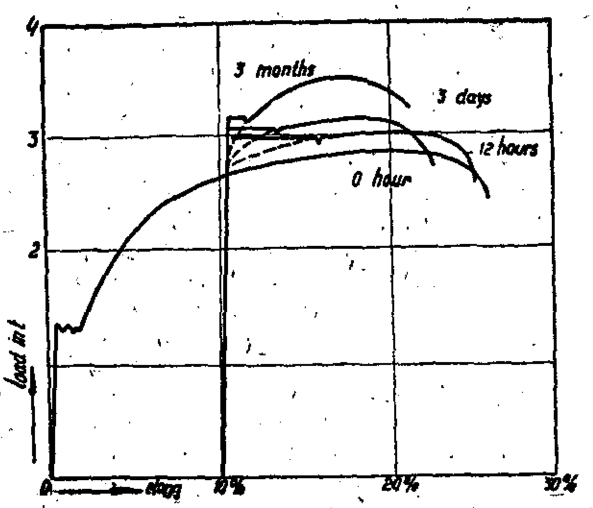

Fig. 14.
Effect of strain aging on the stress-strain curve in *tension.* [Köster 58)].

alloys. Masing 46) and Köster 43) were the first who showed that the tensile strength and the hardness of commercial steel with low carbon content, after quenching from a temperature slightly below 720° and storage at roomtemperature or slightly higher temperature, at first increases while the ductility decreases. The quenched steel is, in consequence of the higher solubility of carbon and nitrogen at high temperature, supersaturated at lower temperatures, so that thermodynamically precipitation of iron carbide and iron nitride is pursued. It is now obvious from the phenomenon of quench-aging and also from the yield phenomenon, that the diffusion rate of carbon and nitrogen in ferrite is rather high. A perceptible increase in the resistance to plastic deformation is attained at room temperature in a few days or even a few hours. From the investigations of Köster 43), Davenport and Bain 45), Andrew and Trent 47) it may be concluded with certainty that precipitation of iron carbide and iron nitride at low temperature causes aging. According to Jensen 48), Whiteley 49) and Köster 43) the degree of saturation of carbon in ferrite at room temperature is approx. 0,006 % C. As to the solubility of nitrogen in ferrite at room temperature, the results obtained by several investigators show a rather appreciable difference. According to Fry 50) and Ehn 51) the solubility is about 0,015 %. Köster 52) however determined the solubility to be approx. 0,001 %. Though this value might be somewhat too low, the agreement between the results obtained by careful measurements of the alteration of the magnetic as well as the electrical properties, indicates that the order of magnitude, a few thousandths of a percent, is probably correct. Carbon, and to a lesser extent nitrogen too, are therefore responsible for the quench-aging effect of soft commercial steel.

It is not clear whether oxygen plays a role in quench-aging or not. Since steel always contains several oxide inclusions, it is extremely difficult to ascertain the percentage of atomic oxygen dissolved in the ferrite, just as the increase of the solubility with the temperature, which is in all probability extremely small. Anyhow, it is not very probable that the oxygen contributes to quench-aging in steels, fully killed with silicon or aluminium. Daniloff, Mehl and Herty 53) concluded that the sensitivity to quench-aging decreased with increasing deoxidation. A distinct difference in the behaviour of the groups of steel examined, exceeding the experimental scatter, is present only between the rimmed and killed steels. The mean carbon percentage of these groups, however, differs likewise strongly. The results will also be affected by the fixation of nitrogen by aluminium in the aluminium-killed steels and the difference in crystal size. Davenport and Bain 45) observed that electrolytic iron, which is rich in oxygen, showed only a slight tendency to quench-aging, even after extra addition of iron oxide. Eilender and Wasmuth 54) observed the same in iron-oxygen alloys containing less than 0,05 % oxygen. It is therefore not very probable that the oxygen in normal mild steel plays a role of any importance with regard to quench-aging. It is obvious that deoxidation with aluminium does decrease the quench-aging effect to some extent, in consequence of its affinity to nitrogen. Addition of a proper amount of Ti, Zr, V and similar elements, which combine strongly with nitrogen and carbon, highly diminishes or completely eliminates the sensitivity to quench-aging, as Eilender, Fry and Gottwald 55) have shown.

Low and Gensamer 11) observed that the ability of mild steel to strain-aging, as far as the return and the increase of the yield point is concerned, did not disappear during treatment in moist hydrogen at 700° C, as long as the carbon content did not decrease below approx. 0,004 %. A decrease of the aging effect, however, became already noticeable at a somewhat higher percentage (fig. 1). When the decarburized and simultaneously denitrided steel, was nitrided, the ability to strain-aging returned. They therefore concluded that both carbon and nitrogen are causes of strain-aging. This conclusion is supported by the observations of Edwards Phillips and Jones 7) and Comstock 17, 18), that steel treated with the proper amounts of elements like Ti, V, Ta etc. which strongly combine with carbon and nitrogen, show practically no aging.

It is still not possible to conclude with certainty, whether oxygen is a cause of strain-aging or not. Since, according to Low and Gensamer, the oxygen content did not diminish during the treatment with moist hydrogen, though the ability to strain-aging disappeared, their conclusion that oxygen is no cause seems fairly well justified. According to Daniloff, Mehl and Herty 53) silicon killed steels show less strain-

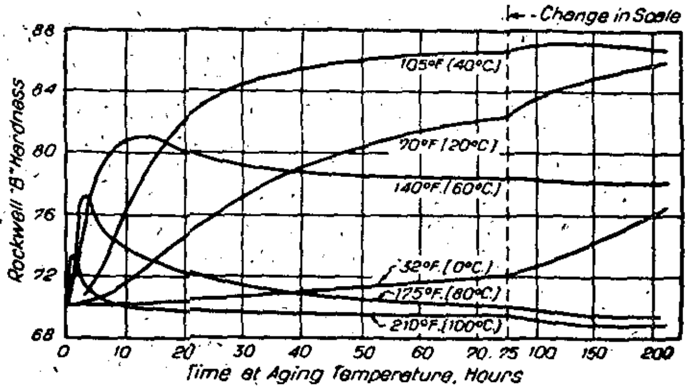

Fig. 15.

Quench aging. of 0,06 per cent carbon steel, No. 1. Hardness after quenching from 1325 degrees Fahr. (720 degrees cent.) and aging at the various indicated temperatures; plotted on linear time scale. [Davenport and Bain 45)].

aging than do rimmed steels, but their data are not very convincing. Davenport and Bain found that electrolytic iron, which was intentionally saturated with oxygen and which contained hardly any carbon and nitrogen, was rather liable to strain-aging. This, however, is the only case known to the author, in which the aging cannot be attributed with the same right to the presence of carbon and nitrogen.

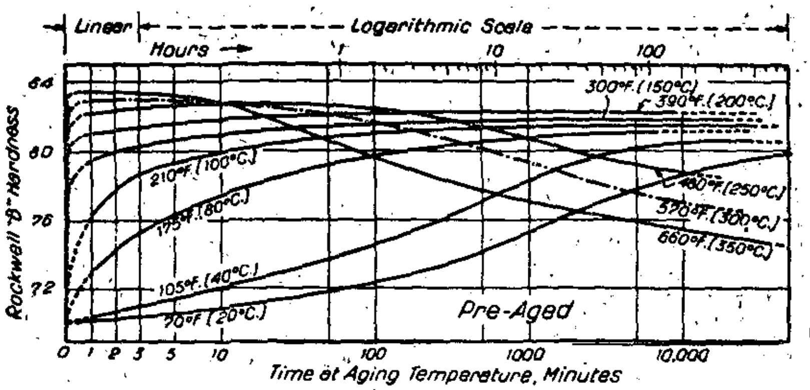

Fig. 16.

Strain aging of steel, hardness after cold-rolling followed by aging at the various indicated temperatures; all pre-aged before cold rolling. [Davenport and Bain 45)].

(Eilender, Cornelius and Menzen 56), likewise conclude from their investigations that blue brittleness, which is nothing else but a manifestation of aging during straining, as has already been pointed out by Fettweiss 57), is caused by nitrogen and not by oxygen. Carbon and nitrogen may therefore be regarded as the only causes of quench-aging strain-aging *).

Köster 43) in particular has accurately investigated the effect of quench-aging on the mechanical properties of mild steel. Fig. 15 represents the relation between the hardness at room temperature and the time of heating at different temperatures after quenching from 720° C, as has been observed by Davenport and Bain 45), in agreement with Köster. The tensile strength principally behaves similarly, whilst the elongation and reduction of ares show the opposite. It is obvious from the results of these investigators that the maximum hardness decreases with increasing temperature. Already at 200° C no maximum is attained at all, but the hardness decreases at once. At 40° C superaging already occurs after about one day. The decrease in the maximum might be explained as follows: The true size of the precipitated particles will show a greater scatter from the mean size as the temperature and in consequence the diffusion rate is higher. As the scatter at the same mean size of the particles is greater the hindrance in the glide planes and consequently the resistance to deformation is lower.

The relation between the hardness at room temperature and the time of aging at several temperatures, with steel that has been plastically deformed, has been investigated by Köster 58), Köckritz 59), Davenport and Bain 45). The data of Davenport and Bain, which are fundamentally in accordance with those of the first-mentioned investigators, are represented in fig. 16. According to Köster the behaviour of the tensile strength is similar, whilst the elongation again shows the opposite effect. From fig. 16 it is evident now that the max-

*) Conclusions, based on the available data obtained with the impact test are of less value, because either the influence of the plastic deformation itself is fully neglected, or the impact values are estimated at room temperature only. To attain a clear picture of the liability to aging from the impact test, it is at least necessary to determine the relation between impact value and temperature in the range from brittle to ductile fracture in the original state of the steel, and also after deformation and after aging separately. This question will be considered more detailed in a subsequent paper.

imum in the hardness does not diminish with increasing temperature, but remains practically the same, or even slightly increases, at least up to 350° C. At 200° C, where on quench-aging no maximum at all occurs, hardly any over-aging is perceptible, even after prolonged heating. At 350° C over-aging still proceeds rather slowly. This behaviour fully corresponds to the behaviour on straining in the blue brittle range, as will be elucidated in more detail in the next section.

The above-mentioned data indicate without any doubt that the mechanism of aging after quenching is fundamentally different from the mechanism of aging after straining, so that the phenomenon of strain-aging cannot be interpreted at all on the basis of a precipitation theory, like the phenomenon of quench-aging. The investigations of Köster, Davenport and Bain and Andrew and Trent 47) clearly show that the precipitation of iron carbide and iron nitride from supersaturated undeformed ferrite, thus the diffusion of carbon and nitrogen in ferrite, occurs at a relatively high velocity even at room temperature. The yield phenomenon itself and the return of the yield phenomenon during strain-aging lead to the same conclusions. It is therefore very unlikely that steel which has been cooled in air, or more slowly, after rolling or annealing at high temperature, still contains some carbon and nitrogen in supersaturated solution. When soft steel, cooled in air is heated slightly above room temperature, the hardness and the tensile strength do not increase. On the contrary, these quantities directly decrease or at most remain unchanged. This means that during cooling the precipitated particles have already obtained the state of overcritical dispersion, as far as the mechanical properties are concerned. On heating magnetic aging indeed occurs, since the maximum magnetic aging effect is just attained at a much greater size of the particles, as has been shown by Köster 52).

It is generally accepted that plastic deformation will stimulate precipitation reactions. Since, apart from exceptional cases, the precipitation has already occurred and reached an overcritical state previously, only a further growth of these particles will be stimulated. Köster's 52) investigations on the precipitations in mild steel with the aid of Fry's etching method indeed support this view. After some hours heating at 100° C fine particles of iron nitride could be observed in the flow lines of plastically deformed Thomas steel with 0,021 % N. At the same time the precipitation in the undeformed regions was still very slight.

When the steel, however, was heated during a long period at 100° C, finally, in about a week, the precipitation in the undeformed regions became as strong as in the flow lines and the test piece was equally darkened by the etching reagent. Incorrectly and in contradiction to the observations already mentioned. Köster himself concluded that the nitride particles were precipitated from supersaturated solution, instead of growing from submicroscopical supercritical particles already present before plastic deformation and heat treatment. From the fact, however, that the stabilized steel was as liable to strain aging as the steel in the original state, Köster rightly concluded that this precipitation was not related to the real mechanism of strain aging. Davenport and Bain obtained the data, shown in fig. 16, with a steel which was stabilized by heating at 100° C during 17 hours and which in consequence contained no supersaturated carbon and nitrogen able to cause aging by precipitation. Still more convincing in this respect are the results of the following investigation. A sheet of normalized, rimmed S. M. steel, with approx. 0,1 % C, was divided in a great number of strips, in which the profile of a tensile test piece was made beforehand. Previous to the aging test, one series of strips was heated during 60 days at 100° C to make precipitation as complete as possible. The other series remained untreated. Strips of both series were put an increasing number of

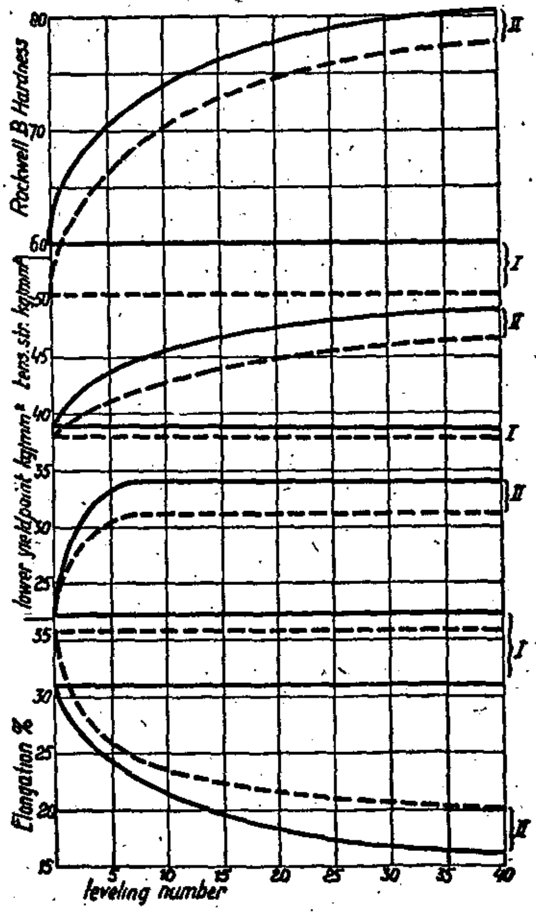

Fig. 17.
Effect of roller levelling (I) and alternate roller levelling and aging (II) (6 h. at 100° C) on the mechanical properties of non-stabilized (———) and stabilized steel (— — —) (60 days at 100° C).

times through a roller leveling machine and within 10 minutes after that subjected to the tension test. The other strips of both series were alternatively leveled and heated six hours at 100° C in the same sequence and then tested. Prolonged heating had hardly any influence. Fig. 17 shows the effect of these treatments on the mechanical properties of the steel. The strain-hardening effect of roller leveling was practically zero (as far as the mechanical properties before aging are concerned). The difference in properties of the strips after deformation and after deformation and aging is therefore exclusively due to the aging effect. It is now obvious from fig. 17 that the liability to strain aging is about the same for steel in the original state and in the stabilized state. With the exception of the lower yield point, which behaves to some extent divergently, the corresponding curves merely show a difference in level due to stabilizing. These results clearly indicate that the strain-aging phenomenon cannot be explained on the basis of the precipitation theory. The supposition that even after an alternating treatment of roller leveling and six hours heating at 100° C up to 40 times, preceded by 60 days heating at 100° C, still some carbon or nitrogen might be in supersaturated solution to cause aging, is untenable. The effect of stabilizing therefore only exists in a further growth of the precipitated particles.

The precipitation theory is still more untenable if we consider the aging effect during straining at high temperatures (blue brittleness). There is not the slightest argument to suppose that any precipitation can take place in this range. On the contrary, elements which are precipitated at room temperature will just go into solution.

The mechanism of strain aging.

Since strain aging cannot be caused by precipitation of carbon and nitrogen, this phenomenon must be attributed, in the author's opinion, to alteration in the state of equilibrium of these atoms in the lattice. As is generally assumed, the crystals of a metal are divided during plastic deformation in smaller fragments, which are only elastically deformed. In the small zones between those fragments, the atoms cannot occupy the normal lattice positions and consequently the lattice is locally in a more or less imperfect state. To explain the initial absence of the yield phenomenon of plastically deformed steel, the assumption was made that the fragments are elastically deformed to such an extent that the state of unlocking just remains maintained. It is plausible now that the deformation of the fragments decreases on storage at room temperature and still more easily at higher temperatures. This will cause a restoration of the state of locking and in consequence the yield phenomenon will return. Since the imperfect zones are thermodynamically less stable than the fragments, it is very probable that the solubility of carbon and nitrogen in the imperfect zones is also greater. The consequence will be that the carbon and nitrogen contents of the imperfect zones, which come into existence during plastic deformation, will try to increase. As has been shown in the preceding pages the diffusion rate of carbon and nitrogen is relatively high, even at room temperature. It is therefore probable that the increase of the resistance to deformation during aging is due to stiffening of the imperfect zones by the increasing contents of carbon and nitrogen. Though the return of the yield phenomenon and the alteration of the other properties are thus closely related, the aging mechanism is to some extent different. This might be the reason that the yield phenomenon is more sensitive to aging and also behaves somwhat differently in other respects.

Since the diffusion rate increases with the temperature, the velocity of aging increases with the temperature. As is obvious from fig. 16 the maximum aging effect at room temperature is not fully reached in 100 days. At 200° C however, a few minutes heating is entirely sufficient. Prolonged heating at 250° C causes over-aging, but even at 350° C the over-aging effect is rather small. It is very probable now that over-aging is related with the primary stages of recrystallisation. Though a microscopically visible stage of recrystallisation of mild steel can hardly be obtained at approx. 500° C, it is very well possible that the formation of nuclei with a perfect lattice will already start in the strongest distorted regions at approx. 250° C. Consequently, the concentration of carbon and nitrogen in these regions diminishes and overaging occurs. At increasing temperature the recrystallisation occurs at a higher rate and becomes more complete. This is also in full accordance with the increase of overaging with time and temperature. As long as no recrystallization starts, the imperfect zones will not be very strongly affected by the tem-

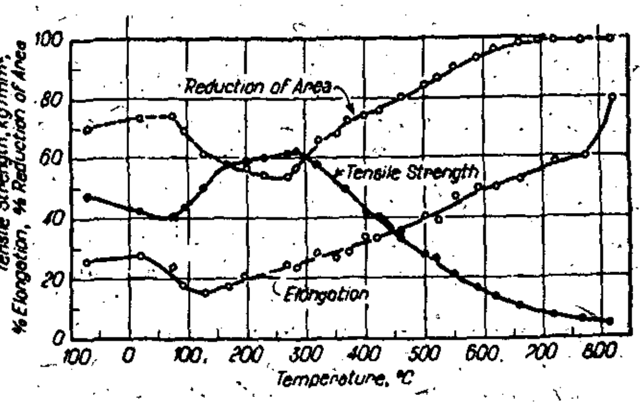

Fig. 18.
Influence of temperature on tensile properties of soft iron. [Reinhold 60)].

perature. Hence, the maximum aging effect will also be fairly independent of the temperature. According to fig. 16 this is indeed observed.

Blue brittleness.

If the plastic deformation is performed at elevated temperature, the resistance to deformation initially decreases in the same way as shown by the plastic metals (fig. 18). The tendency to aging however also increases with increasing temperature. From a certain temperature onwards, dependent on the strain rate, perceptible aging therefore occurs during plastic deformation. In static tension the aging effect becomes already predominant at approx. 80° C. The tensile strength increases and reaches a maximum at 250° C to 300° C. At higher temperature, apart from the normal influence of the temperature itself, overaging

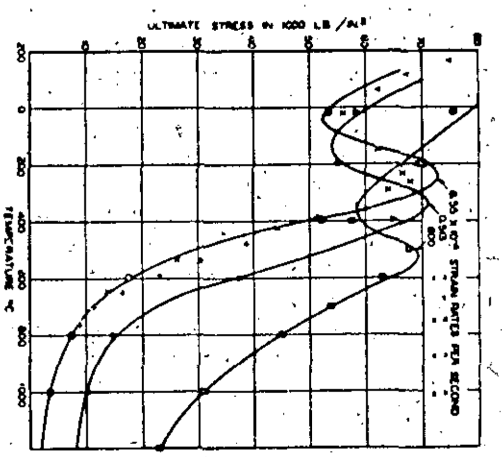

Fig. 19.
Tension tests of mild steel at various temperatures and rates of strain. [Nadaï and Manjoine 63)].

more and more predominates. At approx. 600° C over-aging is apparently complete. As the strain rate increases, the resistance to deformation, apart from the aging effect, increases too. The same stages of aging and overaging likewise are attained at increasing temperatures. This behaviour, already observed by le Chatelier 61) and especially investigated by Körber and Simonsen 62), Manjoine 14) and Nadaï 63), is represented in fig. 19. In tensile and hardness tests a higher temperature than approx. 600° C for the maximum in the curve cannot be attained, even at extremely high strain rates. This, however, is not astonishing, since at this temperature microscopically visible recrystallisation is already possible within a few hours. From fig. 19 it may also be concluded that at very high strain rates a slight aging effect even up to the transition range of ferrite and austenite still occurs.

Quinney 28) and Manjoine 14) have shown that aging during plastic deformation already occurs at room temperature, if the strain rate is extremely low. The minimum in the curve, which represents the relation between tensile strength and temperature (fig. 18 and fig. 19) is then shifted below room temperature. This moreover proves the suggestion of Fettweiss 57) that strain aging and blue brittleness are indeed the same phenomena.
The minimum and the maximum in the tensile strength correspond to a maximum and a minimum in the elongation already occur at somewhat lower temperatures. This is apparently due to a deviation in the behaviour of the uniform elongation.

As is known, a tensile test bar does not strain absolutely uniformly and in all regions at the same time even in the range before maximum load. Consequently final necking has already started to some extent at a lower load and the uniform elongation remains somewhat lower thans corresponds to the true uniform *elongation of the bar. This behaviour probably* will become more pronounced as the temperature increases, in particular when aging occurs during the test. It might therefore be the cause of the deviation in the temperatures of the corresponding maximum and minimum.

The discontinuous straining of the bar is likewise the cause of the strong fluctuations in the stress during testing at temperatures between approx. 100° C and 300° C (fig. 11). In the zones of the bar where the deformation temporarily stops, the state of locking of the lattice is restored. This results in repeated discontinuous yielding up to the moment that final necking starts. As the yield phenomenon at the transition from the elastic state to the plastic state disappears at approx. 300° C, discontinuous yielding during further straining also disappears.

Kenyon and Burns 37, 64) observed that non-aging steels, which indeed showed no change

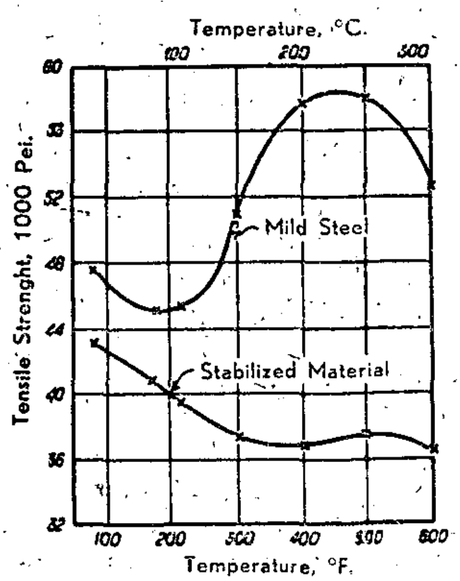

Fig. 20.
Effect of testing temperature on tensile strength of mild steel and new stabilized steel sheets. [Kenyon and Burns 37)].

in the mechanical properties at room temperature after an aging treatment at 100° C, still showed some tendency to aging, when tested in the blue brittle range fig. 20). This may be explained as follows. If the steel is treated with the proper amount of elements, which strongly combine with carbon and nitrogen, the solubility of carbon and nitrogen at room temperature is not sufficient to cause noticeable aging in this range. At increasing temperatures, however, the solubility also increases, so that the ability to aging might still be maintained to some extent in the blue-brittle range. In normal mild steel, the higher solubility of these elements at elevated temperatures certainly plays a role as well. Only after complete decarburizing and de-nitriding, will the steel be free of any tendency to blue-brittleness.

Acknowledgment.

The author wishes to express his sincere thanks to Prof. Dr. Ir. W. F. Brandsma, Department of Metallogy, Technical University, Delft, for his interest shown in the preparation of this paper and for his valuable suggestions; to Prof. Dr. W. G. Burgers, Department of Physical Chemistry, same University, for his sympathetic criticism concerning the author's suggestions on the mechanism of yielding and aging; and to the directors and co-workers of the National Aeronautical Research Institute for indispensable support and assistance.

Samenvatting.

De meest gangbare hypothese ter verklaring van het vloeiverschijnsel in zacht staal, is gebaseerd op het bestaan van een netwerk van cementiet of andere afscheidingen op de kristalgrenzen, dat bezwijkt bij een bepaalde critische spanning. Een nadere beschouwing van de bekende gegevens leidt echter tot de conclusie dat niet het cementiet of enig ander bestanddeel dat als afzonderlijke fase aanwezig is, de oorzaak is, maar dat dit verschijnsel moet worden toegeschreven aan koolstof en stikstof die in het ferriet zelf zijn opgelost. Een nieuwe hypothese is naar voren gebracht, waarbij is aangenomen dat de glijvlakken van het ferriet geblokkeerd worden door de opgeloste koolstof- en stikstofatomen, zolang een critische elastische deformatie van het rooster niet is bereikt. Deze hypothese is ontwikkeld uit Snoek's theorie van de elastische nawerking, volgens welke de koolstof- en stikstofatomen zich in een ongelijke verhouding zullen verdelen over de hoofdrichtingen van het kristalrooster, als dit is onderworpen aan een deformatie, die niet in alle richtingen gelijk is. De verandering in de verdeling van de koolstof- en stikstofatomen, die tot stand komt door een zuiver diffusieproces, zal eveneens een verlaging van de weerstand tegen deformatie op de glijvlakken veroorzaken. Dientengevolge begint het vloeien bij een hogere, critische schuifspanning en gaat daarna vooreerst bij een lagere spanning verder. Aan de hand van de conventionele trekkromme is toegelicht dat met behulp van deze hypothese het vloeiverschijnsel in vele opzichten bevredigend kan worden verklaard. Vooral de grote gevoeligheid van de vloeigrenzen voor de reksnelheid is in overeenstemming met de veronderstelling dat een diffusieproces bij dit verschijnsel een rol speelt. De aanvankelijke afwezigheid van het vloeiverschijnsel in plastisch gedeformeerd staal is toegeschreven aan de blijvend elastische deformatie van de kristalfragmenten, veroorzaakt door de interne spanningen. Het wederoptreden van het vloeiverschijnsel na langer verblijf bij atmosferische of hogere temperaturen is daarom toegeschreven aan een verlaging of opheffing van deze interne spanningen, waardoor de geblokkeerde toestand van het rooster wordt hersteld.

Verder is verduidelijkt, dat de mechanische veroudering en het identieke verschijnsel der blauwbrosheid, niet, zoals de afschrikveroudedering, wordt veroorzaakt door submicroscopische afscheiding van ijzercarbide, -nitride of -oxyde in het ferrietrooster. Dit blijkt uit het essentiële verschil in gedrag van staal bij afschrik- en mechanische veroudering. Oververzadiging en dientengevolge afscheiding is in het bijzonder wel uitgesloten in het temperatuurgebied der blauwbrosheid. Mechanische veroudering is daarom eveneens toegeschreven aan koolstof en stikstof die in het ferriet zijn opgelost. De oplosbaarheid van deze elementen is groter in de verstoorde zones tussen de kristalfragmenten dan in de slechts elastisch vervormde kristalfragmenten zelf, zodat de concentratie in deze zones toeneemt gedurende het verouderingsproces. Verondersteld wordt dat dit de oorzaak is van de verhoogde weerstand tegen plastische deformatie. In dit verband is de over-veroudering toegeschreven aan de vervorming van kernen met perfect rooster in de verstoorde zones, gedurende het primaire stadium der rekristallisatie.

References.

1 A. Nadai. Zeitschr. Techn. Phys. 5 (1924) p. 369.

2 A. Nadai. Plasticity. Mac Graw Hill Book Comp. New York, London.

3 P. Ludwik and R. Scheu. Ber. Werkstoffaussch. des Ver. Deutscher Eisenh. leute no. 70 (1925).

4 P. Ludwik. Zeitschr. Ver. Deutsch. Ing. 70 (1926) p. 379.

5 M. Kuroda. Scientif. Pap. of the Inst. of Phys. and Chem. Research. Tokyo Vol. 34 Part III (1938) p. 1528.

6 C. A. Edwards, H. N. Jones and B. Walters. Journ. Iron and Steel Inst. (1939) no. I p. 341.

7 C. A. Edwards, D. L. Phillips and H. N. Jones. Journ. Iron and Steel Inst. (1940) no. II p. 199.

8 K. Dies. Archiv. Eisenhüttenwes. 16 (1942/44) p. 333.

9 C. Zener and J. H. Hollomon. Trans. Am. Soc. Metals 33 (1944) p. 163.

10 C. A. Edwards, D. L. Phillips and Y. H. Liu. Journ. Iron and Steel Inst. (1943) I p. 145.

11 J. R. Low and M. Gensamer. Metals Technology. Techn. Paper no. 1644 December 1943.

12 F. Fettweiss. Archiv Eisenhüttenwes. 6 (1932/ '33) pag. 149.

13 J. Winlock and R. W. E. Leiter. Trans. Am. Soc. Metals 25 (1937) p. 163.

14 M. J. Manjoine. Journ. Applied Mechanics 11 (1944) p. A 211.

15 J. L. Snoek. Chemisch Weekblad 29 (1942) 454.

16 *J. L. Snoek. New Developments in* Ferromagnetic Materials. Monographs on the Progress of Research in Holland, Elsevier Publishing Comp. Inc. Amsterdam, New York.

17 G. F. Comstock. Proc. Am. Soc. Test. Mat. 43 (1943) p. 521.

18 G. F. Comstock. Trans. Am. Soc. Metals 34 (1945) p. 425.

19 M. Moser. Stahl und Eisen 46 (1928) p. 1601 and 47 (1929) p. 468.

20 F. Körber. Internationaler Kongress für die Materialprüfungen der Technik, Amsterdam 1927 p. 39.

21 W. Kuntze and G. Sachs. Zeitschr. Ver. Deutsch. Ing. 72 (1928) p. 1011.

22 C. W. Mac Gregor. Trans. Am. Soc. Mech. Eng. 53 (1931) p. 187.

23 E. A. Davis. Journ. of Appl. Mech. 6 (1938) p. A 137.

24 A. Kühnel. Zeitschr. Ver. Deutsch. Ing. 72 (1928) p. 1226.

25 F. Körber and A. Pomp. Mitt. K. Wilh. Inst. Eisenforsch. 16 (1934) p. 179.

26 C. F. Elam. Proc. Roy. Soc. Lond. 165 Series A No. 923 (1938) p. 568.

27 J. L. M. Morrison. Engineer 158 (1934) p. 183.

28 H. Quinney. Engineer 157 (1934) p. 332 and 161 (1936) p. 669.

29 I. G. Docherty and F. W. Thorne. Engineering 132 (1931) p. 295.

30 C. Bach and B. Baumann. Festigkeitseigenschaften und Gefügebilder der Konstruktions-Materialiën. Springer. Berlin 1921.

31 E. Siebel and S. Schwaigerer, Archiv. Eisenhüttenwes. 11 (1937/38) p. 319.

32 A. Krisch. Archiv. Eisenhüttenwes. 11 (1937/38) p. 323.

33 H. Esser. Archiv. Eisenhüttenwes. 11 (1937/38) p. 327.

34 G. Welter. Metallwirtsch. 14 (1935) p. 1043.

35 J. Miclowitz. Journ. Appl. Mech. 14 (1947) p. A 21 and p. A 31.

36 F. Körber and A. Pomp. Mitt. K. Wilh. Inst. Eisenforsch. 9 (1927) p. 339.

37 R. L. Kenyon and R. S. Burns. Proc. Am. Soc. Test. Mat. 34 (1934) p. 48.

38 E. Maurer and R. Mailänder. Stahl u. Eisen 45 (1925) p. 409.

39 R. H. Greaves and J. A. Jones. Journ. Iron and Steel Inst. Vol. 112 II (1925) p. 121.

40 H. Bennek. Archiv. Eisenhüttenwes. 16 (1942/ '44) p. 307.

41 D. J. Mac Adam Jr. and R. W. Mebs. Proc. Am. Soc. Test. Mat. 43 (1943) p. 661.

42 D. E. Pfeil. Journ. Iron and Steel Inst. Vol. 118 II (1928) p. 167.

43 W. Köster. Archiv. Eisenhüttenwes. 2 (1928/'29) p. 503.

44 A. Krüger. Archiv. Eisenhüttenwes. 3 (1929/'30) p. 721.

45 E. S. Davenport and E. C. Bain. Trans. Am. Soc. Metals 23 (1935) p. 1047.

46 G. Masing. Archiv. Eisenhüttenwes. 2 (1928/'29) p. 185.

47 J. H. Andrew and E. M. Trent. Journ. Iron and Steel Inst. II (1938) p. 241.

48 T. D. Yensen. Journ. Am. Inst. Eelectr. Eng. (1924) p. 455.

49 J. H. Whiteley. Journ. Iron a Steel Inst. II (1927) p. 293.

50 A. Fry. Kruppsche Monatsheft 4 (1923) p. 137.

51 E. W. Ehn. Metal Progress 19 (1931) p. 59.

52 W. Köster. Archiv. Eisenhüttenwes. 3 (1929/'30) p. 637.

53 B. N. Daniloff, R. F. Mehl and C. H. Herty. Trans. Am. Soc. Metals 24 (1936) p. 595.

54 W. Eilender and R. Wasmuth. Archiv. Eisenhüttenwes. 3 (1929/'30) p. 659.

55 W. Eilender, A. Fry and A. Gottwald. Stahl u. Eisen 54 (1934) p. 545.

56 W. Eilender, P. Cornelius and P. Mensen. Archiv. Eisenhüttenwes. 14 (1939/'49) p. 217.

57 F. Fettweiss. *Stahl u. Eisen 39 (1919) p. 1 and* p. 34.

58 W. Köster. Archiv. Eisenhüttenwes. 6 (1932/'33) p. 55.

59 H. Köckritz. Mitt. Forsch. Inst. der Vereinigte Stahlwerke, Vol. 2 no. 9 (1932).

60 O. Reinhold. Ferrum 13 (1917) p. 97.

61 H. le Chatelier. Revue de Metallurgie 6 (1909) p. 915.

62 F. Körber and J. B. Simonsen. Mitt. K. Wilh. Inst. Eisenf. V (1924) p. 21.

63 A. Nadai and M. J. Manjoine. Journ. Appl. Mech. 9 (1941) p. A 77.

64 R. L. Kenyon and R. S. Burns. Trans. Am. Soc. Metals (1940) p. 292—313.

Completed: December 1947

CCL Class. C 471 : C 740

REPORT S. 341

Experimental Investigation of the Post-Buckling Behaviour of Flat Plates Loaded in Shear and Compression.[1])

by

Prof. Dr Ir A. VAN DER NEUT and IR W. K. G. FLOOR

Contents.

N.B. *The comparison of experimental and theoretical results discussed in section 6, was sponsored by the Netherlands Aircraft Development Board.*

1 Introduction.

Plates loaded beyond their buckling stress are common structural elements in aeroplane structures. The buckling of thin sheet metal plates may be prevented by a system of closely spaced stiffeners. Except for very large aircraft such dense stiffening would result in uneconomic structures; therefore, stiffeners are usually spaced such that plates will buckle at stresses which are too low to be acceptable as ultimate stresses in aeroplane structures. The application of these lightly stiffened plates is based upon the fact, that the structure will take a considerable load in excess of the buckling load of the plate.

A theory of the post-buckling behaviour of thin plates was presented by H. WAGNER in 1929 (*ref.* 1). He assumed, that the plate can take no compressive stresses, each element being loaded in tension. In this way a plate stiffened in two directions can carry shear load; buckles are formed in a direction intermediate between the directions of the stiffeners. This state of stress corresponds to the actual stress distribution when the ratio between the shear load and the buckling load is infinite and the phenomenon is known as the *complete tension field.* Under actual conditions the ratio between the load and the buckling load is finite and the stresses in the plate, though mainly tensile, will also have compressive components. This state of stress is called the *incomplete tension field.* When the load is a compressive load parallel to one system of stiffeners the tensile stresses are not dominant; the problem connected with this type of load is known as the *effective-width* problem and has been extensively investigated. The load system of shear, parallel to the stiffeners, eventually combined with compression in the direction of the stiffeners, has been investigated less extensively. The tests which are reported here are meant to contribute to the knowledge about the incomplete tension field.

The complexity of this problem, due to the multitude of parameters involved, necessitates aircraft designers to apply the general knowledge just for an initial determination of the dimensions. Then definite conclusions on the strength and stiffness are determined from ad-hoc tests on a section of the structure or on a complete structure. This paper will not obviate this procedure, since many of the factors involved have been left out

---

[1]) Full version of a paper presented at the 7th International Congress of Applied Mechanics, September 1948. An abbreviated version will be published in the Proceedings of the Congress.

of consideration; it is, however, hoped that it will help to reduce the gap between the general knowledge about the post-buckling behaviour of stiffened plates and the prediction of strength and stiffness of actual structures.

The test programme was developed by the National Aeronautical Research Institute in 1940 and the tests were completed about 1946. At that time, the only fundamental experimental investigation was that of R. LAHDE and H. WAGNER (*ref.* 2) on long plates having clamped edges. Since in actual structures the restraint given by the stiffeners is far from complete, particularly with stiffeners of open cross section having small torsional stiffness, tests on plates having supported edges will give a better approximation of actual conditions. Therefore, our test programme was arranged for plates having supported edges.

The available theoretical knowledge of the incomplete tension field was confined to the theory of A. KROMM and K. MARGUERRE (*ref.* 3), this theory dealing with the infinitely long plate having supported edges. The approximative character of this solution, originating from the assumed wave form, is apparent from the fact that it does not result in WAGNER's solution for the complete tension field for the limiting condition $\frac{\gamma}{\gamma_{cr}} = \infty$. This result is not surprising, since the assumed wave form agrees with the wave form at the critical load, whereas the amplitude of the waves in the complete tension field is constant along the crest of the tension buckle. Therefore, the theory of *ref.* 3 seemed to be reliable only for loads not far beyond the critical load. The object of the tests was among others to determine the limits of the reliability of this theory.

Considerable theoretical progress is due to W. T. KOITER (*ref.* 4) who, simultaneously, attempted a theoretical investigation at the National Aeronautical Research Institute in 1944.

This theory deals with the infinitely long plate which is supported or clamped at the edges; numerical evaluation of his theory was mainly confined to the case of the supported edges. KROMM and MARGUERRE introduced in their approximative solution 3 parameters: the wave amplitude, the wave length and the direction of the waves. KOITER accepted the same scheme, but in addition he made allowance for the change of the wave form in the direction of the wave crest with increasing $\frac{\gamma}{\gamma_{cr}}$. Following Cox's proposal (*ref.* 5), KOITER assumed that the wave form in the direction of the wave has a constant amplitude over a certain width in the middle of the plate; in the edge strips the amplitude falls off to zero in an appropriate manner consistent with the edge conditions. The width of constant amplitude is the fourth parameter. For γ_{cr} nearly equal to unity, KOITER's solution corresponds essentially to the solution given by KROMM and MARGUERRE. For $\frac{\gamma}{\gamma_{cr}} = \infty$ KOITER's theory yields WAGNER's solution for the complete tension field. W. K. G. FLOOR has compared the results of the tests (*refs.* 6, 7) with the results of KOITER's theory.

The behaviour of a plate after buckling may be expressed by the relations between the external loads at the edges, the relative displacements of the edges and the stresses in the plate. In actual structures the plate is only part of the structure and the load is taken partly by the plate and partly by the stiffeners. Knowing how the plate behaves under load, it is relatively simple to determine the behaviour of the stiffened plate. The stiffeners participate in the distortion of the edges; therefore the load carried by a stiffened structure under specified edge displacements is equal to the sum of the load carried by the plate and the load carried by the stiffeners under the specified distortions. Consequently, a test programme for the investigation of the behaviour of stiffened plates does not require a variety of relative stiffener cross sections, provided the strain of the edges can be varied. In principle this can be achieved by applying compressive load to the stiffeners. In our tests we applied compressive load parallel to the short sides of the rectangular plates. The application of a normal load in the direction of the long sides would have complicated the test rig too much. It was decided to realize a variety of longitudinal edge strains in an indirect way by means of the compression developed in the stiffeners by the tension field. By varying the stiffness of the stiffeners a variety of edge strains can be attained. There is another reason for this procedure. Usually the load of stiffened plates consists of shear and normal load in the Y-direction of one system of stiffeners; the other system of stiffeners being stressed by the loads induced by the tension field in the X-direction. Therefore, a combination of large ε_1 and small shear stresses will not occur and the task of producing appropriate strains ε_1 may be delegated to the tension field. On the other hand the strain ε_2 is produced by circumstances independent of the shear stress; therefore ε_2 should be applied directly.

Choosing the external normal load parallel to the narrow side of the plate, we aimed at representing the conditions in shear webs of aeroplane wings and in skin panels of wings having no longitudinal stiffeners between the spars. Therefore this investigation does not cover the conditions prevailing in stiffened skins of wings and fuselages, where the normal load is parallel to the long sides of the rectangle. Anticipating the conclusions of this paper, it may be stated that the agreement between theory and tests presumably will hold as well for plates loaded in compression along the long side, so the behaviour of these plates might be determined by means of the theory of *ref.* 4.

2 The parameters of the phenomenon.

The state of stress depends upon the displacements at the edges, i. e. upon the strains ε_1 and ε_2 of the edges and the shear angle γ of the rectangle, and upon the geometry of the plate and the mechanical properties of the material.

The geometry is given by the slenderness ratio a/b of the rectangle and the slenderness of its cross section b/t; the mechanical properties in the elastic region are given by E and ν.

Our tests were confined to the elastic region. Due to the formation of waves, permanent deformation will occur at the faces of the plate where large bending stresses add to the membrane stresses, provided that permanent deformation at the rivet or bolt connections is prevented by giving these connections appropriate strength. It is of particular interest to know under what circumstances the first permanent deformation will occur in the plate. The behaviour in excess of that limit is important mainly in connection with the ultimate load. Since the material yields in bending, it is to be expected that the relation between the membrane stresses and the average strains over the plate thickness will not be affected very much by plastic deformation. The increment of stresses after exceeding the yield load might be estimated in applying WAGNER's theory to the load increment.

It appears from the theory for the infinitely long plate $\left(\frac{a}{b} = \infty\right)$, that in the elastic range the parameters can be reduced to four in number; viz. the ratios of ε_1, ε_2 and γ to the critical shear strain γ_{cr} and POISSON's ratio ν. Since ν is very nearly a constant number for the materials employed, this practically means that the parameters, governing the problem are:

$\frac{\varepsilon_1}{\gamma_{cr}}$, $\frac{\varepsilon_2}{\gamma_{cr}}$ and $\frac{\gamma}{\gamma_{cr}}$ or $\frac{\varepsilon_1}{\gamma}$, $\frac{\varepsilon_2}{\gamma}$ and $\frac{\gamma_{cr}}{\gamma}$.

It is obvious that a rectangular plate and an infinitely long plate having the same γ_{cr}, will not have identical stresses for equal ε_1, ε_2 and γ. So, in fact, the stress distribution in the rectangular plate will depend upon a fourth parameter $\frac{a}{b}$. Now, the effect of $\frac{a}{b}$ upon γ_{cr} is only of secondary importance for $\frac{a}{b} > 3$. Though cases of $\frac{a}{b} \precsim 1$ occur in aircraft structures, we have left these conditions out of consideration and decided to have a constant ratio $\frac{a}{b} = 3.16$ during the whole of the test programme. Thus the results will hold for structures having $\frac{a}{b} > 3$ and in this range the parameters can be assumed to be $\frac{\varepsilon_1}{\gamma}$, $\frac{\varepsilon_2}{\gamma}$ and $\frac{\gamma_{cr}}{\gamma}$.

In view of these parameters the best test procedure would be to run a series of tests for constant $\frac{\varepsilon_1}{\gamma}$ and $\frac{\varepsilon_2}{\gamma}$ over an appropriate range of $\frac{\gamma_{cr}}{\gamma}$. The test rig, however, was such that it gave the distortions as a result of the loads applied. In particular this applies to the way in which ε_1 is obtained.

During each series of tests we aimed at a constant 'nominal' $\frac{\varepsilon_2}{\gamma}$, the actual $\frac{\varepsilon_2}{\gamma}$ depending to some extent upon the post-buckling behaviour of the plate, so we had to accept a gradual change of $\frac{\varepsilon_1}{\gamma}$ and $\frac{\varepsilon_2}{\gamma}$ during each test series. This inconvenience is however not very important, since the test results show so much scatter that a more refined test procedure would not have been worthwhile.

The gradual change of $\frac{\varepsilon_1}{\gamma}$ and $\frac{\varepsilon_2}{\gamma}$ gives another effect, that must be taken into account. The critical strain γ_{cr} is not independent of ε_1 and ε_2; each set of values $\frac{\varepsilon_1}{\gamma}$, $\frac{\varepsilon_2}{\gamma}$ will result in a particular γ_{cr}. Therefore, during each series of tests γ_{cr} will change gradually. This means that the evaluation of the test results cannot be based upon the value of γ_{cr} observed in the lower load range. Moreover, it is practically impossible to determine γ_{cr} from the test due to the initial waviness of the plate. Therefore $\gamma_{cr}\left(\frac{\varepsilon_1}{\gamma}, \frac{\varepsilon_2}{\gamma}\right)$ was evaluated from theoretical considerations.

While evaluating the test results it appeared that under certain circumstances γ_{cr} should be replaced by some other quantity. This occurs when $\frac{\varepsilon_2}{\gamma}$ is large and then the deformation is primarily compression and only secondarily shear. Even the infinitely long plate will buckle under these conditions in one single half wave in the same way as with pure compression without shear. When deformations increase, $\frac{\varepsilon_1}{\gamma}$ and $\frac{\varepsilon_2}{\gamma}$ remaining constant, this type of deformation becomes unstable and will suddenly change over from the compression wave into a wave form of the 'diagonal' type. From KOITER's theory FLOOR calculated for the infinitely long plate the shear γ_o at which the 'diagonal' wave contains less elastic energy than the 'compression' wave. For finite lengths this shear γ_o will not necessarily be the shear at which the compression wave disappears, for it may be that the compression wave will be stable with respect to small disturbances. Nevertheless, the shear γ_o will be the unit for measuring γ as soon as diagonal waves are developing and γ_{cr} loses its physical significance.

This is the reason why $\frac{\gamma_{cr}}{\gamma}$ was dropped as a parameter and replaced by $\frac{\gamma_o}{\gamma}$. For the smaller values of $\frac{\varepsilon_2}{\gamma}$ this change is not essential, since in that case $\gamma_o = \gamma_{cr}$. Evaluating quantities depending primarily on the wave form in the Y-direction $\frac{\gamma_{cr}}{\gamma}$ was retained as a parameter; this method simplified the representation of the test results. In determining γ_o it was assumed that $\frac{\gamma_o}{\gamma_{cr}}$ would be equal for the infinitely long plate and the rectangular plate. The ratio $\frac{\gamma_o}{\gamma_{cr}}$, as calculated in *ref.* 7 from KOITER's theory, is given in fig. 5.8.

In principle the range of $\frac{\gamma_o}{\gamma}$ to be investigated can be covered using only one plate having sufficiently small $\frac{t}{b}$. In this way the stresses at the lower end of the $\frac{\gamma_o}{\gamma}$ range can be kept below the yield stress of the material. This method will have the practical disadvantage that the investigation of the range of $\frac{\gamma_o}{\gamma}$ just below unity involves small strains, which cannot be measured reliably. Besides, the initial waviness of thin plates will greatly influence the deformation in this range.

In order to improve conditions the tests were carried out with 3 ratios of $\frac{b}{t}$, viz. $\frac{b}{t} = 357$ (plate no. 2), $\frac{b}{t} = 167$ (plate no. 1) and $\frac{b}{t} = 118$ (plate no. 3).

The range of load parameters investigated is given in table 2.1.

TABLE 2.1.
Range of the investigations.

$\frac{b}{t}$	ε_1/γ		ε_2/γ		$(\gamma_{cr}/\gamma)^{1/3}$		Number of tests
	min	max	min	max	min	max	
118	0.01	0.06	0	0	0.620	1.005	12
118	0.02	0.07	0.17	0.19	0.490	0.750	13
118	0.04	0.09	0.30	0.31	0.415	0.615	15
118	0.06	0.09	0.45	0.56	0.380	0.595	10
118	0.03	0.09	0.63	0.75	0.390	0.655	9
118	0.04	0.08	1.13	1.83	0.415	0.670	8
118	0.06	0.10	1.54	1.94	0.420	0.655	6
167	0.04	0.12	0.02	0.04	0.310	0.575	8
167	0.08	0.13	0.02	0.05	0.340	0.495	3
167	0.12	0.17	0.03	0.04	0.330	0.460	3
167	0.06	0.20	0.01	0.04	0.320	0.585	4
167	0.05	0.11	0.14	0.25	0.310	0.405	5
167	0.07	0.13	0.15	0.21	0.305	0.395	3
167	0.09	0.17	0.14	0.21	0.295	0.390	3
167	0.09	0.20	0.14	0.20	0.295	0.400	3
167	0.06	0.12	0.19	0.26	0.290	0.385	5
167	0.06	0.13	0.20	0.29	0.285	0.370	3
167	0.09	0.17	0.17	0.26	0.275	0.370	3
167	0.08	0.20	0.17	0.25	0.275	0.390	3
167	0.05	0.11	0.26	0.41	0.265	0.360	5
167	0.02	0.13	0.25	0.41	0.270	0.380	3
167	0.07	0.17	0.24	0.36	0.260	0.360	3
167	0.03	0.20	0.24	0.41	0.260	0.360	3
167	0.04	0.10	0.46	0.65	0.270	0.340	5
167	0	0.04	0.67	0.74	0.290	0.340	2
167	0.01	0.07	0.60	0.72	0.290	0.335	2
167	0.09	0.09	0.67	0.92	0.290	0.335	2
357	0	0.11	—0.01	0.03	0.200	0.680	13
357	—0.03	0.16	—0.02	0	0.255	0.685	6
357	0.02	0.10	0.12	0.17	0.215	0.560	12
357	—0.02	0.14	0.10	0.12	0.235	0.570	8
357	0.02	0.10	0.23	0.31	0.200	0.475	8
357	—0.06	0.13	0.24	0.26	0.205	0.450	7
357	—0.03	0.07	0.34	0.36	0.205	0.465	6
357	—0.08	0.11	0.38	0.42	0.190	0.425	7

3 The quantities to be measured.

For given edge strains ε_1 and ε_2 and shear strain γ, the shear load and the normal loads on both edges of the plate are to be determined. The shear load of the panel follows from the externally applied load.

The ratio between γ and the average shear stress $\bar{\tau}$ yields the effective modulus of rigidity $G' = \frac{\bar{\tau}}{\gamma}$.

The normal forces N_1 and N_2 are important for the determination of the loads in the stiffeners of stiffened plates. These forces or the average normal stresses $\bar{\sigma}_1$ and $\bar{\sigma}_2$ can be computed from the membrane stresses in the plate by:

$$\bar{\sigma}_1 = \frac{N_1}{bt} = \frac{1}{b}\int_{-\frac{b}{2}}^{\frac{b}{2}} \sigma_1 \, dy, \qquad (3.1a)$$

$$\bar{\sigma}_2 = \frac{N_2}{at} = \frac{1}{a}\int_{-\frac{a}{2}}^{\frac{a}{2}} \sigma_2 \, dx \qquad (3.1b)$$

For the determination of the rivet loads it is necessary to know the maximum normal stresses $\sigma_{1\,max}$ and $\sigma_{2\,max}$.

The determination of the stresses in the plate requires a knowledge of the maximum membrane stresses σ_1, σ_2 and τ and of the maximum bending and torsional stresses σ_{b1}, σ_{b2} and τ_b.

Neglecting third-order terms, the membrane stresses are given by

$$\sigma_1 = \frac{E}{1-\nu^2}\left[\frac{\partial u}{\partial x} + \nu\frac{\partial v}{\partial y} + \frac{1}{2}\left(\frac{\partial w}{\partial x}\right)^2 + \right.$$
$$\left. + \frac{\nu}{2}\left(\frac{\partial w}{\partial y}\right)^2\right], \qquad (3.2a)$$

$$\sigma_2 = \frac{E}{1-\nu^2}\left[\nu\frac{\partial u}{\partial x} + \frac{\partial v}{\partial y} + \frac{\nu}{2}\left(\frac{\partial w}{\partial x}\right)^2 + \right.$$
$$\left. + \frac{1}{2}\left(\frac{\partial w}{\partial y}\right)^2\right], \qquad (3.2b)$$

$$\tau = \frac{E}{2(1+\nu)}\left[\frac{\partial u}{\partial y} + \frac{\partial v}{\partial x} + \frac{\partial w}{\partial x}\frac{\partial w}{\partial y}\right], \qquad (3.2c)$$

The bending and torsional stresses are given for $z = \pm\frac{t}{2}$ by

$$\sigma_{b1} = \mp\frac{Et}{2(1-\nu^2)}\left[\frac{\partial^2 w}{\partial x^2} + \nu\frac{\partial^2 w}{\partial y^2}\right], \qquad (3.3a)$$

$$\sigma_{b2} = \mp\frac{Et}{2(1-\nu^2)}\left[\nu\frac{\partial^2 w}{\partial x^2} + \frac{\partial^2 w}{\partial y^2}\right], \qquad (3.3b)$$

$$\tau_b = \mp\frac{Et}{2(1+\nu)}\frac{\partial^2 w}{\partial x \partial y}. \qquad (3.3c)$$

The determination of the stresses requires a knowledge of $u\ (x, y)$, $v\ (x, y)$ and $w\ (x, y)$. It appears that the most direct way to determine the stresses is by measuring the strain at an appropriate number of points. At the commencement of our tests the electrical strain gauge technique was not yet developed, so we had to seek alternative methods. It was decided to make elaborate recordings of the wave form by measuring the slopes $\frac{\partial w}{\partial x}$ and $\frac{\partial w}{\partial y}$ and in addition the deflection w. This method is basically insufficient since the membrane stresses depend upon the plane displacements u and v as well. It will be shown how in spite of this lack of information useful conclusions could be drawn by determining average values.

In view of the results obtained, this method seems to be more appropriate than direct strain measurements. Due to initial waviness, the strains in a particular point will be affected very much by the occasional local eccentricity. In order to arrive at fundamental data on the behaviour of plates, strain gauge measurements would have to be made at a great number of points and the recordings would have to be averaged. This method would be lengthy and would give no more information than a method which by origin can produce only average values.

It will appear from § 4, that the longitudinal edges of the plate have been supported in such a way that they could transmit practically no longitudinal load to the supporting stiffeners. Thus it could be assumed that N_1 or $\bar{\sigma}_1$ is independent of x, and hence

$$\bar{\sigma}_1 = \frac{1}{a}\int_{-\frac{a}{2}}^{\frac{a}{2}} \bar{\sigma}_1 \, dx = \frac{1}{ab}\int_{-\frac{a}{2}}^{\frac{a}{2}}\int_{-\frac{b}{2}}^{\frac{b}{2}} \sigma_1 \, dx dy. \qquad (3.4a)$$

Further it was assumed that the edges $x = \pm\frac{a}{2}$ remain straight, which was practically true due to the large bending stiffness of the lateral stiffeners.

Though the lateral stiffeners were rigidly connected to the plate, it was assumed that N_2 is independent of y as well. As to N_2 it was further assumed that the edges $y = \pm\frac{b}{2}$ would remain straight, which was not guaranteed by the test rig. So the force N_2 has been determined with less certainty than the force N_1, which is acceptable since N_2 is of minor importance.

Under the assumptions made, the average stress $\bar{\sigma}_2$ is given by a formula analogous to (3.4a). The average shear stress $\bar{\tau}$ can be expressed in terms of τ in the same manner. The result of the integrations in (3.4a) etc. is:

$$\bar{\sigma}_1 = \frac{E}{1-\nu^2}\,(-\varepsilon_1 - \nu\varepsilon_2 + \varepsilon_{1p} + \nu\varepsilon_{2p}), \quad (3.5a)$$

$$\bar{\sigma}_2 = \frac{E}{1-\nu^2}\,(-\nu\varepsilon_1 - \varepsilon_2 + \nu\varepsilon_{1p} + \varepsilon_{2p}), \quad (3.5b)$$

$$\bar{\tau} = \frac{E}{2(1+\nu)}\,(\gamma - \gamma_p), \quad (3.5c)$$

where

$$\varepsilon_{1p} = \frac{1}{2ab}\int_{-\frac{a}{2}}^{\frac{a}{2}}\int_{-\frac{b}{2}}^{\frac{b}{2}}\left(\frac{\partial w}{\partial x}\right)^2 dxdy, \quad (3.6a)$$

$$\varepsilon_{2p} = \frac{1}{2ab}\int_{-\frac{a}{2}}^{\frac{a}{2}}\int_{-\frac{b}{2}}^{\frac{b}{2}}\left(\frac{\partial w}{\partial y}\right)^2 dxdy, \quad (3.6b)$$

$$\gamma_p = -\frac{1}{ab}\int_{-\frac{a}{2}}^{\frac{a}{2}}\int_{-\frac{b}{2}}^{\frac{b}{2}}\frac{\partial w}{\partial x}\,\frac{\partial w}{\partial y}\,dxdy \quad (3.6c)$$

are quantities that can be determined from the wave pattern, and the strains are defined by the relative displacements of the edges, ε_1 and ε_2 respectively by the compressive strain of the longitudinal and the lateral stiffeners and γ by the shear strain of the panel.

For the determination of σ_1, σ_2 and τ it is again assumed that σ_1 is independent of x, and that σ_2 is independent of y; then τ is constant over the whole plate.

Hence

$$\sigma_1\,(y) = \frac{1}{a}\int_{-\frac{a}{2}}^{\frac{a}{2}}\sigma_1\,dx, \quad (3.7a)$$

$$\sigma_2\,(x) = \frac{1}{b}\int_{-\frac{b}{2}}^{\frac{b}{2}}\sigma_2\,dy, \quad (3.7b)$$

$$\tau = \bar{\tau}. \quad (3.7c)$$

The integrals of σ_1 and σ_2 taken over x and y respectively will contain the terms

$$\frac{\nu E}{1-\nu^2}\int_{-\frac{a}{2}}^{\frac{a}{2}}\left[\frac{\partial v}{\partial y} + \frac{1}{2}\left(\frac{\partial w}{\partial y}\right)^2\right]dx$$

and

$$\frac{\nu E}{1-\nu^2}\int_{-\frac{b}{2}}^{\frac{b}{2}}\left[\frac{\partial u}{\partial x} + \frac{1}{2}\left(\frac{\partial w}{\partial x}\right)^2\right]dy,$$

which cannot be determined from the measurements as far as u and v are concerned. These rather small terms have been approximated by their mean values taken over y and x respectively, yielding

$$\sigma_1\,(y) = \frac{E}{1-\nu^2}\left\{-\varepsilon_1 - \nu\varepsilon_2 + \frac{1}{2a}\int_{-\frac{a}{2}}^{\frac{a}{2}}\left(\frac{\partial w}{\partial x}\right)^2 dx + \nu\varepsilon_{2p}\right\}, \quad (3.8a)$$

$$\sigma_2\,(x) = \frac{E}{1-\nu^2}\left\{-\nu\varepsilon_1 - \varepsilon_2 + \frac{1}{2b}\int_{-\frac{b}{2}}^{\frac{b}{2}}\left(\frac{\partial w}{\partial y}\right)^2 dy + \nu\varepsilon_{1p}\right\}. \quad (3.8b)$$

The bending and torsional stresses (3.3) may be determined from w only. This method proved to be rather complicated and tedious. A more straightforward method was adopted, giving results that agreed well with the exact method. The approximative character of this method seems to be justified also by the approximation introduced in determining the membrane stresses. The approximation consisted in the assumption that the wave form could be approximated by

$$w = f\cos\frac{\pi y}{b}\cos\frac{\pi}{L}\,(x - my).$$

The maximum stresses occur at $x = y = 0$. Then (3.3) yields:

$$\sigma_{b1} = \pm\frac{E}{1-\nu^2}\,(\varepsilon_{1b} + \nu\varepsilon_{2b}), \quad (3.9a)$$

$$\sigma_{b2} = \pm\frac{E}{1-\nu^2}\,(\nu\varepsilon_{1b} + \varepsilon_{2b}), \quad (3.9b)$$

$$\tau_b = \mp\frac{E}{2(1+\nu)}\,\gamma_b, \quad (3.9c)$$

where

$$\varepsilon_{1b} = \frac{\pi^2 ft}{2L^2}\,;\quad \varepsilon_{2b} = \frac{\pi^2 ft}{2L^2}\left(m^2 + \frac{L^2}{b^2}\right);$$
$$\gamma_b = \frac{\pi^2 ft}{L^2}\,m. \quad (3.10)$$

Therefore the determination of these stresses requires the measurement of the amplitude f, the half-wave length L in the direction of x and the cotangent m of the angle between the waves and the direction of x.

Recapitulating, *the quantities to be measured* are:

1. *the relative displacements of the edges,* to be expressed in terms of the longitudinal strain ε_1, the lateral strain ε_2 and the shear strain γ;
2. *the slopes* $\frac{\partial w}{\partial x}$ and $\frac{\partial w}{\partial y}$ *of the plate;*
3. *the amplitude* f, *the half-wave length* L and *the direction* m *of the waves.*

4 The test specimen and the measuring apparatus.

The realization of hinged edges, in contrast to *clamped edges, presents some serious difficulties,* which have been solved in the following way. The test section forms the middle bay of a beam with a shear web, consisting of 5 bays (fig. 4.1).

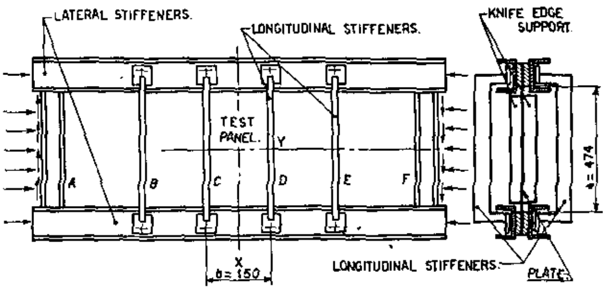

FIGURE 4.1.
Test specimen.

The shear load is applied to the outer bays. Near its ends the web is clamped between two rigid steel stiffeners A and F. The intermediate steel supports B, C, D and E provide a *knife edge* support. Therefore the edge conditions of the outer bays are different from the edge conditions of the three inner bays. In order to compensate for the restraint at A and F the width AB (and EF) is larger than the width of the inner bays. *The ratio* $\frac{\text{AB}}{\text{CD}}$ *has been taken such, that the* critical stress of bay AB, assuming full restraint at A and a hinged support at B, is equal to the critical stress of the bay CD with hinged supports at C and D. This means that near the buckling stress there will be a small interaction between *the first and the second bay. There may be more interaction at higher loads but this positive or* negative restraint at B will be damped out to a negligible amount at C. Therefore bay CD may *be considered to be practically simply supported.*

The short edges of the plate are clamped between two heavy flanges, which means that these ends are rigidly clamped. Since the ratio $\frac{a}{b}$ has been chosen such that the length a is of little importance in determining the behaviour of the plate, the edge conditions here are likewise unimportant.

The supporting members A to F inclusive do not fix the distance between the spar flanges. The task of the longitudinal stiffeners in connecting *the flanges together and maintaining their distance* is delegated to separate steel members, which are connected to the plate as shown in fig. 4.1. Changing these members gives a variety of stiffeners, and hence of $\frac{\varepsilon_1}{\gamma}$.

The spar was loaded by a special rig in shear and compression, such that the bending moment in the plane of the spar would be zero in the centre between C and D.

The *measurements were restricted mainly* to the centre panel. The strain ε_1 was obtained from dial gauges which measured the change of distance between the spar flanges; the strain ε_2 was measured by Huggenberger *tensometers* attached to the spar flanges. The shear strain γ was measured by a dial gauge in the manner

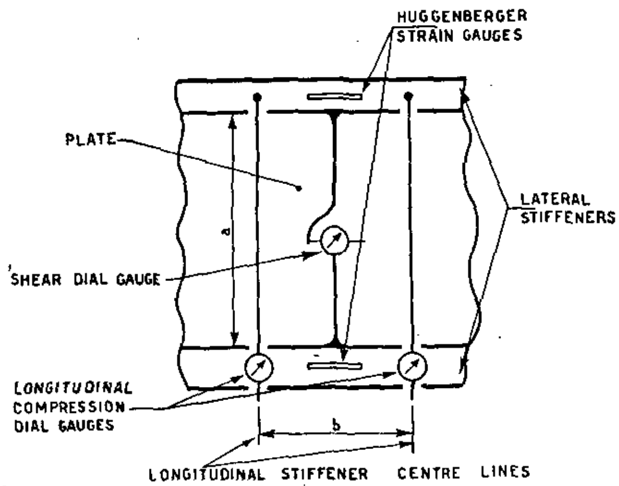

FIGURE 4.2.
Instruments for the measurement of ε_1, ε_2, γ *at the test panel.*

indicated in fig. 4.2. The slopes $\frac{\partial w}{\partial x}$ were recorded at the longitudinal cross sections $y = \pm\ 10\ n$ mm, $n = 0$ to 5 inclusive and the slopes $\frac{\partial w}{\partial y}$ were recorded at the lateral cross sections $x = \pm\ (22 + 30\ n)$ mm, $n = 0$ to 5 inclusive. The slope recorder (fig. 4.3, *ref.* 8) measured the relative movement of two feelers, 10 mm apart, each of which followed the surface of the plate. This instrument was also employed for recording w by fixing the pin carrying the glass scratch plate. In this way the amplitude f was determined.

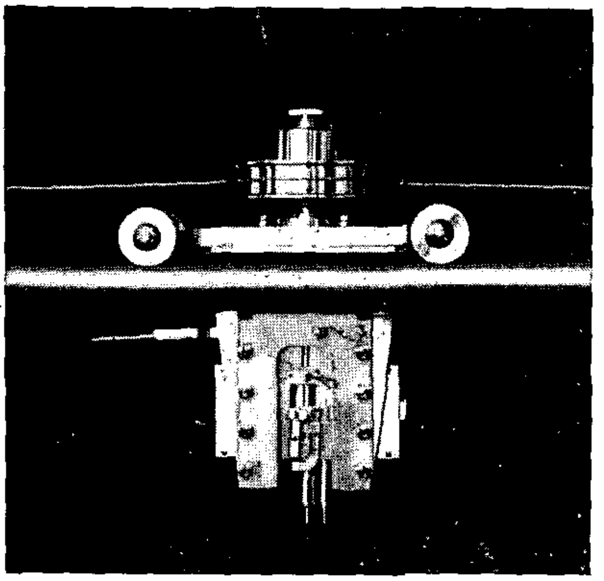

FIGURE 4.3.
Slope recorder.

The recordings gave the half-wave length L as the distance between successive intersections of the curve $\frac{\partial w}{\partial x}$ and the reference line. From the shift of these points of intersection in successive cross sections y the direction of the waves could be obtained.

The amplitudes of the recorded slope curves were, as a matter of fact, very small, thus hampering the direct evaluation of the recordings. In order to facilitate evaluation the recordings were elliptically enlarged by means of a specially designed enlarger, the principle of operation of which has been indicated in fig. 4.4 (*ref.* 8).

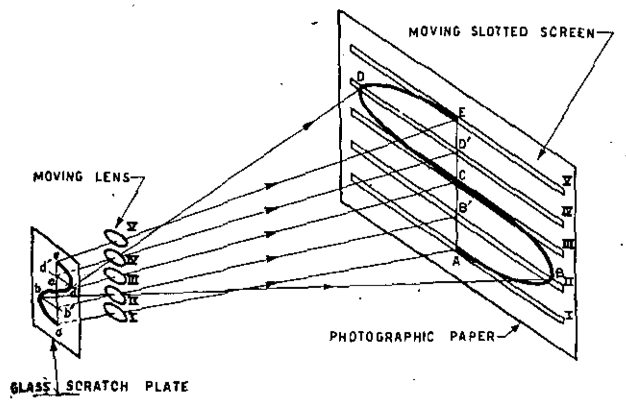

FIGURE 4.4.
Operation scheme of elliptic enlarger.

The maximum magnification in the Z-direction was forty times,but a magnification of twenty times was found convenient and sufficient. In the X- and Y-directions the magnification could be one or two times, the larger magnification being the one used in the evaluation of the results. So the distortion could be up to forty times; usually it was ten times. A record and photograph with a distortion ratio of ten are represented in fig. 4.5.

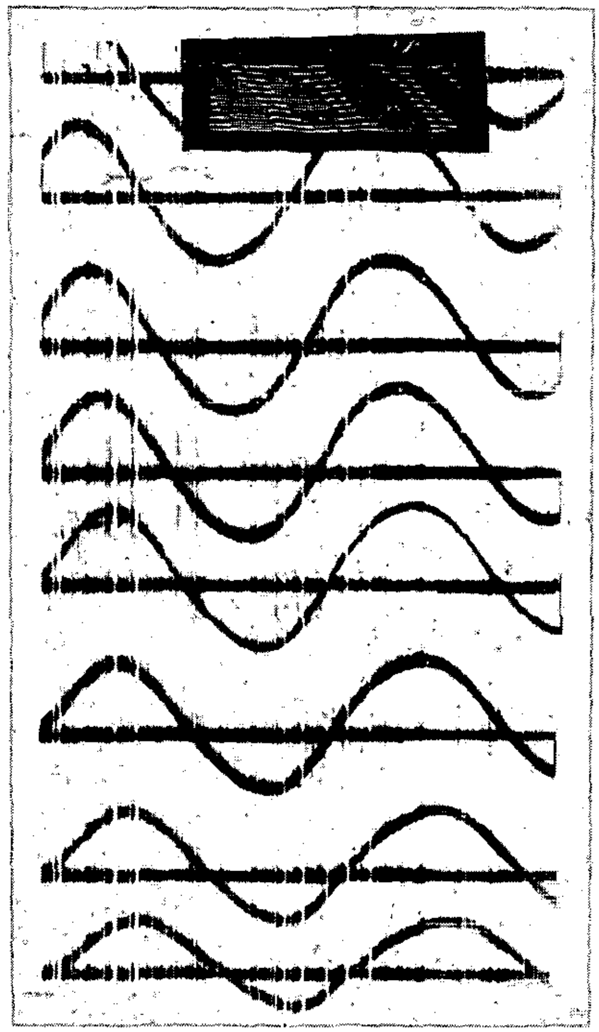

FIGURE 4.5.
Slope recording of a buckled plate and its elliptically enlarged photograph (distortion ratio 20 : 2).

The integrals $\int \left(\frac{\partial w}{\partial x}\right)^2 dx$ and $\int \left(\frac{\partial w}{\partial y}\right)^2 dy$ were computed by an Amsler integrator no. 1 directly from the photographs.

5 The results of the tests.

Since wave formation is the typical feature of the post-buckling behaviour of plates, the tests have been evaluated such that they give information on the functions of w involved in the expressions (3.5), (3.8) and (3.9). The integrals of the slopes included in (3.5) and (3.8) have been expressed in terms of the corresponding quantities for the complete tension field for the same ε_1, ε_2 and γ by means of the coefficients P_{11}, P_{12}, P_{22}. These coefficients will be zero at the critical load and they will be equal to unity for the complete tension field. Thus the coefficients P express the rate of development of the tension field.

The definition of P is:

$$P_{11} = \frac{\varepsilon_{1p}}{e_1}\,, \tag{5.1a}$$

$$P_{12} = \frac{\gamma_p}{g}\,, \tag{5.1b}$$

$$P_{22} = \frac{\varepsilon_{2p}}{e_2}\,, \tag{5.1c}$$

where the quantities e_1, e_2 and g relating to the complete tension field are

$$\frac{e_1}{\gamma} = \frac{\varepsilon_1}{\gamma} + \frac{1}{4}\left\{1 - \frac{\dfrac{\varepsilon_1}{\gamma} + \dfrac{\varepsilon_2}{\gamma}}{\left[1 + \left(\dfrac{\varepsilon_1}{\gamma} - \dfrac{\varepsilon_2}{\gamma}\right)^2\right]^{\frac{1}{2}}}\right\} \times \left\{-(1+\nu)\left(\frac{\varepsilon_1}{\gamma} - \frac{\varepsilon_2}{\gamma}\right) + (1-\nu)\left[1 + \left(\frac{\varepsilon_1}{\gamma} - \frac{\varepsilon_2}{\gamma}\right)^2\right]^{\frac{1}{2}}\right\}, \tag{5.2a}$$

$$\frac{e_2}{\gamma} = \frac{\varepsilon_2}{\gamma} + \frac{1}{4}\left\{1 - \frac{\dfrac{\varepsilon_1}{\gamma} + \dfrac{\varepsilon_2}{\gamma}}{\left[1 + \left(\dfrac{\varepsilon_1}{\gamma} - \dfrac{\varepsilon_2}{\gamma}\right)^2\right]^{\frac{1}{2}}}\right\} \times \left\{(1+\nu)\left(\frac{\varepsilon_1}{\gamma} - \frac{\varepsilon_2}{\gamma}\right) + (1-\nu)\left[1 + \left(\frac{\varepsilon_1}{\gamma} - \frac{\varepsilon_2}{\gamma}\right)^2\right]^{\frac{1}{2}}\right\}, \tag{5.2b}$$

$$\frac{g}{\gamma} = \frac{1-\nu}{2} + \frac{1+\nu}{2}\,\frac{\dfrac{\varepsilon_1}{\gamma} + \dfrac{\varepsilon_2}{\gamma}}{\left[1 + \left(\dfrac{\varepsilon_1}{\gamma} - \dfrac{\varepsilon_2}{\gamma}\right)^2\right]^{\frac{1}{2}}}\,. \tag{5.2c}$$

The integrals included in (3.8) are expressed as multiples λ_1 and λ_2 of the averages ε_{1p} and ε_{2p} by

$$\left[\frac{1}{2a}\int_{-\frac{a}{2}}^{\frac{a}{2}}\left(\frac{\partial w}{\partial x}\right)^2 dx\right]_{\max} = \lambda_1\,\varepsilon_{1p}\,, \tag{5.3a}$$

$$\left[\frac{1}{2b}\int_{-\frac{b}{2}}^{\frac{b}{2}}\left(\frac{\partial w}{\partial y}\right)^2 dy\right]_{\max} = \lambda_2\,\varepsilon_{2p}\,, \tag{5.3b}$$

where λ_1 and λ_2 apply to the maxima of the integrals. In this way the stresses are expressed by

$$\frac{\bar\sigma_1}{\gamma} = \frac{E}{1-\nu^2}\left(-\frac{\varepsilon_1}{\gamma} - \nu\frac{\varepsilon_2}{\gamma} + P_{11}\frac{e_1}{\gamma} + \nu P_{22}\frac{e_2}{\gamma}\right), \tag{5.4a}$$

$$\frac{\bar\sigma_2}{\gamma} = \frac{E}{1-\nu^2}\left(-\nu\frac{\varepsilon_1}{\gamma} - \frac{\varepsilon_2}{\gamma} + \nu P_{11}\frac{e_1}{\gamma} + P_{22}\frac{e_2}{\gamma}\right), \tag{5.4b}$$

$$\frac{\bar\tau}{\gamma} = G' = \frac{E}{2(1+\nu)}\left(1 - P_{12}\frac{g}{\gamma}\right), \tag{5.4c}$$

$$\frac{\sigma_{1\,\max}}{\gamma} = \frac{E}{1-\nu^2}\left(-\frac{\varepsilon_1}{\gamma} - \nu\frac{\varepsilon_2}{\gamma} + \lambda_1 P_{11}\frac{e_1}{\gamma} + \nu P_{22}\frac{e_2}{\gamma}\right), \tag{5.4d}$$

$$\frac{\sigma_{2\,\max}}{\gamma} = \frac{E}{1-\nu^2}\left(-\nu\frac{\varepsilon_1}{\gamma} - \frac{\varepsilon_2}{\gamma} + \nu P_{11}\frac{e_1}{\gamma} + \lambda_2 P_{22}\frac{e_2}{\gamma}\right). \tag{5.4e}$$

In order to account for initial waviness w_o of the plate, ε_{1p} etc. in (3.6a) etc. was replaced by

$$\varepsilon_{1p} = \frac{1}{2ab}\int_{-\frac{a}{2}}^{\frac{a}{2}}\int_{-\frac{b}{2}}^{\frac{b}{2}}\left[\left(\frac{\partial w}{\partial x}\right)^2 - \left(\frac{\partial w_o}{\partial x}\right)^2\right] dxdy \qquad \text{etc.} \tag{5.5}$$

In calculating ε_{1b} etc. it was not possible to account for initial waviness, due to its irregularity and the approximative method of computing ε_{1b} etc. Since these deformations are important only at the higher loads, the contribution of initial waves to the bending stresses is of secondary importance.

P_{11}, P_{12}, P_{22}, λ_1, ε_{1b}, ε_{2b} and γ_b as following from the evaluation of the test results are represented in figs. 5.1 to 5.7 inclusive. As discussed in § 2, P_{22} and ε_{2b} have been given as functions of $\dfrac{\gamma_{cr}}{\gamma}$, whereas the other coefficients have been given as functions of $\dfrac{\gamma_o}{\gamma}$.

The computation of the integral γ_p could not be done by the Amsler integrator and would have been very lengthy. Therefore γ_p was computed from the given shear stress $\bar\tau$ by (3.5c):

$$\gamma_p = \gamma - \frac{\bar\tau}{G}\,. \tag{5.6}$$

To check the reliability of this method, γ_p

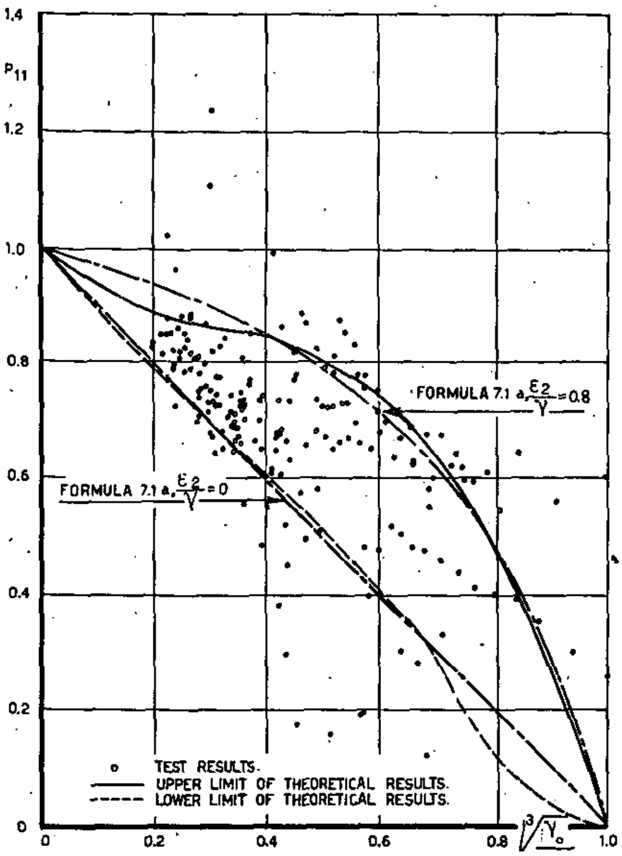

FIGURE 5.1.
Comparison between theoretical and experimental results for P_{11}.

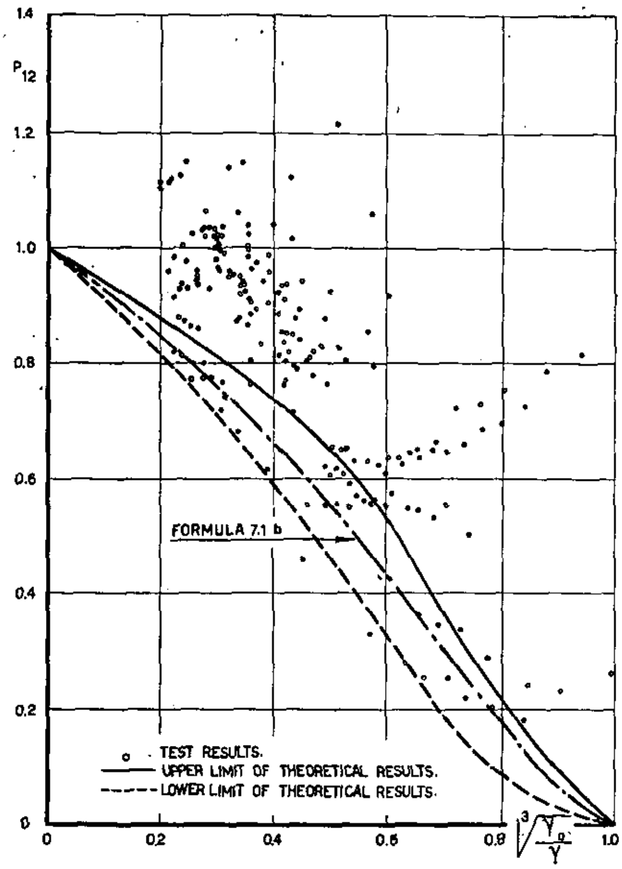

FIGURE 5.2.
Comparison between theoretical and experimental results for P_{12}.

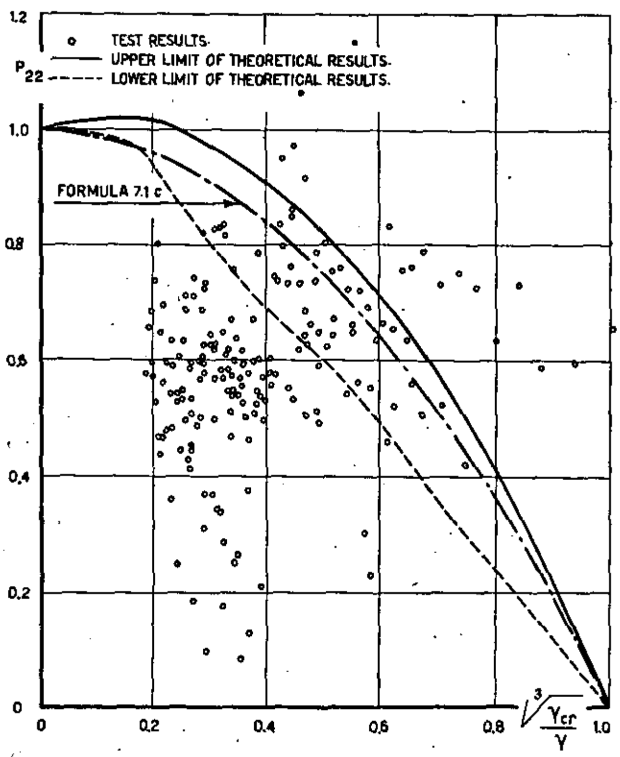

FIGURE 5.3.
Comparison between theoretical and experimental results for P_{22}.

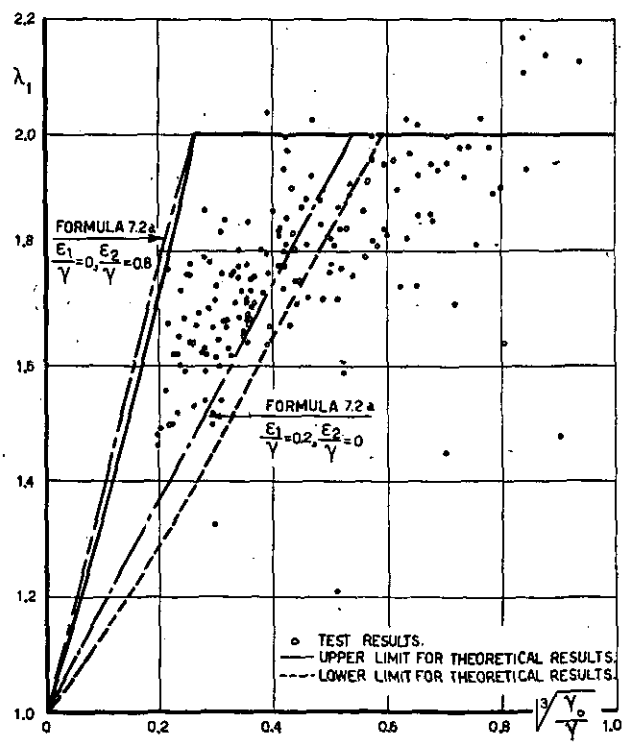

FIGURE 5.4.
Comparison between theoretical and experimental results for λ_1.

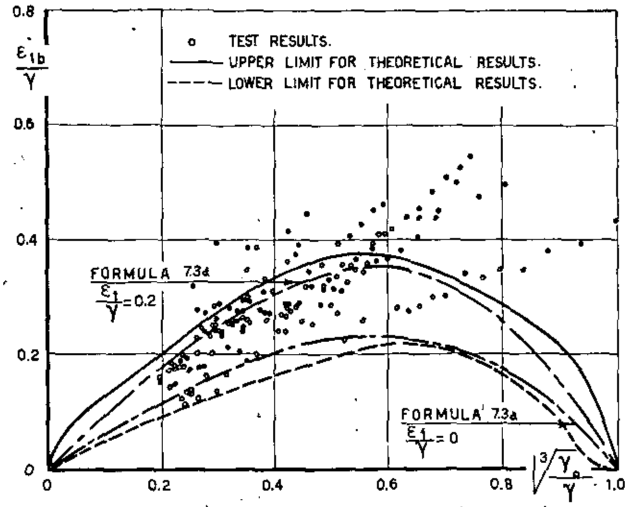

FIGURE 5.5.

Comparison between theoretical and experimental results for $\frac{\varepsilon_{1b}}{\gamma}$.

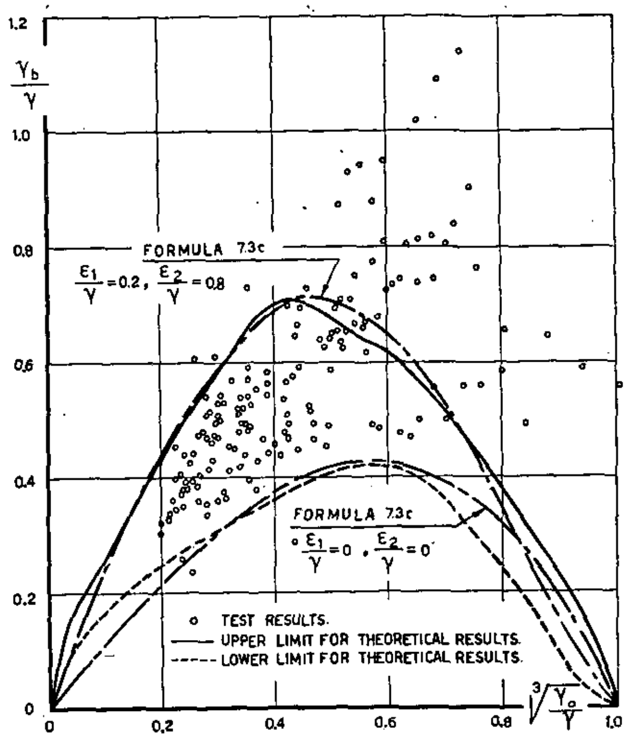

FIGURE 5.7.

Comparison between theoretical and experimental results for $\frac{\gamma_b}{\gamma}$.

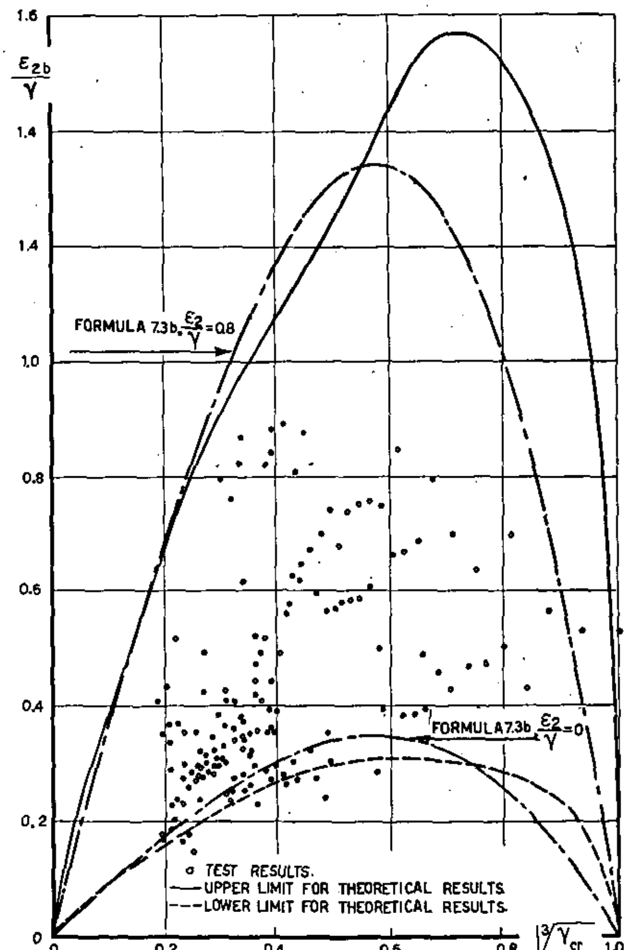

FIGURE 5.6.

Comparison between theoretical and experimental results for $\frac{\varepsilon_{2b}}{\gamma}$.

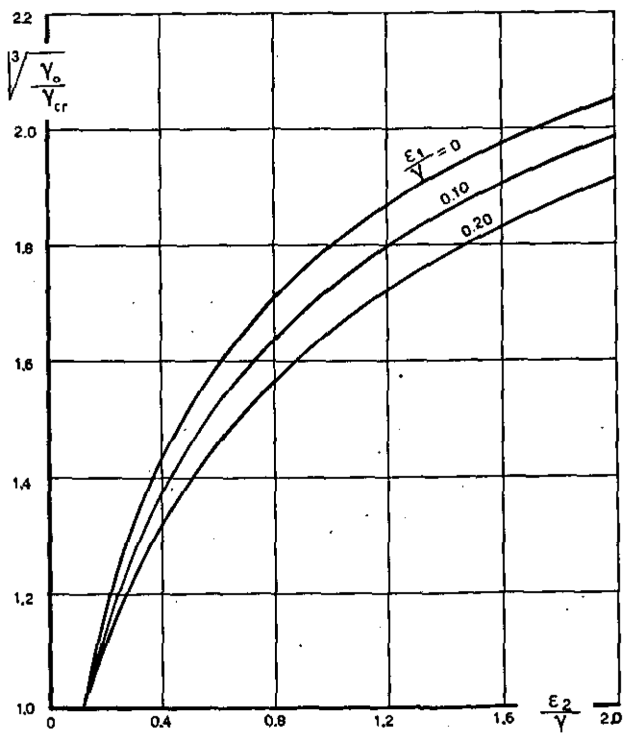

FIGURE 5.8

Diagram of $\frac{\gamma_o}{\gamma_{cr}}$.

was also computed from (3.6c) using the slope recordings for two representative tests on each of the three plates.

In calculating $\bar{\tau}$ from the external loads corrections were made for the influence of friction in the hinged joints of the loading frame. In addition, tests were carried out after removal of the test plate which yielded additional corrections due to the rigidity of the test frame.

In view of the doubtful reliability of these corrections P_{12} was also calculated using the values of γ_p given by equation (5.6) neglecting either the corrections for friction only or else all the corrections in the determination of $\bar{\tau}$.

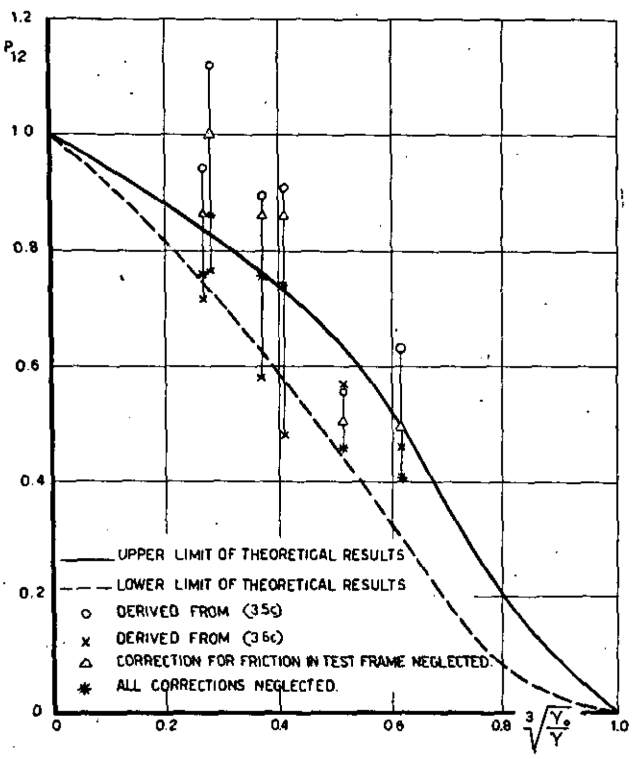

FIGURE 5.9.

Comparison between experimental results obtained after different methods of evaluation.

In fig. 5.9 the results of P_{12} are compared using the values of γ_p as evaluated in the various ways from equations (5.6) and (3.6c).

λ_2 was not computed from the tests, but was assumed to be unity, which is only strictly true for $\frac{a}{b} = \infty$.

From the resultant maximum stresses

$$S_1 = \sigma_{1\ max} \pm |\ \sigma_{1b}\ | \,, \tag{5.7a}$$

$$S_2 = \sigma_{2\ max} \pm |\ \sigma_{2b}\ | \,, \tag{5.7b}$$

$$T = \tau \mp |\ \tau_b\ | \,, \tag{5.7c}$$

the equivalent tensile stress σ_e of HUBER—VON MISES—HENCKY was calculated, viz.:

$$\sigma_e = \left[\ S_1^2 + S_2^2 - S_1 S_2 + 3\,T^2 \right]^{\frac{1}{2}}. \tag{5.7d}$$

Some results concerning the higher loads have been given in table 5.1.

6 Discussion of results and comparison with theory.

Figs. 5.1 to 5.7 inclusive show much scatter of the experimental results, which can be attributed to the variety of values of $\frac{\varepsilon_1}{\gamma}$ and $\frac{\varepsilon_2}{\gamma}$. An attempt to find relations between the characteristic ratios P etc. and $\frac{\varepsilon_1}{\gamma}$ and $\frac{\varepsilon_2}{\gamma}$ failed, for even with fairly constant values of $\frac{\varepsilon_1}{\gamma}$ and $\frac{\varepsilon_2}{\gamma}$ scatter proved to be large. It was, however, possible to make qualitative conclusions on the effect of $\frac{\varepsilon_2}{\gamma}$, which proved to be in agreement with the conclusions following from theory.

In figs. 5.1 to 5.7 inclusive curves have been drawn, which have been calculated on the basis of KOITER's theory (*ref.* 7). In general, the experimental results for P_{11}, ε_{1b}, ε_{2b}, γ_b and λ_1 agree fairly well with the theoretical results.

The experimental results for P_{12}, as originally determined from (5.6) (c.f. § 5), are for the greater part somewhat larger than the theoretical results, particularly in the range of smaller $\frac{\gamma_o}{\gamma}$ values where P_{12} is almost unity and even in a number of tests where P_{12} is larger than unity. This latter fact gives rise to doubt as to the reliability of the experimental results. $P_{12} > 1$ would mean that the incomplete tension field would have less stiffness than the complete tension field, which is physically impossible. It might be that the shear stress is underestimated by an overestimation of certain corrections which have been applied due to friction and rigidity in the test rig.

In this connection it is significant that P_{12}, as determined by (3.6 c) from the slope recordings, agrees reasonably well with theory (fig. 5.9).

The same can be said of the results obtained from (5.6) by neglecting all corrections in $\bar{\tau}$, whereas neglecting only the corrections for friction yields values of P_{12} which are in excess of the theoretical results.

Although the values of P_{12} from (3.6c) and the values obtained from (5.6) by neglecting all or part of the corrections originally applied in

TABLE 5.1.

Equivalent maximum stresses σ_e.

t mm	$\frac{\varepsilon_2}{\gamma}$	τ kg/cm²	σ_e kg/cm²	t	$\frac{\varepsilon_1}{\gamma}$	$\frac{\varepsilon_2}{\gamma}$	τ kg/cm²	σ_e kg/cm²	t	$\frac{\varepsilon_2}{\gamma}$	τ kg/cm²	σ_e kg/cm²
0.42	0.00	494	1410	0.90	0.06	0.02	537	1730	1.27	0.00	399	1310
	0.00	623	2120		0.08	0.03	668	2060		0.00	451	1485
	0.00	740	2500		0.08	0.03	764	2560		0.00	499	1580
	0.12	410	1320		0.11	0.04	1084	3400 1)		0.00	547	1795
	0.12	458	1440		0.08	0.02	540	1690		0.00	598	1840
	0.12	525	1430		0.09	0.03	768	2355		0.00	652	1930
	0.12	579	1910		0.13	0.05	1083	3315 1)		0.00	703	2090
	0.12	653	2070		0.12	0.03	542	1800		0.18	361	1550
	0.26	388	1710		0.13	0.04	770	2425		0.17	434	1780
	0.25	470	1520		0.17	0.04	1050	3390 1)		0.17	505	2020
	0.25	542	1940		0.10	0.03	549	1725		0.17	572	2250
	0.35	289	2110		0.17	0.03	774	2470		0.30	291	1440
	0.36	360	2465		0.20	0.04	1050	3510 1)		0.31	340	1645
	—0.01	475	1355		0.07	0.16	508	2000		0.30	393	1705
	0.00	604	1500		0.08	0.15	641	2405		0.30	441	1920
	0.10	412	1345		0.11	0.14	882	2985		0.30	489	2180
	0.11	464	1585		0.10	0.16	644	2395		0.30	545	2330
	0.11	529	1680		0.13	0.15	886	3460		0.54	219	1560
	0.24	376	1550		0.13	0.15	649	2480		0.45	272	1960
	0.24	451	1660		0.17	0.14	850	3280		0.49	354	2120
	0.40	268	1920		0.15	0.15	651	2510		0.51	403	2480
	0.00	838	2225		0.20	0.14	846	3315				
	0.00	950	2425		0.07	0.21	438	1880				
	0.11	750	2230		0.08	0.20	560	2255				
	0.11	829	2390		0.12	0.19	797	3290				
	0.00	1180	3340 1)		0.09	0.21	565	2285				
	0.00	1064	3090 1)		0.13	0.20	760	3285 1)				
	0.01	1404	3810 1)		0.13	0.19	569	2355				
	0.00	1402	3870 1)		0.17	0.17	816	3245				
					0.15	0.20	573	2325				
					0.20	0.17	810	3470				
					0.07	0.27	383	1875				
					0.08	0.27	442	2105				
					0.11	0.26	710	3245				
					0.10	0.29	446	2150				
					0.13	0.25	685	3560				
					0.13	0.28	449	2160				
					0.17	0.24	697	3070				
					0.15	0.28	452	2160				
					0.20	0.24	650	3385				
					0.06	0.55	205	1705				
					0.10	0.46	291	2485 1)				
					small		1213	2)				
					small		1361	2)				

1) Permanent deformation observed.
2) Heavy permanent deformation.

computing $\bar{\tau}$, have only been determined for a limited number of cases, it is highly probable that all P_{12}-values should be reduced a certain amount. In that case the theoretical results do not seem to be in contrast to the experimental results.

The experimental results for P_{22} in the range of smaller $\frac{\gamma_{cr}}{\gamma}$-values are well below the theoretical values, in particular for the thinnest plate (second plate). This means that the average tensile stresses in the direction of y would be smaller than according to theory. This effect is to be expected, since the theory holding for $\frac{a}{b} = \infty$ cannot account for the reduction of w near the ends $x = \pm\frac{a}{2}$ with plates of finite length. Theory will be in better agreement with conditions at some distance from the ends, therefore with $\sigma_{2\,max}$. The knowledge about $\bar{\sigma}_2$ is of relatively little practical importance, since the direction of y is the direction of the heavy spar booms which are taking the bulk of the external compressive loads.

With $\frac{\gamma_0}{\gamma}$ near unity, therefore in the region not far beyond the critical stress, P_{12}, P_{22}, ε_{1b} and γ_b are well above the theoretical curves, the latter falling off to zero at $\frac{\gamma_0}{\gamma} = 1$ or $\frac{\gamma_{cr}}{\gamma} = 1$. Obviously this deviation between theory and experiment is to be attributed to the initial waviness of the plates, by which the waves are in fact more developed than with initially flat plates. Therefore these deviations do not give rise to doubt on the reliability of the theory.

Permanent deformation occurred at equivalent stresses (as computed from the deformation measurements) of about 3300 kg/cm², whereas the 0.2 % yield stress is about 3500 kg/cm². Neglecting the corrections mentioned in § 5 these equivalent stresses will amount to approximately 3400 kg/cm². Therefore the method in which the maximum stresses have been determined proves to give stresses quite near to actual stresses. The fact that the deformation factors ε_{1b}, ε_{2b} and γ_b as given by theory are in reasonable agreement with the experimentally determined quantities means that the theory presents the possibility of predicting the load at which permanent deformation will occur.

7 Conclusions.

Summarizing, we may conclude that in view of the scatter observed it does not seem worthwhile to strive for an exact theory for the post-buckling behaviour of plates. Due to initial waviness, actual plates will behave in a different way than ideal flat plates. Nevertheless a theory giving an adequate picture of the post-buckling behaviour over the whole range of $\frac{\gamma_0}{\gamma}$ is the best source for general information. Experimental evidence is such that KOITER's theory can be regarded as giving adequate information. Since scatter of experimental results makes it clear that the theoretical results should not be considered reliable up to the last figure, they may be approximated by simple formulae. As such, the following formulae are proposed:

$$P_{11} = 1 - \left(\frac{\gamma_0}{\gamma}\right)^{\frac{1}{3}} + 0.9\frac{\varepsilon_2}{\gamma}\left[\left(\frac{\gamma_0}{\gamma}\right)^{\frac{1}{3}} - 0.75\frac{\gamma_0}{\gamma} - 0.25\left(\frac{\gamma_0}{\gamma}\right)^{3}\right], \tag{7.1a}$$

$$P_{12} = 1 - 0.75\left(\frac{\gamma_0}{\gamma}\right)^{\frac{1}{3}} - 0.65\frac{\gamma_0}{\gamma} + 0.40\left(\frac{\gamma_0}{\gamma}\right)^{2}, \tag{7.1b}$$

$$P_{22} = 1 - \left(\frac{\gamma_{cr}}{\gamma}\right)^{\frac{2}{3}}, \tag{7.1c}$$

$$\lambda_1 = 1 + \frac{1}{0.5 + 0.2\frac{\varepsilon_1}{\gamma} - 0.3\frac{\varepsilon_2}{\gamma}}\left(\frac{\gamma_0}{\gamma}\right)^{\frac{1}{3}} \text{ or } \lambda_1 = 2,$$

whichever is the smallest, (7.2a)

$$\lambda_2 = 1, \tag{7.2b}$$

$$\varepsilon_{1b} = 0.6\left(1 + 2.5\frac{\varepsilon_1}{\gamma}\right)\left[\left(\frac{\gamma_0}{\gamma}\right)^{\frac{1}{3}} - \frac{\gamma_0}{\gamma}\right], \tag{7.3a}$$

$$\varepsilon_{2b} = 0.9\left(1 + 3.6\frac{\varepsilon_2}{\gamma}\right)\left[\left(\frac{\gamma_{cr}}{\gamma}\right)^{\frac{1}{3}} - \frac{\gamma_{cr}}{\gamma}\right], \tag{7.3b}$$

$$\gamma_b = 1.1\left(1 + 1.5\frac{\varepsilon_1}{\gamma}\right)\left[\left(\frac{\gamma_0}{\gamma}\right)^{\frac{1}{3}} - \frac{\gamma_0}{\gamma}\right] + 6\left[0.6\frac{\varepsilon_2}{\gamma} - \left(\frac{\varepsilon_2}{\gamma}\right)^{2} + 0.6\left(\frac{\varepsilon_2}{\gamma}\right)^{3}\right] \times \left[\left(\frac{\gamma_0}{\gamma}\right)^{\frac{1}{3}} - 3\frac{\gamma_0}{\gamma} + 2\left(\frac{\gamma_0}{\gamma}\right)^{\frac{5}{3}}\right]. \tag{7.3c}$$

Substituting these characteristic wave form ratios into (3.9), (5.4) and (5.7) the stresses and the effective rigidity are obtained.

8 Notations.

a	free length of the plate $> b$
b	width of the plate
e_1, e_2	values of ε_{1p}, ε_{2p} for the complete

	tension field (eqs. 5.2)
f	amplitude of the waves
g	value of γ_p for the complete tension field (eqs. 5.2)
m	cotangent of the angle between the X-axis and the direction of the waves
t	thickness of the plate
u, v, w	displacements of an arbitrary point in the middle plane ($z=0$) of the plate in the X-, Y-, and Z-directions
x, y, z	coordinates in the longitudinal and lateral directions and normal to the plane of the plate (fig.4.1)
E	modulus of elasticity
G	modulus of rigidity
G'	effective modulus of rigidity of the buckled plate
L	half-wave length measured in the X-direction
N_1, N_2	normal tensile forces in the plate in the X- and Y-directions
P_{11}, P_{12}, P_{22}	characteristic ratios for the wave form (eqs. 5.1)
S_1, S_2, T	maximum normal and shear stresses (eqs. 5.7)
γ	shear angle of the rectangular plate, following from the displacement of the edges.
γ_{cr}	critical shear strain at which buckling occurs
γ_b	shear strain in the faces of the plate $\left(z=\pm\frac{t}{2}\right)$ caused by bending
γ_o	shear strain at which the diagonal wave formation starts
γ_p	contribution of the waves to γ (eqs.3.6)
ε_1, ε_2	compressive strains in the longitudinal and lateral edges of the plate
ε_{1b}, ε_{2b}	tensile strains in the faces of the plate $\left(z=\pm\frac{t}{2}\right)$ caused by bending
ε_{1p}, ε_{2p}	contribution of the waves to the tensile strains in the plate (eqs. 3.6)
λ_1, λ_2	strain ratio defined by eqs. (5.3)
ν	POISSON's ratio
σ_1, σ_2	tensile membrane stresses in the plate in the X- and Y-directions
$\bar{\sigma}_1$, $\bar{\sigma}_2$	average membrane stresses (eqs. 3.1 and 3.5)
σ_{b1}, σ_{b2}	bending stresses
σ_e	equivalent tensile stress of HUBER—VON MISES—HENCKY
τ	shear stress in the plate
$\bar{\tau}$	average shear stress (eqs. 3.5)

9 References.

1. WAGNER, H.: Ebene Blechwandträger mit sehr dünnem Stegblech. Zeitschr. f. Flugt. und Motorluftsch. f. 1929. Also: Flat sheet metal girders with very thin metal web, parts I, II, III; Techn. Mem. nos. 604, 605, 606, NACA 1931.

2. LAHDE, R. und WAGNER, H.: Versuche zur Ermittlung des Spannungszustandes in Zugfeldern; Luftfahrtforsch. 1936, Bd. 13. Also: Tests for the determination of the stress condition in tension fields; Techn. Mem. no. 809, NACA 1936.

3. KROMM, A. und MARGUERRE, K.: Verhalten eines von Schub- und Druckkräften beanspruchten Plattenstreifens oberhalb der Beulgrenze; Luftfahrtforsch. 1937, Bd. 14.

4. KOITER, W. T.: Het schuifplooiveld bij groote overschrijdingen van de knikspanning. Rapport S. 295, Nationaal Luchtvaartlaboratorium, Amsterdam 1944. English abstract: Theoretical Investigation of the Diagonal Tension Field of Flat Plates, Amsterdam 1946.

5. COX, H. L.: Buckling of thin plates in compression. Aer. Res. Comm. Rep. and Mem. no. 1554 (1933).

6. VAN DER NEUT, A.; FLOOR, W. K. G.; BINKHORST, I.: Experimental investigation of the post-buckling behaviour of stiffened, flat, rectangular plates under combined shear and compression, Part I. Report S. 300, Nationaal Luchtvaartlaboratorium, Amsterdam 1947.

7. FLOOR, W. K. G.: Experimental investigation of the post-buckling behaviour of stiffened, flat, rectangular plates under combined shear and compression. Part II, Report S. 328, Nationaal Luchtvaartlaboratorium, Amsterdam 1947.

8. —: Description of a slope recorder and an elliptic enlarger, Report S. 316, Nationaal Luchtvaartlaboratorium, Amsterdam 1946.

Acknowledgement.

The authors wish to express their thanks to the N.V. Nederlandse Verenigde Vliegtuig- fabrieken Fokker, Amsterdam, who donated the test rig and the material for the test specimens. Further thanks are due to those of the personnel of the Nationaal Luchtvaartlaboratorium, Amsterdam, who contributed to the preparation and the performance of the tests and the evalution of the test results, in particular to Mr. J. H. RONDEEL for his important contributions to the development of the instruments mentioned. Finally, acknowledgement is made to Mr. L. S. D. MORLEY for his care in reading and improving the English text of this report.

Completed: August 1948.

CLL Class. C 46 : B 106

REPORT S. 346

The Elastic Overall Instability of Sandwich Plates with Simply-Supported Edges

by

Ir F. J. PLANTEMA and Dr A. C. DE KOCK

Summary.

The energy method for calculating buckling loads of sandwich plates, developed by the first author, is applied to a simply-supported infinitely long plate subjected to shear. The results are compared with those obtained in previous papers and are presented in a number of simple graphs.

Non-dimensional interaction curves for combined compression or tension and shear are given and, finally, all of the results obtained by means of the energy method are recapitulated.

Contents.

N.B. This investigation was carried out by order of the Netherlands Aircraft Development Board.

1 Introduction.

In a previous report of the N.L.L. (*ref.* 1), VAN WIJNGAARDEN calculated the buckling loads of flat, infinitely long sandwich plates having simply-supported edges and subjected to a combination of compression or tension and shear. It was shown in which way exact solutions can be obtained but the numerical calculations appeared hardly practicable. Therefore, these calculations were carried out for a simplified wave form which does not satisfy the dynamic boundary conditions. Consequently, the results were not considered sufficiently reliable — the buckling load of a simple plate under shear loading, obtained by this method, being overestimated by 27 %.

In order to obtain more reliable results for sandwich plates subjected to shear, an energy method was developed which was verified by applying it to plates under uniaxial or biaxial compression (*refs.* 2, 3, 4). It is assumed that the faces are isotropic (E_f, ν_f) and that the core is isotropic in the XY plane (E_c, ν_c) but may have a modulus of rigidity G_{cn} for shear in planes perpendicular to the XY plane which differs from that for shear in the XY plane (G_c). In this report the application of the energy method to infinitely long plates under shear loading is discussed. A comparison is made with the results obtained in *ref.* 1.

The same problem has also been dealt with by BIJLAARD (*ref.* 5), whose method of solution is based, however, on some rather intuitive assumptions (c.f. *ref.* 2) and who only gives a formal solution. The present results are compared with those of *ref.* 5, making an acceptable assumption for the wave lengths in the latter case.

It is to be noted that in all of these investigations the results apply to antisymmetrical (or in-phase) buckling, the distance between the faces being assumed to remain constant during buckling [1]). It has been shown in *ref.* 1 that this assumption is justified for the overall-buckling case, but in certain circumstances wrinkling failure may be critical rather than overall buckling (c.f. *ref.* 6).

No recomputation of the buckling loads of plates under a combination of compression or tension and shear is given. It may be assumed that the non-dimensional interaction curves for such combinations which can be derived from *ref.* 1, will be reliable for all practical purposes. Such interaction curves are given in this report. For convenience, all the results obtained for plates having simply-supported edges have been recapitulated in a final section of this report.

2 Pure shear. The method of solution and the results.

The general formulae for the calculation of the buckling loads are derived in *refs.* 2, 3 and 4. They are:

$$\tfrac{1}{2} P_x \int_0^a\int_0^b \left(\frac{\partial w}{\partial x}\right)^2 dx\,dy + \tfrac{1}{2} P_y \int_0^a\int_0^b \left(\frac{\partial w}{\partial y}\right)^2 dx\,dy + P_{xy}\int_0^a\int_0^b \frac{\partial w}{\partial x}\frac{\partial w}{\partial y}\,dx\,dy =$$

$$= \tfrac{1}{2} B \int_0^a\int_0^b \Lambda(w_b)\,dx\,dy + B_f\int_0^a\int_0^b \Lambda(w)\,dx\,dy + \tfrac{1}{2} S\int_0^a\int_0^b \left\{\left(\frac{\partial w_s}{\partial x}\right)^2 + \left(\frac{\partial w_s}{\partial y}\right)^2\right\} dx\,dy, \qquad (2.1)$$

$$S\frac{\partial w_s}{\partial x} = -B\frac{\partial}{\partial x}(\Delta w_b);\quad S\frac{\partial w_s}{\partial y} = -B\frac{\partial}{\partial y}(\Delta w_b). \qquad (2.2)$$

The solution is obtained by making a reasonable assumption for w_b, computing $\partial w_s/\partial x$ and $\partial w_s/\partial y$ from (2.2) and substituting these expressions into (2.1).

For pure shear we adopt the wave form assumption (*ref.* 7)

$$w_b = W_i \sin\frac{\pi y}{b}\sin\frac{\pi}{l}\left(x + \frac{mb}{\pi}\cos\frac{\pi y}{b} - \tfrac{1}{2} mb\right), \qquad (2.3)$$

containing two parameters l (the half wave length) and m. This wave form has sinusoidal nodal lines, intersecting the edges $y = 0$ and $y = b$ of the plate perpendicularly and having a maximum slope $\frac{dy}{dx} = \frac{1}{m}$ at $y = \tfrac{1}{2} b$ (fig. 2.1). For a simple plate, it is known from *ref.* 7 that the buckling load is overestimated by only 1 %, this close agreement being due to the fact that all boundary conditions are satisfied.

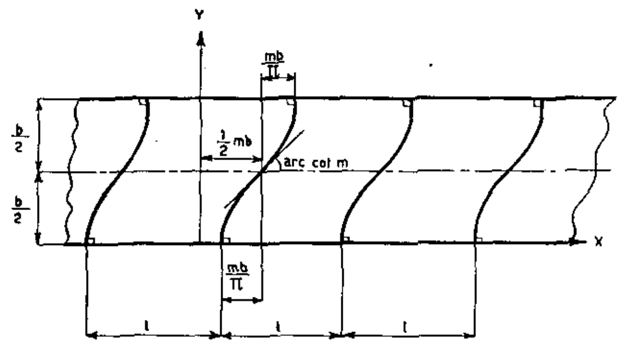

FIGURE 2.1.

Sandwich plate with assumed pattern for w_b. Nodal lines: $x = \tfrac{1}{2}\, mb + nl - \frac{mb}{\pi}\cos\frac{\pi y}{b}$ $(n = 0, \pm 1, \ldots)$

The derivation of the formula for the critical value of P_{xy} from (2.1) to (2.3) incl. is given in appendix A. It finally leads to

$$P_{xy} = \frac{\text{constant}}{\lambda\sqrt{\mu}}\, F(\lambda, \mu), \qquad (2.4)$$

where $\lambda = l^2/b^2$, $\mu = m^2$ and $F(\lambda, \mu)$ is a fraction whose numerator is of the fourth degree in both λ and μ and whose denominator is quadratic in both λ and μ.

The solutions for a number of values of s and τ were determined by a numerical procedure (appendix A). The results are presented in the form of dimensionless quantities k_b and k_s, defined by

$$P_{xy} = k_b\frac{\pi^2 B}{b^2} = k_s\, S. \qquad (2.5)$$

The values of $\frac{l}{b}$, m, k_b and $k_s = \frac{1}{s}\,k_b$ are given in table 2.1 and figs. 2.2 to 2.4 incl. for the ranges $0 \leqq s \leqq 3$ and $360 \leqq \tau \leqq 7500$.

In figs. 2.5 and 2.6 the values of l/b, k_b and k_s are given for $s > 2$, these values have been computed as explained in section 3 and appendix B.

[1]) This is also true for the numerical results given in *ref.* 1; c.f. section 5 of *ref.* 4.

TABLE 2.1.

Numerical results for pure shear loading.

(1)	(2)	(3)	(4)	(5)	(6)	(7)	(8)	(9)	(10)	(11)
s	τ	t	k_b	λ	μ	l/b	m	k_s	k_b ref. 1	k_b ref. 5
0	—	0	$5.377/\tau$	1.579	0.101	1.256	0.318	∞	$6.78/\tau$	$5.35/\tau$
0.05	360	18	0.0837	0.490	0.388	0.700	0.623	1.674	0.0940	0.0792
	1300	65	0.0657	0.2580	0.600	0.508	0.774	1.314	0.0682	0.0632
	3000	150	0.0600	0.1696	0.758	0.412	0.869	1.200	0.0600	0.0582
	7500	375	0.0563	0.1054	0.910	0.325	0.954	1.126	0.0529	0.0549
0.2	360	72	0.256	0.2668	0.604	0.517	0.776	1.280	0.262	0.246
	1300	260	0.228	0.1406	0.813	0.375	0.901	1.140	0.228	0.222
	3000	600	0.219	0.0921	0.924	0.303	0.961	1.095	0.217	0.215
	7500	1500	0.213	0.0579	1.015	0.241	1.007	1.065	0.210	0.209
0.5	360	180	0.570	0.2070	0.704	0.455	0.838	1.140	0.566	0.553
	1300	650	0.538	0.1083	0.905	0.329	0.951	1.076	0.520	0.534
	3000	1500	0.527	0.0725	0.970	0.269	1.015	1.054	0.517	0.524
	7500	3750	0.519	0.0441	1.085	0.210	1.041	1.038	0.537	—
0.8	360	288	0.868	0.2147	0.715	0.462	0.845	1.085	0.851	0.843
	1300	1040	0.838	0.1191	0.884	0.345	0.939	1.048	0.824	0.819
	3000	2400	0.829	0.0771	1.000	0.278	1.000	1.036	0.826	0.812
	7500	6000	0.821	0.0510	1.052	0.226	1.024	1.026	0.898	—
1.2	360	432	1.237	0.3010	0.639	0.549	0.798	1.031	1.164	1.207
	1300	1560	1.218	0.2210	0.730	0.470	0.854	1.015	1.149	1.190
	3000	3600	1.214	0.1940	0.766	0.441	0.874	1.012	1.148	1.188
	7500	9000	1.210	0.1760	0.795	0.419	0.890	1.008	1.234	1.184
3.0	360	1080	2.386	0.8720	0.490	0.933	0.700	0.795	2.080	2.386
∞	—	∞	5.414	1.575	0.752			0	6.78	5.35

$$P_{xy} = k_b \frac{\pi^2 B}{b^2} = k_s S;\ k_b = s k_s$$

3 Discussion of the results for pure shear.

Comparing figs. 2.2 and 2.3 with figs. 5.1 and 5.2, which apply to longitudinal compression P_x (*ref.* 4), it appears that the character of the curves in the corresponding graphs is the same. The curves for P_{xy}/S of fig. 2.2 are lying slightly higher than the curves for P_x/S of fig. 5.2, whereas the curves for l/b of fig. 2.3 are lying considerably higher than the corresponding curves in fig. 5.1, the asymptote being located at $l/b = 1.255$ instead of at $l/b = 1$.

For longitudinal compression it was proved in *ref.* 4 that the influence of τ vanishes when $s > 2$. It is clear that the same phenomenon occurs for shear loading at approximately the same value of s (c.f. figs. 2.2 to 2.4). The calculation for $s > 3$ was not carried out. Instead, as explained in appendix B, Bijlaard's method (*ref.* 5) was used in this range. The results are given in figs. 2.5 and 2.6 and may be represented by the following empirical formulae

$$k_s = \frac{5.35}{s + 3.8} \quad ; \quad \frac{l}{b} = \frac{5}{4}\,\frac{4s - 3}{4s + 1}\,, \qquad (3.1)$$

valid for $s > 2$ and any τ.

The values of l/b are somewhat smaller than those computed by means of the energy method (c.f. fig. 2.3), but the values of k_s and k_b from both methods are for practical purposes identical.

In columns 10 and 11 of table 2.1 the values of k_b according to *refs.* 1 and 5 are given. The values given in col. 10 have been read from the appropriate graphs of *ref.* 1. In *ref.* 5, however, only a formal solution is given. The values given in col. 11 have therefore been computed from eqs. (6) and (15) of *ref.* 5 and fig. 2 of *ref.* 9,[1]) assuming that l/b has the value given in col. 7 of table 2.1. The validity of the latter assumption has been checked for some representative cases (compare appendix B). The minimum of k_s proved to correspond to somewhat smaller values of l/b than those given in col. 7 of table 2.1, which is in agreement with the results mentioned in the preceding paragraph. The numerical differences are, however, quite negligible.

Comparing the results given in cols. 4 and 10 it appears that positive as well as negative differences occur which are, in general, small except for very small values of s.

The results of *ref.* 1 in the range $s \geqq 0.5$ show the curious behaviour that k_b does not decrease monotonically for increasing τ, but has a minimum

[1]) Fig. 2 of *ref.* 9 gives the same information as fig. 2 of *ref.* 5 to a more appropriate scale.

at a certain intermediate value of τ and then rises again. It is certain that *ref.* 1 yields results which are larger than the exact values where they exceed those given in col. 4. It is probable that the results of *ref.* 1 underestimate the exact values when they are more than a few per cent less than those of col. 4.

A comparison of col. 4 with col. 11 shows that the results of *ref.* 5 are systematically slightly smaller than those obtained in this report. The method of *ref.* 5 yields an approximation which will most probably be also quite satisfactory in other cases. Therefore, in calculating the buckling loads for plates having clamped edges this method can safely be adopted. According to *ref.* 5, the results obtained in this way should be somewhat too small, which would infer that both the results given in col. 4 and those given in col. 11 would be very close to the exact results.

With regard to the values of m, given in fig. 2.4, it is to be noted that in the practically important range the angles arc cot m (fig. 2.1) range from 45° to 55°. For a simple plate ($s = \infty$) $m = 0.867$ and arc cot $m = 49°$, which values are approached asymptotically by the curves of fig. 2.4. (For the case $s = 0$, which also represents a simple plate, reference is made to appendix C.)

It must finally be observed that these graphs do not cover the condition of wrinkling instability and are only valid for the elastic range. With regard to the former observation, it is possible that the region of small wave lengths in figs. 2.2 to 2.4 incl. (e.g. $l/b < 0.3$) will have no practical significance owing to wrinkling instability being more critical than overall instability. Particular attention should be given to this possibility when $E_{cn} \leqq E_c$, whereas for cores of honeycomb or similar materials ($E_{cn} >> E_c$) the danger of wrinkling failure is more remote [1]).

With regard to buckling at stresses approaching or exceeding the yield stresses, the development of a programme of tests to verify the theoretical results has lead to the impression that with the existing face and core materials this possibility is far from remote (c.f. appendix C).

An attempt to extend the theory to the plastic buckling range appears to be worthwhile.

---

[1]) Formulae for wrinkling instability are summarized in *ref.* 6.

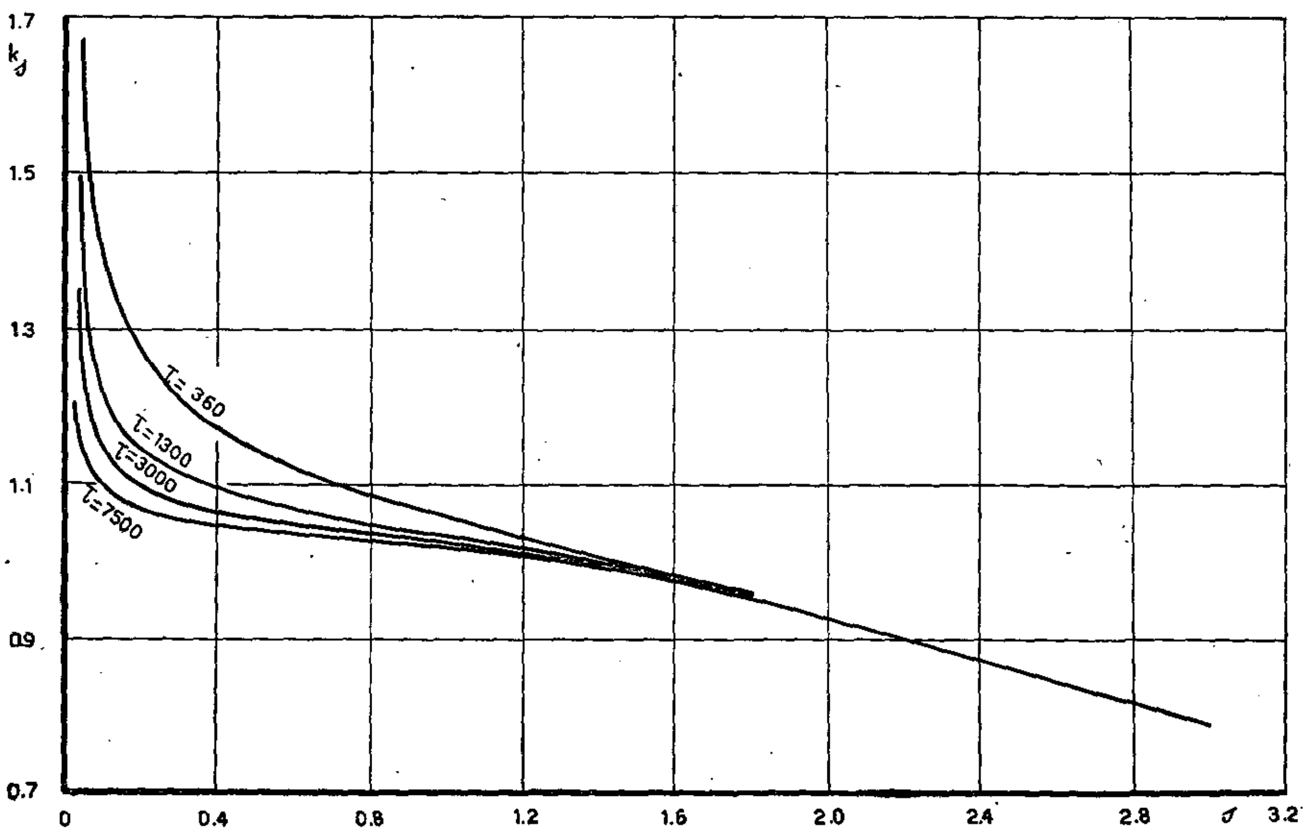

FIGURE 2.2.

Buckling loads for infinitely long plates under pure shear.

$P_{xy} = k_S S$. (For $s>2$ see fig. 2.5).

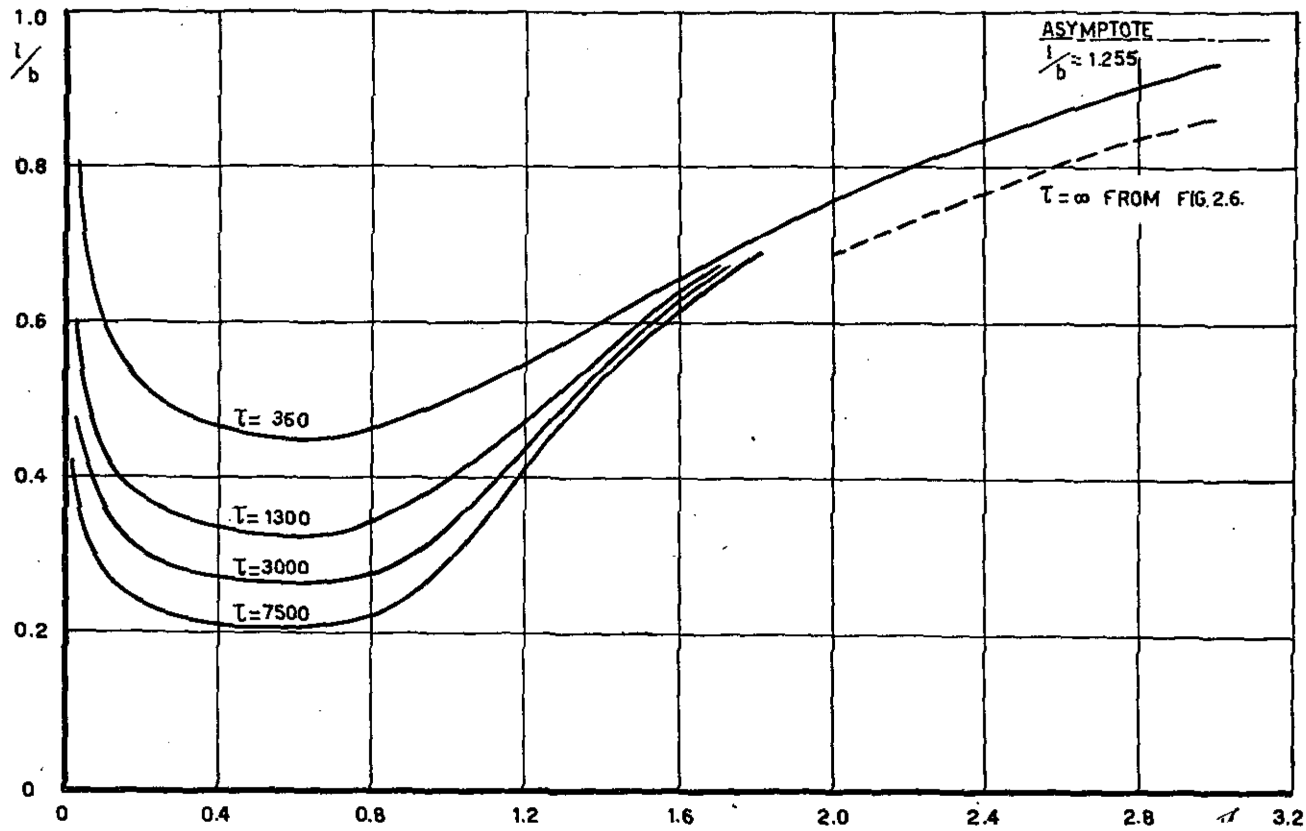

FIGURE 2.3.

Half-wave lengths for infinitely long plates under pure shear. (For $s > 2$ see fig. 2.6).

4 Combined loading.

It was not considered worthwhile to recompute the buckling loads for plates loaded by a combination of compression or tension and shear by the energy method. In order to improve the results given in *ref.* 1, the following method will be adequate for all practical purposes.

From the graphs given in *ref.* 1 the values of P_x, P_y, P_{xy}, P'_x, P'_y and P'_{xy} can be read, where the latter three symbols denote the buckling load of the plate when it is subjected to longitudinal compression only, lateral compression only or shear only. From these values the non-dimensional interaction surface of the values of P_x/P'_x, P_y/P'_y and P_{xy}/P'_{xy} can be constructed. It is now assumed [1]) that this surface would also be obtained if P_{xy} and P'_{xy} were computed from the energy method instead of from the method used in *ref.* 1.

Interaction curves derived from *ref.* 1 are given in figs. 4.1 and 4.2. The calculations have been performed for various combinations of the parameters s and τ, which are related to the parameters $\frac{\lambda^2}{2\varepsilon}$ and δ^* from *ref.* 1 by means of $\frac{1}{s} = \frac{\pi^2\lambda^2}{2\varepsilon}$ and $\tau = \frac{1}{\delta^*}$.

The results have shown that the influence of large variations of τ is negligible and, moreover, in the case of combined longitudinal compression (or tension) and shear, that the effect of varying s is sufficiently small to permit the drawing of one curve representing all combinations of s and τ which occur in practice.

Thus the curve of fig. 4.1 is valid for all combinations of s and τ and the curves of fig. 4.2 correspond to $s = 10$, 1 and 0.1 with arbitrary values of τ.

Incidentally, it may be remarked that the curve of fig. 4.1 can very nearly be approximated by the formula $\left(\frac{P_{xy}}{P'_{xy}}\right)^2 = 1 - \frac{P_x}{P'_x}$.

The curves of fig. 4.2, though resembling high-degree parabolas, cannot be represented by simple formulae. For determining the buckling loads with combined loading, e.g. longitudinal compression and shear, P'_x and P'_{xy} are read from figs. 2.2 and 5.1, P_x/P'_x and P_{xy}/P'_{xy} from fig. 4.1 and P_x and P_y can be computed.

[1]) A substantiation of this assumption and further information on the interaction curves are given in appendix D.

5 Recapitulation of the results given in ref. 4 and in this report.

5.1 The results given in *ref.* 4 and in this report all apply to the elastic overall instability of sandwich plates, having isotropic faces and a core which is isotropic in planes parallel to the middle plane of the sandwich, and which may have a modulus of rigidity for shear in planes perpendicular to the latter plane which differs from that for shear in this plane. The sandwich plate has simply-supported edges.

In *ref.* 4 the formula for instability of a rectangular plate under biaxial compression is given, which may be written in the form

$$\left(P_x\frac{n_x{}^2b^2}{a^2} + P_y\, n^2_y\right) = S\left(\frac{n_x{}^2b^2}{a^2} + n^2_y\right)^2 \left[\frac{1}{s + \dfrac{n_x{}^2b^2}{a^2} + n^2_y} + \frac{1}{t}\right], \tag{5.1}$$

where a and b are the length and width, n_x and n_y are the number of longitudinal and lateral half waves and P_x and P_y are the longitudinal and lateral compression per unit run. For given s, t and P_y/P_x, the values of n_x and n_y must be chosen so as to minimize P_x and P_y, both n_x and n_y being of course an integer.

Numerical results and simple formulae have been derived for infinitely long plates ($a = \infty$). These are as follows:

Longitudinal compression.

For $0 < s < 1.8$ and $360 < \tau < 7500$ the values of P_x/S and l/b (l being the half wave length) are given in figs. 5.1 and 5.2. For $s > 1.5$ they may be computed from the simple formulae

$$\frac{P_x}{S} = \frac{4s}{(s+1)^2}; \quad \lambda = \frac{s-1}{s+1}. \tag{5.2}$$

Lateral compression.

The buckling load is given by the formula

$$\frac{P_y}{S} = \frac{1}{1+s} + \frac{1}{t}, \tag{5.3}$$

where the term $1/t$ may be neglected for nearly all practical purposes.

Shear.

The values of k_b and k_s, defined by eq. (2.5), and of l/b are given in figs. 2.2 to 2.6 incl. and in

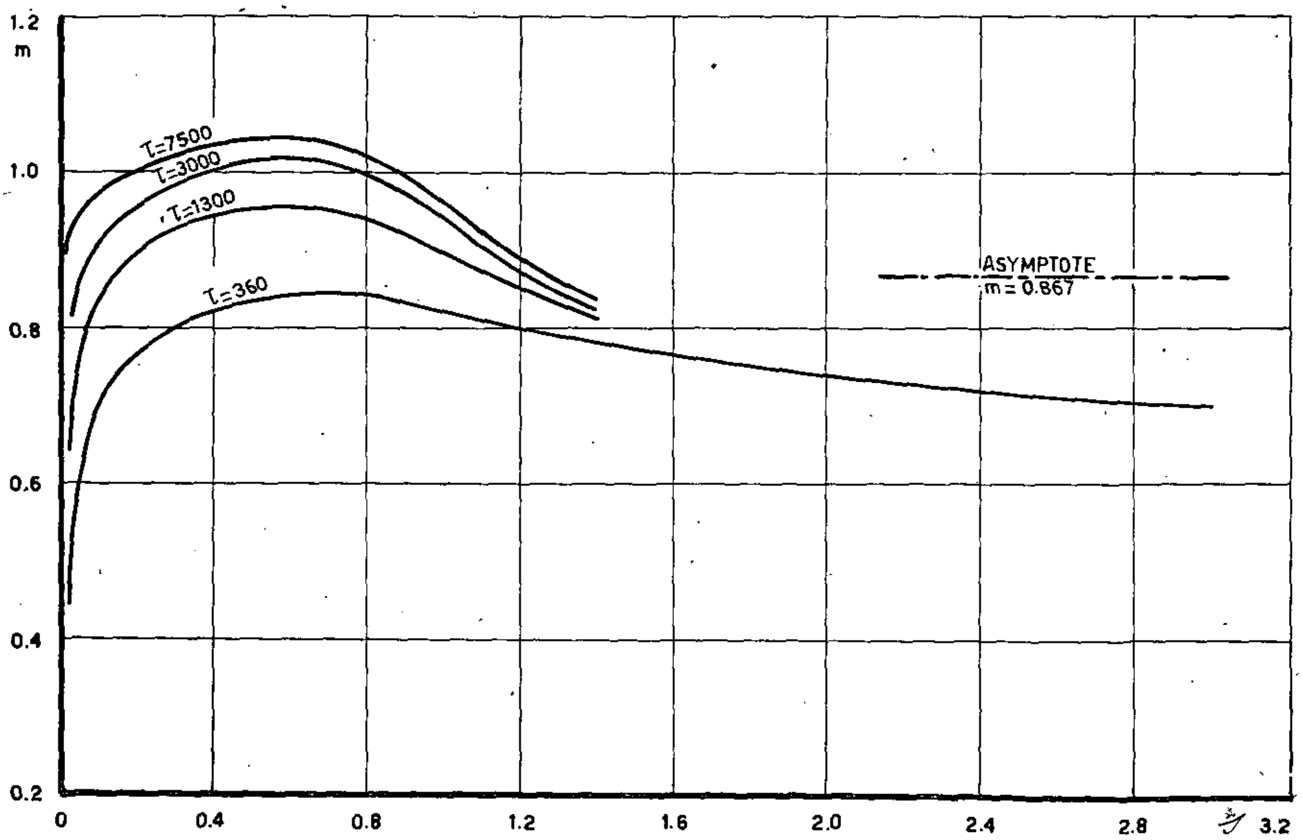

FIGURE 2.4.
Infinitely long plate under pure shear.
Relation between m, s and τ.

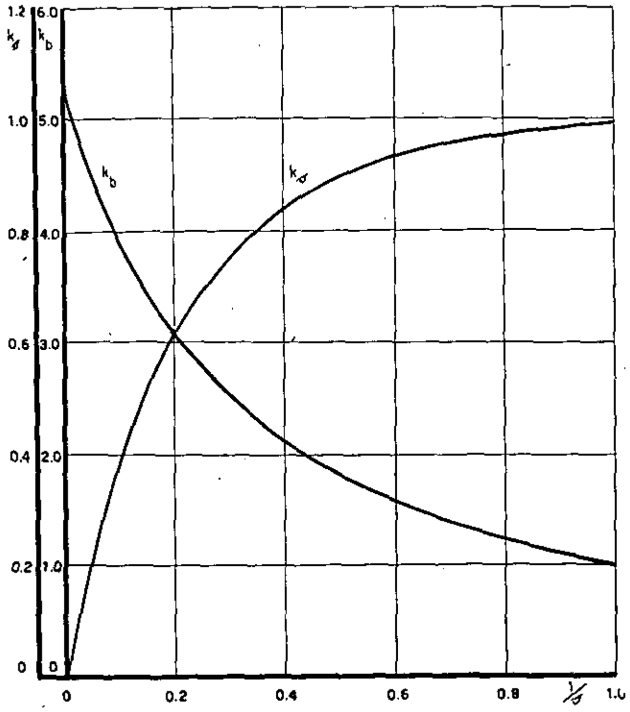

FIGURE 2.5.

Buckling loads for infinitely long plates under pure shear when $s > 2$.

$$P_{xy} = k_b \frac{\pi^2 B}{b^2} = k_s S.$$

$$k_b = s\ k_s \simeq \frac{5.35s}{s+3.8}$$

table 2.1.

Approximate formulae for $s > 2$ are

$$\frac{P_{xy}}{S} = \frac{5.35}{s+3.8}; \quad \frac{l}{b} = \frac{5}{4}\ \frac{4s-3}{4s+1}. \qquad (3.1)$$

The latter formula yields somewhat smaller values than those computed from the energy method (c.f. section 3).

Combined loading.

The combinations of loads leading to instability of the sandwich plate are given by the interaction curves of figs. 4.1 and 4.2.

In these graphs, the buckling loads attained when only one of the components of the external loading is present, are denoted by a dash; these buckling loads follow from the graphs and formulae mentioned in the preceding part of this section.

5.2 The results obtained by BIJLAARD's method of computing the buckling loads (*ref.* 5) are in close agreement with those obtained in this report. The former method is particularly attractive when the buckling load of a simple plate ($S = \infty$) under otherwise identical circumstances is known as a function of the wave length.

5.3 In the region of small wave lengths, i.e. for $s < 1.0$ (approx.) and τ large, wrinkling instability may be more critical than overall instability, especially when the transverse compressive stiffness of the core is not large compared with that in the plane of the plate.

5.4 It would seem that with existing face and core materials buckling may quite well occur in the plastic range. An extension of the theory to plastic buckling therefore appears to be worthwhile.

6 Notations.

b	width of plate (fig. 2.1)
c	thickness of core; suffix c relates to the core.
f	thickness of face; suffix f relates to the face.
k_b, k_s	buckling load parameters, c.f. eq.(2.5)
l	half-wave length with infinitely long plate (fig. 2.1)
m	parameter defining the slope of the nodal lines (fig. 2.1)
$s =$	b^2S/π^2B.
$t =$	$b^2S/2\pi^2B_f$.
$w =$	$w_b + w_s$, i.e. the actual deflection.
w_b	component of deflection due to bending of sandwich plate.
w_s	component of deflection due to shear deformation of the core.

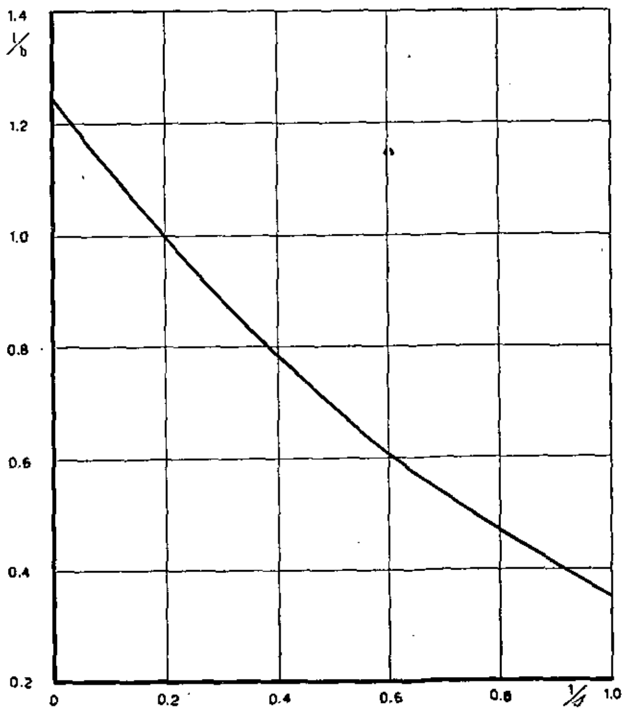

FIGURE 2.6.

Half-wave lengths for infinitely long plates under pure shear when $s>2$.

$$\frac{l}{b} \simeq \frac{5}{4}\ \frac{4s-3}{4s+1}$$

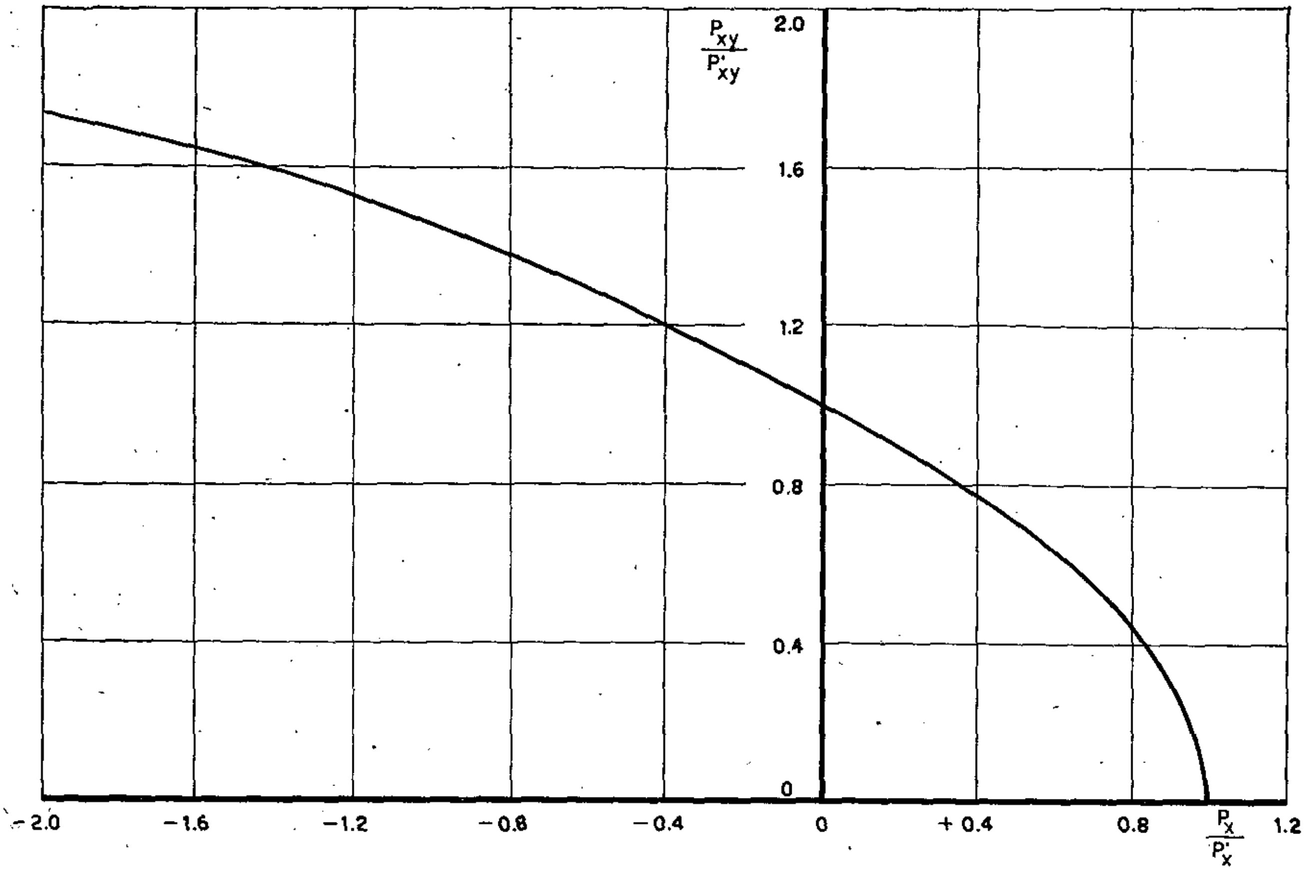

FIGURE 4.1.

Non-dimensional interaction curve for combined longitudinal compression (tension) and shear (Valid for any s and τ).

x, y coordinates in middle plane of sandwich.

$B = \dfrac{E_f f\,(c+f)^2}{2\,(1-\nu_f{}^2)} + \dfrac{E_c c^3}{12\,(1-\nu_c{}^2)}$, i.e. the bending stiffness of sandwich per unit run.

$B_f = \dfrac{E_f f^3}{12(1-\nu_f{}^2)}$, i.e. the bending stiffness of one face per unit run.

E YOUNG's modulus in XY-plane.

G_{cn} shear modulus of core in planes perpendicular to XY-plane.

P_x, P_y, P_{xy} external longitudinal compression, lateral compression and shear per unit run at the stability limit.

P'_x, P'_y, P'_{xy} symbols used for combined loading, denoting the buckling load of the plate subjected to longitudinal compression only, lateral compression only or shear only.

$S = \dfrac{(c+f)^2}{c}\,G_{cn}$, i.e. the shear stiffness of sandwich plate per unit run.

W arbitrary constant in eq. (2.3).

$\lambda =$ l^2/b^2.

$\mu =$ m^2.

$\tau =$ $\dfrac{t}{s} = \dfrac{B}{2B_f} \approx 3\left(1+\dfrac{c}{f}\right)^2$.

$\nu =$ $\dfrac{1}{B}\left\{\dfrac{\nu_f E_f f\,(c+f)^2}{2(1-\nu_f{}^2)} + \dfrac{\nu_c E_c\, c^3}{12\,(1-\nu_c{}^2)}\right\}$, i.e. the effective POISSON's ratio of the sandwich plate.

Δ, Λ c.f. appendix A.

7 References.

1. VAN WIJNGAARDEN, A. The elastic stability of flat sandwich plates. Report S. 319. Versl. en Verh. of the Nationaal Luchtvaartlaboratorium, Amsterdam. Vol. XIII, pp. S 37—S 56 (1947).
2. PLANTEMA, F. J. Calculation of the buckling load of sandwich plates by the energy method, I. Report S. 332 of the Nationaal Luchtvaartlaboratorium, Amsterdam, (April 1948, Dutch with English summary).
3. PLANTEMA, F. J. Calculation of the buckling load of sandwich plates by the energy method, II. Report S. 333 of the Nationaal Luchtvaartlaboratorium, Amsterdam (April 1948, Dutch with English summary).
4. PLANTEMA, F. J. Some investigations on the Euler instability of flat sandwich plates with simply-supported edges. Paper to be published in the Proc. VII Int. Congr. of Appl. Mech. 1948 (Also available as Report S. 337 of the Nationaal Luchtvaartlaboratorium, Amsterdam, June 1948).

5. Bijlaard, P. P. On the elastic stability of sandwich plates. I and II. Proc. Kon. Ned. Ak. v. Wet. (Roy. Neth. Ac. of Sciences), L, 1 and 2, pp. 79—87 and 186—193 (1947).
6. Plantema, F. J. Literature search on sandwich constructions I. Report S. 334 of the Nationaal Luchtvaartlaboratorium, Amsterdam (April 1948, Dutch with English summary).
7. Koiter, W. T. Theoretical investigation of the diagonal tension field of flat plates. Report S. 295 of the Nationaal Luchtvaartlaboratorium, Amsterdam (Oct. 1944, Dutch with English abstract).
8. Koiter, W. T. The effective width of infinitely long flat rectangular plates under various conditions of edge restraint. Report S. 287 of the Nationaal Luchtvaartlaboratorium, Amsterdam (Dec. 1943, Dutch with English abstract).
9. Southwell, R. V. and Skan, S. W. On the stability under shearing forces of a flat elastic strip. Proc. Royal Soc. London, ser. A, vol. 105, No. 733 (May 1, 1924).
10. Schmieden, C. Das Ausknicken eines Plattenstreifens unter Schub- und Druckkräften. Ztschr. f. angew. Math. u. Mech., Bd. 15, Hft. 5, S. 278 (Okt. 1935).

Completed: December 1948.

Appendix A. Derivation of the formula for the buckling load.

For the infinitely long plate the first integrations in eq. (2.1) may be carried out between the limits 0 and $2l$ instead of 0 and a, which infers that the change of potential energy of the external loads and the total elastic energy are equalized per wave length. The integration between 0 and b may be replaced by an integration between 0 and $\frac{1}{2}b$ for wave form (2.3). Substituting $P_x = P_y = 0$, $w = w_b + w_s$ and (2.2) and introducing s and t, eq. (2.1) becomes

$$P_{xy}\int_0^{2l}\int_0^{\frac{1}{2}b}\left\{\frac{\partial}{\partial x}\Phi(w_b)\right\}\left\{\frac{\partial}{\partial y}\Phi(w_b)\right\}dx\,dy =$$

$$\frac{B}{2}\left[\frac{s+t}{t}\int_0^{2l}\int_0^{\frac{1}{2}b}(\Delta w_b)^2 dx\,dy + \right.$$

$$+\frac{b^4}{\pi^4 st}\int_0^{2l}\int_0^{\frac{1}{2}b}\left\{\Delta(\Delta w_b)\right\}^2 dx\,dy +$$

$$-\frac{2b^2}{\pi^2 t}\int_0^{2l}\int_0^{\frac{1}{2}b}(\Delta w_b)\left\{\Delta(\Delta w_b)\right\}dx\,dy +$$

$$-2(1-\nu)\int_0^{2l}\int_0^{\frac{1}{2}b}\left\{\Gamma(w_b) + \frac{s}{t}\Gamma(\Phi(w_b))\right\}dxdy +$$

$$\left. + \frac{b^2}{\pi^2 s}\int_0^{2l}\int_0^{\frac{1}{2}b}\Psi(\Delta w_b)\,dx\,dy\right]. \qquad (A.1)$$

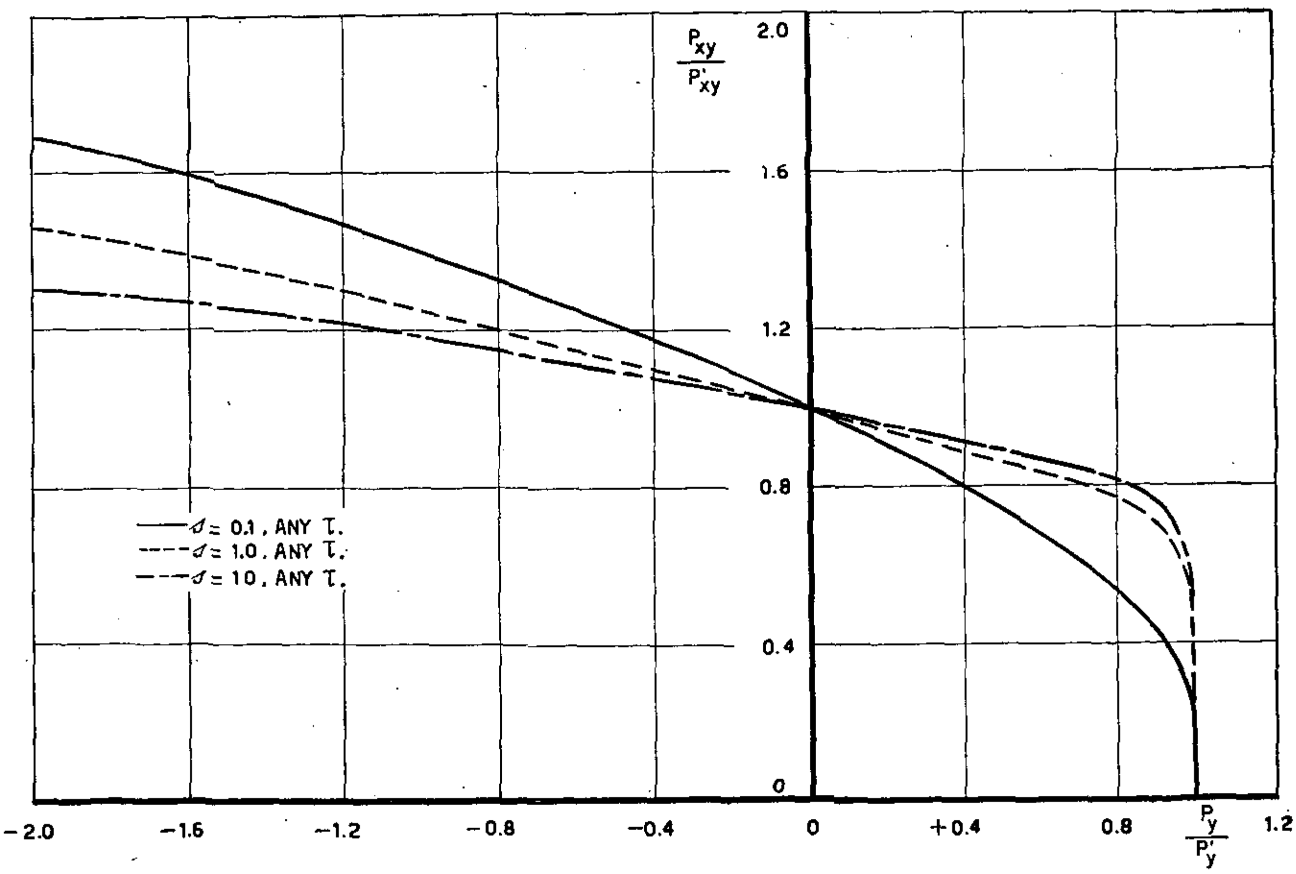

FIGURE 4.2.

Non-dimensional interaction curves for combined lateral compression (tension) and shear.

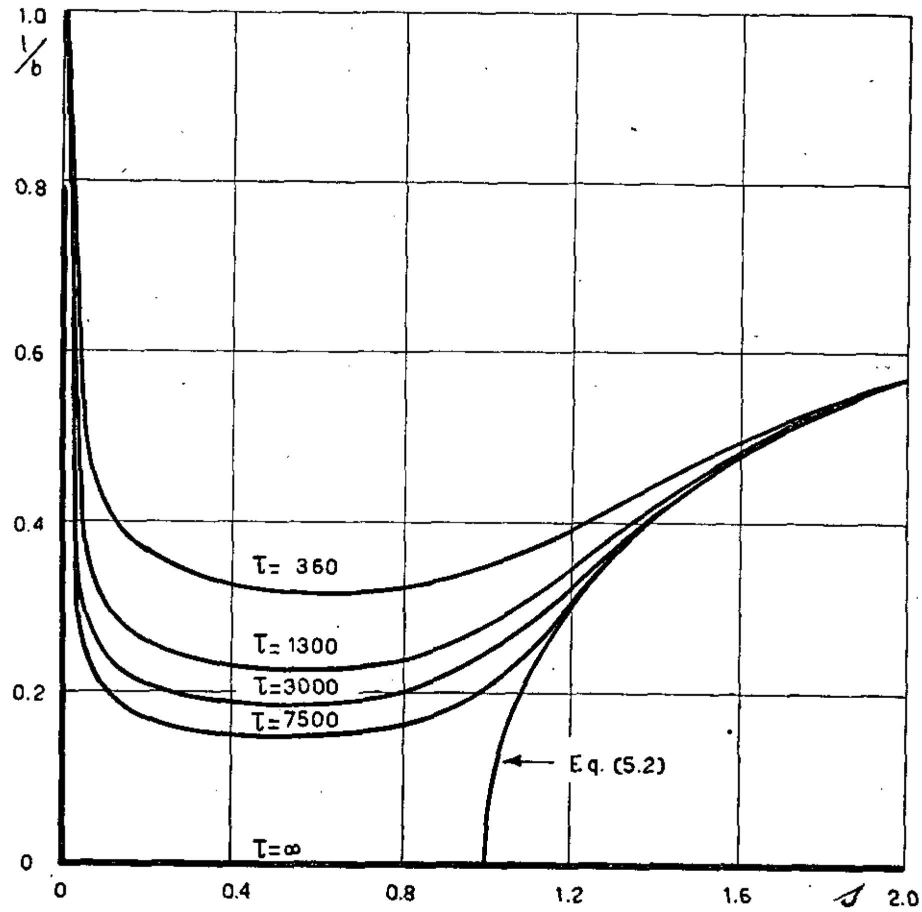

FIGURE 5.1.

Half-wave lengths for infinitely long plates under longitudinal compression; for s>1.5 see eq. (5.2).

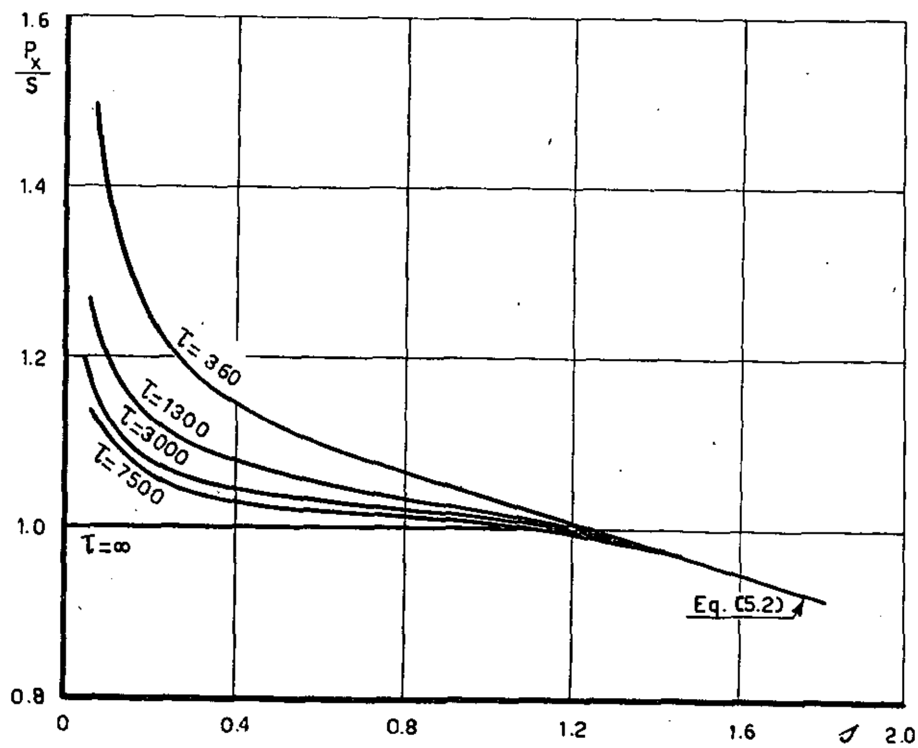

FIGURE 5.2.

Buckling loads for infinitely long plates under longitudinal compression; for s>1.5 see eq. (5.2).

The right hand side may be simplified to

$$\frac{B}{2}\left[\int_0^{2l}\int_0^{\frac{1}{2}b}\left[(\Delta w_b)^2+\frac{s}{t}\left\{\Delta\Phi(w_b)\right\}^2\right]dx\,dy+\right.$$

$$-2(1-\nu)\int_0^{2l}\int_0^{\frac{1}{2}b}\Gamma\left\{w_b+\frac{s}{t}\Phi(w_b)\right\}dx\,dy+$$

$$\left.+\frac{b^2}{\pi^2 s}\int_0^{2l}\int_0^{\frac{1}{2}b}\Psi(\Delta w_b)\,dx\,dy\right]. \qquad (A.2)$$

The operators Λ, Δ, Γ, Ψ and Φ are defined by:

$$\Lambda(\ldots)=\left[\Delta(\ldots)\right]^2-2(1-\nu)\Gamma(\ldots),$$

$$\Delta(\ldots)=\frac{\partial^2(\ldots)}{\partial x^2}+\frac{\partial^2(\ldots)}{\partial y^2},$$

$$\Gamma(\ldots)=\frac{\partial^2(\ldots)}{\partial x^2}\cdot\frac{\partial^2(\ldots)}{\partial y^2}-\left(\frac{\partial^2(\ldots)}{\partial x\,\partial y}\right)^2,$$

$$\Psi(\ldots)=\left(\frac{\partial(\ldots)}{\partial x}\right)^2+\left(\frac{\partial(\ldots)}{\partial y}\right)^2,$$

$$\Phi(\ldots)=\frac{b^2}{\pi^2 s}\Delta(\ldots)-(\ldots).$$

From the fact that the theorem proved by KOITER in the appendix to *ref.* 8 $\left(\iint\Gamma(w)dx\,dy\right.$ is zero in the case of a closed domain bounded by straight lines on which the argument w is a constant) is a particular case of a more general theorem, the conditions of which are satisfied by the chosen expression for w, it follows that the integrals

$$\int_0^{2l}\int_0^{\frac{1}{2}b}\Gamma(w_b)\,dx\,dy \text{ and } \int_0^{2l}\int_0^{\frac{1}{2}b}\Gamma(\Delta w_b)\,dx\,dy$$

vanish (c.f. appendix E).

The solution of equation (A. 1) can be written in the form (2.5). The derivation of the expression for k_b requires an elaborate system of elementary differentiations and integrations, which will be omitted. The final result is

$$k_b=sk_s=\frac{105\pi}{2048\tau}\cdot\frac{\lambda^4 a_1+\lambda^3 a_2+\lambda^2 a_3+\lambda a_4+a_5}{\lambda\sqrt{\mu}\,(\lambda^2 a_6+\lambda a_7+a_8)},$$

where $\lambda=\dfrac{l^2}{b^2}$, $\mu=m^2$. (A. 3)

$$\left.\begin{aligned}
a_1&=128\left\{s^2+(s+1)\,t+1\right\},\\
a_2&=32\ \left\{s(s+t)\,(15\mu+8)+3t(21\mu+4)+\right.\\
&\quad\left.+(255\mu+16)\right\},\\
a_3&=16\ \left\{s(s+t)\,(5\mu^2+12\mu+8)+2t\,(35\mu^2+\right.\\
&\quad\left.+45\mu+12)+(735\mu^2+504\mu+48)\right\},\\
a_4&=\ 2\ \left\{t(35\mu^3+120\mu^2+144\mu+64)+\right.\\
&\quad\left.+2(525\mu^3+1120\mu^2+720\mu+128)\right\},
\end{aligned}\right\}(A.4)$$

$$\left.\begin{aligned}
a_5&=63\mu^4+280\mu^3+480\mu^2+384\mu+128,\\
a_6&=35(s+1)\,(s+4),\\
a_7&=\ 7\ \left\{2s(4\mu+5)+5(7\mu+5)\right\},\\
a_8&=24\mu^2+56\mu+35.
\end{aligned}\right\}(A.4)$$

The determination of the minimum value of k_b or k_s as a function of λ and μ was carried out by writing down the simplest of the two extremum conditions $\partial k/\partial\lambda=0$ and $\partial k/\partial\mu=0$, which proved to be the former, being an algebraic equation of the sixth degree in λ and μ. This equation was solved for λ by substituting a number of well-chosen values of μ. The pairs of corresponding values of λ and μ were then substituted into eq. (A.3) and the minimum of k was determined by plotting k against μ. This procedure infers that the accuracy of the values of λ and μ corresponding to the minimum of k is less than the accuracy with which this minimum is determined; nevertheless, the error never exceeded 1 %.

Appendix B. Approximation for $s > 2$.

In the range $s > 2$ the influence of τ on the buckling load vanishes and in determining the solution we may take τ infinitely large. Eq. (A. 3) is then simplified, but it remains a rather complex expression and, therefore, no attempt was made to use that expression in obtaining the required information. It has been shown in section 3 that the results of *ref.* 5 are for practical purposes identical to those of this report, which permits the use of the data given in *ref.* 5.

When $\tau=\infty$ the buckling load according to *ref.* 5 follows from

$$\frac{1}{P_{xy}}=\frac{1}{P_E}+\frac{1}{P_S}, \qquad (B.\ 1)$$

where P_E is the buckling load according to the normal plate theory ($S=\infty$) and P_S is the buckling load of a hypothetical plate having infinite bending stiffness and shear stiffness S, assuming in both cases that the wave pattern is *the same* as occurs when the actual sandwich plate becomes unstable. These buckling loads P_E and P_S are given in *ref.* 5 as

$$P_E=k_1\frac{B}{b^2} \text{ and } P_S=S\sqrt{1+\lambda}, \qquad (B.\ 2)$$

where k_1 is a function of λ given in fig. 2 of *ref.* 5 [1]). Eq. (B. 1) can now be written in the form

---

[1]) Actually, the more accurate fig. 2 of *ref.* 9 has been used. It is of interest to note that in the case of longitudinal compression we have according to *ref.* 2 : $P_S=S\ (1+\lambda)$. For a sandwich strut or strip, as well as for an infinitely long plate under lateral compression, $P_S=S$.

$$\frac{1}{k_s} = \frac{\pi^2 s}{k_1} + \frac{1}{\sqrt{1+\lambda}}, \qquad \text{(B. 3)}$$

and it remains to determine the maximum of the right hand side as a function of λ. The minima of k_s and k_b and the corresponding values of l/b are plotted in figs. 2.5 and 2.6 as a function of $1/s$. Approximate formulae for $s>2$ are given as eqs. (3.1) in the body of this report.

For $s>100$ the buckling load is represented with an error of less than 5 % by

$$P_{xy} = \frac{5.35}{s} S = 5.35 \frac{\pi^2 B}{b^2}, \qquad \text{(B. 4)}$$

which is the exact expression for a simple plate ($S = \infty$).

It has been shown in section 3 that the energy method of this report yields slightly higher buckling loads. For the case $\tau = s = \infty$ eq. (A. 3) reduces to

$$k_b = \frac{3\pi}{128\lambda\sqrt{\mu}} \left\{ 8\lambda^2 + 2\,(15\mu + 8)\,\lambda + 5\mu^2 + 12\mu + 8 \right\}. \qquad \text{(B.5)}$$

The extremum conditions $\partial k_b/\partial\lambda = \partial k_b/\partial\mu = 0$ yield $\lambda = 1.575$; $\mu = 0.752$; $k_b \doteq 5.414$. (B. 6)

It must further be observed that at large values of s the tacit assumption made throughout this report that the core carries only a small part of the loads may no longer be valid, which would infer that the expression for S and the approximation $\tau = 3(1+c/f)^2$ must be replaced by more accurate expressions. It can be shown that a more accurate expression for S is

$$S = \frac{(c+f)^2}{c} G_{cn} \left[1 - \frac{E_c\,(1-\nu_f^2)}{3 E_f\,(1-\nu_c^2)} \right].$$

The correction factor

$$\frac{E_c\,(1-\nu_f^2)}{3 E_f\,(1-\nu_c^2)} \approx \frac{\pi^2 cf}{3 b^2\,(1-\nu_c)} \, \frac{G_c}{G_{cn}} \, s$$

may be disregarded for practical purposes as long as it remains small, e.g. less than 0.05. Assuming $b/c > 20$, $c/f > 10$, $G_{cn} \geqq G_c$, we find that no correction will be necessary as long as s does not exceed 50. Since for $s>50$ the influence of the finite value of S is already rather small, the simple expression $S = (c+f)^2\, G_{cn}/c$ appears to be satisfactory for any value of s.

With regard to τ, the more accurate expression $\tau \doteq B/2B_f$ can be used when necessary.

Appendix C. Supplementary discussion of the results.

1 Comparison of the cases $s=0$ and $s=\infty$.

The cases $s=0$ and $s=\infty$ both represent buckling of a simple plate. In the former case the core stiffness vanishes and the buckling load is equal to twice the buckling load of one face by itself.

For the latter load table 2.1 yields

$(P_{xy})_{\text{face}} = 5.377\pi^2\, B_f/b^2$.

At first sight, it is surprising that the constant 5.377 in this formula differs from the constant 5.414 found in the case $s = \infty$. This difference can only be caused by a different wave-form assumption.

The wave depth w is a superposition of w_b and w_s. In the case $s = \infty$ the latter component vanishes so that $w = w_b$, c.f. eq. (2.3). In the case $s = 0$ the middle plane of the face is not strained by the buckling deformations, which infers that $w_b = 0$ and $w = w_s$. From eq. (2.2) it appears that w_s is proportional to Δw_b and it is therefore confirmed that the wave form in the case $s = 0$ is indeed different from that in the case $s = \infty$. It is interesting to note that the wave form w_s yields a better approximation to the exact result than the wave form w_b.

The wave forms can also be found from eq. (A. 1).

Substituting $t = s = \infty$ we obtain

$$P_{xy} \iint \frac{\partial w_b}{\partial x} \frac{\partial w_b}{\partial y}\, dx\, dy = \tfrac{1}{2}\,(B + 2B_f) \iint (\Delta w_b)^2\, dx\, dy.$$

Substituting $s = 0$ we obtain

$$P_{xy} \iint \frac{\partial \Delta w_b}{\partial x} \frac{\partial \Delta w_b}{\partial y}\, dx\, dy = B_f \iint (\Delta\Delta w_b)^2\, dx\, dy.$$

Since in the former case the wave form is w_b, the latter case must correspond to a wave form Δw_b.

With the sandwich subjected to biaxial compression the wave forms w_b and w_s are similar (*ref.* 4). Consequently, the above-mentioned paradox does not occur in this case.

2 Some practical data.

Some figures relating to a proposed programme of compression and shear tests will now be given.

The test panels are assumed to have duralumin or high-tensile steel faces, $f = 0.5$ mm and $f = 1$ mm, and Dufaylite honeycomb or onazote cores, $c = 10$ mm and $c = 25$ mm.

The width of all panels is 30 cm.

The material properties are assumed to be

steel: $E_f = 2 \,.\, 10^6$ kg/cm², $\nu_f = 0.3$,
duralumin: $E_f = 0.73 \,.\, 10^6$ kg/cm², $\nu_f = 0.3$,
Dufaylite: $G_{cn} = 280$ kg/cm²,
onazote: $G_{cn} = 100$ kg/cm².

The duralumin faces are glued to both honeycomb and onazote cores; the steel faces only to honeycomb cores.

The computed values of s range from 0.18 to 1.27 and those of τ from 360 to 7800.

The compression panels will have sufficient length to be considered as infinitely long and their longitudinal edges will be simply-supported, so that the theory of *ref.* 4 is applicable. The computed elastic buckling stresses are above the yield stress of the face material for 3 out of the 9 panels (2 duralumin-honeycomb and 1 steel-honeycomb). The computed values of l/b range from 0.16 to 0.37. The ratio of the buckling load to the buckling load of a simple plate having the same bending stiffness as the sandwich ranges from 1/3 to 1/20; this ratio may be considered to represent most adequately the influence of the finite transverse shear stiffness of the sandwich.

It should be noted that the figures given above probably correspond to the lower end of the range of s that will occur in practical applications. The widths of the test panels were restricted to 30 cm in view of the dimensions available in the testing machine at the N.L.L. Since s is proportional to b^2, much larger values than 1.3 may occur in practice, as well as correspondingly larger values of l/b and of the buckling load ratio mentioned in the preceding paragraph.

3 Preliminary proposals for panel design.

Pending the results of further research, in particular regarding the efficiency of sandwich panels, the following procedure is proposed.

We assume that a panel of 70 cm width, which may approximately be considered as infinitely long, has to be designed for buckling under a combination of $P_x = 450$ kg/cm and $P_{xy} = 150$ kg/cm. The faces consist of duralumin, $E_f = 0.73.10^6$ kg/cm², $\nu_f = 0.3$. A honeycomb or lightweight foam core is to be used, so that we may neglect the part of the loads carried by the core.

According to Huber's yield criterion the ideal load is $(P_x^2 + 3P_{xy}^2)^{\frac{1}{2}} = 520$ kg/cm. Choosing the ideal stress as 2600 kg/cm² we find $f = 0.1$ cm.

From figs. 2.2 and 5.2 we observe that P_x' and P'_{xy} will be approximately equal, so that $P_x/P_x' \approx 3\ P_{xy}/P'_{xy}$. From fig. 4.1 we thus find $P_x/P'_x = 0.9$ and therefore $P_x' = 500$ kg/cm.

We now assume that either c or G_{cn} (i.e. the core material) is chosen. As an example of the first case we take $c = 2$ cm.

Then we compute successively

$\tau = 3(1+c/f)^2 = 3\ .\ 21^2 = 1323.$

$$B = \frac{E_f f\ (c+f)^2}{2(1-\nu_f^2)} = \frac{0.73\ .\ 10^6\ .\ 0.1\ .\ 4.41}{2\ .\ 0.91} = \\ = 1.77\ .\ 10^5 \text{ kg/cm},$$

$$\frac{P_x'b^2}{\pi^2 B} = \frac{500\ .\ 70^2}{\pi^2\ .\ 1.77\ .\ 10^5} = 1.4 = s\,\frac{P_x'}{S}.$$

From fig. 5.2 we now easily find $s = 1.45$ and

$$S = s\ \frac{\pi^2 B}{b^2} = 520 \text{ kg/cm};\ G_{cn} = \frac{2\ .\ 520}{4.41} = \\ = 236 \text{ kg/cm}^2.$$

For the second case we assume $G_{cn} = 250$ kg/cm². We then compute

$$B = 2\tau B_f = 2\tau\ \frac{0.73\ .\ 10^6\ .\ 0.1^3}{12\ .\ 0.91} = 134\,\tau,$$

$$t\,\frac{P_x'}{S} = \tau\frac{P_x'b^2}{\pi^2 B} = \frac{500\ .\ 4900}{\pi^2\ .\ 134} = 1850,$$

$$\tau = 3(1 + 10c)^2;\ c + 0.1 = 0.1\sqrt{\tau/3};\ c = \\ = 0.1\sqrt{\tau/3} - 0.1,$$

$$S = \frac{(c+0.1)^2}{c}\ 250 = \frac{0.833\,\tau}{0.1\sqrt{\tau/3} - 0.1},$$

$$s = \frac{4900\ S}{\pi^2\ .\ 134\,\tau} = \frac{30.9}{\sqrt{\tau/3} - 1},$$

$$\tau = 3\left(1 + \frac{30.9}{s}\right)^2;\ t\frac{P_x'}{S} = \tau s\frac{P_x'}{S} = \\ = 1850;\ \frac{c}{f} = \frac{30.9}{s}.$$

We can now choose s, compute τ, read P_x'/S from fig. 5.2 and compute $t\ P_x'/S$. After some trials we find that $t\ P_x'/S = 1850$ corresponds to $s = 1.62$ and $c = \frac{30.9}{1.62}\ 0.1 = 1.91$ cm.

A rather rougher but quicker procedure may be used when it appears that s will not exceed approx. 1.5. In that case we observe from fig. 5.2 that P'_x/S roughly equals unity. We therefore find that $S \approx 500$ and in the first case G_{cn} follows as $G_{cn} = \frac{2}{4.41}\,500 = 227$ kg/cm², whereas in the second case $\frac{(c+0.1)^2}{c} = \frac{500}{250} = 2;\ c = 1.8$. This method is somewhat unconservative when actually P_x' is somewhat smaller than S; for $s < 1.2$ it is conservative.

Appendix D. The interaction curves for combined loading.

The interaction curves for the combinations of longitudinal or lateral compression (tension) and shear (figs. 4.1 and 4.2) have been determined from the graphs given in *ref.* 1. A minor difficulty is that P'_y is not given explicitly in *ref.* 1. Its value was computed from eq. (5.3), which can also be easily derived from eq. (6.14) of *ref.* 1 when it is observed that for pure lateral compression $l = \infty$.

The curves for combinations of lateral compression and shear show that up to a certain value $P_{xy\text{ crit.}}$ of the shear, the compression P_y is equal to that at $P_{xy} = 0$. This phenomenon was already known for the simple plate (*ref.* 10) and it is clear that, as for the simple plate, buckling of the sandwich at $P_{xy} \leqq P_{xy\text{ crit.}}$ will occur with a cylindrical wave form ($l = \infty$).

The values of $P_{xy\text{ crit}}$ are not given in *ref.* 1 and for reasons to be stated hereafter they were computed from the energy method.

All points of the interaction curve satisfy the buckling condition eq. (2.1), where $P_x = 0$. The wave form (2.3) can be retained; for pure lateral compression ($l = \infty$) it yields the same result as given by the rigorous treatment. Also for $P_{xy} \leqq P_{xy\text{ crit.}}$ we have $l = \infty$, which infers that the external shear loading does not contribute to the change of potential energy ($\partial w/\partial x = 0$).

From eq. (2.1), where $P_x = 0$, can be derived an expression

$$P_{xy} = P_{xy}\ (m,\ l,\ P_y) \tag{D. 1}$$

where, when prescribing P_y, m and l must be computed so as to minimize P_{xy}.

Combining the extremum conditions $\dfrac{\partial P_{xy}}{\partial m} = \dfrac{\partial P_{xy}}{\partial l} = 0$ with eq. (D. 1) it is found that, when $P_y \rightarrow P'_y$ (i.e. $l \rightarrow \infty$), then

$$P_{xy\text{ crit.}} = \frac{3\pi\sqrt{6}}{16}\,\frac{\pi^2 B}{b^2}\,\frac{s}{t}\sqrt{\frac{(s+1)\ \{2(s+1)^2 + t(s+1) + ts\}\ \{2(s+1)\ (s+4)^2 + s(s+1) + 2st(s+4)\}}{(s+1)^2\ (s+4)}} \tag{D. 2}$$

whence

$$\frac{P_{xy\text{ crit.}}}{P'_y} = \frac{3\pi\sqrt{6}}{16}\sqrt{\frac{(s+1)\ \{2(s+1)^2 + t(s+1) + ts\}\ \{2(s+1)\ (s+4)^2 + s(s+1) + 2st(s+4)\}}{(s+1)\ (s+4)\ (s+t+1)}} \tag{D. 3}$$

The cases $s = \infty$, $t = \infty$, and $s = 0$, $t = 0$, both corresponding to the simple plate, give respectively;

$m = \dfrac{1}{3}\sqrt{6}$; $\dfrac{P_{xy\text{ crit.}}}{P'_y} = \dfrac{3\pi\sqrt{6}}{8} = 2.885$ (exact value 2.87, *ref.* 10),

$m = \dfrac{1}{12}\sqrt{6}$; $\dfrac{P_{xy\text{ crit.}}}{P'_y} = \dfrac{3\pi\sqrt{6}}{8} = 2.885$ (loc.cit.),

the wave forms being different and corresponding to the cases referred to in appendix C 1.

A graph has been drawn (fig. D. 1) showing the variation of $\dfrac{P_{xy\text{ crit.}}}{P'_y}$ with s (i.e. with the influence of the finite shear stiffness of the core), for various values of τ.

It is evident that the influence of τ vanishes when $s > 1$. For values of s between 0 and 1, minimum values are attained which decrease as τ increases. For very small values of s, the influence of the faces asserts itself and is shown by the values $\dfrac{P_{xy\text{ crit.}}}{P'_y}$ increasing sharply to 2.885.

The values of $P_{xy\text{ crit.}}$ computed from the energy method prove to be in good agreement with the values which may be estimated from the curves of fig. 4.2. This is a rather convincing proof of the validity of the basic assumption made in section 4 that the interaction curves will not be significantly influenced by the method of computation.

No interaction curves for combinations of P_x and P_y have been given, because they proved to be unsuitable for accurate interpolation. If this case has to be calculated, the solution of eq. (5.1) can be performed simply and rapidly. For an infinitely long plate, eq. (5.1) can be simplified by substituting $a/n_x = l$ and $n_y = 1$, which yields

$$P_x + P_y\lambda = S(1+\lambda)^3\left[\frac{1}{1+(1+s)\lambda} + \frac{1}{t\lambda}\right]. \tag{D.4.}$$

Appendix E. Some remarks on the integral $I = \iint (w_{xx}w_{yy} - w_{xy}{}^2)\,dx\,dy$. [1])

In *ref.* 8 it is shown that

$$I = \iint_A (w_{xx}w_{yy} - w_{xy}{}^2)\ dx\ dy = 0$$

in the case of a rectangular domain A, on the boundary of which the function w is a constant. This is a particular case of a more general property which will now be investigated.

The integrand $D = w_{xx}w_{yy} - w_{xy}{}^2$ can be con-

[1]) For convenience, differentiation of w with respect to x will hereafter be denoted by adding a suffix x to w, etc.

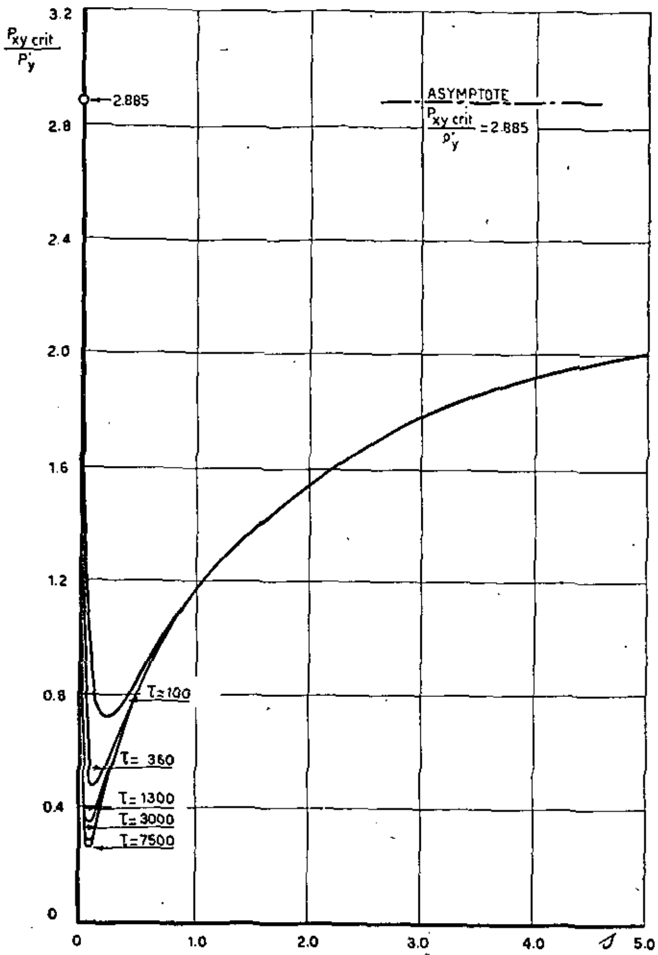

FIGURE D. 1.

Variation of $\frac{P_{xy\ crit.}}{P'_y}$ *with s for various values of* τ .

sidered as the JACOBIAN of the functions $\xi = w_x$, $\eta = w_y$. So, by a transformation from the XY plane to a plane with coordinates ξ and η, the integral will be transformed into $I = \iint \xi \, d\eta$, the integration being taken over the region A' into which the rectangle is transformed. The condition $I = 0$ requires that the total area of this region should be zero. This requirement is obviously satisfied if $D = 0$ everywhere in the rectangle, in which case the rectangle is transformed into one point. Then the surface $w = w(x, y)$ is developable i.e. it consists merely of points where the curvature is parabolic.

Now, a surface $w = w(x, y)$ will be considered which is not developable, the function $w(x, y)$ being for simplicity supposed analytic in the interior of a rectangle in the XY-plane. In order that the total area of the image in the $\xi\ \eta$ plane is zero, the contour of the rectangle must be mapped on a single line in the $\xi\ \eta$ plane. This will be the case if the contour in the XY plane can be divided into two parts, such that to any point of the first part a point of the second part can be joined, having equal values of ξ and η. Then the two parts of the contour are mapped on the same curve of the $\xi\ \eta$ plane. This is seen to be the case if the function $w(x, y)$ satisfies certain conditions of symmetry as is shown by the following examples.

Examples.

1. A simple example is furnished by the function $w\ (x, y) = \sin\frac{\pi x}{a}\sin\frac{\pi y}{b}$. The rectangle is defined by (0,0); (2a, 0); (2a, ½b); (0, ½b).

Then $\xi = w_x = \frac{\pi}{a} \cos \frac{\pi x}{a} \sin \frac{\pi y}{b}$,

$$\eta = w_y = \frac{\pi}{b} \sin \frac{\pi x}{a} \cos \frac{\pi y}{b}.$$

The correspondence between the XY plane and the $\xi\ \eta$ plane is given by the following table.

	x	y	$w_x = \xi$	$w_y = \eta$
CB	$0 \to \frac{1}{2}a$	$0 \to 0$	$0 \to 0$	$0 \to \pi/b$
BE	$\frac{1}{2}a \to a$	$0 \to 0$	$0 \to 0$	$\pi/b \to 0$
EF	$a \to {}^3/_2a$	$0 \to 0$	$0 \to 0$	$0 \to -\pi/b$
FN	${}^3/_2a \to 2a$	$0 \to 0$	$0 \to 0$	$-\pi/b \to 0$
NL	$2a \to 2a$	$0 \to \frac{1}{2}b$	$0 \to \pi/a$	$0 \to 0$
LG	$2a \to {}^3/_2a$	$\frac{1}{2}b \to \frac{1}{2}b$	$\pi/a \to 0$	$0 \to 0$
GD	${}^3/_2a \to a$	$\frac{1}{2}b \to \frac{1}{2}b$	$0 \to -\pi/a$	$0 \to 0$
DH	$a \to \frac{1}{2}a$	$\frac{1}{2}b \to \frac{1}{2}b$	$-\pi/a \to 0$	$0 \to 0$
HA	$\frac{1}{2}a \to 0$	$\frac{1}{2}b \to \frac{1}{2}b$	$0 \to \pi/a$	$0 \to 0$
AC	$0 \to 0$	$\frac{1}{2}b \to 0$	$\pi/a \to 0$	$0 \to 0$

The table is graphically illustrated by fig. E. 1. It is seen that the image of the contour of the rectangle in the XY plane consists of line segments on the axes of coordinates in the $\xi\ \eta$ plane enclosing a total area of zero. It is also clearly seen that the integral is zero when extended over a smaller area, for instance CEDA or EFGD.

The line segments AB, BD, DF, FL are the projections on the XY plane of the locus of the points on the surface $w = w\ (x, y)$ where the curvature is parabolic, i.e. the locus of the points for which the GAUSSIAN modulus of curvature $K = \frac{1}{R_1 R_2}$, is zero. This locus consists of the arcs BM*A, BS*D, FT*D and FU*L.

2. A somewhat more intricate example is furnished by the fuction $w\ (x, y) = \sin\frac{\pi y}{b}\sin\frac{\pi}{l}A$, where $A = x + \frac{mb}{\pi}\cos\frac{\pi y}{b} - \frac{1}{2}\,mb$, in the region $0 \leqq x \leqq 2l;\ 0 \leqq y \leqq \frac{1}{2}b$.

Then $\xi = w_x = \frac{\pi}{l}\sin\frac{\pi y}{b}\cos\frac{\pi}{l}\,A$;

$$\eta = w_y = \frac{\pi}{b}\cos\frac{\pi y}{b}\sin\frac{\pi}{l}A - \frac{\pi m}{l}\sin^2\frac{\pi y}{b}\cos\frac{\pi}{l}\,A.$$

The correspondence between the XY plane and the ξ η plane is given by the following table.

	x	y	ξ	η	for $\frac{b}{l}=\frac{1}{2};\ m=\frac{1}{3}$ $\frac{l}{\pi}\xi$	$\frac{l}{\pi}\eta$
OD	$0 \to \frac{1}{2}l$	$0 \to 0$	$0 \to 0$	$-\frac{\pi}{b}\sin\beta \to +\frac{\pi}{b}\cos\beta$	$0 \to 0$	$-0.59 \to +1.91$
DE	$\frac{1}{2}l \to l$	$0 \to 0$	$0 \to 0$	$+\frac{\pi}{b}\cos\beta \to +\frac{\pi}{b}\sin\beta$	$0 \to 0$	$+1.91 \to +0.59$
EF	$l \to {}^3/_2 l$	$0 \to 0$	$0 \to 0$	$+\frac{\pi}{b}\sin\beta \to -\frac{\pi}{b}\cos\beta$	$0 \to 0$	$+0.59 \to -1.91$
FA	${}^3/_2 l \to 2l$	$0 \to 0$	$0 \to 0$	$-\frac{\pi}{b}\cos\beta \to -\frac{\pi}{b}\sin\beta$	$0 \to 0$	$-1.91 \to -0.59$
AB	$2l \to 2l$	$0 \to \frac{1}{2}b$	$0 \to +\frac{\pi}{l}\cos\alpha$	$-\frac{\pi}{b}\sin\beta \to -\frac{\pi m}{l}\cos\alpha$	$0 \to +0.97$	$-0.59 \to -0.32$
BG	$2l \to {}^3/_2 l$	$\frac{1}{2}b \to \frac{1}{2}b$	$+\frac{\pi}{l}\cos\alpha \to -\frac{\pi}{l}\sin\alpha$	$-\frac{\pi m}{l}\cos\alpha \to +\frac{\pi m}{l}\sin\alpha$	$+0.97 \to -0.26$	$-0.32 \to +0.08$
GH	${}^3/_2 l \to l$	$\frac{1}{2}b \to \frac{1}{2}b$	$-\frac{\pi}{l}\sin\alpha \to -\frac{\pi}{l}\cos\alpha$	$+\frac{\pi m}{l}\sin\alpha \to +\frac{\pi m}{l}\cos\alpha$	$-0.26 \to -0.97$	$+0.08 \to +0.32$
HK	$l \to \frac{1}{2}l$	$\frac{1}{2}b \to \frac{1}{2}b$	$-\frac{\pi}{l}\cos\alpha \to +\frac{\pi}{l}\sin\alpha$	$+\frac{\pi m}{l}\cos\alpha \to -\frac{\pi m}{l}\sin\alpha$	$-0.97 \to +0.26$	$+0.32 \to -0.08$
KC	$\frac{1}{2}l \to 0$	$\frac{1}{2}b \to \frac{1}{2}b$	$+\frac{\pi}{l}\sin\alpha \to +\frac{\pi}{l}\cos\alpha$	$-\frac{\pi m}{l}\sin\alpha \to -\frac{\pi m}{l}\cos\alpha$	$+0.26 \to +0.97$	$-0.08 \to -0.32$
CO	$0 \to 0$	$\frac{1}{2}b \to 0$	$+\frac{\pi}{l}\cos\alpha \to 0$	$-\frac{\pi m}{l}\cos\alpha \to -\frac{\pi}{b}\sin\beta$	$+0.97 \to 0$	$-0.32 \to -0.59$

where $\alpha = \frac{\pi}{2}\,m\,\frac{b}{l};\ \beta = \frac{\pi - 2}{2}\,m\,\frac{b}{l}$.

The values given in the last two columns are for $\frac{b}{l} = \frac{1}{2}$; $m = \frac{1}{3}$, from which fig. E. 2 is readily derived.

The area enclosed by the image of the contour of the rectangle OABC in the ξ η plane is zero, as this image consists of line segments which are described twice in opposite directions when the contour of OABC is followed entirely.

Although the latter does not apply to the halves OEHC and EABH separately, the integral I nevertheless vanishes for each half, which is evident from an inspection of the images in the ξ η plane, taking into account that the boundaries of the areas EHN and NBO in the ξ η plane are followed in opposite directions (clockwise, respectively counterclockwise), so that these areas cancel out. The same result follows from the fact that the contours of these rectangles consist of pairs of points such that the values of ξ and η in these points are equal.

For $\frac{b}{l} = \frac{1}{2}$, $m = \frac{1}{3}$ the locus of parabolic points is computed.

From $D = w_{xx}\, w_{yy} - w_{xy}{}^2 = 0$ it follows

$$x = \frac{l}{\pi}\left[m\left(\frac{\pi}{2} - \cos\frac{\pi y}{b}\right)\operatorname{tg}\alpha\text{-arc tg}\left\{\sec\alpha\ \operatorname{cotg}\frac{\pi y}{b}\left(\sin\frac{\pi y}{b} \pm 1\right)\right\}\right],$$

which is the equation of the projection of this locus on the XY plane.

The results are shown in fig. E. 2 (dotted lines). From this graph it is also evident that I must be zero and that the same is true for parts OEHC and EABH separately.

When w is constant on the boundary of the rectangle $(0,0)$; $(a,0)$; (a, b); $(0, b)$ it is clearly a

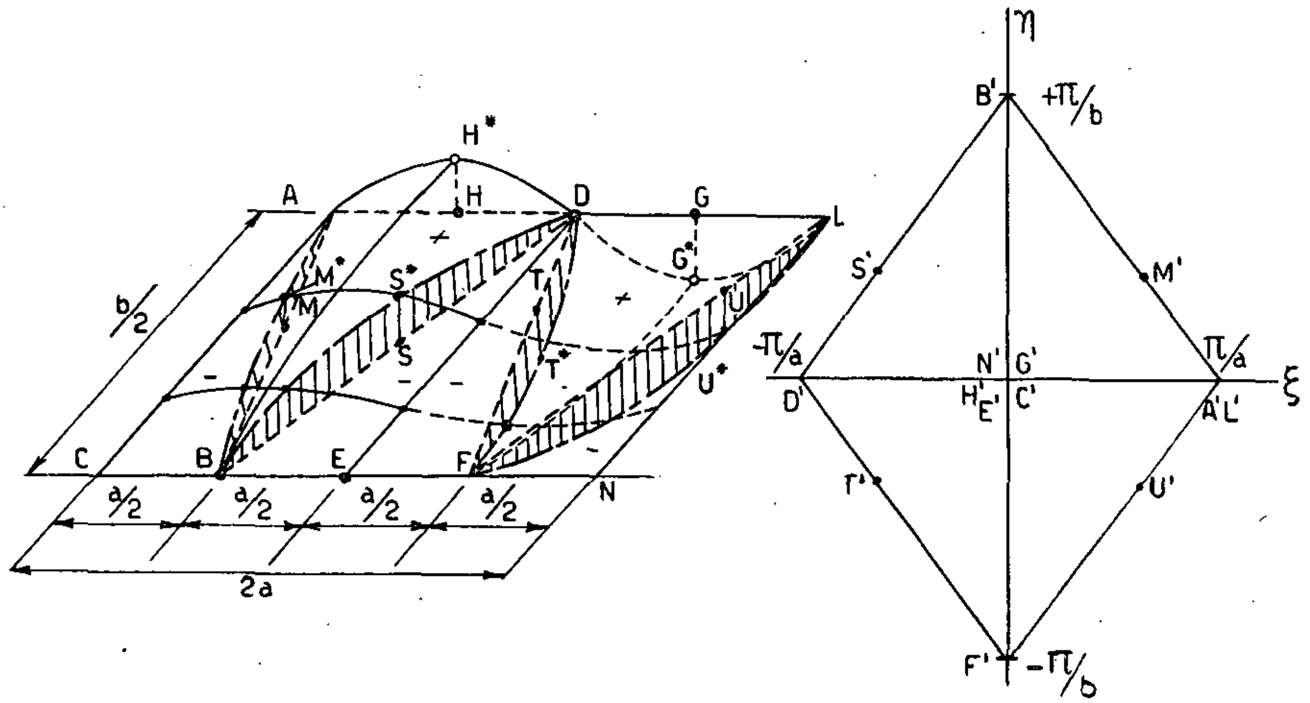

FIGURE E.1.

Perspective view of the surface $w\ (x, y) = \sin \frac{\pi x}{a} \sin \frac{\pi y}{b}$ *with its parabolic curves (left hand side) and mapping of the contour on the* $\xi\ \eta$ *plane (right hand side).*

particular case of the foregoing more general one, as in this case the points on the contour satisfy the condition mentioned above. In this case the proof that I vanishes can immediately be derived from the application of the integral formula of GAUSS—BONNET to the rectangle, according to which

$$\oint \frac{ds}{\rho_g} + \iint D\ dx\ dy = 2\pi.$$

When w = const. the sides of the rectangle are geodetics, hence the geodetic curvature ρ_g is infinite and the contour integral of the geodetic curvature vanishes apart from the contributions at every corner, which are equal to the external angle. Thus

4. $\frac{\pi}{2} + \iint D\ dx\ dy = 2\pi$, from which it follows that $\iint D\ dx\ dy = 0$.

Finally, a few further remarks may be made:

1. The extremes of the w surface are mapped on the origin of the $\xi\ \eta$ plane, $w_x = \xi$ and $w_y = \eta$ being zero; e.g. G* and H* of fig. E. 1 and K, M, N, P of fig. E. 2.
2. $I = \iint\limits_A D\ dx\ dy$ is independent of the orientation of the axes of coordinates, provided they are rectangular, D being an invariant for all systems of such axes.
3. $I = \iint\limits_A D\ dx\ dy$ taken over a closed domain is defined as the whole curvature of the domain, i.e. the area described on a sphere of unit radius by radii drawn parallel to the normals of the surface along the boundary. Thus the whole curvature equals a solid angle the extent of which depends solely on the boundary conditions, provided that the surface contains no singular points inside the boundary. Integrating for instance over a semisphere one finds $I = 2\pi$; integrating over a cone the result is zero as the contribution to the whole curvature by the radii of the sphere drawn parellel to the boundary normals along the base of the cone is cancelled by the contribution of the normals through the top of the cone.
4. In all cases hitherto encountered $\int_0^a \int_0^b \left\{(\Delta w)_{xx}\ (\Delta w)_{yy} - (\Delta w)^2_{xy}\right\} dx\, dy$ vanishes when $\int_0^a \int_0^b (w_{xx}\, w_{yy} - w_{xy}{}^2)\, dx\, dy$ vanis-

hes, both integrals taken over the same rectangle. A general proof of this statement, however, has so far not been given.

5. While the foregoing is not a rigid mathematical proof of a general theorem, it has been demonstrated that certain additional instances occur, where $\iint D\,dx\,dy$ is zero, other than for the case mentioned in *ref.* 8.

Acknowledgement. The advice and assistance of Dr. R. Timman, research engineer at the NLL, in preparing this appendix are gratefully acknowledged.

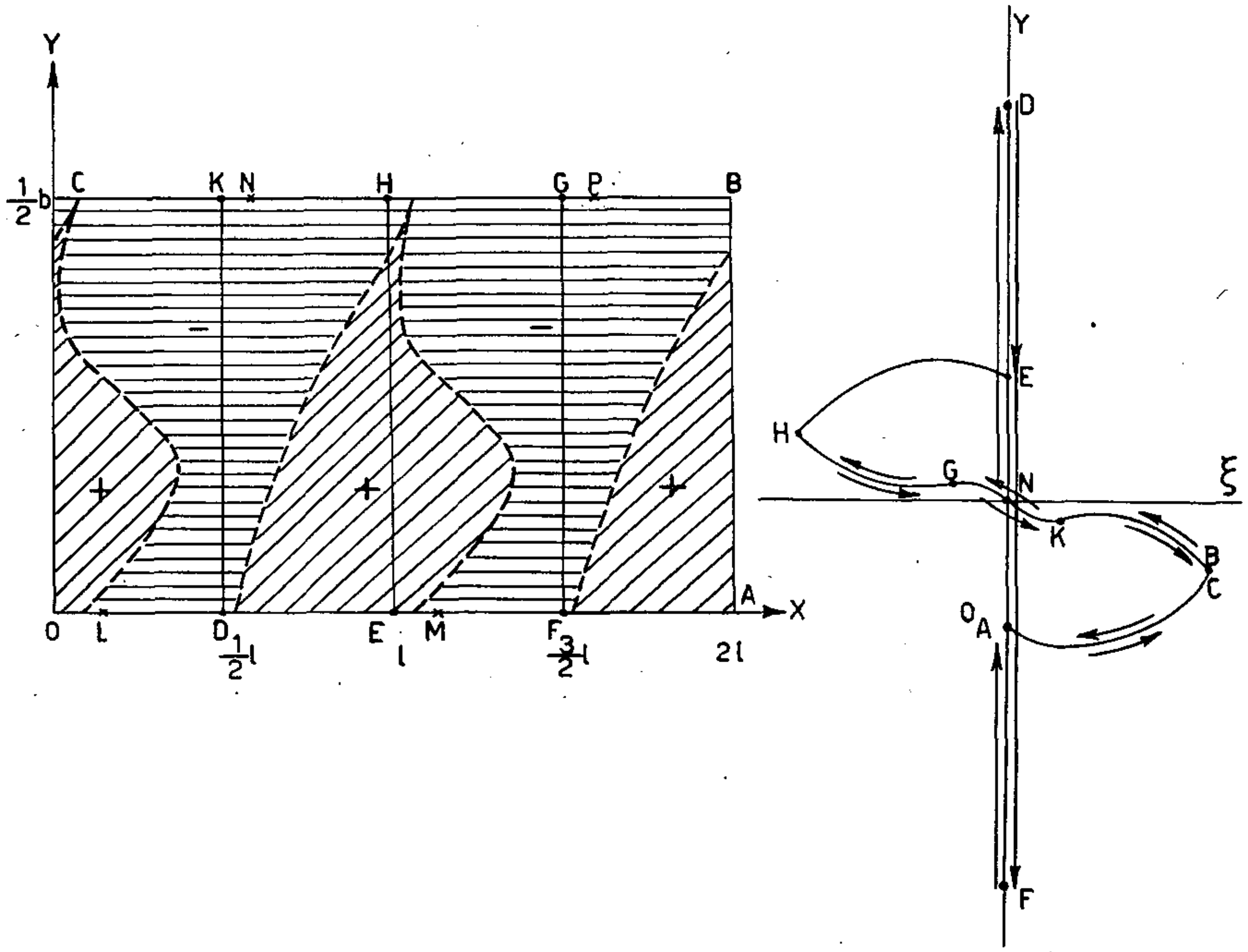

FIGURE E.2.

Projection on the XY plane of the parabolic curves on the surface

$w(x,y) = \sin\frac{\pi y}{b}\sin\frac{\pi}{l}\left(x+\frac{mb}{\pi}\cos\frac{\pi y}{b} - \tfrac{1}{2}mb\right)$ *(left hand side) and mapping of the contour on the* $\xi\,\eta$ *plane (right hand side).*

REPORT S. 347.

Load Distribution and Relative Stiffness Parameters for a Reinforced Flat Plate containing a Rectangular Cut-out under Plane Loading

by

L. S. D. MORLEY.

Summary.

A method is given for the determination of the load distribution and relative stiffness parameters for a three bay flat monocoque plate containing a rectangular cut-out in the centre bay and under plane loading. Conventional shell theory is used and no new principles or assumptions are introduced. The paper serves as an introduction to a general theory for the distribution of loads throughout open and closed shells containing cut-outs.

Contents.

N.B. This report was prepared in charge of the *Netherlands Aircraft Development Board.*

1 Introduction.

One of the most pertinent problems in the theory of aircraft structures is the determination of the stress distribution in the neighbourhood of a large rectangular cut-out in a reinforced monocoque structure. Examples of such cut-outs are the openings required in fuselages for doors, etc. and the openings in wings required for retraction of the undercarriage mechanism. Also, especially for flutter calculations, it is necessary to have a reliable estimation of the stiffness of such structures.

There does not appear to be much available literature on this type of problem. P. Kuhn and other authors (refs. 2 and 3) have devised an approximate solution for the flat plate with a rectangular cut-out under a pure tension load only. This consists essentially of the substitute stringer method of shear-lag analysis and solutions are given for two and three substitute stringers. An article by D. Williams (ref. 4) considers the effect of cover discontinuities on the strength and stiffness of stressed skin wings, but the method does not permit of generality. It is therefore intended to present a method which permits of some considerable generality, which is based on conventional shell theory and does not require the introduction of extraneous assumptions.

It is not proposed to deal with the general problem in this paper, which is intended merely to serve as an introduction to the general theory. With this in view, a very simple problem has been chosen which consists of a flat three bay reinforced monocoque plate containing a rectangular cut-out in the centre bay. In total there are $2n + 1$ stringers and $2m - 1$ discontinuous stringers for the plate with an odd number of stringers which is considered here; an even number of stringers requiring simple and obvious modifications in the formulation. The plate has a high degree of symmetry which permits an extremely rapid computation of the load distribution throughout the plate.

The problem of discrete stringers has been chosen because uniformly distributing the stringers does not appear to cause worthwhile advantages and is of doubtful practical significance for plates having a moderate number of stringers. Furthermore, discrete stringers allow the investigation of the effect of reinforcing the stringers bordering the cut. However, because of the introductory nature of the paper, it has been decided not to investigate this effect and other current problems such as the decay of the stress perturbations in a many bayed plate, the effect of the bending of stringers and ribs in the plane of the sheet, etc.

Conventional shell theory has been used and it has not been found necessary to introduce any new assumptions and principles. Conventional shell theory infers that the shear stress in a panel is constant and this will be very nearly true provided that the length of the panel is not too great. For long panels, one must consider the exponential decay of the forces which entails some additional labour, although the solution is yielded by a similar procedure as presented here. T. Rand (ref. 5) has made an extensive investigation of the usually accepted approximations used in shell theory.

For the plate considered the solution is mathematically exact within the confines of conventional shell theory. As usual, the ribs and stringers are assumed to have vanishing rigidity in bending in the plane of the sheet. This immediately infers that the axial load in the discontinuous stringers at the cut-out must be zero. This is quite justifiable for it can be shown that the ribs must possess an extremely high rigidity in bending in the plane of the sheet in order to influence the stringer loads in this manner.

The flat plate considered is shown in fig. 1 and it is assumed to have complete symmetry about the X and Y axes, so that for symmetrical loading such as uniform tension, pure bending and pure shear, as shown in fig. 2, the degree of redundancy is reduced fourfold. The number of redundancies can easily be assessed, for when all the axial loads in the stringers are known the internal load distribution is completely specified. Since the constant shear in the panels infers a linear variation of axial load along each bay, it is necessary only to define the axial loads in the stringers at the intersection of stringers and ribs.

Attention can now be confined to one quadrant of the plate and for convenience this is chosen as the second quadrant because the resulting formulation is rendered somewhat simpler. The redundancies are chosen as the axial loads in the stringers at rib 1, this choice being discussed in more detail later on in the analysis. The values of the redundancies are found by making the strain energy stored in the plate a minimum.

One numerical example is considered in detail for a 13-stringer plate having 5 discontinuous stringers. It is shown that the problem of pure shear (case (c)) yields the simplest and most rapid solution. Numerical computation has been reduced to a minimum by the artifice of operating on only one bay.

2 The reinforced flat plate.

The structure considered for this analysis is a flat plate of monocoque construction having three equal bays with a rectangular cut-out in the centre bay. For simplicity, the analysis will be restricted to plates having complete symmetry about a pair of rectangular axes with their origin at the centroid of the plate, as shown in fig. 1.

The plate is made of thin sheet metal and is reinforced with four transverse ribs and a system of longitudinal stringers. To simplify further the analysis, it is assumed that the ribs and stringers have constant and equal cross-sectional areas A_R and A_S respectively and that the sheet has constant thickness t. In conformity with usual shell analysis, the part of the sheet which is considered effective in carrying axial stresses is added to the cross sectional area of the ribs and stringers to form the total effective cross-sectional area resisting axial stresses. Furthermore, it is assumed that

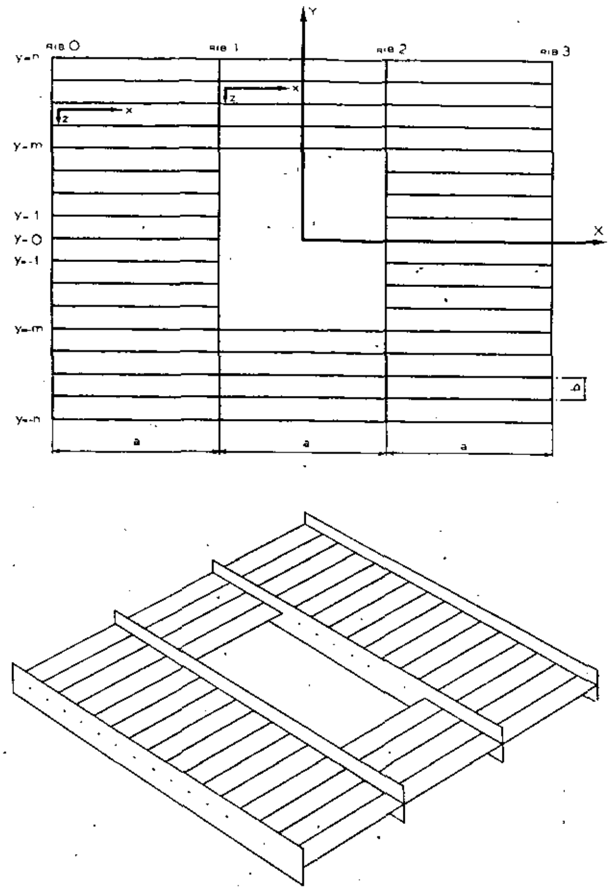

Perspective view.

Fig. 1

The flat monocoque plate.

the neutral axes of the ribs and stringers lie on the skin line and that they have vanishing rigidity in bending in the plane of the sheet. It is convenient to choose rectangular systems of axes x—z for each panel as shown in fig. 1.

Finally, Hooke's law is assumed to be valid and buckling is excluded.

3 The redundancies.

In general, the plate shown in fig. 1 possesses $4\ (n-m)$ redundancies or statical indeterminacies and when these are known the stress distribution in the whole plate is completely specified. However, for the separate loading conditions of Tension, Bending and Shear (as in fig. 2 for cases (a), (b) and (c) respectively) there is an immediate reduction in the number of redundancies which is due to the symmetry of the geometry and stress distributions about the rectangular axes X and Y. It is proposed to deal only with these three regular distributions of loading since they are of the greatest interest, but the method given in this paper can cope with any distribution of the external forces.

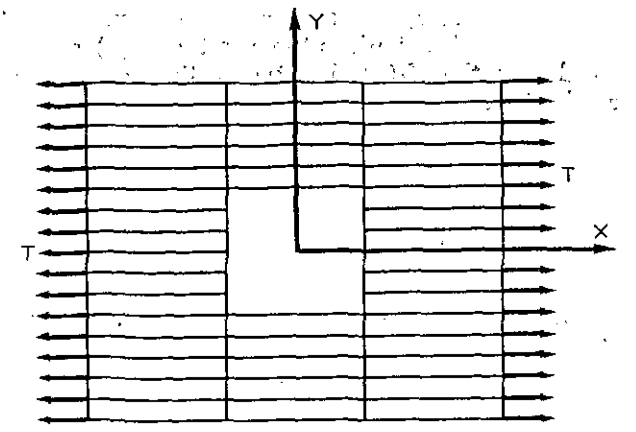

case (a)

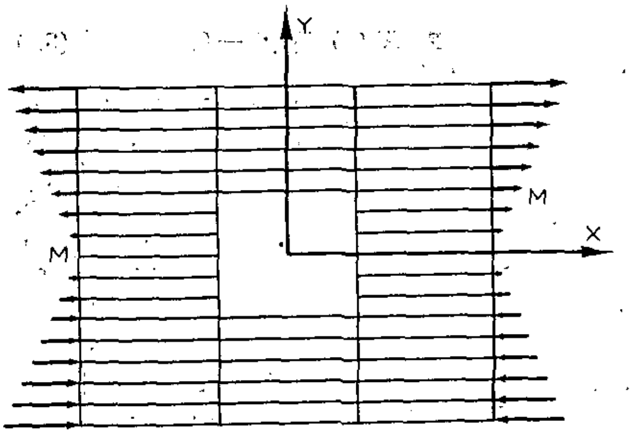

case (b)

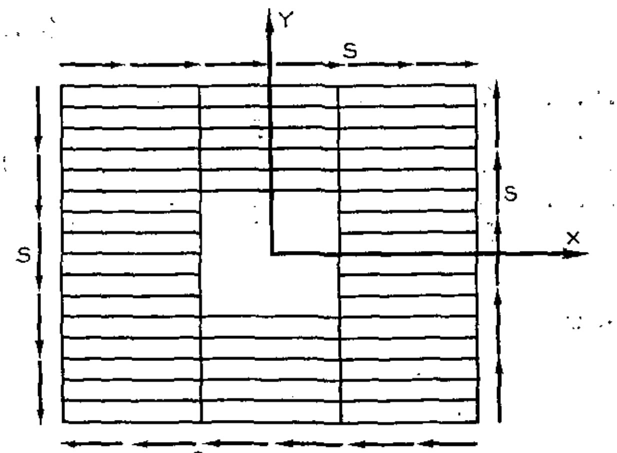

case (c)

Fig. 2

The loading cases.

Now, it follows that the stress distributions for the various loading conditions will satisfy the underlying symmetrical properties with respect to the X and Y axes, viz.:

case	stress	X axis	Y axis
case (a)	p s q	sym. antisym. sym.	sym. antisym. sym.
case (b)	p s q	antisym. sym. antisym.	sym. antisym. sym.
case (c)	p s q	antisym. sym. antisym.	antisym. sym. antisym.

where p is an axial stress in a stringer, s is a shear stress in a panel and q is an axial stress in a rib; eg. for case (b), the axial stresses in the stringers are antisymmetrically distributed about the X axis and symmetrically distributed about the Y axis.

It is therefore evident that attention may now be confined to one quadrant of the plate, thereby reducing the redundancies to $n-m$ in number. At least, there are $n-m$ redundancies for cases (a) and (b) but it will be shown later that there are only $n-m-1$ redundancies for case (c).

There is complete freedom in the choice of the statically indeterminate quantities provided that they are linearly independent of one another; they may be taken as axial loads in the stringers, shears in the panels, axial loads in the ribs or they can even be a combination of these possibilities. A careful choice of the redundant quantities will, however, entail a considerable reduction in the algebraic formulation and arithmetic computation. With this in view, the redundancies have been chosen as axial load distributions in the stringers at rib 1. Here, $2m-1$ of the loads are zero, which is a direct consequence of the inability of the ribs to resist bending in the plane of the sheet, so that $n-m+1$ linearly independent axial load distributions can always be found.

Following the procedure of E b n e r and K ö l l e r (ref. 1), these distributions $X_i(y)$ will be chosen so that they are statically zero and contribute nothing to any boundary conditions that may exist, while the particular solution $X_0(y)$ may be taken as any statically correct distribution which also satisfies the boundary conditions. The $X_i(y)$ then constitute the redundancies of the problem and it is necessary to find the particular linear combination of them which satisfies the condition for minimum strain energy in the plate. If the distributions $X_i(y)$ were not chosen as being statically zero, the ensuing strain energy analysis would be rendered more complicated because when the condition of minimum strain energy is imposed it would be necessary to impose a restriction on the variations of the redundancies, and this infers the existence of two extra "redundancies".

The axial load $P_1(y)$ in the yth stringer at rib 1 consists of a linear combination of the $X_i(y)$ and is

$$P_1(y) = X_0(y) + \sum_i \alpha_i X_i(y), \qquad (3.1)$$

where $i = 1, 2, 3, \ldots\ldots n - m$ for cases (a) and (b) and $i = 1, 2, 3, \ldots\ldots n - m - 1$ for case (c). The equations of equilibrium that $P_1(y)$ must satisfy are:

$$\left.\begin{array}{ll}
\text{for case (a)} & 2 \sum\limits_{y=m}^{n} P_1(y) = 2 \sum\limits_{y=m}^{n} X_0(y) = T, \text{ the total applied tension,} \\
\text{for case (b)} & 2 \sum\limits_{y=m}^{n} yP_1(y) = 2 \sum\limits_{y=m}^{n} yX_0(y) = M, \text{ the total applied moment,} \\
\text{and case (c)} & \sum\limits_{y=m}^{n} yP_1(y) = \sum\limits_{y=m}^{n} yX_0(y) = 0, \\
 & 2 \sum\limits_{y=m}^{n} P_1(y) = 2 \sum\limits_{y=m}^{n} X_0(y) = aS, \text{ where } S \text{ is the applied shear/unit run.}
\end{array}\right\} \qquad (3.2)$$

The last equation for case (c) is the boundary condition which reduces the number of redundancies by one. This condition is essentially depending on the antisymmetry about the Y-axis of the axial loads in the stringers.

The choice of the distributions for $X_0(y)$ and $X_i(y)$ is quite arbitrary provided that they satisfy the appropriate conditions (3.2) and are linearly independent. The linear independency of the distributions can be expressed by the non-vanishing of the following determinants:

$$\text{for cases (a) and (b)} \quad \begin{vmatrix}
X_0(n) & X_1(n) & \cdots & X_{n-m-1}(n) & X_{n-m}(n) \\
X_0(n-1) & X_1(n-1) & \cdots & X_{n-m-1}(n-1) & X_{n-m}(n-1) \\
\cdots & \cdots & \cdots & \cdots & \cdots \\
X_0(m+1) & X_1(m+1) & \cdots & X_{n-m-1}(m+1) & X_{n-m}(m+1) \\
X_0(m) & X_1(m) & \cdots & X_{n-m-1}(m) & X_{n-m}(m)
\end{vmatrix} \neq 0$$

$$(3.3)$$

$$\text{and for case (c)} \quad \begin{vmatrix}
1 & n & X_1(n) & \cdots & X_{n-m-2}(n) & X_{n-m-1}(n) \\
1 & n-1 & X_1(n-1) & \cdots & X_{n-m-2}(n-1) & X_{n-m-1}(n-1) \\
\cdots & \cdots & \cdots & \cdots & \cdots & \cdots \\
1 & m+1 & X_1(m+1) & \cdots & X_{n-m-2}(m+1) & X_{n-m-1}(m+1) \\
1 & m & X_1(m) & & X_{n-m-2}(m) & X_{n-m-1}(m)
\end{vmatrix} \neq 0$$

It is, however, rather more convenient when choosing the distributions to make the $X_0(y)$ orthogonal with the $X_i(y)$, i.e. they satisfy conditions of the type

$$\sum_{y=m}^{n} X_0(y)\, X_i(y) = 0, \qquad (3.4)$$

as then there is some considerable simplification in the computational work. To achieve this orthogonality, it is only necessary to choose the distributions $X_0(y)$ in a certain manner, so that they consist of a linear combination of the two natural distributions, viz. uniform tension and simple bending, and satisfy the appropriate conditions (3.2). It can be verified that the correct distributions are:

$$\left.\begin{array}{ll}
\text{case (a)} & X_0(y) = \dfrac{T}{2e} \quad \Big\} \; y = n, n-1, \ldots\ldots m+1, m \\
\text{case (b)} & X_0(y) = \dfrac{My}{2gb} \quad \Big\} \; y = -m, -m-1, \ldots\ldots -n+1, -n \\
\text{case (c)} & X_0(y) = -\dfrac{aS}{2(ge - f^2)}(fy - g); \; y = n, n-1, \ldots\ldots m+1, m \\
 & = -\dfrac{aS}{2(ge - f^2)}(fy + g); \; y = -m, -m-1, \ldots\ldots -n+1, -n \\
\text{where: } & e = n - m + 1 \\
 & f = \sum\limits_{y=m}^{n} y = \tfrac{1}{2}\{n(n+1) - m(m-1)\} \\
 & g = \sum\limits_{y=m}^{n} y^2 = \tfrac{1}{6}\{n(n+1)(2n+1) - m(m-1)(2m-1)\}
\end{array}\right\} \qquad (3.5)$$

and then the only remaining condition is that the $X_i(y)$ are statically zero to achieve the desired orthogonality relations.

The foregoing will be clarified by considering a particular example, such as $n=6$ and $m=3$ for the plate shown in fig. 1. There are then three redundancies for cases (a) and (b), and only two for case (c). Suitable $X_i(y)$ distributions are shown in fig. 3 and the $X_0(y)$ have been determined according to equations (3.5). It can be verified that the distributions are linearly independent by making the appropriate substitutions into the determinants (3.3).

4 The loads in the plate.

The problem has now resolved into the determination of the expression $P_1(y)$, or in other words it remains only to find the values of the coefficients α_i so as to obtain a complete specification of the load or stress distribution in the plate. It is now proposed to express this load distribution throughout the plate in terms of the α_i in preparation for the strain energy analysis.

The load distribution in the stringers at rib 0 must match the boundary conditions existing there, thus they are given by

$$\left.\begin{aligned} P_0(y) &= \frac{T}{2n+1} \quad \text{for case (a)}, \\ P_0(y) &= \frac{3My}{n(n+1)(2n+1)b} \quad \text{for case (b)}, \\ P_0(y) &= 0 \quad \text{for case (c)}, \end{aligned}\right\} \quad (4.1)$$

these expressions remaining valid for $-n \leq y \leq n$.

In the following general expressions for the load distribution throughout the structure, the appropriate values of $P_0(y)$, $P_1(y)$ etc. must be substituted depending on the particular case under consideration. Now, 'simplified shell theory' infers a linear variation of axial load along each bay, hence the axial load along the stringers may be expressed by

$$\left.\begin{aligned} P_1(y,x) &= P_0(y) + \frac{x}{a}\{P_1(y) - P_0(y)\}, \\ P_2(y,x) &= P_1(y) + \frac{x}{a}\{P_2(y) - P_1(y)\}, \\ P_3(y,x) &= P_2(y) + \frac{x}{a}\{P_3(y) - P_2(y)\}, \end{aligned}\right\} \quad (4.2)$$

the expressions remaining valid only for the first, second and third bays respectively.

This linear variation of end load in the stringers infers that the shear is constant in each panel, so that from elementary considerations of equilibrium the shear in the top panel of the first bay must be

$$S_1(n) = S + \frac{1}{a}\{P_1(n) - P_0(n)\},$$

where S is the applied shear per unit run. In the second panel down, the shear is

$$S_1(n-1) = S_1(n) + \frac{1}{a}\{P_1(n-1) - P_0(n-1)\},$$

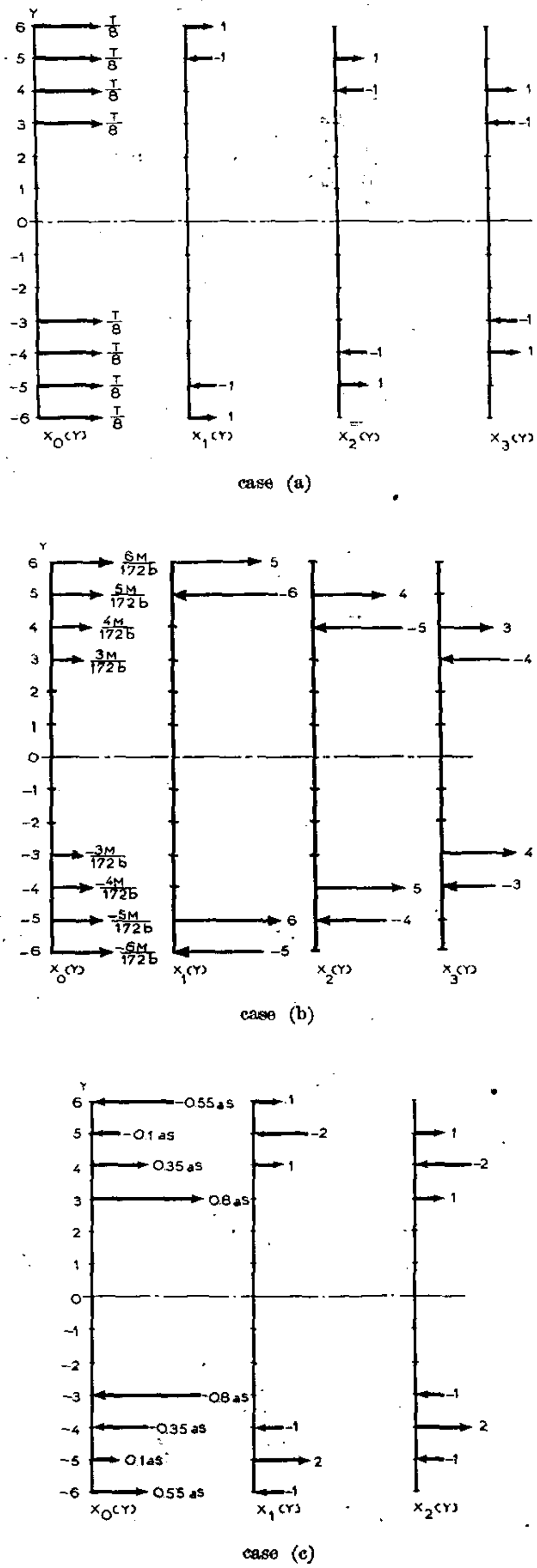

Fig. 3

Linearly independent distributions of axial load in the stringers at Rib 1, for $n=6$ and $m=3$.

so that in the yth panel of the first, second and third bays respectively

$$\left.\begin{aligned} S_1(y) &= S + \frac{1}{a}\sum_{j=y}^{n}\{P_1(j)-P_0(j)\}, \\ S_2(y) &= S + \frac{1}{a}\sum_{j=y}^{n}\{P_2(j)-P_1(j)\}, \\ S_3(y) &= S + \frac{1}{a}\sum_{j=y}^{n}\{P_3(j)-P_2(j)\}. \end{aligned}\right\} \quad (4.3)$$

It follows that the axial loads at the yth stringer in the ribs, are respectively

$$\left.\begin{aligned} Q_0(y) &= b\sum_{j=y+1}^{n}\{S-S_1(j)\}, \\ Q_1(y) &= b\sum_{j=y+1}^{n}\{S_1(j)-S_2(j)\}, \\ Q_2(y) &= b\sum_{j=y+1}^{n}\{S_2(j)-S_3(j)\}, \\ Q_3(y) &= b\sum_{j=y+1}^{n}\{S_3(j)-S\}. \end{aligned}\right\} \quad (4.4)$$

Finally, the constant shear in the panels infers a linear variation of the rib axial loads between successive stringers. Hence, the axial load along a rib between the y th and $y-1$ th stringers is

$$\left.\begin{aligned} Q_0(y,z) &= Q_0(y) + \frac{z}{b}\{Q_0(y-1)-Q_0(y)\}, \\ Q_1(y,z) &= Q_1(y) + \frac{z}{b}\{Q_1(y-1)-Q_1(y)\}, \\ Q_2(y,z) &= Q_2(y) + \frac{z}{b}\{Q_2(y-1)-Q_2(y)\}, \\ Q_3(y,z) &= Q_3(y) + \frac{z}{b}\{Q_3(y-1)-Q_3(y)\}, \end{aligned}\right\} \quad (4.5)$$

noting that

$$Q_0(n) = Q_1(n) = Q_2(n) = Q_3(n) = 0.$$

The symmetrical properties of the plate and stress distributions permit a great simplification of these general formulae and they are summarized for the separate loading cases.

	Case (a)	Case (b)	Case (c)
$P_0(y)$	$\dfrac{T}{2n+1}$	$\dfrac{3My}{n(n+1)(2n+1)b}$	0
$P_1(y)$	$X_0(y)+\sum_i \alpha_i X_i(y)$	$X_0(y)+\sum_i \alpha_i X_i(y)$	$X_0(y)+\sum_i \alpha_i X_i(y)$
$P_2(y)$	$P_1(y)$	$P_1(y)$	$-P_1(y)$
$P_3(y)$	$P_0(y)$	$P_0(y)$	0
$P_1(y,x)$	$P_0(y)+\frac{x}{a}\{P_1(y)-P_0(y)\}$	$P_0(y)+\frac{x}{a}\{P_1(y)-P_0(y)\}$	$\frac{x}{a}P_1(y)$
$P_2(y,x)$	$P_1(y)$	$P_1(y)$	$\left(1-2\frac{x}{a}\right)P_1(y)$
$P_3(y,x)$	$P_1(y)+\frac{x}{a}\{P_0(y)-P_1(y)\}$	$P_1(y)+\frac{x}{a}\{P_0(y)-P_1(y)\}$	$\left(\frac{x}{a}-1\right)P_1(y)$
$S_1(y)$	$\frac{1}{a}\sum_{j=y}^{n}\{P_1(j)-P_0(j)\}$	$\frac{1}{a}\sum_{j=y}^{n}\{P_1(j)-P_0(j)\}$	$S+\frac{1}{a}\sum_{j=y}^{n}P_1(j)$
$S_2(y)$	0	0	$3S-2S_1(y)$
$S_3(y)$	$-S_1(y)$	$-S_1(y)$	$S_1(y)$
$Q_0(y)$	$-b\sum_{j=y+1}^{n}S_1(j)$	$-b\sum_{j=y+1}^{n}S_1(j)$	$b\sum_{j=y+1}^{n}\{S-S_1(j)\}$
$Q_1(y)$	$-Q_0(y)$	$-Q_0(y)$	$-3Q_0(y)$
$Q_2(y)$	$-Q_0(y)$	$-Q_0(y)$	$3Q_0(y)$
$Q_3(y)$	$Q_0(y)$	$Q_0(y)$	$-Q_0(y)$
$Q_0(y,z)$	$Q_0(y)+\frac{z}{b}\{Q_0(y-1)-Q_0(y)\}$	$Q_0(y)+\frac{z}{b}\{Q_0(y-1)-Q_0(y)\}$	$Q_0(y)+\frac{z}{b}\{Q_0(y-1)-Q_0(y)\}$
$Q_1(y,z)$	$-Q_0(y,z)$	$-Q_0(y,z)$	$-3Q_0(y,z)$
$Q_2(y,z)$	$-Q_0(y,z)$	$-Q_0(y,z)$	$3Q_0(y,z)$
$Q_3(y,z)$.	$Q_0(y,z)$	$Q_0(y,z)$	$-Q_0(y,z)$

5 The strain energy analysis.

The coefficients α_i can be determined from a strain energy analysis by equating to zero the derivatives with respect to the total strain energy stored in the structure. The strain energy equations will be formulated in general terms and then the individual cases may be examined later.

The total strain energy stored in the stringers is denoted by U_{STR} and is

$$U_{STR} = \frac{1}{2\,EA_s} \sum_{y=-n}^{n} \int_0^a \{ P_1^2(y,x) + P_2^2(y,x) + P_3^2(y,x) \}\,dx = \frac{1}{2\,EA_s} \sum_{y=-n}^{n} \int_0^a \{ 2\,P_1^2(y,x) + P_2^2(y,x) \}\,dx = \frac{a}{6\,EA_s} \sum_{y=-n}^{n} \{ 2\,P_0^2(y) + 3\,P_1^2(y) + P_2^2(y) + 2\,P_0(y)P_1(y) + P_1(y)P_2(y) \}$$

and differentiating with respect to α_i

$$\frac{\partial U_{STR}}{\partial \alpha_i} = \frac{a}{6\,EA_s}\frac{\partial}{\partial \alpha_i} \sum_{y=-n}^{n} \{ 4\,P_1^2(y) + P_1(y)P_2(y) \}, \tag{5.1}$$

because $P_2^2(y) = P_1^2(y)$, and $P_0(y)$ and $\sum\limits_{y=-n}^{n} P_0(y)P_1(y)$ are independent of α_i, remembering that $P_0(y)$ consists of the particular solution $X_0(y)$, equation (3.5), plus the statically zero distributions $X_i(y)$.

The total strain energy stored in the sheet in shear is denoted by U_S and is

$$U_S = \frac{ab}{\mu t} \sum_{y=1}^{n} \{ S_1^2(y) + S_2^2(y) + S_3^2(y) \} = \frac{ab}{\mu t} \sum_{y=1}^{n} \{ 2\,S_1^2(y) + S_2^2(y) \}$$

and differentiating with respect to α_i,

$$\frac{\partial U_S}{\partial \alpha_i} = \frac{ab}{\mu t}\frac{\partial}{\partial \alpha_i} \sum_{y=1}^{n} \{ 2\,S_1^2(y) + S_2^2(y) \}. \tag{5.2}$$

Finally, the total strain energy stored in the ribs in tension is denoted by U_R and is

$$U_R = \frac{1}{EA_R} \sum_{y=1}^{n} \int_0^b \{ Q_0^2(y,z) + Q_1^2(y,z) + Q_2^2(y,z) + Q_3^2(y,z) \}\,dz = \frac{2}{EA_R} \sum_{y=1}^{n} \int_0^b \{ Q_0^2(y,z) + Q_1^2(y,z) \}\,dz = \frac{2\,b}{3\,EA_R} \sum_{y=1}^{n} \{ Q_0^2(y) + Q_0^2(y-1) + Q_0(y)Q_0(y-1) + Q_1^2(y) + Q_1^2(y-1) + Q_1(y)Q_1(y-1) \}$$

and differentiating with respect to α_i

$$\frac{\partial U_R}{\partial \alpha_i} = \frac{2\,b}{3\,EA_R}\frac{\partial}{\partial \alpha_i} \sum_{y=1}^{n} \{ Q_0^2(y) + Q_0^2(y-1) + Q_0(y)Q_0(y-1) + Q_1^2(y) + Q_1^2(y-1) + Q_1(y)Q_1(y-1) \}. \tag{5.3}$$

Whence the coefficients α_i are found from the condition that the strain energy is a minimum, viz.

$$\frac{\partial U}{\partial \alpha_i} = \frac{\partial U_{STR}}{\partial \alpha_i} + \frac{\partial U_S}{\partial \alpha_i} + \frac{\partial U_R}{\partial \alpha_i} = 0, \tag{5.4}$$

which yields a set of simultaneous linear equations for the determination of the coefficients. There will be $n-m$ such equations for cases (a) and (b), and $n-m-1$ equations for case (c).

Now, referring to the table which gives a summary of the loads throughout the structure, it will be seen that the expressions (5.1), (5.2) and (5.3) can be considerably simplified for the individual cases. It can be readily verified that equation (5.4) resolves into the following equations for cases (a), (b) and (c) respectively.

For case (a),

$$5\,a_{i_{STR}} + \left(\frac{b}{a}\right)\left(\frac{A_s}{at}\right)\left(\frac{E}{\mu}\right) 6\,a_{i_S} + \left(\frac{b}{a}\right)^3 \left(\frac{A_s}{A_R}\right) 2\,a_{i_R} = 0, \tag{5.4a}$$

where $a_{i_{STR}} = \sum\limits_{y=m}^{n} P_1(y)\dfrac{\partial P_1(y)}{\partial \alpha_i}$,

$$a_{i_S} = a^2 \sum_{y=m+1}^{n} S_1(y)\frac{\partial S_1(y)}{\partial \alpha_i},$$

$$a_{i_R} = \left(\frac{a}{b}\right)^2 \sum_{y=1}^{n} \left[\{ 2\,Q_0(y) + Q_0(y-1) \} \frac{\partial Q_0(y)}{\partial \alpha_i} + \{ 2Q_0(y-1) + Q_0(y) \} \frac{\partial Q_0(y-1)}{\partial \alpha_i} \right]$$

for $i = 1, 2, 3 \ldots\ldots n-m$.

For case (b),

$$5\,b_{i_{STR}} + \left(\frac{b}{a}\right)\left(\frac{A_s}{at}\right)\left(\frac{E}{\mu}\right) 6\,b_{i_S} + \left(\frac{b}{a}\right)^3 \left(\frac{A_s}{A_R}\right) 2\,b_{i_R} = 0, \tag{5,4b}$$

where $b_{i_{STR}} = \sum\limits_{y=m}^{n} P_1(y)\dfrac{\partial P_1(y)}{\partial \alpha_i}$,

$$b_{i_S} = a^2 \sum_{y=1}^{n} S_1(y)\frac{\partial S_1(y)}{\partial \alpha_i},$$

$$b_{i_R} = \left(\frac{a}{b}\right)^2 \sum_{y=1}^{n} \left[\{ 2\,Q_0(y) + Q_0(y-1) \} \frac{\partial Q_0(y)}{\partial \alpha_i} + \{ 2\,Q_0(y-1) + Q_0(y) \} \frac{\partial Q_0(y-1)}{\partial \alpha_i} \right]$$

for $i = 1, 2, 3 \ldots\ldots n-m$.

Finally, for case (c),

$$3\,c_{i_{STR}} + \left(\frac{b}{a}\right)\left(\frac{A_s}{at}\right)\left(\frac{E}{\mu}\right) 18\,c_{i_S} + + \left(\frac{b}{a}\right)^3 \left(\frac{A_S}{A_R}\right) 10\,c_{i_R} = 0, \quad (5.4c)$$

where $c_{i_{STR}} = \sum_{y=m}^{n} P_1(y) \frac{\partial P_1(y)}{\partial \alpha_i}$,

$$c_{i_S} = a^2 \sum_{y=m}^{n} S_1(y) \frac{\partial S_1(y)}{\partial \alpha_i},$$

$$c_{i_R} = \left(\frac{a}{b}\right)^2 \sum_{y=m+1}^{n} \Big[\{ 2\,Q_0(y) + Q_0(y-1) \} \frac{\partial Q_0(y)}{\partial \alpha_i} + \{ 2\,Q_0(y-1) + Q_0(y) \} \frac{\partial Q_0(y-1)}{\partial \alpha_i} \Big]$$

for $i = 1, 2, 3 \ldots\ldots n - m - 1$.

6 The relative stiffness parameters.

The relative stiffness parameter η is defined as the ratio of the stiffnesses of the plate with and without cut-out. It is given by the ratio of the strain energies, viz.

$$\eta = \frac{U_0}{U_{STR} + U_S + U_R}, \quad (6.1)$$

where U_0 is the strain energy of the plate without cut-out. For the computation of U_0, it is assumed that the sheet and stringers are continuous across the cut-out.

It is convenient to re-express (6.1) in terms of the 'non-dimensional strain energy' components, viz.

$$\eta = \frac{U'_0}{U'_{STR} + U'_S + U'_R}, \quad (6.2)$$

where for case (a)

$$\left.\begin{aligned}
U'_0 &= \frac{3T^2}{2(2n+1)},\\
U'_{STR} &= \frac{1}{3}\left\{\frac{2T^2}{2n+1} + 5 \sum_{y=m}^{n} P_1^2(y)\right\},\\
U'_S &= 2\left(\frac{b}{a}\right)\left(\frac{E}{\mu}\right)\left(\frac{A_s}{at}\right)\left\{\frac{m(4m^2-1)T^2}{12(2n+1)^2} + a^2 \sum_{y=m+1}^{n} S_1^2(y)\right\},\\
U'_R &= \frac{4}{3}\left(\frac{b}{a}\right)\left(\frac{A_S}{A_R}\right) \sum_{y=1}^{n} \{ Q_0^2(y) + Q_0^2(y-1) + Q_0(y)Q_0(y-1) \}.
\end{aligned}\right\} \quad (6.3a)$$

In deriving the expression for U'_{STR}, it must be remembered that $P_1(y)$ is composed of the particular solution (3.5) and statically zero distributions of forces. For the derivation of U'_S, it is known that

$$S_1(y) = \frac{T}{2n+1} \cdot \frac{1}{2a} \cdot (2y-1), \text{ for } y = 1, 2, \ldots m.$$

The relative stiffness parameter for case (b) is of no major significance, but for completeness the expressions will be quoted here.

For case (b)

$$\left.\begin{aligned}
U'_0 &= \frac{9M^2}{2n(n+1)(2n+1)b^2},\\
U'_{STR} &= \frac{1}{3}\left\{\frac{6M^2}{n(n+1)(2n+1)b^2} + 5 \sum_{y=m}^{n} P_1^2(y)\right\},\\
U'_S &= 2\left(\frac{b}{a}\right)\left(\frac{E}{\mu}\right)\left(\frac{A_S}{at}\right) a^2 \sum_{y=1}^{n} S_1^2(y),\\
U'_R &= \frac{4}{3}\left(\frac{b}{a}\right)\left(\frac{A_S}{A_R}\right) \sum_{y=1}^{n} \{ Q_0^2(y) + Q_0^2(y-1) + Q_0(y)Q_0(y-1) \}.
\end{aligned}\right\} \quad (6.3b)$$

Finally, for the important case of shear loading the expressions become,

for case (c)

$$\left.\begin{aligned}
U'_0 &= 3n\left(\frac{b}{a}\right)\left(\frac{E}{\mu}\right)\left(\frac{A_s}{at}\right) . a^2S^2,\\
U'_{STR} &= \sum_{y=m}^{n} P_1^2(y),\\
U'_S &= 3\left(\frac{b}{a}\right)\left(\frac{E}{\mu}\right)\left(\frac{A_S}{at}\right)\{ (4.5m - n)a^2S^2 + 2a^2 \sum_{y=m+1}^{n} S_1^2(y) \},\\
U'_R &= \frac{20}{3}\left(\frac{b}{a}\right)\left(\frac{A_S}{A_R}\right)\Big\{ 0.25\left(\frac{b}{a}\right)^2 m^3 . a^2S^2 + \sum_{y=m+1}^{n} [Q_0^2(y) + Q_0^2(y-1) + Q_0(y)Q_0(y-1)] \Big\}.
\end{aligned}\right\} \quad (6.3c)$$

In deriving the expressions for case (c), we have used the condition that $S_1(y)$ is composed of the particular solution plus statically zero distributions of shear. Also, the axial load in rib 0 is known to be

$$Q_0(y) = \frac{1}{2}\left(\frac{b}{a}\right) . y . aS, \; y = 0, 1, 2, \ldots\ldots m,$$

since

$$S_1(y) = 1.5\,S \text{ for } \quad y = 1, 2, \ldots\ldots\ldots m.$$

7 Numerical Examples.

The load distribution in a particular plate will now be calculated for the three loading cases, where $n = 6$ and $m = 3$ and where the values of the non-dimensional parameters are

$$\frac{b}{a} = \frac{1}{3}; \quad \frac{A_S}{at}\,\frac{E}{\mu} = 1.0; \quad \frac{A_S}{A_R} = \frac{1}{4}.$$

The redundancies $X(y)$ are chosen to have the distributions as shown in fig. 3.

Case (a): Tension.

For convenience, the total applied tension will be taken as $T = 13$ units; and for the particular distributions of the $X(y)$ it is readily deduced that the axial loads in the stringers at ribs 0 and 1 are respectively

$$\begin{aligned}
&P_0(6) = 1, \quad && P_1(6) = 1.625 + \alpha_1 ,\\
&P_0(5) = 1, && P_1(5) = 1.625 - \alpha_1 + \alpha_2 ,\\
&P_0(4) = 1, && P_1(4) = 1.625 \quad - \alpha_2 + \alpha_3 ,\\
&P_0(3) = 1, && P_1(3) = 1.625 \quad - \alpha_3 ;\\
&P_0(2) = 1, && P_1(2) = 0 \quad ,\\
&P_0(1) = 1, && P_1(1) = 0 \quad ,\\
&P_0(0) = 1, && P_1(0) = 0 \quad .
\end{aligned}$$

From equation (4.3), the shear $S_1(y)$ in the yth panel of the first bay is given by

$$aS_1(y) = \sum_{j=y}^{6} \{ P_1(j) - P_0(j) \}$$

and hence

$$\begin{aligned}
aS_1(6) &= .625 + \alpha_1 ,\\
aS_1(5) &= 1.25 \quad + \alpha_2 ,\\
aS_1(4) &= 1.875 \quad + \alpha_3 ,\\
aS_1(3) &= 2.5 \quad ,\\
aS_1(2) &= 1.5 \quad ,\\
aS_1(1) &= 0.5 \quad .
\end{aligned}$$

From equation (4.4), the axial load in rib 0 at the yth stringer is given by

$$\frac{a}{b}\, Q_0(y) = - \sum_{j=y+1}^{6} aS_1(j),$$

so that

$$\begin{aligned}
\frac{a}{b}\, Q_0(6) &= 0,\\
\frac{a}{b}\, Q_0(5) &= -0.625 - \alpha_1 ,\\
\frac{a}{b}\, Q_0(4) &= -1.875 - \alpha_1 - \alpha_2 ,\\
\frac{a}{b}\, Q_0(3) &= -3.75 \quad - \alpha_1 - \alpha_2 - \alpha_3 ,\\
\frac{a}{b}\, Q_0(2) &= -6.25 \quad - \alpha_1 - \alpha_2 - \alpha_3 ,\\
\frac{a}{b}\, Q_0(1) &= -7.75 \quad - \alpha_1 - \alpha_2 - \alpha_3 ,\\
\frac{a}{b}\, Q_0(0) &= -8.25 \quad - \alpha_1 - \alpha_2 - \alpha_3 .
\end{aligned}$$

For the chosen values of the non-dimensional parameters, equations (5.4a) resolve into

$$5\, a_{i_{STR}} + 2\, a_{i_S} + 0.01852\, a_{i_R} = 0,$$

where

$$\begin{aligned}
a_{1_{STR}} &= 2\alpha_1 - \alpha_2 ,\\
a_{2_{STR}} &= -\alpha_1 + 2\alpha_2 - \alpha_3 ,\\
a_{3_{STR}} &= \quad - \alpha_2 + 2\alpha_3 ,
\end{aligned}$$

$$\begin{aligned}
a_{1_S} &= 0.625 + \alpha_1 ,\\
a_{2_S} &= 1.25 \quad + \alpha_2 ,\\
a_{3_S} &= 1{,}875 \quad + \alpha_3
\end{aligned}$$

$$\begin{aligned}
a_{1_R} &= 145.625 + 32\,\alpha_1 + 27\,\alpha_2 + 21\,\alpha_3 ,\\
a_{2_R} &= 141.25 \quad + 27\,\alpha_1 + 26\,\alpha_2 + 21\,\alpha_3 ,\\
a_{3_R} &= 129.375 + 21\,\alpha_1 + 21\,\alpha_2 + 20\,\alpha_3 ,
\end{aligned}$$

whence the three simultaneous equations for the determination of α_1, α_2 and α_3 are

$$\begin{aligned}
12.593 \quad \alpha_1 - 4.5 \quad \alpha_2 + 0.38889\,\alpha_3 &= -3.9468,\\
-4.5 \quad \alpha_1 + 12.481 \quad \alpha_2 - 4.6111 \quad \alpha_3 &= -5.1157,\\
0.38889\,\alpha_1 - 4.6111\,\alpha_2 + 12.370 \quad \alpha_3 &= -6.1458,
\end{aligned}$$

these equations yielding the following values of the coefficients

$$\begin{aligned}
\alpha_1 &= -0.62400,\\
\alpha_2 &= -0.94071,\\
\alpha_3 &= -0.82791.
\end{aligned}$$

The loads throughout the structure are now completely specified and are summarized below for one quadrant of the plate.

$$\begin{aligned}
&P_0(6) = 0.07692\,T, \quad && P_1(6) = 0.07700\,T,\\
&P_0(5) = 0.07692\,T, && P_1(5) = 0.10064\,T,\\
&P_0(4) = 0.07692\,T, && P_1(4) = 0.13368\,T,\\
&P_0(3) = 0.07692\,T, && P_1(3) = 0.18869\,T,\\
&P_0(2) = 0.07692\,T, && P_1(2) = 0,\\
&P_0(1) = 0.07692\,T, && P_1(1) = 0,\\
&P_0(0) = 0.07692\,T, && P_1(0) = 0,
\end{aligned}$$

where $P_0(y)$ and $P_1(y)$ are the axial loads in the yth stringer at the intersection of ribs 0 and 1 respectively.

$$\begin{aligned}
&S_1(6) = 0.00008\,T/a, \quad && S_2(6) = 0,\\
&S_1(5) = 0.02379\,T/a, && S_2(5) = 0,\\
&S_1(4) = 0.08055\,T/a, && S_2(4) = 0,\\
&S_1(3) = 0.19231\,T/a, &&\\
&S_1(2) = 0.11538\,T/a, &&\\
&S_1(1) = 0.03846\,T/a, &&
\end{aligned}$$

where $S_1(y)$ is the shear in the panel in the first bay bounded by the y th and $y-1$ th stringers and similarly $S_2(y)$ is the shear in the corresponding panel in the middle bay.

$$\begin{aligned}
&Q_0(6) = 0, \quad && Q_1(6) = 0,\\
&Q_0(5) = -0.00003\,T, && Q_1(5) = 0.00003\,T,\\
&Q_0(4) = -0.02387\,T, && Q_1(4) = 0.02387\,T,\\
&Q_0(3) = -0.03480\,T, && Q_1(3) = 0.03480\,T,\\
&Q_0(2) = -0.09891\,T, && Q_1(2) = 0.09891\,T,\\
&Q_0(1) = -0.13737\,T, && Q_1(1) = 0.13737\,T,\\
&Q_0(0) = -0.15019\,T, && Q_1(0) = 0.15019\,T,
\end{aligned}$$

where $Q_0(y)$ and $Q_1(y)$ are the axial loads in ribs 0 and 1 respectively at the intersection of the y th stringer.

Substituting the above values into equations (6.2) and (6.3a) it can be readily verified that the numerical value of the relative stiffness parameter is $\eta = 0.516$.

Case (b): Bending.

For convenience, the total applied moment will be taken as $M/b = 182$ units and for the particular distributions of $X(y)$ shown in fig. 3 it can be verified that

$$\begin{aligned}
P_0(6) &= 6, & P_1(6) &= 6.3488 + 5\,\alpha_1 \\
P_0(5) &= 5, & P_1(5) &= 5.2907 - 6\,\alpha_1 + 4\,\alpha_2\,, \\
P_0(4) &= 4, & P_1(4) &= 4.2326 \qquad - 5\,\alpha_2 + 3\,\alpha_3\,, \\
P_0(3) &= 3, & P_1(3) &= 3.1744 \qquad\qquad - 4\,\alpha_3\,, \\
P_0(2) &= 2, & P_1(2) &= 0, \\
P_0(1) &= 1, & P_1(1) &= 0, \\
P_0(0) &= 0. & P_1(0) &= 0.
\end{aligned}$$

The shear $S_1(y)$ is given by equation (4.3)

$$\begin{aligned}
aS_1(6) &= 0.34884 + 5\,\alpha_1\,, \\
aS_1(5) &= 0.63952 - \alpha_1 + 4\,\alpha_2\,, \\
aS_1(4) &= 0.87208 - \alpha_1 - \alpha_2 + 3\,\alpha_3\,, \\
aS_1(3) &= 1.0465 - \alpha_1 - \alpha_2 - \alpha_3\,, \\
aS_1(2) &= -0.95349 - \alpha_1 - \alpha_2 - \alpha_3\,, \\
aS_1(1) &= -1.9535 - \alpha_1 - \alpha_2 - \alpha_3\,,
\end{aligned}$$

and the axial load $Q_0(y)$ in rib 0 is given by equation (4.4), so that

$$\begin{aligned}
\frac{a}{b}\,Q_0(6) &= 0, \\
\frac{a}{b}\,Q_0(5) &= -0.34884 - 5\,\alpha_1\,, \\
\frac{a}{b}\,Q_0(4) &= -0.98836 - 4\,\alpha_1 - 4\,\alpha_2\,, \\
\frac{a}{b}\,Q_0(3) &= -1.8604 - 3\,\alpha_1 - 3\,\alpha_2 - 3\,\alpha_3\,, \\
\frac{a}{b}\,Q_0(2) &= -2.9069 - 2\,\alpha_1 - 2\,\alpha_2 - 2\,\alpha_3\,, \\
\frac{a}{b}\,Q_0(1) &= -1.9535 - \alpha_1 - \alpha_2 - \alpha_3\,, \\
\frac{a}{b}\,Q_0(0) &= 0.
\end{aligned}$$

For the chosen values of the non-dimensional parameters, equations (5.4) resolve into

$$5b_{i_{STR}} + 2b_{i_S} + 0.01852 b_{i_R} = 0,$$

where

$$\begin{aligned}
b_{1_{STR}} &= 61\,\alpha_1 - 24\,\alpha_2\,, \\
b_{2_{STR}} &= -24\,\alpha_1 + 41\,\alpha_2 - 15\,\alpha_3\,, \\
b_{3_{STR}} &= -15\,\alpha_2 + 25\,\alpha_3\,,
\end{aligned}$$

$$\begin{aligned}
b_{1_S} &= 2.0930 + 30\,\alpha_1\,, \\
b_{2_S} &= 3.5465 + 20\,\alpha_2\,, \\
b_{3_S} &= 4.4767 + 12\,\alpha_3\,,
\end{aligned}$$

$$\begin{aligned}
b_{1_R} &= 112.19 + 300\,\alpha_1 + 180\,\alpha_2 + 84\,\alpha_3\,, \\
b_{2_R} &= 100.28 + 180\,\alpha_1 + 160\,\alpha_2 + 84\,\alpha_3\,, \\
b_{3_R} &= 75.616 + 84\,\alpha_1 + 84\,\alpha_2 + 72\,\alpha_3\,,
\end{aligned}$$

whence the three simultaneous equations for the determination of α_1, α_2 and α_3 are

$$\begin{aligned}
370.56\,\alpha_1 - 116.67\,\alpha_2 + 1.5556\,\alpha_3 &= -6.2636, \\
-116.67\,\alpha_1 + 277.96\,\alpha_2 - 73.444\,\alpha_3 &= -8.9500, \\
1.5556\,\alpha_1 - 73.4444\,\alpha_2 + 150.33\,\alpha_3 &= -10.354,
\end{aligned}$$

these equations yielding the following values of the coefficients

$$\begin{aligned}
\alpha_1 &= -0.044991, \\
\alpha_2 &= -0.090716, \\
\alpha_3 &= -0.11270.
\end{aligned}$$

These values of the coefficients give the following distributions of load throughout one quadrant of the plate

$$\begin{aligned}
P_0(6) &= 0.032967\,M/b, & P_1(6) &= 0.033648\,M/b, \\
P_0(5) &= 0.027473\,M/b, & P_1(5) &= 0.028559\,M/b, \\
P_0(4) &= 0.021978\,M/b, & P_1(4) &= 0.023890\,M/b, \\
P_0(3) &= 0.016484\,M/b, & P_1(3) &= 0.019436\,M/b, \\
P_0(2) &= 0.010989\,M/b, & P_1(2) &= 0, \\
P_0(1) &= 0.005495\,M/b, & P_1(1) &= 0, \\
P_0(0) &= 0, & P_1(0) &= 0,
\end{aligned}$$

where $P_0(y)$ and $P_1(y)$ are the axial loads in the yth stringer at the intersection of ribs 0 and 1 respectively.

$$\begin{aligned}
S_1(6) &= 0.000681\,M/ab, & S_2(6) &= 0, \\
S_1(5) &= 0.001767\,M/ab, & S_2(5) &= 0, \\
S_1(4) &= 0.003680\,M/ab, & S_2(4) &= 0, \\
S_1(3) &= 0.007115\,M/ab, \\
S_1(2) &= -0.003874\,M/ab, \\
S_1(1) &= -0.009368\,M/ab,
\end{aligned}$$

where $S_1(y)$ is the shear in the panel in the first bay bounded by the yth and y—1th stringer, and similarly $S_2(y)$ is the shear in the corresponding panel in the middle bay.

$$\begin{aligned}
Q_0(6) &= 0, & Q_1(6) &= 0, \\
Q_0(5) &= -0.000227\,M/b, & Q_1(5) &= 0.000227\,M/b, \\
Q_0(4) &= -0.000816\,M/b, & Q_1(4) &= 0.000816\,M/b, \\
Q_0(3) &= -0.002042\,M/b, & Q_1(3) &= 0.002042\,M/b, \\
Q_0(2) &= -0.004414\,M/b, & Q_1(2) &= 0.004414\,M/b, \\
Q_0(1) &= -0.003123\,M/b, & Q_1(1) &= 0.003123\,M/b, \\
Q_0(0) &= 0, & Q_1(0) &= 0,
\end{aligned}$$

where $Q_0(y)$ and $Q_1(y)$ are the axial loads in ribs 0 and 1 respectively, at the intersection of the yth stringer.

The relative stiffness parameter for this case has no major practical significance ($\eta \approx 1.0$).

Case (c): Shear.

The applied shear will be taken as $aS = 1$ unit; and for the distributions of $X(y)$ shown in fig. 3 it can be verified that

$$\begin{aligned}
P_0(6) &= 0, & P_1(6) &= -0.55 + \alpha_1 \\
P_0(5) &= 0, & P_1(5) &= -0.1 - 2\,\alpha_1 + \alpha_2\,, \\
P_0(4) &= 0, & P_1(4) &= +0.35 + \alpha_1 - 2\,\alpha_2\,, \\
P_0(3) &= 0, & P_1(3) &= +0.8 + \alpha_2\,, \\
P_0(2) &= 0, & P_1(2) &= 0, \\
P_0(1) &= 0, & P_1(1) &= 0, \\
P_0(0) &= 0, & P_1(0) &= 0.
\end{aligned}$$

From equation (4.3), the shear $S_1(y)$ in the yth panel of the first bay is

$$aS_1(y) = aS + \sum_{j=y}^{6} \{ P_1(j) - P_0(j) \},$$

and hence

$$\begin{aligned}
aS_1(6) &= 0.45 + \alpha_1 \\
aS_1(5) &= 0.35 - \alpha_1 + \alpha_2\,, \\
aS_1(4) &= 0.70 - \alpha_2\,, \\
aS_1(3) &= 1.5, \\
aS_1(2) &= 1.5, \\
aS_1(1) &= 1.5.
\end{aligned}$$

From equation (4.4), the axial load in rib 0 at the yth stringer is given by

$$\frac{a}{b}\,Q_0(y) = \sum_{j=y+1}^{6} \{ aS - aS_1(j) \},$$

so that

$$\frac{a}{b}\,Q_0(6) = 0,$$
$$\frac{a}{b}\,Q_0(5) = 0.55 - \alpha_1,$$
$$\frac{a}{b}\,Q_0(4) = 1.2 \qquad - \alpha_2,$$
$$\frac{a}{b}\,Q_0(3) = 1.5$$
$$\frac{a}{b}\,Q_0(2) = 1.0$$
$$\frac{a}{b}\,Q_0(1) = 0.5$$
$$\frac{a}{b}\,Q_0(0) = 0.$$

For the chosen values of the non-dimensional parameters, equations (5.4) resolve into:

$$3\,c_{i_{STR}} + 6\,c_{i_S} + 0.09260\,c_{i_R} = 0,$$

where

$$c_{1STR} = \quad 6\,\alpha_1 - 4\,\alpha_2\,;\ c_{1S} = \quad 0.10 + 2\,\alpha_1 - \quad \alpha_2,$$
$$c_{2STR} = -4\,\alpha_1 + 6\,\alpha_2,\ c_{2S} = -0.35 - \quad \alpha_1 + 2\,\alpha_2,$$
$$c_{1_R} = -3.4 \ + 4\,\alpha_1 + \alpha_2,$$
$$c_{2_R} = -6.85 + 4\,\alpha_2 + \alpha_1,$$

whence the two *simultaneous equations* for the determination of α_1 and α_2 are

$$30.370\,\alpha_1 - 17.907\,\alpha_2 = -0.28519,$$
$$-17.907\,\alpha_1 + 30.370\,\alpha_2 = \quad 2.7343\ ;$$

these equations yielding the following values of the coefficients

$$\alpha_1 = 0.06702,$$
$$\alpha_2 = 0.12955.$$

These values of the coefficients give the following distributions of load throughout one quadrant of the plate

$P_0(6) = 0,$	$P_1(6) = -0.48298\,aS,$
$P_0(5) = 0,$	$P_1(5) = -0.10449\,aS,$
$P_0(4) = 0,$	$P_1(4) = \quad 0.15792\,aS,$
$P_0(3) = 0,$	$P_1(3) = \quad 0.92955\,aS,$
$P_0(2) = 0,$	$P_1(2) = \quad 0,$
$P_0(1) = 0,$	$P_1(1) = \quad 0,$
$P_0(0) = 0,$	$P_1(0) = \quad 0,$

where $P_0(y)$ and $P_1(y)$ are the axial loads in the yth stringer at the intersection of ribs 0 and 1 respectively.

$S_1(6) = 0.51702\,S,$	$S_2(6) = 1.96595\,S,$
$S_1(5) = 0.41253\,S,$	$S_2(5) = 2.17494\,S,$
$S_1(4) = 0.57045\,S,$	$S_2(4) = 1.85910\,S,$
$S_1(3) = 1.5\,S,$	
$S_1(2) = 1.5\,S,$	
$S_1(1) = 1.5\,S,$	

where $S_1(y)$ is the shear in the panel in the first bay bounded by the yth and y—1th stringers, and $S_2(y)$ is the shear in the corresponding panel of the middle bay.

$Q_0(6) = 0,$	$Q_1(6) = \quad 0,$
$Q_0(5) = 0.16100\,aS,$	$Q_1(5) = -0.48298\,aS,$
$Q_0(4) = 0.35682\,aS,$	$Q_1(4) = -1.07045\,aS,$
$Q_0(3) = 0.50000\,aS,$	$Q_1(3) = -1.5\,aS,$
$Q_0(2) = 0.33333\,aS,$	$Q_1(2) = -1.0\,aS,$
$Q_0(1) = 0.16667\,aS,$	$Q_1(1) = -0.5\,aS,$
$Q_0(0) = 0,$	$Q_1(0) = \quad 0,$

where $Q_0(y)$ and $Q_1(y)$ are the axial loads in ribs 0 and 1 respectively, at the intersection of the yth stringer.

It is to be noted that for case (c)

$$S_2(y) = 3\,S - 2\,S_1(y)$$

and

$$Q_1(y) = -3\,Q_0(y).$$

Substituting the above values into equations (6.2) and (6.3c) it can be readily verified that *the numerical value of the relative stiffness parameter* is $\eta = 0.546$.

Several important conclusions follow from these results and are summarized below for the three separate cases.

Case (a). Tension.

(I) The maximum tension occurs in stringer 3 bordering the cut-out and is 2.5 times the external tension applied to one stringer.

(II) The maximum shear in the panels can be determined by inspection and a redundancy calculation is not required. This maximum value of the shear occurs in the end bays between stringers *m* and *m* — 1 and its value is given by

$$S(m) = \frac{2\,m - 1}{2\,a} \cdot \frac{T}{2\,n + 1}.$$

(III) The maximum axial load in the ribs occurs at stringer 0 and is twice the external load applied to one stringer.

(IV) The relative stiffness parameter is $\eta = 0.516$.

Case (b). Bending.

The perturbations due to the presence of the cut-out are very small.

Case (c). Shear.

(I) The maximum value of the shear occurs in the middle bay between stringers 5 and 4 and is 2.2 times the applied shear. The distribution of shear in these panels does not appear to vary *much from the general rule*

$$S_2(y) = \frac{n}{n - m}\,S.$$

(II) *Again, the maximum axial load occurs* in the stringer 3 bordering the cut-out and is $0.93\,aS$.

(III) The maximum axial load occurs in the centre ribs at stringer m and is $\frac{3\,b}{2\,a}\,.\,m\,.\,aS$. This value holds for any given number of stringers and does not require a redundancy calculation.

(IV) The relative stiffness parameter is $\eta = 0.546$.

8 Nomenclature.

a	distance between ribs.
$a_{i_{STR}}, a_{i_S}, a_{i_R}$	coefficients appertaining to case (a) and defined in the text.
A_S	cross-sectional area of a stringer plus effective area of sheet.
A_R	cross-sectional area of a rib plus effective area of sheet.
b	distance between stringers.
$b_{i_{STR}}, b_{i_S}, b_{i_R}$	coefficients appertaining to case (b) and defined in the text.
$c_{i_{STR}}, c_{i_S}, c_{i_R}$	coefficients appertaining to case (c) and defined in the text.
E	Young's modulus.
m, n	there are $2\,n+1$ stringers and $2\,m-1$ discontinuous stringers.
M	total applied moment.
p	axial stress in a stringer.
$P_0(y)$, $P_1(y)$ etc.	axial loads in the yth stringer at rib 0, rib 1 etc.
$P_1(y,x)$, $P_2(y,x)$, $P_3(y\,x)$	axial load distributions along the yth stringer in the first, second and third bays respectively.
q	axial stress in a rib.
$Q_0(y)$, $Q_1(y)$ etc.	axial loads in rib 0, rib 1 etc. at the yth stringer.
$Q_0(y,z)$, $Q_1(y,z)$ etc.	axial load distributions in rib 0, rib 1 etc. between the yth and $y-1$th stringers.
s	shear stress in a panel.
S	applied shear per unit run.
$S_1(y)$, $S_2(y)$, $S_3(y)$	shears in the panel between the yth and $y-1$th stringers of the first, second and third bays respectively.
T	total applied tension.
t	thickness of sheet.
U	total strain energy stored in the plate.
U_{STR}	total strain energy stored in the stringers.
U_S	total strain energy stored in the sheet.
U_R	total strain energy stored in the ribs.
x, z	rectangular systems of axes for each panel as shown in fig. 1.
X, Y	rectangular axes with origin at the centroid of the plate.
$X_0(y)$	a statically correct distribution of axial load in the stringers at rib 1 and satisfying the boundary conditions.
$X_i(y)$	a statically zero distribution of axial load in the stringers at rib 1 and contributing nothing to the boundary conditions.
y	current stringer number.
α_i	coefficient which is determined by a strain energy analysis.
η	relative stiffness parameter.
μ	shear modulus.

9 References

1 EBNER, H. and KÖLLER, H. Über den Kraftverlauf in längs- und querversteiften Scheiben. Luftfahrtforschung. Vol. XV, 1938 pp. 527—542.

2 KUHN, P. and MOGGIO, E. M. Stresses around rectangular cut-outs in skin-stringer panels under axial loads. N.A.C.A. A.R.R. L-399, 1942.

3 KUHN, P., DUBERG, J. E., and DISKIN, S. H. Stresses around rectangular cut-outs in skin-stringer panels under axial loads — II. N.A.C.A. A.R.R. L-368, 1943.

4 WILLIAMS, D. Openings in stressed-skin wings. Aircraft Engineering. Vol. X, 1938, pp. 3—6.

5 RAND, T. Statik för flygplanskal. Kungliga Tekniska Högskolans Avhandlingar, No. 54, Stockholm 1948.

Completed: December 1948.

REPORT S. 362.

Load Distribution and Relative Stiffness Parameters for a Reinforced Circular Cylinder containing a Rectangular Cut-out

by

L. S. D. MORLEY and W. K. G. FLOOR.

Summary.

This paper presents an exact method for the determination of the load distribution and relative stiffness parameters for a reinforced circular cylinder, having three bays and with a rectangular cut-out in the centre bay, undergoing torsion, bending, shear and tension. The method is exact within the confines of conventional shell theory and it has not been found necessary to introduce new assumptions. An appendix briefly deals with the problem of the many-bayed circular cylinder.

Numerical examples are given for the various loading cases. The large influence of the higher harmonic terms for the axial load distributions in the stringers indicates that the stress perturbations arising from the presence of the cut-out will rapidly diffuse along the length of the cylinder, this following from the principle of De St. Venant.

Contents.

1 Introduction

In aircraft fuselages there are often large rectangular cut-outs such as openings for passenger and baggage doors and there is usually some doubt as to the precise state of stress and stiffness for this region. Clearly, it is first necessary to determine the most economical structure with regard to the saving of weight, but this is not possible until detailed information and data are at our disposal. However, for monocoque fuselages, the modern practice seems to be tending towards merely stiffening the rings (frames) and stringers (longerons) bordering the cut-out (for pressurized fuselages it is customary to spike the doors around the cut). Even with this simple structure, a high complexity of stress can exist. Certain panels and stringers may buckle because of the extremely high loads in the stringers at the edges of the cut and there may be some yielding of the rivets; also, tension fields will probably form in the panels *adjacent to these stringers — at least for asymmetrical loading as typified by cases* (3a), (1b) and (3b) of this paper. (See fig. 2).

In commencing this study, it has been found advisable *to investigate a very simple structure* which essentially consists of a non-buckling circular monocoque fuselage possessing a high degree of geometrical and elastic symmetry, having three bays with the rectangular cut-out in the centre bay. The cylinder is reinforced longitudinally by *a system of uniformly spaced and equal stringers*, while in the transverse direction it is reinforced by four rings, the rings bordering the cut having different sectional properties to the outer pair of rings. The analysis as presented does not take into account the effect of reinforcing the stringers *bordering the cut, but this effect can also be* considered with some additional labour. It is believed that the effect of this latter reinforcing will not influence the overall load distribution to a very great degree, although, of course, the stress in these stringers will be reduced *proportionately. The effect of increasing the* thickness of the sheet covering in the centre bay can be exactly determined by making minor alterations in the strain energy coefficients A_i and B_i which are explicitly defined at a later stage. These fundamental coefficients, in *fact, refer to a highly specialised structure.* In appendix A, the method is briefly described for the determination of the load distribution throughout a many-bayed circular cylinder. For cylinders not having a circular cross-section, the same analysis is still valid if the suggestions made by *Ebner and Köller* (ref. 1) with regard to the orthogonal properties of the statically zero distributions of axial load are incorporated.

Several authors have investigated the problem using various assumptions and analogies which may give rather erroneous results (see for example refs. 2, 3 and 4), but *Cicala* (ref. 5) was the first to consider the effect of the flexibility of the rings, which pay a major contribution in the distribution of the perturbation stresses arising from the cut-out. Cicala investigated the infinite cylinder under the action of asymmetrical loading conditions which are typified by cases (3a), (1b) and (3b) of the present paper. This analysis does not take into account the exact effect of changing the sectional properties of the rings bordering the cut-out. In fact, it is easily demonstrated that for equal stresses the rings bordering the cut-out should be three times as heavy as the outer rings for the asymmetrical loading of a three-bay cylinder (c.f. table 4.1).

The analysis presented here is fundamentally the same as used by the first author in the solution of the flat monocoque plate containing a rectangular cut-out (ref. 6). It essentially consists of a strain-energy analysis where the deformations of all the component parts are considered, using the principles and assumptions of the conventional (or simplified) shell theory of ref. 1. It has not been found necessary to introduce any new principles or assumptions. Conventional shell theory assumes that the shear is constant in a panel which infers that the stringer axial load varies linearly along each bay, and in addition it is assumed that the rings have vanishing rigidity for bending out of their planes. Rand (ref. 7) has made an extensive investigation into the validity of these assumptions.

The problem resolves into the determination of the coefficients for the discrete Fourier series which gives the most general distribution of axial load in the stringers at the intersection of ring 1. These coefficients are found from a rectangular system of linear simultaneous equations which are merely statements of certain boundary conditions (the rectangular system containing more unknowns than equations), this system being transformed into a square system of simultaneous linear equations from which the Fourier coefficients are eventually determined. There are an infinity of such transformations, but there is only one that will make the total strain energy stored in the structure a minimum. The square system of simultaneous equations is equal in number to half the number of panels that have been removed to form the cut-out, so that when only two panels have been removed the Fourier coefficients are explicitly defined. When these Fourier coefficients have been determined, the stress perturbations and the relative stiffness parameters are easily evaluated by using the appropriate expressions.

Sometimes it might be convenient to replace the actual cylinder having a reasonably large number of discrete stiffeners by a cylinder with continuously distributed stiffeners when calculating the stress distribution.

However, when in the case of continuously distributed stiffeners any singularity in the stress distribution should occur at the edges of the cut-out, such a simplification would yield unreliable results.

In that case, even replacing a great number of discrete stiffeners by a smaller number could not be relied upon without careful investigation.

In Appendix B of this paper there is a short note concerning the stress perturbations in a three-bay circular cylinder undergoing torsion and with an infinitely thin slit in the centre bay, it being assumed that the stringers are uniformly distributed over the periphery of the cylinder. It is shown, that no singularity exists in the stress distribution at the edges of the cut-out.

2 The reinforced circular cylinder.

The fuselage considered in the analysis is a monocoque cylinder of circular cross-section as shown in fig. 1, where free warping of the end sections is permitted. The method developed in this paper permits, however, the determination of the stresses in cylinders having different end conditions.

The cylinder is made of thin sheet metal and is reinforced by four transverse rings, each one having a constant cross-section — the two outer rings having the same cross-section and the two inner rings being identical. The distance between the rings is, for simplicity, assumed to be the same, but this is not a necessary assumption. The cylinder is reinforced longitudinally by a system of $2n$ stringers which are equally spaced and have the same and constant cross-sectional area. The cut-out is assumed to extend from the mth to the $2n-m$th stringer, there being no local edge reinforcing. The cylinder is assumed to possess geometrical and elastic symmetry about the X—Y and Y—Z planes.

In the nomenclature it will be observed for instance that I is the "effective" moment of inertia of the outer rings, and this is meant to include that portion of the sheet covering which may be considered as working in conjunction with the ring.

In addition to the foregoing assumptions, the stringers are considered as offering negligibly small resistance to bending, and the rings are assumed to have finite rigidity in bending in their plane, but vanishing rigidity in bending out of their plane as well as in torsion. Finally, Hooke's law is assumed to remain valid during all the deformations that are experienced by the structure.

3 The redundancies.

The cylinder shown in fig. 1 has in general $4(m-1)$ redundancies or statical indeterminacies and when these are known the stress distribution in the whole structure is completely specified. When the external loads are symmetrically or asymmetrically disposed (ref. fig. 2), there is an immediate fourfold reduction in the number of redundancies because of the geometrical and elastic symmetry about the X—Y and Y—Z planes. It is proposed to deal only with the six regular distributions of external loading shown in fig. 2 since these have the greatest interest. By regular distributions, it is meant that the loads are applied according to the elementary theories, i. e. equal axial load in all the stringers, the engineers

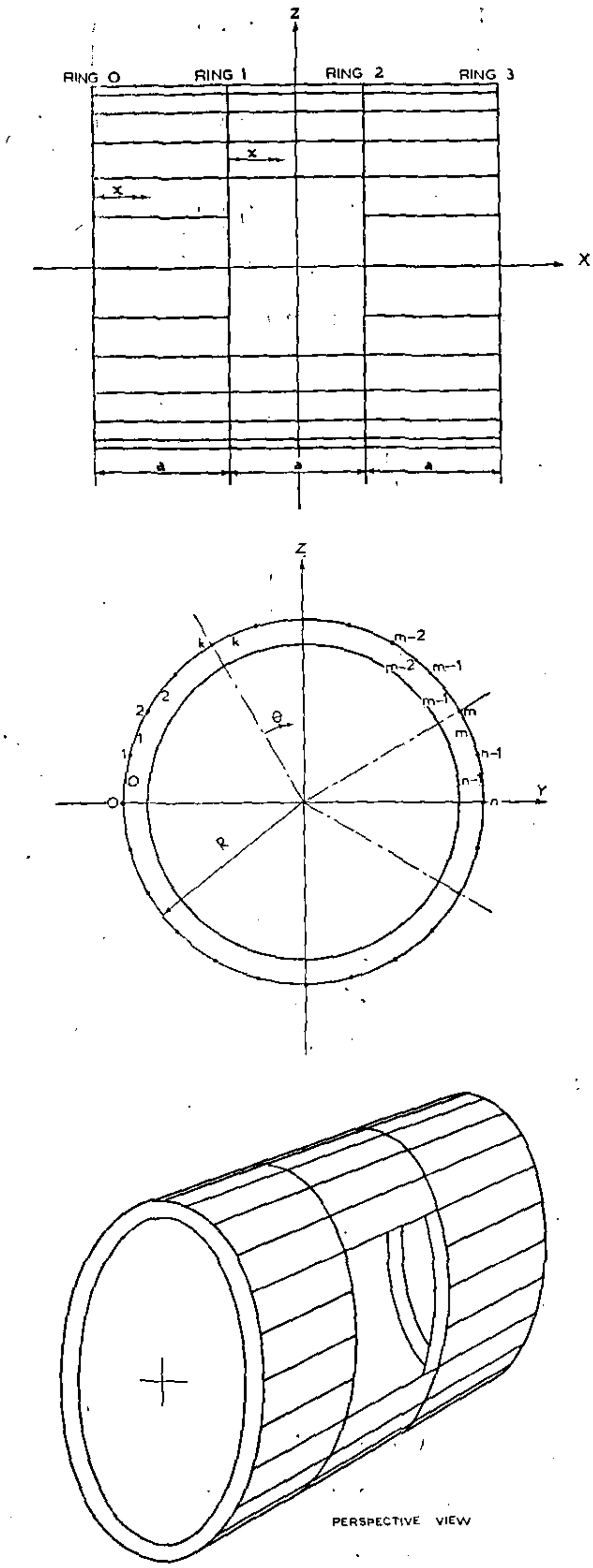

Fig. 1. The monocoque circular cylinder.

theory of bending and the Bredt-Batho theory of torsion. The methods developed in this paper are, however, not restricted to these distributions of the external loads.

It follows that the stress distributions for the various cases possess the symmetrical properties about the X—Y and Y—Z planes as shown in table 3.1. So for case (3a) for example, the axial stresses in the stringers and the bending and circumferential stresses in the rings are symmetrical about the X—Y plane and asymmetrical about the Y—Z plane; while the shearing stresses in the panels and rings are asymmetrically disposed about the X—Y plane — the former being symmetrical and the latter asymmetrical with respect to the Y—Z plane.

Therefore, it is evident that attention may now be confined to the quarter portion of the cylinder formed by the intersection of the X—Y and Y—Z planes, thereby reducing the redundancies to $m - 1$.

As mentioned in a previous paper concerning a

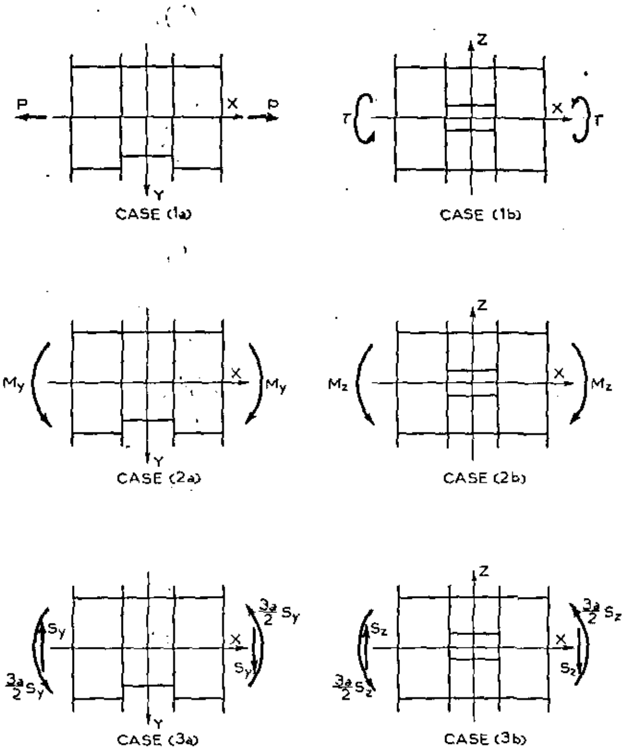

Fig. 2. Showing the various loading cases.

similar problem in flat plates (ref. 6), there is complete freedom in the choice of the statically indeterminate quantities provided that they are linearly independent of one another. It is again convenient to choose the redundancies as axial load distributions in the stringers at ring 1, where these axial loads are zero in the stringers $m + 1$ to n, since it is assumed that the rings are unable to resist bending out of their planes. For the regular circular cylinder having equal panels and stringers, it is possible to achieve the solution with some considerable elegance as compared with the procedure adopted for the flat plate. The reason for this is that because of the cyclic symmetry of the cylinder, a great number of symmetrical planes are at our disposal where the orthogonality of trigonometric terms can be used to some advantage. For the flat plate, there is only one central axis of symmetry present and the trigonometric terms can only be used to advantage when the external axial loads are symmetrical about this plane and then it is necessary to assume that the ribs are rigid.

For the cylinder under investigation, appropriate axial load distributions in the stringers at ring 1 are given by

$$\left.\begin{aligned} P_1(k) &= \alpha_0 + \alpha_1 \cos\frac{k\pi}{n} + \\ &\quad + \sum_{i=2}^{n} \alpha_i \cos\frac{ik\pi}{n} \text{ for cases (a)}, \\ \text{and} & \\ P_1(k) &= \alpha_1 \sin\frac{k\pi}{n} + \\ &\quad + \sum_{i=2}^{n-1} \alpha_i \sin\frac{ik\pi}{n} \text{ for cases (b)}, \end{aligned}\right\} \quad (3.1)$$

where α_0 and α_1 are determined from the overall equilibrium requirements and the α_i constitute the "redundancies" of the problem. It is readily verified that the α_i distributions are statically zero.

It will be noticed in equation (3.1), however, that there are $n-1$ unknowns or "redundancies" for cases (a) and $n-2$ unknowns for cases (b), so the α_i are not independent of one another. Their dependence is due to the boundary conditions existing in the cut-out region, viz. zero axial load in the discontinuous stringers at the cut-out and zero shear in the panels removed to form the cut-out. It is convenient to ignore this dependence until the final stages of the strain energy analysis.

4 The loads in the cylinder.

Preparatory to the strain energy analysis, it is necessary to have a complete specification of the loads in the structure in terms of the α_i coefficients. The specification of these loads will be formulated in general terms and the explicit expressions are summarized in table 4.1, where the various summations have been completed.

In conventional shell theory, it is assumed that the stringer axial load varies linearly along each bay. Hence, the axial load at a current point x in the kth stringer is given by

$$\left.\begin{aligned} P_1(k,x) &= P_0(k) + \frac{x}{a}\{P_1(k) - P_0(k)\}, \\ P_2(k,x) &= P_1(k) + \frac{x}{a}\{P_2(k) - P_1(k)\}, \\ P_3(k,x) &= P_2(k) + \frac{x}{a}\{P_3(k) - P_2(k)\}, \end{aligned}\right\} \quad (4.1)$$

the expressions remaining valid only for the first, second and third bays respectively.

This linear variation of axial load in the stringers infers that the shear is constant in each panel, so that from elementary considerations of equilibrium it is found that the shear in the kth panel (i. e. bounded by the $k+1$th and kth stringers) of the first, second and third bays is respectively

$$\left.\begin{aligned} S_1(k) &= \frac{1}{a}\sum_{j=0}^{k}\{P_1(j) - P_0(j)\} + \\ &\qquad + \text{some constant}, \\ S_2(k) &= \frac{1}{a}\sum_{j=0}^{k}\{P_2(j) - P_1(j)\} + \\ &\qquad + \text{some constant}, \\ S_3(k) &= \frac{1}{a}\sum_{j=0}^{k}\{P_3(j) - P_2(j)\} + \\ &\qquad + \text{some constant}, \end{aligned}\right\} \quad (4.2)$$

where the constant is determined from overall equilibrium requirements.

It remains now to determine the forces in the rings. The rings are loaded by the difference in the shear flows of the two adjacent bays, viz. rings 0, 1, 2 and 3 are loaded by the following shears respectively

$$\left.\begin{aligned} S'_0(k) &= S_1(k) - S(k), \\ S'_1(k) &= S_2(k) - S_1(k), \\ S'_2(k) &= S_3(k) - S_2(k), \\ S'_3(k) &= S\ (k) - S_3(k), \end{aligned}\right\} \quad (4.3)$$

where $S(k)$ is the external shear distribution.

The forces in the rings are determined from the equations of equilibrium of a sector of the ring. The equations of equilibrium of the kth sector of a ring (fig. 3) are

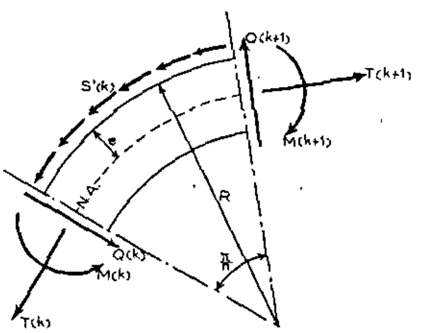

Fig. 3. Showing the forces acting on the neutral axis of the kth sector of a ring.

$$\left.\begin{aligned} &\{T(k+1) - T(k)\}\cos\frac{\pi}{2n} + \\ &\quad + \{Q(k+1) + Q(k)\}\sin\frac{\pi}{2n} - \\ &\quad - 2RS'(k)\sin\frac{\pi}{2n} = 0, \\ &\{T(k+1) + T(k)\}\sin\frac{\pi}{2n} - \\ &\quad - \{Q(k+1) - Q(k)\}\cos\frac{\pi}{2n} = 0, \\ &(R-e)\{T(k+1) - T(k)\} + \\ &\quad + \{M(k+1) - M(k)\} - \\ &\quad - R^2\left(\frac{\pi}{n}\right)S'(k) = 0. \end{aligned}\right\} \quad (4.4)$$

The following are two typical solutions of the equations (4.4) and may be verified by substitution.

(i) When $S'(k) = \dfrac{\sin \dfrac{i(2k+1)\pi}{2n}}{\sin \dfrac{i\pi}{2n}}$,

then $Q(k) = Rq_i \sin \dfrac{ik\pi}{n}$,

$T(k) = Rt_i \cos \dfrac{ik\pi}{n}$,

$M(k) = -R^2 m_i \cos \dfrac{ik\pi}{n}$.

(ii) When $S'(k) = \dfrac{\cos \dfrac{i(2k+1)\pi}{2n}}{\sin \dfrac{i\pi}{2n}}$,

then $Q(k) = Rq_i \cos \dfrac{ik\pi}{n}$,

$T(k) = -Rt_i \sin \dfrac{ik\pi}{n}$,

$M(k) = R^2 m_i \sin \dfrac{ik\pi}{n}$,

where $q_i = -\dfrac{\cot \dfrac{i\pi}{2n} \sin^2 \dfrac{\pi}{2n}}{\sin \dfrac{\pi}{2n}(i+1) \sin \dfrac{\pi}{2n}(i-1)}$,

$t_i = \dfrac{\sin \dfrac{\pi}{n}}{\cos \dfrac{i\pi}{n} - \cos \dfrac{\pi}{n}}$,

$m_i = \left(\dfrac{R-e}{R}\right) t_i + \tfrac{1}{2}\left(\dfrac{\pi}{n}\right) \operatorname{cosec}^2 \dfrac{i\pi}{2n}$.

It is assumed for the sake of simplicity, that the ring forces vary linearly over each sector of the ring. The exact expressions can be very easily written down, but when determining the strain energy of a ring sector it will be discovered that the work becomes most tedious. The influence of the shearing deformations in the rings will be neglected in the strain energy analysis, so it is not necessary to consider their circumferential variation.

The bending moments at a current point θ in rings 0, 1, 2 and 3 are given respectively by

$$\left.\begin{aligned}
M_0(k,\theta) &= M_0(k) + \frac{n\theta}{\pi}\{M_0(k+1) - M_0(k)\},\\
M_1(k,\theta) &= M_1(k) + \frac{n\theta}{\pi}\{M_1(k+1) - M_1(k)\},\\
M_2(k,\theta) &= M_2(k) + \frac{n\theta}{\pi}\{M_2(k+1) - M_2(k)\},\\
M_3(k,\theta) &= M_3(k) + \frac{n\theta}{\pi}\{M_3(k+1) - M_3(k)\},
\end{aligned}\right\} \quad (4.5)$$

and the corresponding axial loads in the rings are given respectively by

$$\left.\begin{aligned}
T_0(k,\theta) &= T_0(k) + \frac{n\theta}{\pi}\{T_0(k+1) - T_0(k)\},\\
T_1(k,\theta) &= T_1(k) + \frac{n\theta}{\pi}\{T_1(k+1) - T_1(k)\},\\
T_2(k,\theta) &= T_2(k) + \frac{n\theta}{\pi}\{T_2(k+1) - T_2(k)\},\\
T_3(k,\theta) &= T_3(k) + \frac{n\theta}{\pi}\{T_3(k+1) - T_3(k)\}.
\end{aligned}\right\} \quad (4.6)$$

Table (4.1) gives the explicit expressions for $P(k)$, $S(k)$, $Q(k)$, $T(k)$ and $M(k)$ for the various cases under consideration.

5 The strain energy analysis.

The coefficients α_i are determined from the rectangular set of $n-m$ linear simultaneous equations, each containing $n-1$ unknowns

$$\left.\begin{aligned}
&P_1(k) = 0,\ k = m+1,\ m+2, \ldots n,\\
&\qquad \text{for cases (1a), (2a), (3a) and (2b),}\\
&\text{or}\\
&S_2(k) = 0,\ k = m,\ m+1, \ldots n-1,\\
&\qquad \text{for cases (1b) and (3b).}
\end{aligned}\right\} \quad (5.1)$$

These equations are statements of the boundary conditions existing in the cut-out region, viz. the axial load is zero in the discontinuous stringers at the cut-out and the shear is zero in the panels which have been removed to form the cut-out. It is appropriate to explain in some detail the particular choices of the equations (5.1).

For cases (1a), (2a) and (2b) where the shear $S_2(k)$ is always zero in the middle bay it is obviously necessary to choose the first of equations (5.1). For case (3a), the first equation is still sufficient, for since $S_2(k)$ is an odd function it automatically infers that the second equation is satisfied. For cases (1b) and (3b), and also for case (3a) if so desired, the second equation of (5.1) is sufficient to ensure that all the boundary conditions in the cut-out region are satisfied.

The rectangular system of $n-m$ linear simultaneous equations (5.1) is insufficient for the determination of the $n-1$ unknown coefficients α_i for the cases (a), or the $n-2$ coefficients α_i for the cases (b), i. e. there are more unknowns than equations. *It is convenient to make some* transformation, e. g.

$$\left.\begin{aligned}
&\alpha_i = a_{m+1,i}\lambda_{m+1} + a_{m+2,i}\lambda_{m+2} +\\
&\qquad + \ldots + a_{n,i}\lambda_n, \text{ for cases (a),}\\
&\text{or}\\
&\alpha_i = a_{m,i}\lambda_m + a_{m+1,i}\lambda_{m+1} +\\
&\qquad + \ldots + a_{n-1,i}\lambda_{n-1}, \text{ for cases (b),}
\end{aligned}\right\} \quad (5.2)$$

so that the rectangular system is transformed into a square system of linear simultaneous equations. The coefficients λ are now the unknown quantities and the a's are as yet arbitrary constants. It is now possible to solve the transformed equations for the λ's and then substituting these values into the expressions (5.2) the values of the α_i coefficients may be found.

There are, of course, an infinite number of such transformations (5.2), but there is only one that will make the strain energy stored in the structure a minimum. It is proposed to determine this particular transformation for cases (1a) and (1b) only, since the transformations for the other cases follow easily by analogy.

Proceeding thus, it is necessary to examine the variation of the total strain energy stored in the structure with respect to the typical coefficient α_i, viz.

$$\frac{\partial U}{\partial \alpha_i} = \frac{\partial U_{STR}}{\partial \alpha_i} + \frac{\partial U_S}{\partial \alpha_i} + \frac{\partial U_{RM}}{\partial \alpha_i} + \frac{\partial U_{RT}}{\partial \alpha_i}, \quad (5.3)$$

where the strain energy is composed of the S.E. of the stringers, the S.E. of the sheet covering and the S.E. of the rings for bending and circumferential deformations of the rings. The strain energy of the rings due to shear in their planes is of second order and will therefore be neglected. Thus, equation (5.3) becomes

$$\frac{\partial U}{\partial \alpha_i} = \frac{\partial}{\partial \alpha_i} \sum_{k=0}^{2n-1} \left[\frac{1}{2\,EA_S} \int_0^a \{ 2\,P_1^2(k,x) + P_2^2(k,x) \}\, dx + \frac{aR}{2\,\mu t} \cdot \frac{\pi}{n} \{ 2\,S_1^2(k) + S_2^2(k) \} + \right.$$

$$\left. + \frac{R}{2\,E} \int_0^{\frac{\pi}{n}} \left\{ \frac{2\,M_0^2(k,\theta)}{I} + \frac{2\,M_1^2(k,\theta)}{I} + \frac{2\,T_0^2(k,\theta)}{A_R} + \frac{2\,T_1^2(k,\theta)}{A_R} \right\} d\theta \right]. \quad (5.4)$$

Referring to table 4.1 and making the appropriate substitutions and completing the various summations, it is readily verified that

$$\left.\begin{aligned} \frac{\partial U}{\partial \alpha_i} &= \frac{5}{3} \cdot \frac{na}{EA_S} \cdot A_i \alpha_i \quad \text{for case (1a),} \\ &\text{and} \\ \frac{\partial U}{\partial \alpha_i} &= \frac{na}{EA_S} \cdot B_i \alpha_i \quad \text{for case (1b),} \end{aligned}\right\} \quad (5.5)$$

where

$$A_i = 1 + {}^3/_{10} \left(\frac{E}{\mu}\right) \left(\frac{A_S}{at}\right) \left(\frac{R}{a}\right) \left(\frac{\pi}{n}\right) \operatorname{cosec}^2 \frac{i\pi}{2\,n} + $$
$$+ {}^1/_{10} \left(\frac{R}{a}\right)^3 \left(\frac{A_S R^2 m^2_i}{I} + \right.$$
$$\left. + \frac{A_S R^2 m^2_i}{I} \right) \left(\frac{\pi}{n}\right) \left(2 + \cos \frac{i\,\pi}{n}\right) +$$
$$+ {}^1/_{10} \left(\frac{R}{a}\right)^3 \left(\frac{A_S}{A_R} + \frac{A_S}{A_R}\right) \left(\frac{\pi}{n}\right) t^2_i \left(2 + \cos \frac{i\,\pi}{n}\right),$$

and

$$B_i = 1 + {}^3/_2 \left(\frac{E}{\mu}\right) \left(\frac{A_S}{at}\right) \left(\frac{R}{a}\right) \left(\frac{\pi}{n}\right) \operatorname{cosec}^2 \frac{i\,\pi}{2\,n} + $$
$$+ {}^1/_6 \left(\frac{R}{a}\right)^3 \left(\frac{A_S R^2 m^2_i}{I} + \right.$$
$$\left. + \frac{9 A_S R^2 m^2_i}{I} \right) \left(\frac{\pi}{n}\right) \left(2 + \cos \frac{i\,\pi}{n}\right) +$$
$$+ {}^1/_6 \left(\frac{R}{a}\right)^3 \left(\frac{A_S}{A_R} + \frac{9 A_S}{A_R}\right) \left(\frac{\pi}{n}\right) t^2_i \left(2 + \cos \frac{i\,\pi}{n}\right).$$

Now, the variations of the strain energy given in (5.5) are not independent of one another for various values of the integer i. Throughout the variation of the strain energy, the appropriate restrictions given in equation (5.1) must be conformed with. So, using the method of indeterminate multipliers, the independent variations of the strain energy are expressed by

$$\left.\begin{aligned} \frac{\partial U}{\partial \alpha_i} &= \sum_{k=m+1}^{n} \lambda_k \cdot \frac{\partial P(k)}{\partial \alpha_i} \quad \text{for case (1a),} \\ &\text{and} \\ \frac{\partial U}{\partial \alpha_i} &= \sum_{k=m}^{n-1} \lambda_k \cdot \frac{\partial S(k)}{\partial \alpha_i} \quad \text{for case (1b),} \end{aligned}\right\} \quad (5.6)$$

or in more explicit terms,

$$\left.\begin{aligned} \alpha_i &= \frac{1}{A_i} \sum_{k=m+1}^{n} \lambda_k \cos \frac{ik\pi}{n} \quad \text{for case (1a),} \\ &\text{and} \\ \alpha_i &= \frac{1}{B_i} \sum_{k=m}^{n-1} \lambda_k \frac{\cos \dfrac{i(2\,k+1)\pi}{2\,n}}{\sin \dfrac{i\,\pi}{2\,n}} \quad \text{for case (1b),} \end{aligned}\right\} \quad (5.7)$$

since the indeterminate multipliers λ are independent of an arbitrary constant multiplier.

The transformation (5.2) has therefore been found which enables the coefficients α_i to be determined so that the strain energy stored in the structure is a minimum.

Equations (5.1) and the appropriate transformations are summarized for the various cases in table 5.1. Explicit expressions are also given for the coefficients α_i when, $n - m = 1$, and when $n - m = 2$ for case (2b).

6 The relative stiffness parameters.

The relative stiffness parameter is defined as the ratio of the stiffness of the continuous cylinder with that of the cylinder containing a cut-out. Therefore it is expressed by the ratios of the strain energies, viz.

$$\eta = \frac{U_0}{U}, \quad (6.1)$$

where U_0 is the strain energy of the reinforced cylinder formed by continuing the stringers and sheet covering across the cut-out region.

Now, since the α_i distributions are orthogonal statically zero groups of forces the strain energy of the cylinder with cut-out may be expressed by

$$U = U_0 + \tfrac{1}{2} \sum_{i=2}^{n, \text{ or } n-1} \alpha_i \frac{\partial U}{\partial \alpha_i}, \tag{6.2}$$

so that the expression for the relative stiffness parameter becomes

$$\eta = \frac{1}{1+K}, \tag{6.3}$$

where

$$K = \frac{1}{2\,U_0} \sum_{i=2}^{n, \text{ or } n-1} \alpha_i \frac{\partial U}{\partial \alpha_i}$$

and

$$\frac{\partial U}{\partial \alpha_i} = \frac{5\,na}{3\,EA_S}\,\alpha_i A_i \text{ for cases (1a), (2a) and (2b),}$$

or

$$\frac{\partial U}{\partial \alpha_i} = \frac{na}{EA_S}\,\alpha_i B_i \text{ for cases (3a), (1b) and (3b).}$$

The derivation of K requires no further explanation and the relative stiffness parameters are given explicitly in table 6.1 for the various cases.

7 Numerical examples.

The load distribution in a particular three-bay cylinder and the stiffness reduction factor have been calculated for the six loading cases of fig. 2 when $n=6$ and when the values of the non-dimensional parameters are

$$\left(\frac{E}{\mu}\right)\left(\frac{A_S}{at}\right) = 1.5; \quad \left(\frac{R}{a}\right) = 1.5;$$
$$\left(\frac{A_S R^2}{I}\right) = 3000; \quad \left(\frac{A_S}{A_R}\right) = 1.0.$$

All rings are assumed identical and with zero eccentricity.

In addition, calculations have been carried out for case (1b), i. e. torsion, assuming $n=12$, where the values of the non-dimensional parameters are either the same as for $n=6$, or

$$\left(\frac{E}{\mu}\right)\left(\frac{A_S}{at}\right) = 0.75; \quad \left(\frac{R}{a}\right) = 1.5;$$
$$\left(\frac{A_S R^2}{I}\right) = 1500; \quad \left(\frac{A_S}{A_R}\right) = 0.5,$$

the total stiffener area being the same as for $n=6$ in the latter case.

Case (1a), $m=5$.

For convenience the total applied normal load has been taken as $P=2\,n=12$ units. In table 7.1 results for A_i and α_i, calculated after table 5.1, as well as results for P_0, P_1, S_1, T_0 and M_0 as determined after table 4.1 are presented. The stiffness reduction factor η which was calculated after table 6.1, is given in table 7.11.

Case (2a), $m=5$.

For convenience, the total applied bending moment has been taken as $M_y = nR = 6\,R$ units. Numerical results are presented in tables 7.2 and 7.11.

Case (3a), $m=5$.

For convenience, the total applied shear load has been taken as $S_y = \dfrac{2\,R}{a}\,n = 18$ units. Numerical results are presented in tables 7.3 and 7.11.

Case (1b), $m=5$.

For convenience, the total applied torque has been taken as $T = \dfrac{2\,\pi R^2}{a} = 3\,\pi R$ units. Numerical results are given in tables 7.4 and 7.11.

Case (2b), $m=4$.

For convenience, the total applied bending moment has been taken as $M_z = nR = 6\,R$ units. Numerical results are given in tables 7.5 and 7.11.

Case (3b), $m=5$.

For convenience, the total applied shear load has been taken as $S_z = \dfrac{2\,R}{a}\,n = 18$ units. Numerical results are presented in tables 7.6 and 7.11.

Case (1b), $m=4$.

For convenience, the total applied torque has been taken as $T = \dfrac{2\,\pi R^2}{a} = 3\,\pi R$ units. Substitution of the expression (5.7) for α_i, where B_i is given in table 7.7, in the rectangular system of linear simultaneous equations after table 5.1 yields

$$0.080411\,\lambda_5 - 0.154538\,\lambda_4 + 1 = 0,$$
$$-0.154538\,\lambda_5 + 0.329229\,\lambda_4 + 1 = 0.$$

By substituting the solution $\lambda_5 = -186.658$, $\lambda_4 = -90.654$ in (5.7) the values for α_i, given in table 7.7, were obtained. The results for P_1, S_1, S_2, T_0 and M_0 are also given in table 7.7. The stiffness reduction factor η, calculated after table 6.1, is given in table 7.11.

Case (1b), $n=12$, $m=11$.

For convenience, the total applied torque has been taken as $T = \dfrac{2\,\pi R^2}{a} = 3\,\pi R$ units. Numerical results are presented in tables 7.8 and 7.11.

Case (1b), $n=12$, $m=11$, $\left(\dfrac{E}{\mu}\right)\left(\dfrac{A_S}{at}\right) = 0.75$, etc.

For convenience, the total applied torque has been taken as $T = \dfrac{2\,\pi R^2}{a} = 3\,\pi R$ units. Numerical results are presented in tables 7.9 and 7.11.

Case (1b), $n=12$, $m=10$, $\left(\dfrac{E}{\mu}\right)\left(\dfrac{A_S}{at}\right) = 0.75$, etc.

For convenience, the total applied torque has been taken as $T = \frac{2\pi R^2}{a} = 3\pi R$ units. Substitution of the expression (5.7) for α_i, where B_i is given in table 7.10, in the rectangular system of linear simultaneous equations after table 5.1 yields

$$3.27716\,\lambda_{10} - 2.01745\,\lambda_{11} + 1 = 0,$$
$$-2.01745\,\lambda_{10} + 2.11021\,\lambda_{11} + 1 = 0.$$

By substituting the solution $\lambda_{10} = -1.45064$, $\lambda_{11} = -1.86076$ in (5.7) the values for α_i, given in table 7.10, were obtained. The results for S_1 and S_2 are also given in table 7.10. The stiffness reduction factor η, calculated after table 6.1, is given in table 7.11.

Several important conclusions follow from these results and are summarized below for each case.

Case (1a), normal load.

(I) The maximum normal load occurs in stringer 5 bordering the cut-out and is 1.8 times the external normal load applied to one stringer.

(II) The maximum shear in the panels can be determined by inspection and a redundancy calculation is not required. This maximum value of the shear occurs in the end bays between stringers m and $m+1$ and is given by

$$S_1(m) = \frac{n-m-0.5}{2n} \cdot \frac{P}{a}.$$

(III) The maximum normal load in the rings occurs at stringer 6 and is 0.24 times the external normal load applied to one stringer.

(IV) The maximum bending moment in the rings occurs at stringer 6 and is 0.0098 R times the external load applied to one stringer.

(V) The stiffness is not seriously reduced, $\eta = 0.878$.

Case (2a), bending across the cut-out.

(I) The maximum normal load occurs in stringer 5 bordering the cut-out and is 1.6 times the maximum external normal load, applied to stringer 6.

(II) The maximum shear in the panels can be determined by inspection and a redundancy calculation is not required. This maximum value of the shear stress occurs in the end bays between stringers m and $m+1$ and its value is given by

$$S_1(m) = \frac{aM_y}{nR}\left[\tfrac{1}{2} + \sum_{m+1}^{n-1} \cos\frac{i\pi}{n}\right].$$

(III) The maximum normal load in the rings occurs at stringer 6 and is 0.24 times the maximum external normal load, applied to stringer 6.

(IV) The maximum bending moment in the rings occurs at stringer 6 and is 0.0016 times the external bending moment, M_y.

(V) The stiffness is not seriously reduced, $\eta = 0.783$.

Case (3a), shear load across the cut-out.

(I) The maximum normal load in the stringers can be determined by inspection and a redundancy calculation is not required. This maximum value of the load occurs at the outer rings in stringers 0 and n. It is the maximum external normal load applied to one stringer,

$$P_{0(m)} = \frac{3\,aS_y}{2\,nR}.$$

(II) The maximum shear in the panels occurs in the middle bay between stringers 2 and 3 and is $\frac{1.3}{a}$ times the maximum external normal load applied to stringer 6.

(III) The maximum normal load occurs in the middle rings at stringer 6 and is 0.23 times the maximum external normal load applied to stringer 6.

(IV) The maximum bending moment occurs in the middle rings at stringer 6 and is 0.0076 R times the maximum external normal load applied to stringer 6.

(V) The stiffness is only slightly reduced, $\eta = 0.967$.

Case (1b), torsion.

(I) The maximum normal load occurs in stringer 4 at the middle rings and is $\frac{0.16}{R}$ times the external torque, T.

(II) The maximum shear in the panels occurs in the middle bay between stringers 4 and 5, i. e. in the panel adjacent to the cut-out, and is $\frac{0.31}{aR}$ times the external torque, T.

(III) The maximum normal load in the middle rings occurs at stringer 5 and is $\frac{0.13}{R}$ times the external torque, T.

(IV) The maximum bending moment in the middle rings occurs at stringer 5 and is 0.0075 times the external torque, T.

(V) The stiffness is considerably reduced, $\eta = 0.362$.

Case (2b), bending parallel to the cut-out.

(I) The maximum load occurs in stringer 4, bordering the cut-out, at the middle rings and is 1.4 times the maximum external normal load, applied to stringer 3.

(II) The maximum shear in the panels occurs in the end bays between stringers 4 and 5 and is $\frac{0.32}{a}$ times the maximum external normal load, applied to stringer 3.

(III) The maximum normal load in the rings occurs at stringer 5, and is 0.15 times the maximum external normal load, applied at stringer 3.

(IV) The maximum bending moment in the rings occurs at stringer 5 and is 0.0014 times the external bending moment, M_z.

(V) The stiffness is not seriously reduced, $\eta = 0.828$.

Case (3b), shear load parallel to the cut-out.

(I) The maximum normal load occurs in stringer 4 at the middle rings and is 2.2 times the maximum external normal load, applied to stringer 3.

(II) The maximum shear in the panels occurs in the middle bay between stringers 4 and 5, i. e. in the panel adjacent to the cut-out, and is $\frac{3.3}{a}$ times the maximum external normal load, applied to stringer 3.

(III) The maximum normal load in the middle rings occurs at stringer 5 and is 1.6 times the maximum external normal load, applied to stringer 3.

(IV) The maximum bending moment in the middle rings occurs at stringer 5 and is 0.029 R times the maximum external normal load, applied to stringer 3.

(V) The stiffness is considerably reduced, $\eta = 0.192$.

Case (1b), torsion, $m = 4$.

(I) The maximum normal load occurs in stringer 3 at the middle rings, and is $\frac{0.63}{R}$ times the external torque, T.

(II) The maximum shear in the panels occurs in the middle bay between stringers 3 and 4, i. e. in the panel adjacent to the cut-out, and is $\frac{0.74}{aR}$ times the external torque, T.

(III) The maximum normal load in the middle rings occurs at stringer 2 and is $\frac{0.52}{R}$ times the external torque, T.

(IV) The maximum bending moment in the middle rings occurs at stringer 2 and is 0.030 times the external torque, T.

(V) The stiffness is excessively reduced, $\eta = 0.025$.

Case (1b), torsion, $n = 12$, $m = 11$.

(I) The maximum shear in the panels occurs in the middle bay between stringers 10 and 11, i. e. in the panels adjacent to the cut-out, and is $\frac{0.22}{aR}$ times the external torque, T.

(II) The stiffness is not seriously reduced, $\eta = 0.825$.

Case (1b), torsion, $n = 12$, $m = 11$, $\left(\frac{E}{\mu}\right)\left(\frac{A_s}{at}\right) = 0.75$, etc.

(I) The maximum shear in the panels occurs in the middle bay between stringers 10 and 11, i. e. in the panel adjacent to the cut-out, and is $\frac{0.21}{aR}$ times the external torque, T.

(II) The stiffness is not seriously reduced, $\eta = 0.780$.

(III) The effect of doubling the stiffener cross sections on the overall behaviour of the construction is relatively small.

Case (1b), torsion, $n = 12$, $m = 10$, $\left(\frac{E}{\mu}\right)\left(\frac{A_s}{at}\right) = 0.75$, etc.

(I) The maximum shear in the panels occurs in the middle bay between stringers 9 and 10, i. e. in the panel adjacent to the cut-out, and is $\frac{0.40}{aR}$ times the external torque, T.

(II) The stiffness is considerably reduced, $\eta = 0.348$.

(III) Comparison with $n = 6$, $m = 5$, $\left(\frac{E}{\mu}\right)\left(\frac{A_s}{at}\right) = 1.5$, etc. shows that the stiffness reduction ratio is governed mainly by the relative circumferential width of the cut-out, i. e. the ratio $\frac{n-m}{n}$. It decreases very rapidly with increasing $\frac{n-m}{n}$.

8 Nomenclature.

The following nomenclature is used in this paper,

a	is the length of a bay.
A_i	is the ith strain energy coefficient for cases (1a), (2a) and (2b) and is explicitly given in the text.
A_R	is the effective cross-sectional area of the rings (other than those bordering the cut-out).
$\bar{A}_R$	is the effective cross-sectional area of the rings bordering the cut-out.
A_S	is the effective cross-sectional area of a stringer.
B_i	is the ith strain energy coefficient for cases (3a), (1b) and (3b) and is explicitly given in the text.
e	is the eccentricity of the neutral axis of the rings (other than those bordering the cut-out) from the centre line of the sheet covering.
$\bar{e}$	is the eccentricity of the neutral axis of the rings bordering the cut-out.
E	is Young's modulus for all components.
i	is an integer greater than unity.
I	is the effective moment of inertia of the rings (other than those bordering the cut-out).
$\bar{I}$	is the effective moment of inertia of the rings bordering the cut-out.
k	is the current stringer or panel number.
m	there are $2n - 2m - 1$ discontinuous stringers.

m_i is the ith factor concerning the bending moments in the rings (other than those bordering the cut-out) and is given explicitly in the text.

$\bar{m}_i$ is the ith factor concerning the bending moments in the rings bordering the cut-out and is given explicitly in the text.

K is a stiffness factor and is defined in the text.

$M_0(k)$, $M_1(k)$ etc. are the bending moments at the kth stringer in rings 0, 1 etc. respectively.

$M_0(k,\theta)$, $M_1(k,\theta)$ etc. are the bending moments at a current point θ in the kth sector of rings 0, 1 etc. respectively.

M_y is the total externally applied bending moment about the X—Z plane (case (2a)).

M_z is the total externally applied bending moment about the X—Y plane (case (2b)).

n there are a total of $2\,n$ stringers.

$P_0(k)$, $P_1(k)$ etc. are the axial loads in the kth stringer at rings 0, 1 etc. respectively.

$P_1(k,x)$, $P_2(k,x)$ and $P_3(k,x)$ are the axial loads in the kth stringer at a current point x of the first, second and third bays respectively.

P is the total externally applied tension (case (1a)).

q_i is the ith factor concerning the shear in the rings.

$Q_0(k)$, $Q_1(k)$ etc. are the shearing forces at the kth stringer in rings 0, 1 etc. respectively.

R is the radius of curvature of the centre line of the sheet covering.

$S_1(k)$, $S_2(k)$ and $S_3(k)$ are the shears per unit run in the kth panel (i.e. bounded by the kth and $k+1$th stringers) in the first, second and third bays respectively.

$S'_0(k)$, $S'_1(k)$ etc. are the differences of shear flows in the kth panels which load rings 0, 1 etc. respectively.

$S(k)$ is the running externally applied shear to the kth panel.

S_y is the total externally applied force parallel to the Y axis (case (3a)).

S_z is the total externally applied force parallel to the Z axis (case (3b)).

t is the thickness of the sheet covering.

t_i is the ith factor concerning the circumferential tension in the rings.

$T_0(k)$, $T_1(k)$ etc. are the circumferential tensions at the kth stringer in rings 0, 1 etc. respectively.

$T_0(k,\theta)$, $T_1(k,\theta)$ etc. are the circumferential tensions at a current point θ in the kth sector of rings 0, 1 etc. respectively.

T is the total externally applied torque (case (1b)).

U is the total strain energy stored in the structure.

U_0 is the total strain energy stored in the structure when there is no cut-out.

U_{RM} is the total strain energy stored in all the rings for bending deformations.

U_{RT} is the total strain energy stored in all the rings for circumferential extensions.

U_S is the total strain energy stored in the sheet covering.

U_{STR} is the total strain energy stored in all the stringers.

x is a longitudinal co-ordinate for each panel (fig. 1).

X, Y, Z is a system of rectangular axes defined in fig. 1.

α_0, α_1 are statically determinate coefficients.

α_i is the ith statically indeterminate coefficient.

η is the relative stiffness parameter.

θ is an angular co-ordinate for each sector (fig. 1).

λ_k is the kth indeterminate multiplier.

μ is the shear modulus.

There are a few additional symbols introduced in the appendices, but these are defined as they are introduced.

9 References.

1 EBNER, H. and KÖLLER, H. Zur Berechnung des Kraftverlaufes in versteiften Zylinderschalen. Luftfahrtforschung, vol. XIV, pp. 607—626 (1937).

2 KITTELSEN, H. M. Openings in circular fuselages. Aircraft Engineering, vol. XII, no. 131, pp. 73—75 (March 1940).

3 GOLOLOBOV, M. M. Shear distribution due to twist in a cylindrical fuselage with a cut-out. Journal of the Aeronautical Sciences, vol. 14, no. 4, pp. 253—256 (April 1947).

4 LANGHAAR, H. L. and SMITH, C. R. Stresses in cylindrical semimonocoque open beams. Journal of the Aeronautical Sciences, vol. 14, no. 4, pp. 211—220 (April 1947).

5 CICALA, P. Effects of cut-outs in semimonocoque structures. Journal of the Aeronautical Sciences, vol. 15, no. 3, pp. 171—179 (March 1948).

6 MORLEY, L. S. D. Load distribution and relative stiffness parameters for a reinforced flat plate containing

a rectangular cut-out under plane loading. Report S. 347 of the Nationaal Luchtvaartlaboratorium, Amsterdam (1948).

7 RAND, T. Statik för flygplanskal. Kungliga Tekniska Högskolans Avhandlingar, No. 54, Stockholm 1948.

8 HOFF, N. J. Stresses in a reinforced monocoque cylinder under concentrated symmetric transverse loads. Journal of Applied Mechanics, vol. 11, no. 4, pp. A-235—239 (December 1944).

9 BESKIN, L. Local stress distribution in cylindrical shells. Journal of Applied Mechanics, vol. 13, no. 2, pp. A-137—147 (June 1946).

Acknowledgement.

The authors would like to acknowledge the kind help and assistance given by Mr. W. S. Hemp (Senior Lecturer in the Theory of Structures) and Mr. A. Robinson (Senior Lecturer in Mathematics) both of the College of Aeronautics, Cranfield, England, in the preparation by the first author of a thesis dealing with a problem that is closely allied with the subject matter of this paper. Some of these suggestions have been incorporated in this paper.

Appendix A. Concerning the transformations for a cylinder with 2 p + 1 bays.

The method will be briefly described for the solution of the regular circular cylinder with $2p+1$ bays and containing a rectangular cut-out in the $p+1$th bay, i. e. in the centre bay, as shown below.

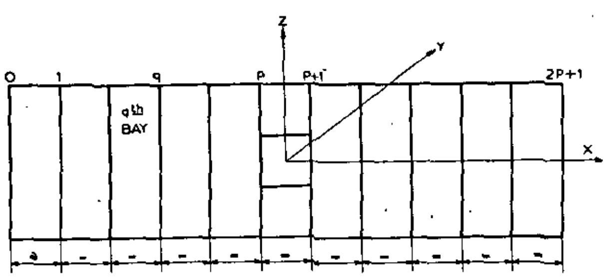

It is still assumed that there is complete geometrical and elastic symmetry about the X—Y and Y—Z planes so that the symmetrical properties of the stress distributions given in table 3.1 are still true. In addition, it is assumed that the bays are equal in every respect with, of course, the exception of the cut-out bay. These restrictions are not essential characteristics of the analysis, but they simplify the symbolization.

The cylinder is now loaded at rings 0 and $2p+1$ and the redundancies are again chosen as the axial loads in the stringers at the ring bordering the cut-out, i. e. the pth ring. The most general distributions, observing the symmetrical properties about the X—Y plane, are given by

$$\left.\begin{aligned} P_p(k) &= \alpha_0 + \alpha_{1,p}\cos\frac{k\pi}{n} + \\ &+ \sum_{i=2}^{n} \alpha_i \cos\frac{ik\pi}{n} \quad \text{for cases (a)}, \end{aligned}\right\} \quad (A.1)$$

or

$$\left.\begin{aligned} P_p(k) &= \alpha_{1,p}\sin\frac{k\pi}{n} + \\ &+ \sum_{i=2}^{n-1} \alpha_i \sin\frac{ik\pi}{n} \quad \text{for cases (b)}, \end{aligned}\right\} \quad (A.1)$$

where α_0 and $\alpha_{1,p}$ are again determined from the overall equilibrium requirements.

Now, since the α_i distributions are statically zero and orthogonal (i. e. the mixed coefficients in the strain energy expressions are all zero), the axial loads in the stringers at any other ring q are given by

$$\left.\begin{aligned} P_q(k) &= \alpha_0 + \alpha_{1,q}\cos\frac{k\pi}{n} + \\ &+ \sum_{i=2}^{n} \tau_{i,q}\,\alpha_i \cos\frac{ik\pi}{n} \quad \text{for cases (a)}, \\ &\text{and} \\ P_q(k) &= \alpha_{1,q}\sin\frac{k\pi}{n} + \\ &+ \sum_{i=2}^{n-1} \tau_{i,q}\,\alpha_i \sin\frac{ik\pi}{n} \quad \text{for cases (b)}, \end{aligned}\right\} \quad (A.2)$$

where $\tau_{i,q}$ is the diffusion constant at ring q for the unit trigonometric distribution of axial forces of order index i applied to the stringers at ring P. The diffusion constants τ have the same value for the sine and cosine distributions of same order index. In addition, for the particular structure under consideration

$$\left.\begin{aligned} &\tau_{i,q} = |\tau_{i,2p+1-q}| \qquad q \leq p, \\ &\tau_{i,0} = \tau_{i,2p+1} = 0, \\ \text{and} \\ &\tau_{i,p} = |\tau_{i,p+1}| = 1. \end{aligned}\right\} \quad (A.3)$$

Ebner and Köller (ref. 1) have dealt with the computation of these diffusion constants τ, although it seems as if some additional tabulation and/or nomographs are required for the important case of the circular cylinder.

Using the expressions (A.2) the shears in the panels and the ring forces may be determined in terms of the α_i coefficients, assuming that the diffusion constants τ have already been computed. The general expressions are for cases (a)

$$\left.\begin{aligned} S_q(k) &= \frac{1}{2a}(\alpha_{1,q} - \alpha_{1,q-1})\,\frac{\sin\frac{(2k+1)\pi}{2n}}{\sin\frac{\pi}{2n}} + \\ &+ \frac{1}{2a}\sum_{i=2}^{n}(\tau_{i,q} - \tau_{i,q-1})\alpha_i\,\frac{\sin\frac{i(2k+1)\pi}{2n}}{\sin\frac{i\pi}{2n}}, \\ Q_q(k) &= \frac{R}{2a}\sum_{i=2}^{n}(\tau_{i,q+1} - 2\tau_{i,q} + \\ &+ \tau_{i,q-1})\,\alpha_i q_i \sin\frac{ik\pi}{n}, \end{aligned}\right\} \quad (A.4a)$$

$$\left.\begin{aligned}
T_q(k) &= \frac{R}{2a}\sum_{i=2}^{n}(\tau_{i,q+1}-2\tau_{i,q}+\\
&\qquad +\tau_{i,q-1})\,\alpha_i t_i\cos\frac{ik\pi}{n},\\
M_q(k) &= -\frac{R}{2a}\sum_{i=2}^{n}(\tau_{i,q+1}-2\tau_{i,q}+\\
&\qquad +\tau_{i,q-1})\,\alpha_i m_i\cos\frac{ik\pi}{n},\ q\neq p, p+1,\\
M_p(k) &= -\frac{R}{2a}\sum_{i=2}^{n}(\tau_{i,p+1}-2+\\
&\qquad +\tau_{i,p-1})\,\alpha_i\overline{m}_i\cos\frac{ik\pi}{n},
\end{aligned}\right\}\text{(A. 4a)}$$

and for cases (b) they are

$$\left.\begin{aligned}
S_q(k) &=\\
&-\frac{1}{2a}(\alpha_{1,q}-\alpha_{1,q-1})\frac{\cos\dfrac{(2k+1)\pi}{2n}}{\sin\dfrac{\pi}{2n}}-\\
&-\frac{1}{2a}\sum_{i=2}^{n-1}(\tau_{i,q}-\tau_{i,q-1})\,\alpha_i\frac{\cos\dfrac{i(2k+1)\pi}{2n}}{\sin\dfrac{i\pi}{2n}},\\
Q_q(k) &= -\frac{R}{2a}\sum_{i=2}^{n-1}(\tau_{i,q+1}-2\tau_{i,q}+\\
&\qquad +\tau_{i,q-1})\,\alpha_i q_i\cos\frac{ik\pi}{n},\\
T_q(k) &= \frac{R}{2a}\sum_{i=2}^{n-1}(\tau_{i,q+1}-2\tau_{i,q}+\\
&\qquad +\tau_{i,q-1})\,\alpha_i t_i\sin\frac{ik\pi}{n},\\
M_q(k) &= -\frac{R}{2a}\sum_{i=2}^{n-1}(\tau_{i,q+1}-2\tau_{i,q}+\\
&\qquad +\tau_{i,q-1})\,\alpha_i m_i\sin\frac{ik\pi}{n},\ q\neq p, p+1\\
M_p(k) &= -\frac{R}{2a}\sum_{i=2}^{n-1}(\tau_{i,p+1}-2+\\
&\qquad +\tau_{i,p-1})\,\alpha_i\overline{m}_i\sin\frac{ik\pi}{n}.
\end{aligned}\right\}\text{(A. 4b)}$$

For the determination of the α_i coefficients the fundamental equations are the same as equations (5.1). The transformations are of the same character except that the expressions for A_i and B_i must be modified to

$$\begin{aligned}
A_i \text{ and } B_i &= 4\varphi_i+\\
&+3\left(\frac{E}{\mu}\right)\left(\frac{A_S}{at}\right)\left(\frac{R}{a}\right)\left(\frac{\pi}{n}\right)\chi_i\operatorname{cosec}^2\frac{i\pi}{2n}+\\
&+\left(\frac{R}{a}\right)^3\left(\frac{A_S R^2 m^2{}_i\psi_i}{I}+\frac{A_S R^2\overline{m}^2{}_i\overline{\psi}_i}{\overline{I}}\right)\left(\frac{\pi}{n}\right)\times\\
\times&\left(2+\cos\frac{i\pi}{n}\right)+\left(\frac{R}{a}\right)^3\left(\frac{A_S\psi_i}{A_R}+\frac{A_S\overline{\psi}_i}{\overline{A}_R}\right)\times\\
&\times\left(\frac{\pi}{n}\right)t^2{}_i\left(2+\cos\frac{i\pi}{n}\right),
\end{aligned}\qquad\text{(A. 5)}$$

where

$$\begin{aligned}
\varphi_i &= (2+\tau_{i,p+1}\tau_{i,p})+\\
&\quad +2\sum_{q=1}^{p}(\tau^2_{i,q}+\tau_{i,q}\tau_{i,q-1}+\tau^2_{i,q-1}),\\
\chi_i &= (\tau_{i,p+1}-\tau_{i,p})^2+2\sum_{q=1}^{p}(\tau_{i,q}-\tau_{i,q-1})^2,\\
\psi_i &= 2\sum_{q=0}^{p-1}(\tau_{i,q+1}-2\tau_{i,q}\tau_{i,q-1})^2,\\
\overline{\psi}_i &= (\tau_{i,p+1}-2+\tau_{i,p-1})^2.
\end{aligned}$$

It is to be noted that $A_i\neq B_i$ because $\tau_{i,q}=\tau_{i,2p+1-q}$ for the evaluation of A_i, and $\tau_{i,q}=-\tau_{i,2p+1-q}$ for the evaluation of B_i. Using the new expressions (A. 5) for A_i and B_i, the coefficients α_i may be determined in precisely the same way as for the three-bay cylinder which is one particular case of these general formulae.

When evaluating the relative stiffness parameters for this general case, it is of interest to note that now

$$\left.\begin{aligned}
&\frac{\partial U}{\partial\alpha_i}=\frac{1}{12}\cdot\frac{na}{EA_S}\cdot A_i\alpha_i,\\
\text{or}\quad&\\
&\frac{\partial U}{\partial\alpha_i}=\frac{1}{12}\cdot\frac{na}{EA_S}\cdot B_i\alpha_i.
\end{aligned}\right\}\text{(A. 6)}$$

Appendix B. Concerning uniformly distributed stringers.

The object of this appendix is to consider the case of uniformly distributed stringers over the periphery of the cylinder for cut-out problems. Hoff and Beskin (refs. 8 and 9) have made investigations using this assumption for complete cylinders under the action of concentrated loads and have obtained satisfactory results.

As mentioned in sec. 1, the reliability of this assumption could be checked by investigating whether singularities are found in the distribution of stresses at the edges of the cut-out in a cylinder having continuously distributed stringers.

It is not proposed to enter into any generality here, so we shall consider only the problem of the three-bay circular cylinder undergoing torsion with an infinitely thin slit in the centre bay at $\theta=0$. All the rings are assumed to be identical and with zero eccentricity.

The axial load per unit run in the sheet at ring 1 is assumed to be given by:

$$\left.\begin{aligned}
&P_1(\theta)=\sum_{i=2}^{\infty}\alpha_i\sin i\theta,\\
&\text{so that}\\
&S_1(\theta)=\frac{T}{2\pi R^2}-\frac{R}{a}\sum_{i=2}^{\infty}\frac{\alpha_i}{i}\cos i\theta,\\
&Q_0(\theta)=-\frac{R^2}{a}\sum_{i=2}^{\infty}\frac{\alpha_i}{i(i^2-1)}\cos i\theta,\\
&T_0(\theta)=\frac{R^2}{a}\sum_{i=2}^{\infty}\frac{\alpha_i}{(i^2-1)}\sin i\theta,\\
&M_0(\theta)=\frac{R^3}{a}\sum_{i=2}^{\infty}\frac{\alpha_i}{i^2(i^2-1)}\sin i\theta,
\end{aligned}\right\}\text{(B. 1)}$$

and the other forces may be obtained from comparison with case (1b) in table 4.1.

Thus the rectangular system of equations now becomes

$$\frac{T}{2\pi R^2} + 2\sum_{i=2}^{\infty}\frac{\alpha_i}{i} = 0, \qquad (B.2)$$

and the transformation which makes the strain energy a minimum is

$$\alpha_i = \frac{\lambda}{iB_i}. \qquad (B.3)$$

It is easily verified that

$$B_i = 1 + 6\left(\frac{E}{\mu}\right)\left(\frac{t^*}{t}\right)\left(\frac{R^2}{a^2}\right)\cdot\frac{1}{i^2} + 20\left(\frac{R^3}{a^3}\right)\left(\frac{R^3t^*}{I}\right)\cdot\frac{1}{i^4(i^2-1)^2},$$

where the strain energies of the shear and circumferential tensions in the rings have been neglected, and t^* is the imaginary thickness of the sheet covering in tension.

The α_i coefficients are therefore defined explicitly by

$$\alpha_i = -\frac{\dfrac{Ta}{4\pi R^3}}{iB_i\sum_{i=2}^{\infty}\dfrac{i}{i^2B_i}} \qquad (B.4)$$

where the sum to infinity may easily be found and will always be finite.

The shear in the sheet in the centre bay is given by

$$S_2(\theta) = \frac{T}{2\pi R^2}\left[1 - \frac{\sum_{i=2}^{\infty}\dfrac{\cos i\theta}{i^2B_i}}{\sum_{i=2}^{\infty}\dfrac{1}{i^2B_i}}\right], \qquad (B.5)$$

which after substituting

$$B_i = 1 + \frac{c}{i^2} + \frac{d}{i^4(i^2-1)^2}$$

may be written as

$$S_2(\theta) = \frac{T}{2\pi R^2} \times$$

$$\times \frac{\sum_{i=2}^{\infty}\dfrac{1}{i^2} - \sum_{i=2}^{\infty}\dfrac{\cos i\theta}{i^2} - \sum_{i=2}^{\infty}p_i(1-\cos i\theta)}{\sum_{i=2}^{\infty}\dfrac{1}{i^2} - \sum_{i=2}^{\infty}p_i}$$

where

$$p_i = \frac{c + \dfrac{d}{i^2(i^2-1)^2}}{i^4 + ci^2 + \dfrac{d}{(i^2-1)^2}}$$

In accordance with the examples considered in sec. 7, it was assumed that

$$\left(\frac{E}{\mu}\right)\left(\frac{t^*}{t}\right) = 1.5, \quad \left(\frac{R}{a}\right) = 1.5, \quad \frac{R^2at^*}{I} = 3000$$

giving $c = 20.25$ and $d = 303750$, which yields

$$\sum_{i=2}^{\infty} p_i = 0.471.$$

The summation

$$\sum_{i=2}^{\infty} p_i(1-\cos i\theta)$$

was carried out numerically for a number of values of

$$0 \leq \theta \leq \pi.$$

The remaining summations are independent of c and d, their values following from

$$\sum_{i=2}^{\infty}\frac{1}{i^2} = \frac{\pi^2}{6} - 1,$$

$$\sum_{i=2}^{\infty}\frac{\cos i\theta}{i^2} = \frac{\pi^2}{6} - \frac{\pi\theta}{2} + \frac{\theta^2}{4} - \cos\theta,$$

this summation being valid only for $0 \leq \theta \leq \pi$.

Numerical results for $S_2(\theta)$ are presented in table B.1 and fig. B.1. The following conclusions can be drawn from these results:

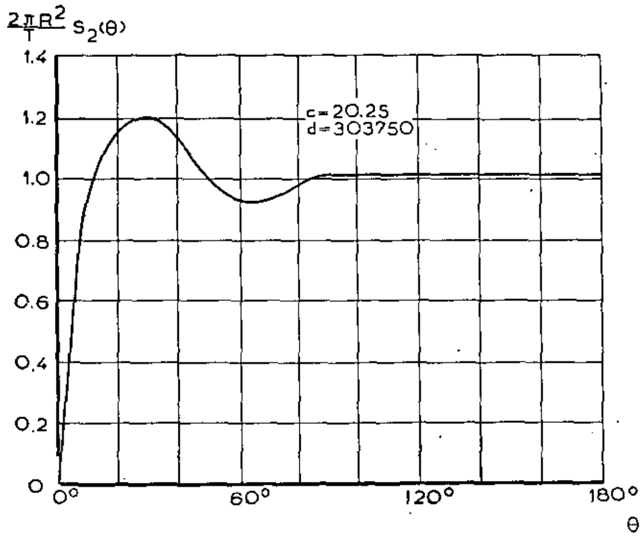

Fig. B.1. Relation between θ and S_2.

(I) No singularity exists in the stress distribution at the edge of the cut-out, the shear stresses decreasing gradually to zero when approaching this edge.

(II) When θ increases from 0 to π the shear S_2 increases rapidly at first until it reaches a maximum, after which it decreases slowly and approaches closely to the shear in the corresponding cylinder without cut-out.

(III) *A quantitative comparison* between the results obtained for cylinders with continuously distributed stiffeners and for cylinders having discrete stiffeners is not possible, the width of the cut-out in the circumferential direction being different in both cases. In fig. B. 2 the relation between θ and S_2 has been presented for continuously distributed and several cases of discrete stiffeners. It is observed that the increase of m from 10 to 11 for $n = 12$ and the increase of m from 4 to 5 for $n = 6$ results in a much closer approach to the curve for continuously distributed stiffeners in the neighbourhood of the cut-out. For $n = 12$ and $m = 11$ the curve for discrete stiffeners shows already a quite close resemblance to the curve for continuously distributed stiffeners, especially for $\theta > 30°$. It can be concluded that the method of replacing discrete stiffeners by continuously distributed stiffeners will yield reliable results provided the number of stringers is not too small, because the general character of the relation between θ and S_2 is the same for both cases in fig. B. 2.

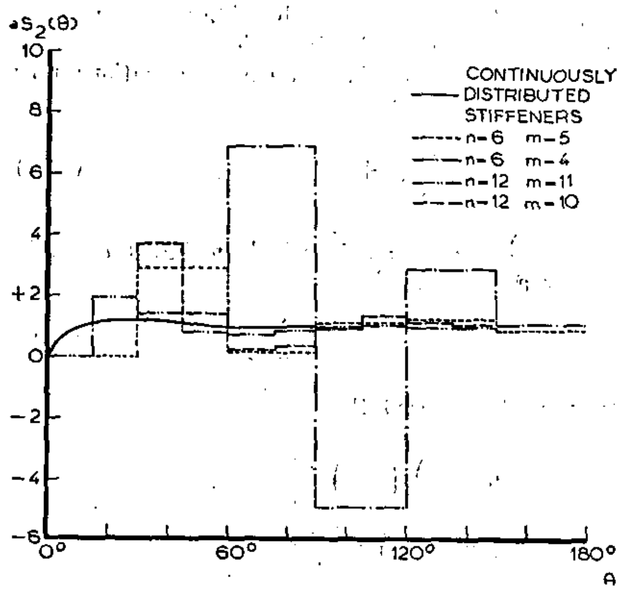

Fig. B. 2. Comparison between results for cylinders loaded in torsion and having discrete and continuously distributed stiffeners.

TABLE 3.1.

Properties of the Stresses.

Case	Stress	X—Y plane	Y—Z plane
(1a)	p	SYM	SYM
	s	ASYM	ASYM
	t	SYM	SYM
	q	ASYM	SYM
	m	SYM	SYM
(2a)	p	SYM	SYM
	s	ASYM	ASYM
	t	SYM	SYM
	q	ASYM	SYM
	m	SYM	SYM
(3a)	p	SYM	ASYM
	s	ASYM	SYM
	t	SYM	ASYM
	q	ASYM	ASYM
	m	SYM	ASYM
(1b)	p	ASYM	ASYM
	s	SYM	SYM
	t	ASYM	ASYM
	q	SYM	ASYM
	m	ASYM	ASYM
(2b)	p	ASYM	SYM
	s	SYM	ASYM
	t	ASYM	SYM
	q	SYM	SYM
	m	ASYM	SYM
(3b)	p	ASYM	ASYM
	s	SYM	SYM
	t	ASYM	ASYM
	q	SYM	ASYM
	m	ASYM	ASYM

where p is a stringer axial stress,
s is a panel shearing stress,
t is a ring circumferential stress,
q is a shearing stress in a ring,
m is a stress in a ring due to bending.

TABLE 6.1.

The relative stiffness parameters.

The relative stiffness parameter η is given by

$$\eta = \frac{1}{1+K}.$$

The following table gives the explicit expressions for K for the various cases.

Case	K
(1a)	$\frac{10\,n^2}{9\,P^2} \sum_{i=2}^{n} \alpha_i^2 A_i$
(2a)	$\frac{5\,n^2}{9} \left(\frac{R}{M_y}\right)^2 \sum_{i=2}^{n} \alpha_i^2 A_i$
(3a)	$\frac{4}{3}\left(\frac{R}{a}\right)\left(\frac{n}{S_y}\right)^2 \sum_{i=2}^{n} \alpha_i^2 B_i \Big/ \left\{3\left(\frac{a}{R}\right) + \frac{\pi}{n \sin^2 \frac{\pi}{2\,n}} \left(\frac{E}{\mu}\right)\left(\frac{A_S}{at}\right)\right\}$
(1b)	$\frac{2\,\pi n}{3}\left(\frac{\mu}{E}\right)\left(\frac{at}{A_S}\right)\left(\frac{R}{a}\right)\left(\frac{R}{T}\right)^2 \sum_{i=2}^{n-1} \alpha_i^2 B_i$
(2b)	$\frac{5\,n^2}{9}\left(\frac{R}{M_z}\right)^2 \sum_{i=2}^{n-1} \alpha_i^2 A_i$
(3b)	$\frac{4}{3}\left(\frac{R}{a}\right)\left(\frac{n}{S_z}\right)^2 \sum_{i=2}^{n-1} \alpha_i^2 B_i \Big/ \left\{3\left(\frac{a}{R}\right) + \frac{\pi}{n \sin^2 \frac{\pi}{2\,n}} \left(\frac{E}{\mu}\right)\left(\frac{A_S}{at}\right)\right\}$

TABLE 7.1.

Numerical results for case (1a).

i	A_i	α_i	k	P_0	P_1	$a\,S_1$	T_0	$\frac{1}{R}\,M_0$
—	—	—	0	1	0.7935	— 0.1033	+ 0.0418	+ 0.00071
—	—	—	1	1	1.1857	+ 0.0825	— 0.0412	— 0.00124
2	273.521	— 0.00182507	2	1	0.8795	— 0.0381	+ 0.0260	+ 0.00130
3	8.06964	+ 0.0618609	3	1	1.1040	+ 0.0660	— 0.0041	+ 0.00112
4	1.99982	— 0.249621	4	1	0.6683	— 0.2658	+ 0.0450	— 0.00166
5	1.49068	+ 0.334878	5	1	1.7657	+ 0.5	— 0.1668	— 0.00475
6	1.41891	— 0.351817	6	1	0	0	+ 0.2404	+ 0.00976

TABLE 7.2.

Numerical results for case (2a).

i	A_i	α_i	k	P_0	P_1	$a\,S_1$	T_0	$\frac{1}{R}\,M_0$
—	—	—	0	+ 1	+ 1.2065	+ 0.1033	— 0.0418	+ 0.00071
—	—	—	1	+ 0.8660	+ 0.6803	— 0.0825	+ 0.0412	— 0.00124
2	273.521	+ 0.00182507	2	+ 0.5	+ 0.6205	+ 0.0381	— 0.0260	+ 0.00130
3	8.06964	— 0.0618609	3	0	— 0.1040	— 0.0660	+ 0.0041	+ 0.00112
4	1.99982	+ 0.249621	4	— 0.5	— 0.1683	+ 0.2658	— 0.0450	— 0.00166
5	1.49068	— 0.334878	5	— 0.8660	— 1.6318	— 0.5	+ 0.1668	— 0.00475
6	1.41891	+ 0.351817	6	— 1	0	0	— 0.2404	+ 0.00976

TABLE 7.3.

Numerical results for case (3a).

i	B_i	α_i	k	P_0	P_1	$a\,S_1$	$a\,S_2$	T_0	$\frac{1}{R}\,M_0$
—	—	—	0	+ 3	+ 1.215	— 0.893	— 1.215	— 0.0456	+ 0.00120
—	—	—	1	+ 2.598	+ 0.669	— 2.822	— 2.553	+ 0.0410	— 0.00111
2	2267.30	+ 0.000621311	2	+ 1.5	+ 0.675	— 3.647	— 3.902	— 0.0310	+ 0.00061
3	57.5575	— 0.0244747	3	0	— 0.244	— 3.891	— 3.414	+ 0.0363	+ 0.00020
4	7.76103	+ 0.181510	4	— 1.5	— 0.006	— 2.398	— 3.401	— 0.0895	+ 0.00086
5	3.82629	— 0.368164	5	— 2.598	— 1.701	— 1.5	0	+ 0.1791	— 0.00497
6	3.31279	+ 0.425232	6	— 3	0	0	0	— 0.2262	+ 0.00764

TABLE 7.4.

Numerical results for case (1b).

i	B_i	α_i	k	P_1	$a\,S_1$	$a\,S_2$	T_0	$\frac{1}{R}\,M_0$
—	—	—	0	0	+ 1.051	+ 0.899	0	0
—	—	—	1	— 0.158	+ 0.893	+ 1.215	+ 0.0405	+ 0.00081
2	2267.30	— 0.00950032	2	+ 0.039	+ 0.931	+ 1.137	— 0.0482	— 0.00365
3	57.5575	+ 0.216065	3	+ 0.655	+ 1.586	— 0.172	— 0.0950	+ 0.00343
4	7.76103	— 0.925135	4	— 1.547	+ 0.039	+ 2.922	+ 0.3748	+ 0.01280
5	3.82629	+ 0.870883	5	+ 1.461	+ 1.5	0	— 0.4162	— 0.02350

TABLE 7.5.

Numerical results for case (2b).

i	A_i	α_i	k	P_0	P_1	$a\,S_1$	T_0	$\frac{1}{R}\,M_0$
—	—	—	0	0	0	— 0.0156	0	0
—	—	—	1	0.5	0.564	+ 0.0488	— 0.0118	— 0.00044
2	273.521	+ 0.00236495	2	0.866	0.805	— 0.0124	+ 0.0278	— 0.00176
3	8.06964	— 0.0925607	3	1	0.842	— 0.1703	+ 0.0142	+ 0.00221
4	1.99982	+ 0.323460	4	0.866	1.361	+ 0.3248	— 0.1218	+ 0.00439
5	1.49068	— 0.250534	5	0.5	0	— 0.1753	+ 0.1462	— 0.00854

TABLE 7.6.

Numerical results for case (3b).

i	B_i	α_i	k	P_0	P_1	$a\,S_1$	$a\,S_2$	T_0	$\frac{1}{R}\,M_0$
—	—	—	0	0	0	+ 3.543	+ 4.110	0	0
—	—	—	1	1.5	+ 1.089	+ 3.133	+ 1.931	— 0.151	+ 0.0030
2	2267.30	+ 0.0354557	2	2.598	+ 0.721	+ 1.256	+ 0.488	+ 0.180	— 0.0137
3	57.5575	— 0.806365	3	3	— 1.444	— 3.188	+ 3.376	+ 0.355	+ 0.0128
4	7.76103	+ 3.45265	4	2.598	+ 6.640	+ 0.854	— 9.904	— 1.399	+ 0.0478
5	3.82629	— 3.25018	5	1.5	— 4.952	— 5.598	0	+ 1.553	— 0.0878

TABLE 7.7.

Numerical results for case (1b), $m = 4$.

i	B_i	α_i	k	P_1	$a\,S_1$	$a\,S_2$	T_0	$\frac{1}{R}\,M_0$
—	—	—	0	0	+ 0.977	+ 1.046	— 0.038	— 0.0204
—	—	—	1	— 0.937	+ 0.040	+ 2.919	— 0.770	+ 0.0027
2	2267.30	— 0.142593	2	+ 3.921	+ 3.962	— 4.923	+ 1.647	+ 0.0932
3	57.5575	+ 1.66798	3	— 5.941	— 1.979	+ 6.958	— 0.833	— 0.0475
4	7.76103	— 0.398066	4	+ 3.479	+ 1.5	0	— 0.481	— 0.0882
5	3.82629	— 4.27260	5	0	+ 1.5	0	0	0

TABLE 7.8.

Numerical results for case (1b), $n = 12$, $m = 11$.

i	B_i	α_i	k	$a\,S_1$	$a\,S_2$
—	—	—	0	0.999	1.002
—	—	—	1	1.003	0.993
2	5174.61	— 0.000541240	2	1.006	0.988
3	145.794	+ 0.0124267	3	0.998	1.004
4	16.9052	— 0.076888	4	0.979	1.042
5	5.46588	+ 0.178929	5	0.972	1.055
6	3.31279	— 0.226530	6	1.015	0.970
7	2.60479	+ 0.221069	7	1.100	0.800
8	2.27407	— 0.190526	8	1.103	0.793
9	2.09102	+ 0.148657	9	0.846	1.308
10	1.98517	— 0.101292	10	0.477	2.045
11	1.92919	+ 0.0512125	11	1.5	0

TABLE 7.9.

Numerical results for case (1b), $n=12$, $m=11$, $\left(\frac{E}{\mu}\right)\left(\frac{A_S}{at}\right)=0.75$, etc.

i	B_i	α_i	k	$a\,S_1$	$a\,S_2$
—	—	—	0	1.000	0.999
—	—	—	1	1.005	0.990
2	2587.80	— 0.00068343	2	1.005	0.990
3	73.397	+ 0.015588	3	0.992	1.015
4	8.9526	— 0.091682	4	0.973	1.055
5	3.23294	+ 0.19103	5	0.976	1.048
6	2.15639	— 0.21976	6	1.034	0.932
7	1.80240	+ 0.20174	7	1.115	0.771
8	1.63704	— 0.16713	8	1.079	0.841
9	1.54551	+ 0.12700	9	0.798	1.403
10	1.49257	— 0.085074	10	0.522	1.956
11	1.46460	+ 0.042598	11	1.5	0

TABLE 7.10.

Numerical results for case (1b), $n=12$, $m=10$, $\left(\frac{E}{\mu}\right)\left(\frac{A_S}{at}\right)=0.75$, etc.

i	B_i	α_i	k	$a\,S_1$	$a\,S_2$
—	—	—	0	1.016	0.967
—	—	—	1	1.021	0.957
2	2587.80	— 0.00421503	2	0.996	1.008
3	73.397	+ 0.0809695	3	0.925	1.149
4	8.9526	— 0.359999	4	0.880	1.241
5	3.23294	+ 0.468023	5	1.000	1.000
6	2.15639	— 0.190188	6	1.307	0.386
7	1.80240	— 0.145086	7	1.446	0.107
8	1.63704	+ 0.366968	8	0.803	1.395
9	1.54551	— 0.439912	9	— 0.395	3.790
10	1.49257	+ 0.377438	10	1.5	0
11	1.46460	— 0.215043	11	1.5	0

TABLE 7.11.

Numerical results for the relative stiffness parameter η.

Case	m	n	$\frac{EA_S}{at}$	$\frac{A_S}{A_R}$	$\frac{A_S R^2}{I}$	η
(1a)	5	6	1.5	1.0	3000	0.8782
(2a)	5	6	1.5	1.0	3000	0.7829
(3a)	5	6	1.5	1.0	3000	0.9669
(1b)	5	6	1.5	1.0	3000	0.3624
(2b)	4	6	1.5	1.0	3000	0.8282
(3b)	5	6	1.5	1.0	3000	0.1921
(1b)	4	6	1.5	1.0	3000	0.0249
(1b)	11	12	1.5	1.0	3000	0.8248
(1b)	11	12	0.75	0.5	1500	0.7802
(1b)	10	12	0.75	0.5	1500	0.3480

TABLE B. 1.

Numerical results for the relation between θ and S_2.

θ (radian)	0	$\frac{\pi}{180}$	$\frac{\pi}{36}$	$\frac{\pi}{18}$	$\frac{\pi}{6}$	$\frac{\pi}{3}$	$\frac{\pi}{2}$	$\frac{2\pi}{3}$	$\frac{5\pi}{6}$	π
$\frac{2\pi R^2}{T} S_2$	0	0.15	0.62	0.97	1.20	0.93	1.01	1.01	1.01	1.01

C. C. L. Class. B 276

REPORT V. 1543.

Drawing Sphere for Analysis of Flight Test Results

by

Ir. S. WYNIA and Ir. L. R. LUCASSEN.

Summary.

A *drawing sphere*, an octant gauge and a great-circle gauge are described. These tools have been designed and constructed to facilitate and accelerate the analysis of flight test results. An example of their application is included.

Contents.

1 Introduction.

The determination of aeroplane motions from observations of flight test instruments often necessitates tedious calculations, particularly for unsteady asymmetric flight conditions. This is mainly due to the fact that, in general, neither a gyrohorizon nor a lateral bank indicator indicates the true bank of the aeroplane. A similar difficulty occurs with the socalled side-slip indicator, which generally does not measure the side-slip angle, i. e. the angle between the airspeed vector and the plane of symmetry. Laborious calculations, based on spherical trigonometry, are inevitable to compute the exact values of angle of incidence, side-slip and lateral bank.

Therefore, the problem has been studied whether a device might be developed to facilitate and accelerate the "translation" of instrument readings into quantities determining the attitude of an aeroplane and the direction of its velocity relative to the air. A study of literature revealed that two ingenious mechanical computors, able to visualise the relative positions of several systems of axes have been built in France (*refs.* 1 and 2). Their construction is rather complicated and their use limited to the vertical spin. Similar devices are described in *refs.* 3 and 4.

A new method for the approximate solution of spherical trigonometric problems is described below. Use is made of a drawing sphere and two drawing-aids, viz. an octant gauge and a great-circle gauge. A short account on their construction is also given in *ref.* 5.

2 General data and construction.

2.1 *Sphere.*

Some general data of the drawing sphere (fig. 1) as constructed by the National Aeronautical Research Institute are as follows

diameter	$d \approx$	55 cm (1 ft. 9.6 inch.)
surface	$\pi d^2 \approx$	9500 cm² (10.2 sq.ft.)
free surface available	$\approx$	99.9 %
weight	$\approx$	30 kg (66 lbs.)

The sphere has been made of an oxygen bottle which was originally part of a V-1 flying bomb. After removing the steel wire strips, which served to strengthen the bottle, its shape was improved by subjecting it to an internal water pressure of about 25 atm. (355 lbs./sq. inch.). As the shape obtained was still far from being spherical, a skin had to be attached to the bottle. To this end some hundred dove tail strips were welded to the steel surface, in order to give a solid attachment. The steel surface was cleaned by sandblasting and covered with asphalt to prevent corrosion.

The skin consists of wood-granite (Sorel cement), stuck to the steel. The ultimate shape was obtained between the centres of a lathe by means of a circular mould. The surface, after further careful preparation has been finished with dull white lacquer. It appeared to lend itself properly to pencil drawing. Lines may easily be wiped out with eraser or a wet cloth.

2.2 *Support.*

The construction of the support is shown in fig. 1. The sphere is sustained on the outer end of a 90 degrees arm allowing the sphere to rotate on a central axis; the other end of the arm is mounted on a vertical sliding piece in such a way that rotation on a horizontal axis is possible.

The sliding piece moves along a vertical column by means of which the sphere can be fixed at various heights. Placing the sphere in any desired position is facilitated by balancing the mounting system.

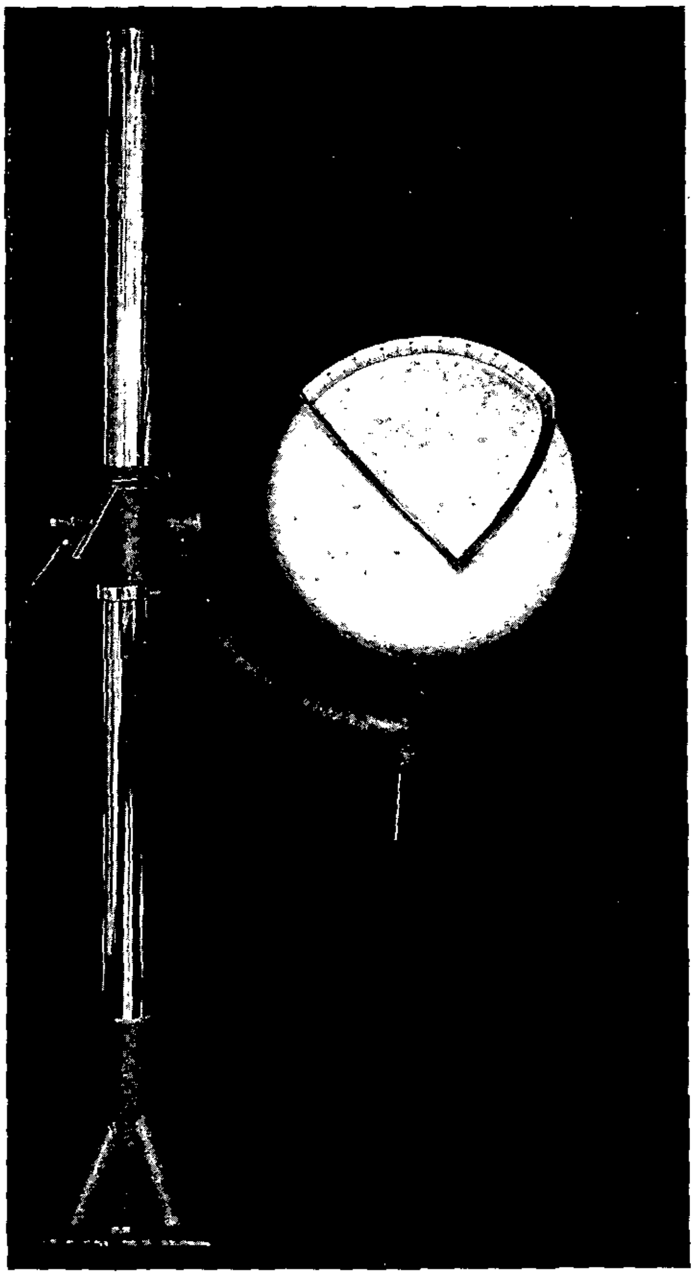

Fig. 1. Drawing sphere and support.

2.3 *Octant gauge.*

The octant gauge is a valuable aid for carrying out geometrical drawings and measurements on the sphere surface, in particular for finding the pole of a greatcircle. It consists of three 90 degrees arcs, combined to a rectangular spherical triangle. The sides are graduated in half degrees. One degree is about 0.5 cm ($\approx {}^{13}/_{64}$ inch.), so that tenths of degrees can be estimated. The construction is shown in fig. 1. Its weight is only 0.6 kg ($\approx$ 1.5 lbs) as the main parts have been made from aluminium alloy.

2.4 *Great-circle gauge.*

Another aid to facilitate the drawing of great-circles on the sphere is a 150 degrees great-circle gauge, graduated in half degrees (fig. 2). A short cross-bar, attached perpendicularly to the middle of the gauge, makes the desired positioning on the surface possible. The weight and material of this tool are the same as that of the octant gauge.

3 **Application of the sphere and drawing-aids.**

As an illustration of the several ways in which these tools may be used, one application with regard to the evaluation of flight test results will be described here.

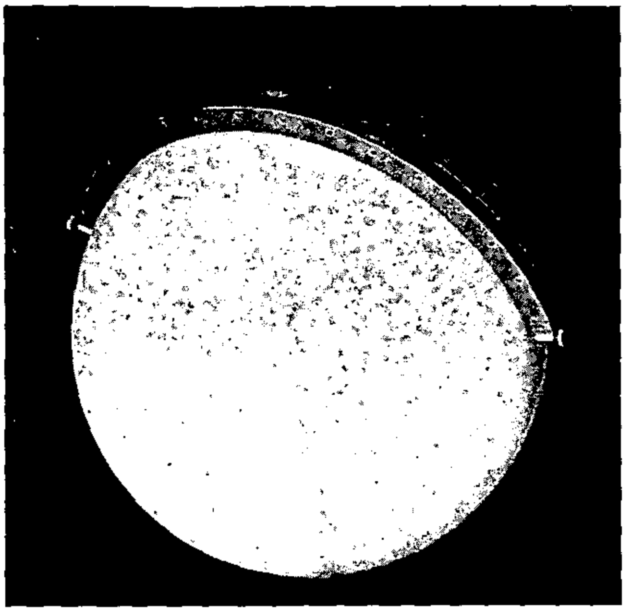

Fig. 2. Great-circle gauge.

Suppose that the following six quantities have been obtained from the aeroplane instrument readings (see fig. 3):

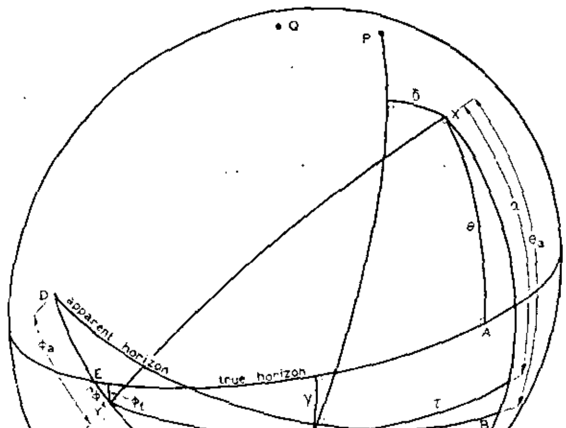

Fig. 3. δ is the angle of side-slip as measured by the instrument described in *ref.* 6, i.e. the angle between the longitudinal axis of an aeroplane and the plane through the airspeedvector and the pole P of the apparent horizon.

- δ indication of side slip indicator,
- θ true fore and aft level, } from gyro-horizon,
- ϕ angle of roll about longitudinal axis } from gyro-horizon,
- θ_a indication of pendulum fore and aft level,
- ϕ_a indication of pendulum bank indicator,
- γ flight-path angle from altitude and airspeed *time histories.*

The problem is now to find the angles of incidence α, of sideslip τ and of lateral bank ϕ_t.

It will be obvious that a numerical solution of this problem, even apart from the derivation of the necessary formulae, takes rather a long time (about one hour). The use of this method is therefore justified only if highly accurate values are required. The drawing sphere, however, provides the important advantage of a rapid solution with reasonable accuracy.

Proceed then as follows to solve the problem mentioned above. To simplify the description, the angular points and sides of the octant gauge are called A_g, B_g, C_g, and a_g, b_g, c_g respectively.

a Put the octant gauge in an arbitrary position on the sphere and draw the great-circles XY, YZ and ZX.

b Mark on ZY the points D and E so that YD and YE are equal to the given ϕ_a and ϕ. Mark point B on XZ so that XB is equal to θ_a. Draw the "apparent horizon" DB with the great-circle gauge.

c Put side a_g of the octant gauge on DB and mark on the sphere the pole P of DB in the angular point A_g.

d Put the angular point A_g on E. Side a_g then passes through X. Turn the gauge on E until arc XB_g is equal to θ. Mark point A in B_g. Mark the true horizon by drawing EA along c_g; mark also its pole Q which coincides with C_g.

e Measure the desired value of the lateral bank ϕ_t along the great circle through Y perpendicular to EA.

It is left to the reader to find the method for determining α and τ.

The complete solution of this problem takes about ten minutes only. An accuracy of the order of one or two tenths of a degree can be obtained. Another advantage over the numerical method is, that the drawings on the sphere give a very clear picture of the aeroplane's attitude.

The example explained above is only one of the many problems which may be solved easily in the way described. It is believed that a broad field of applications for the drawing sphere exists.

4 References.

1. CHAFFOIS, J. Calculateurs mécaniques de caractéristiques de vrille libre en soufflerie verticale. Publ. Scient. et Techn., Min. de l'Air. Note Techn. No. 18, 1945.
2. DUBOIS, G. Etude expérimentale de la vrille. Publ. Scient. et Techn., Min. de l'Air. Bull. des Serv. Techn. No. 107.
3. THIEL, G. und HUFFSCHMIDT, A. Der Trudelwindkanal der DVL. Jahrb. 1942 der deutschen Luftf.f. Seite I, 419.
4. BAUMHAUER, A. G. VON. Sphero-triangulator. R. S. L.-Rapport V. 402. 8-7-1930.
5. WYNIA, S. Rekenbol voor de uitwerking van meetresultaten in willekeurige vliegtoestanden. N. L. L.-Rapport V. 1476, Sept. 1948.
6. MUNSTER, G. VAN en DIJKMAN, R. Beproevingen van een sliphoekmeter met gesloepte windvaan en aanwijzingen voor het gebruik ervan. N. L. L.-Rapport V. 1454, Mei 1949.

CCL Class. E 004

REPORT V. 1547.

The Effect of a Spring Tab Elevator on the Static Longitudinal Stability of an Aeroplane

by

Ir. A. J. MARX and Drs. J. BUHRMAN.

Summary.

An investigation is made of the influence of a spring tab provided elevator on the static longitudinal stability. It appears that in most cases the stick fixed stability is decreased as a result of the action of the spring in the control mechanism.

An expression for the stability margin stick fixed is given bij formula (3.8).

The influence of the spring on stick free stability is negligible.

Contents.

N.B. The investigation was carried out by order of the Netherlands Aircraft Development Board.

1 Introduction.

In considering the stick fixed longitudinal stability of an aeroplane it is usually assumed, that the stick fixed condition of flight implies an invariable position of the elevator. This is no longer true in the case of a spring tab provided elevator because of the action of the spring element, which is installed in the control circuit between stick and elevator.

Therefore it is investigated in this report how stability is affected by the application of the spring tab. Effects of friction in the control mechanism are neglected.

2 General description and principle of the spring tab.

The spring tab is used in order to reduce the control-forces of heavy and fast aeroplanes. The operating principle is elucidated with fig. 1. The elevator lever AB is freely hinged at A, whereas the tab lever CD is rigidly connected to the tab. When the pilot pulls his control the spring S is deflected, which causes a deflection of the tab depending on the exerted force and the stiffness of the spring. For a given spring constant the tab deflection is large when the control force is high. So the spring tab may be considered as a geared tab with a variable gear, which is high

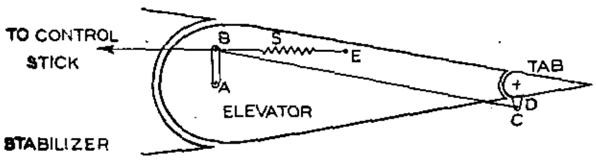

Fig. 1.

in case of high control forces. It is obvious, that increasing the stiffness of the spring decreases the effectiveness of the system.

In an earlier report [1]) of the National Aeronautical Research Institute (N. L. L.) the authors considered the influence of the spring tab on the control force as a function of speed.

3 Static longitudinal stability.

3.1 *Stick fixed.*

The equilibrium of the steady flight condition is defined to be statically stable if as a result of a disturbance in wing incidence (or lift coefficient) a pitching moment is generated, which tends to decrease the disturbance or

$$\frac{dc_m}{d\alpha} < 0 \qquad (3.1)$$

when tailheavy pitching moments are defined to be positive.

Two modes of static stability are distinguished,

[1]) Report V. 1398.

stick fixed and stick free. The former is related to the condition, that the stick is held in an invariable position.

For a normal elevator this implies a constant elevator angle; this however, is no longer true for a spring tab elevator, as the spring allows a deflection of the control surface with stick fixed (see the sketch in fig. 1).

In the usual notation (§ 5) the pitching moment of the whole aeroplane in steady flight can be written

$$c_m = c_{m0} + (h - h_0)c_a - \overline{V}\left[\frac{a_1}{a}\left(1 - \frac{d\varepsilon}{d\alpha}\right)c_a + a_1\sigma + a_2\beta + a_3\beta' + a_{3S}\gamma\right] = 0. \quad (3.2)$$

An increase Δc_a in the liftcoefficient brings about a change in pitching moment:

$$\Delta c_m = (h - h_0)\Delta c_a - \overline{V}\left[\frac{a_1}{a}\left(1 - \frac{d\varepsilon}{d\alpha}\right)\Delta c_a + a_2\Delta\beta + a_{3S}\Delta\gamma\right] \quad (3.3)$$

Furthermore the elevator hinge moment can be written, when the tab hinge moment is neglected and the elevator is statically balanced (see notations):

$$c_H = \frac{b_1}{a}\left(1 - \frac{d\varepsilon}{d\alpha}\right)c_a + b_1\sigma + b_2\beta + b_3\beta' + b_{3S}\gamma - \frac{Sl_1C}{\frac{1}{2}\rho V^2 F_\beta t_\beta} = 0. \quad (3.4)$$

The last term of the right-hand side of (3.4) represents the hinge moment created by the spring; C is the spring constant, l_1 the length of the elevator lever and S the deflection of the spring (positive, when the spring is elongated).

In fig. 2 two positions of the elevator control

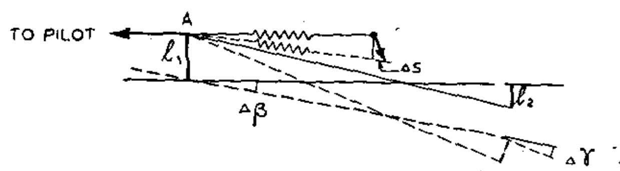

Fig. 2.

surfaces are drawn in the stick fixed case. Note that the point A remains in the same position and that $\Delta\beta$ and $\Delta\gamma$ have the same sign.

From this figure it appears that

$$\Delta\gamma = \frac{l_1}{l_2}\Delta\beta \quad (3.5)$$

and

$$\Delta S = l_1\Delta\beta. \quad (3.6)$$

When a disturbance Δc_a occurs, the new position of the surfaces will be such, that

$$\Delta c_H = \frac{b_1}{a}\left(1 - \frac{d\varepsilon}{d\alpha}\right)\Delta c_a + b_2\Delta\beta + b_{3S}\Delta\gamma - \frac{\Delta S l_1 C}{\frac{1}{2}\rho V^2 F_\beta t_\beta} = 0. \quad (3.7)$$

Eliminating $\Delta\gamma$, ΔS and $\Delta\beta$ from (3.3), (3.5), (3.6) and (3.7) gives for the static margin stick fixed K_n:

$$K_n = -\frac{\Delta c_m}{\Delta c_a} = (h_0 - h) + \overline{V}\,\frac{1 - \frac{d\varepsilon}{d\alpha}}{a}\left[a_1 - \frac{b_1\left(a_2 + \frac{l_1}{l_2}a_{3S}\right)}{b_2 + \frac{l_1}{l_2}b_{3S} - \frac{l_1C}{\frac{1}{2}\rho V^2 F_\beta t_\beta}}\right]. \quad (3.8)$$

For a normal elevator the static margin is simply

$$H_n = (h_0 - h) + \overline{V}\,\frac{1 - \frac{d\varepsilon}{d\alpha}}{a}a_1. \quad (3.9)$$

If both b_2 and b_1 are negative (the elevator is not aerodynamically overbalanced and does not trail against the local wind) the formulae (3.8) and (3.9) show that the spring tab causes a loss in stick fixed stability as all other quantities, except b_{3S}, between the square brackets in (3.8) are positive. Even if b_2 is slightly positive and b_1 negative the stick fixed stability is decreased. Normally speaking it can be said that a gain in stability due to the spring tab is only possible if $b_1 > 0$. In general, however, a spring tab will be seldom combined with a closely balanced elevator.

In all cases a large value of C (stiff spring) corresponds with a small stability change.

In the next paragraph this change in stability will be compared with the stability change as a result of freeing the stick.

3.2 *Stick free.*

According to the well-known theory the "static margin stick free" K_n' in case of a statically balanced normal elevator can be represented by

$$K_n' = (h_0 - h) + \overline{V}\,\frac{1 - \frac{d\varepsilon}{d\alpha}}{a}\left(a_1 - \frac{b_1}{b_2}a_2\right) \quad (3.10)$$

Comparison of (3.9) and (3.10) shows that the change in stability on freeing the stick depends on $\frac{b_1}{b_2}$; a positive (negative) value of $\frac{b_1}{b_2}$ corresponds with a loss (gain) in stability.

If we assume the hinge moment of the tab to be small there can only be a minor deflection in the spring S (see fig. 1) in the stick free case. From that it follows, that the free floating angle of the elevator with spring tab is almost the same as for the normal elevator. So it can be concluded, that the influence of the spring tab on stick free stability is negligible.

Finally it appears from (3.8) and (3.10) that in most cases the change in stability due to the spring tab is a fraction of that due to freeing the stick.

4 Conclusions.

In this report the influence of a spring tab elevator on the static longitudinal stability is investigated. The static margin stick fixed for the normal elevator and the spring tab provided elevator are given in the formulae (3.9) and (3.8). It appears from these formulae, that in most cases ($b_1 < 0$ and $b_2 < 0$) the stability is decreased as a result of the spring action by an amount which is a fraction of the stability loss due to freeing the stick with tab locked.

The stick free stability is almost unaffected by the application of the spring tab.

5 Notations

F wing area
F_H area of the horizontal tail surface
F_β area of the elevator
t wing chord
t_β elevator chord
l_H distance of aerodynamic centre of tail aft of aerodynamic centre of the aeroplane without tail
$\overline{V}$ $\left(=\frac{l_H F_H}{Ft}\right)$ tail volume
V forward speed of the aeroplane
ρ air density
α incidence of zero lift line
α_H tail incidence
β elevator deflection (positive when downward)
β' deflection of the fixed tab (positive when downward)
γ deflection of the spring tab (positive when downward)
ε downwash angle
σ tail plane setting
c_a lift coefficient
c_{aH} tail lift coefficient
a $=\frac{\partial c_a}{\partial \alpha}$
c_m pitching moment coefficient $\left(\frac{M}{\frac{1}{2}\rho V^2 F t}\right.$; positive when tailheavy$\left.\right)$
c_{m_0} c_m when $c_a = 0$ for aircraft without tail
c_H elevator hinge moment coefficient $\left(\frac{H}{\frac{1}{2}\rho V^2 F_\beta t_\beta}\right.$; positive in the same sense as $c_m\left.\right)$
a_1 $=\frac{\partial c_{aH}}{\partial \alpha_H}$
a_2 $=\frac{\partial c_{aH}}{\partial \beta}$
a_3 $=\frac{\partial c_{aH}}{\partial \beta'}$
a_{3S} $=\frac{\partial c_{aH}}{\partial \gamma}$
b_1 $=\frac{\partial c_H}{\partial \alpha_H}$
b_2 $=\frac{\partial c_H}{\partial \beta}$
b_3 $=\frac{\partial c_H}{\partial \beta'}$
b_{3S} $=\frac{\partial c_H}{\partial \gamma}$
ht distance of centre of gravity of the aeroplane aft of leading edge of chord
$h_0 t$ distance of aerodynamic centre of the aeroplane without tail aft of leading edge of chord
K_n static margin stick fixed
K_n' static margin stick free
$l_1 l_2$ lever lengths (see fig. 2)
C spring constant
S spring deflection.

Completed: November 1949.

V 8